Influence of temperature on natural vibrations of steel bridges

by

C.N.Kortendijk

to obtain the degree of Master of Science
at the Delft University of Technology,
to be defended publicly on December 9, 2020.

Committee

Prof. dr. A.V. Metrikine	TU Delft	Chair
dr. E. Lourens	TU Delft	Daily supervisor
Ir. C. Kasbergen	TU Delft	Assessor
Ir. F. Besseling	Witteveen+Bos	Daily supervisor
Ir. C. Jolink	Witteveen+Bos	Daily supervisor

Contents

1 Summary

In the 1960s, after the second world war, dozens of steel bridges were (re-)built in the Netherlands. In this period the weight and intensity of freight traffic was significantly lower than it has been in recent years. Many of these old bridges, now loaded beyond their original design strength, are starting to show signs of metal fatigue. Fatigue-cracks and other defects induce a local drop in stiffness, influencing the eigenfrequencies of local vibrations modes of the bridge. Vibration based Structural Health Monitoring (SHM) is a promising method that aims to detect these small fatigue cracks, by measuring the forced and free vibrations of the bridge. One recurring problem in vibration based SHM-research, is the operational and environmental variability. This variability has a significant effect on the dynamic characteristics, potentially masking the measurable consequences of small defects.

Environmental variabilities such as ambient temperature, solar radiation, wind and rain, influence the temperature of the bridge, and are thought to be a major cause of the daily variation in eigenfrequencies. In order to overcome the uncertainty due to these daily variations, extensive research has been performed on filtering methods and machine learning approaches, but these methods show poor performance. Very limited research has been performed on determining the exact cause of daily variability in the dynamic characteristics of steel bridges. A better understanding of the underlying mechanisms might improve the usability of future SHM-campaigns. Therefore the Haringvlietbrug, a 1 km long 10 span continuous steel box girder bridge in the Netherlands, is selected to study the influence of temperature on natural vibrations of steel bridges.

A set of 92 strain sensors and 54 temperature sensors was already mounted on the Haringvlietbrug, for a recalculation and prediction of remaining structural lifetime. Additional temperature sensors were placed, capturing vertical and horizontal gradients of the asphalt and deck plate temperature. A LVDT displacement sensor was placed at a roller-support, in order to verify axial elongation of the bridge. The bulk of the measurements were carried out between May 22 and June 12 2020. All strain and temperature measurements were downsampled to 1 sample per minute, low-pass filtering was applied and sensors were compensated for temperature drift.

Asphalt reached temperatures of up to 54.9°C on Aug 07, 2020, but no strain measurements are available after June 12 2020. A warm period where all sensors were available is from May 30 to June 01 2020. In this period temperature of the the top asphalt layer shows a daily cycle with approximately 12°C at night and up to 45°C at 14:00. The top and bottom asphalt sensors are just 40 mm apart, and yet show temperature differences of up to 6°C. In the heat of the day, the bottom of the 10 mm steel deck plate was up to 4 °C cooler than the bottom asphalt sensor, these sensors were 20 mm apart. Above the box girder, significantly higher deck plate temperatures were reached, and cooling in the evening was slower, than for the cantilevers. This is attributed to air inside the box-girder acting as a heat buffer and an insulator against the environment. Steel traffic barriers were found to cast partial shade on the asphalt in the mornings and evenings, strongly influencing the local deck temperature.
At sunrise and sunset, solar radiation affected the lower parts of the vertical East- and West box wall respectively, causing a significant local temperature rise. During the heat of the day, the cantilevers cast shade on the box walls, and they remain relatively cool. Daily strain variation for the box walls of 150 $\mu\varepsilon$ from trough to crest were found.

A 3D FE-Model of the bridge was created, with the intention of reproducing temperature induced stress and stain in the bridge, based on the recorded temperatures at the distinct sensor locations. The 2D temperature distribution inside the bridge was modelled with 11 load cases containing piecewise linear temperature interpolation functions between sensor positions. Measured temperatures were converted to load case solicitation factors, obtaining simulated stress and strain at the sensor positions for each minute in the period of interest. FEM results were compared against strain measurements to asses the validity of the model. On most days deviations in stress and strain were below 30% for most sensors, with the lower part of the West box wall an outlier showing 50% deviation. Local heating of the lower parts of the box wall at sunrise and sunset induces significant stress and strain along the entire cross-section, with the estimated local compression stress change in the box wall reaching over 40 MPa. Days with rain show larger deviations between model and measurements. Addressing these deviations is recommended, but would require more information from specific additional sensor locations.

Sub-models of the bridge are evaluated to determine influence of temperature induced stress on dynamic characteristics. For each sub-model the first eigenmode is considered. For higher modes the change of frequency due to temperature induced stress diminishes. The rib-deck spanning 2 crossbeams was evaluated analytically as a 1D beam-column and showed a 0.8% change of its first eigenfrequency, due to stress variations in the period of interest. The asphalt deck plate composite was evaluated as a 2D-plate using the Rayleigh-Ritz procedure. Compression stress in the longitudinal direction was found to be largest, both in absolute value as in daily variance, but the strain in the transversal direction, smaller both in size and variance, was found to be governing for the composite deck plate vibrations. A shift of 1.3% of the first eigenfrequency was predicted. Side-way vibrations of a longitudinal rib, acting as a deck stiffener, are predicted using FEM, and the influence of the daily stress change results in a 0.2% change in the first eigenfrequency.

Finally the influence of asphalt non-linearity is evaluated. The supplied asphalt properties do not fully cover all required temperatures and loading frequencies. Therefore master curves have been constructed in order to study potential effects at higher temperatures and frequencies. A sigmoid function was fitted to this master curve, and using the WLF-equation the sigmoid could be shifted once again to obtain asphalt properties for all temperatures and frequencies of interest.
Asphalt was found to have significant influence on local vibrations of subsystems containing the asphalt- deck plate composite. The 2D asphalt- deck plate composite that was shown to have a frequency shift of 1.3% due to temperature induced stress, showed a 53% drop in eigenfrequency due to temperature dependent asphalt properties. The rib-deck beam-column is expected to have a 5.3% drop in the first eigenfrequency due to asphalt temperature, while temperature induced stress induced only a 0.8% frequency drop. The temperature dependent asphalt properties also influence the fundamental mode of the entire bridge, a $\approx 1\%$ change in eigenfrequency of the bridge was found. While temperature induced stress influence on dynamic characteristics diminishes for higher modes, the influence of asphalt stiffness is expected to be similar for all modes.

Asphalt non-linearity was found to be the dominant factor in the change of dynamic characteristics due to environmental variability. Therefore it is advised to thoroughly cover asphalt non-linearity in future SHM-campaigns.

2 Introduction

Maintenance planning of bridges is generally supported by an inspection regime. As an alternative to traditional visual inspections, modern Structural Health Monitoring (SHM) techniques could be used. One of these techniques is vibration-based monitoring. Previous research results indicate the effects of temperature on the dynamic characteristics to be very significant. As a consequence, temperature effects may overrule the effect of minor structural damage, and thus need to be filtered out. While black box approaches using mathematical or AI techniques to filter out the temperature effects do exist to some extent, a better fundamental understanding of the relations between (differential) temperature deviations and vibration modes may contribute to deal with this phenomenon. To obtain this understanding, a set of research questions is formulated in chapter 2.1.

2.1 Research Questions

Main research question

How do temperature changes due to environmental influences, affect vibration characteristics of steel bridge decks?

Sub questions

The sub questions are grouped according to the orange boxes in figure 2.1.

Sub-questions concerning the temperature distribution

1. What are the temperature distributions that occur in the bridge due to environmental influences?
2. To what extent can these complex 3D temperature distributions be simplified in order to obtain homogeneous or linear-varying component temperatures?

Sub-questions concerning temperature induced strains

3. Which altered strain distributions in structural components occur due to environmental changes?
4. How do these altered strain distributions influence the dynamic characteristics of the structural components of interest?

Sub-questions concerning temperature induced stresses

5. Which altered stress distributions in structural components occur due to environmental changes?
6. How do these altered stress distributions influence the dynamic characteristics of the structural components of interest?

Sub-questions concerning changing material properties

7. Which material properties change due to temperature distributions?
8. How do these changing properties influence the dynamic characteristics of the structural components of interest?

Sub-questions relating the vibrations to the temperature measurements

9. What is the relation between the expected dynamic properties of the system and the measured temperature data?
10. Which temperature sensor layout is required in order to predict this change of dynamic characteristics?

2.2 Methodology

To answer the research question, the behaviour of the Haringvlietbrug will be studied, using measurements and a FE-model of the bridge. The flowchart of this process can be seen in figure 2.1.

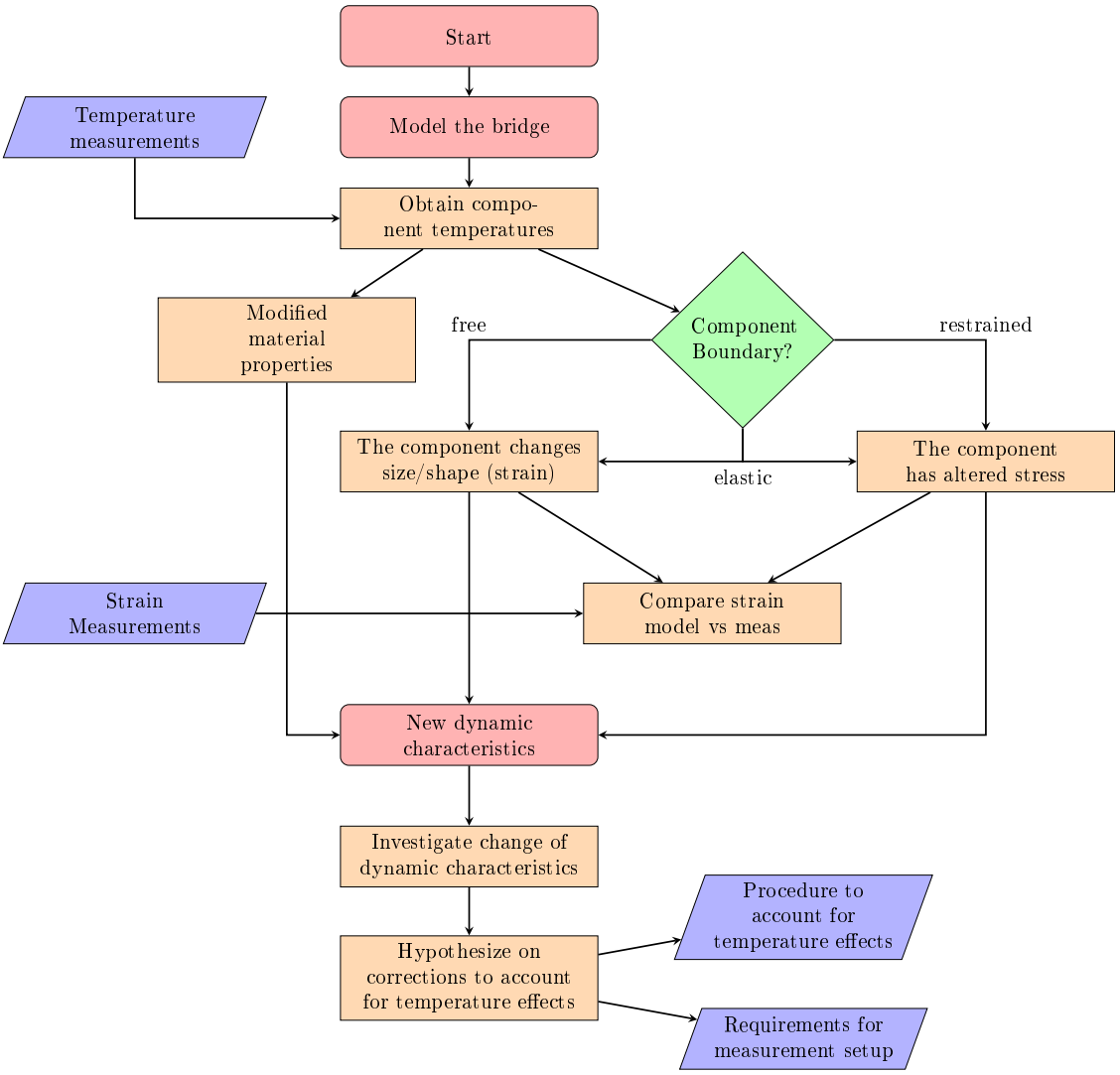

Figure 2.1: Analysis flowchart

3 Literature Review

3.1 Temperature distribution in bridges

The temperature distribution in bridges is not homogeneous, but can vary due to e.g. solar radiation, wind, rain, convection and radiation. Research was carried out on the measured and expected temperature distributions in bridges, in order to design a temperature sensor layout for the Haringvlietbrug. The goal is to capture all expected temperature gradients with the sensors, and later model these in a Finite Element Model of the bridge.

3.1.1 Design codes

The current code for temperature loads on structures in the Netherlands is part of the Eurocode, and the "NEN-EN 1991-1-5 +NB2019" [1] and [2] specifically. Eurocode allows the temperature load to be split in 4 parts:

- Homogeneous temperature
- Linear temperature gradient around z-z axis
- Linear temperature gradient around y-y axis
- Non-linear gradient

Chapter 6 of [1] and [2] deals with bridges specifically. It splits the temperature load in 3 parts:

Homogeneous temperature This part is based on the shadow air temperature T. The Haringvlietbrug has a steel deck, and thus the maximum homogeneous design temperature is $T_{e,max} = T_{max} + 16°C$ while the is $T_{e,min} = T_{min} - 3°C$. If no specific data is available $T_{max} = 30°C$ and $T_{min} = -25°C$ and thus the homogeneous bridge temperature varies between $-28°C$ and $+46°C$

Vertical temperature gradient The National annex [2] requires a non-linear approach to the vertical temperature gradient as can be seen in figure 3.1.

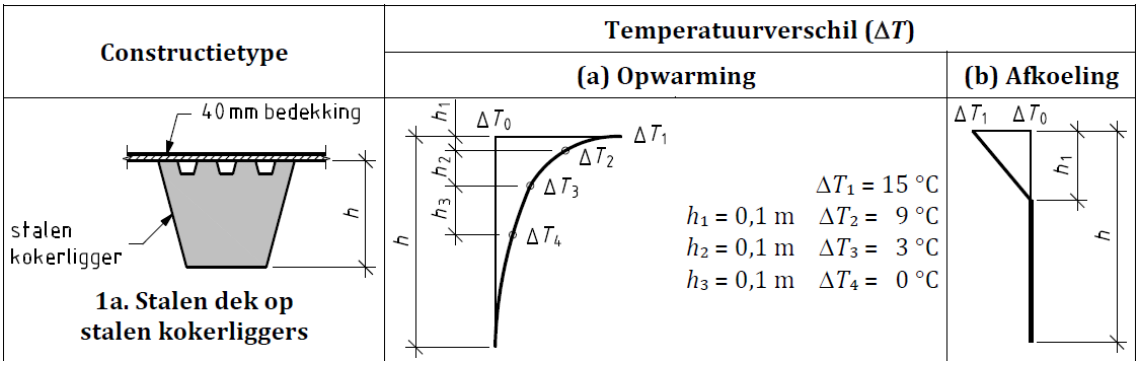

Figure 3.1: Non-linear vertical temperature gradient from NEN-EN 1991-1-5 NB:2011

Horizontal temperature gradient In case the bridge is oriented in a way such that some areas are exposed to sunlight for prolonged period the Dutch Annex to Eurocode [2] requires a linear horizontal temperature gradient with a $\Delta T = 5^{\circ}C$ or higher.

Combining the gradients The worst case of the following combinations needs to be taken into account:

$$\begin{array}{rlll} I) & 1.0\Delta T_{M,heat} & +0.35 & \Delta T_{N,exp} \\ II) & 1.0\Delta T_{M,cool} & +0.35 & \Delta T_{N,con} \\ III) & 0.75\Delta T_{M,heat} & +1.0 & \Delta T_{N,exp} \\ IV) & 0.75\Delta T_{M,cool} & +1.0 & \Delta T_{N,con} \end{array} \tag{3.1}$$

with:$\Delta T_{M,heat}$ = gradient due to heating
$\Delta T_{M,cool}$ = gradient due to cooling
$\Delta T_{N,exp}$ = homogeneous temperature resulting in thermal expansion$\Delta T_{N,con}$ = homogeneous temperature res

Comparison to other codes Rimal & Sindeler [3] have compared the temperature loads of CSN 73 6203, ENV 1991-2-5 (predecessor to current Eurocode) and DIN 1072 for different bridge types. They found a significant difference between the DIN and the other 2 codes for the load during cooling of the bridge. The DIN created negative bending moment in a span, while the other 2 resulted in zero bending moment.

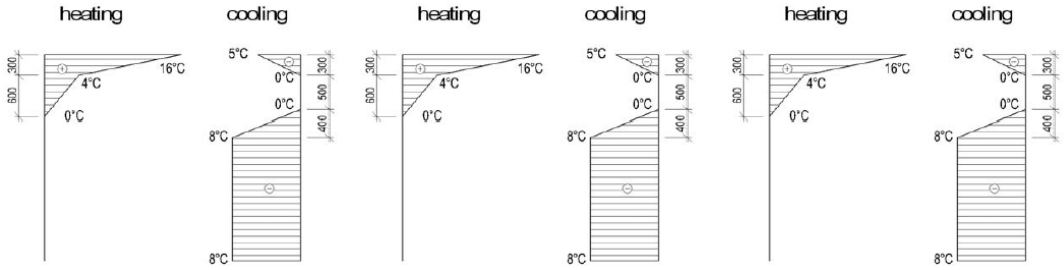

(a) CSN 73 6203 (b) ENV 1991-2-5 (c) DIN 1072

Figure 3.2: Inhomogeneous temperature loads from different codes.(Rimal and Sindler [3])

3.1.2 Measurements of bridge temperatures

Ding and Wang [4] have analysed 5 years of temperature measurements of the Runyang cable stayed flat steel box girder. This bridge is oriented in a north-south direction. A cross-section of the bridge, and the extreme measured values can be seen in figure 3.3. They found the temperature distribution to be laterally symmetrical,where the deck had internal temperature differences, while the temperature of the bottom plate was homogeneous.
Internal temperature differences between elements were calculated. In the vertical direction, the gradient varied between -3 and +15 °C: the bottom plate temperature varied between 3 degrees cooler and 15 degrees warmer than the simultaneous deck plate temperature. In the horizontal direction the maximum positive and negative temperature gradient inside the deck plate varied between -10 and 8.5 °C .
Using a Weibull distribution the gradients with a 100 year return period are derived to be -3.7 to +17.3 °C in the vertical direction, and -13.8 to +10.3 °C in the horizontal direction.

Zhu et al. [5] investigated one year of temperature data of the Benniu bridge in China. This is is a steel truss bridge. They found that the bottom of the bridge was warmer at night, due to radiative heat from ground and water. Box shaped truss members showed internal temperature differences, where the bottom plate temperature lagged behind the top plate temperature. This was attributed to lack of direct solar radiation on the bottom plate. For H shaped members this effect was less pronounced.

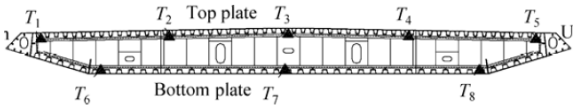

(a) Bridge geometry

Measurement point	Maximum temperature, T_{max}/°C	Minimum temperature, T_{min}/°C	Annual temperature difference, $(T_{max}-T_{min})$/°C
T_1	46.96	−5.40	52.36
T_2	47.93	−4.14	51.07
T_3	52.81	−5.46	58.27
T_4	48.10	−4.30	52.40
T_5	45.81	−5.55	51.36
T_6	39.96	−3.09	43.05
T_7	39.92	−2.91	42.83
T_8	39.09	−3.04	42.13

(b) Measured temperatures

Figure 3.3: Geometry and measurements of Runyang Bridge. (Ding and Wang [4])

3.1.3 Numerical approaches

Thepchatri et.al [6] and Yargicoglu & Johnson [7] have shown in 1977 that it is possible to model the 2D-temperature distribution in a bridge using the Ordinary Differential Equation (ODE) for heat flow. They used weather data with ambient temperature, solar radiation and wind speed, and required material parameters for conduction, radiation and transmission. They also found the most extreme environmental conditions to take place on a clear night, followed by a clear day. They also found [6]: *"on a clear sunny day, the maximum incoming solar radiation occurs at about noon, the peak ambient temperature occurs at 4.00 PM, and yet the top surface temperature is found to occur around 2.00 PM."* While the heat-flow model in [6] only allowed sun from the top due to computational complexity, in later years others have refined this. Tong et al [8] allowed for separate intensities of diffuse and direct solar light, which improved the results. It however still requires temperature measurements to fit some model parameters. Tong et al[8] modelled a box shaped girder and a pi-shaped girder for a heat transfer equation. They found strong vertical temperature gradients. And a small gradient along the West-East axis of the deck plate, where the center was warmer than the edges. Small temperature differences were found between the East and the West box wall.

3.1.4 Temperature summary

The following assumptions on temperature distributions will be taken into account when designing the temperature sensor layout for the Haringvlietbrug.

- Significant vertical temperature gradients were found.
- The bottom plate of box girder bridges was found to have a homogeneous temperature.
- No significant temperature difference between West and East side of a bridge were found.
- The deck plate has internal temperature differences. The gradients were found to be symmetric, with the center of the deck plate warmer than the edges.
- Solar radiation and convection were found to be the dominating parameters for the heat-flow model of bridge temperature during the day.

3.2 Asphalt properties

The 10 mm thick steel deck plate of the Haringvlietbrug contains two 30 mm layers of asphalt. The following sections show that asphalt has significant non-linearity. The expectation is that these non-linear asphalt properties might play a significant role in local deck plate vibrations, and thus chapter 8 will be devoted to asphalt material modelling.

3.2.1 Temperature coefficient of Asphalt

Temperature induced strain in a material is calculated as in equation 3.2. In linear models α_T is a constant, independent of temperature or whether the material is warming up or cooling down. Asphalt is not a linear material, and the temperature coefficient is not a constant. In [9] the distinction is made between the coefficient of thermal contraction (CTC) and the coefficient of thermal expansion (CTE). Experiments were carried out on cores drilled from Interstate 40 in New Mexico, United States. The results in table 3.1 and figure 3.4 show the CTC varies between $0.33 \cdot 10^{-5}$ and $3.11 \cdot 10^{-5} \varepsilon/^{\circ}C$ over the full temperature range between -20 and $+55$ $^{\circ}C$. The CTE varies between $2.38 \cdot 10^{-5}$ and $3.12 \cdot 10^{-5} \varepsilon/^{\circ}C$. It is further noted [9] that the temperature coefficient in the vertical is almost equal to the temperature coefficient in the horizontal direction. The temperature coefficients are independent of the air-void ratio. The origin of the aggregate does have a significant influence of up to 22% on the CTE, see figure 3.5.

$$\varepsilon = \alpha_T \cdot \Delta T \tag{3.2}$$

Where:

$$\begin{aligned} \varepsilon &= \text{strain in m/m} \\ \alpha_T &= \text{Temperature Coefficient in } \varepsilon/^{\circ}C \\ \Delta T &= \text{Change of temperature in } ^{\circ}C \text{ or } ^{\circ}K \end{aligned}$$

Table 3.1: Thermal coefficients of asphalt. (Islam et al. [9])

	CTC and CTE (10^{-5} per °C)	
Temperature range (°C)	CTC	CTE
−20 to −5	0.33	3.12
−5 to 10	1.92	2.81
10–25	2.94	2.38
25–40	3.11	2.56
40–55	2.57	2.63

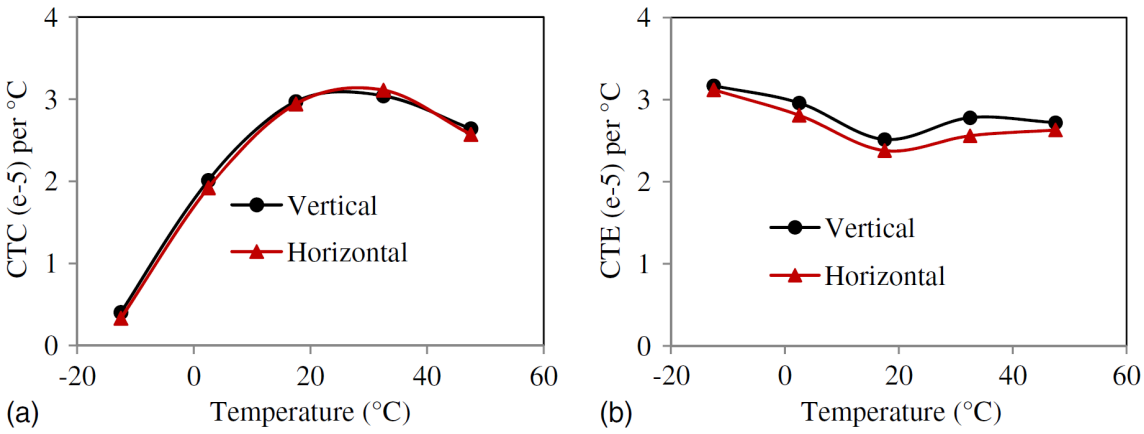

Figure 3.4: Thermal coefficients of asphalt. (Islam et al. [9])

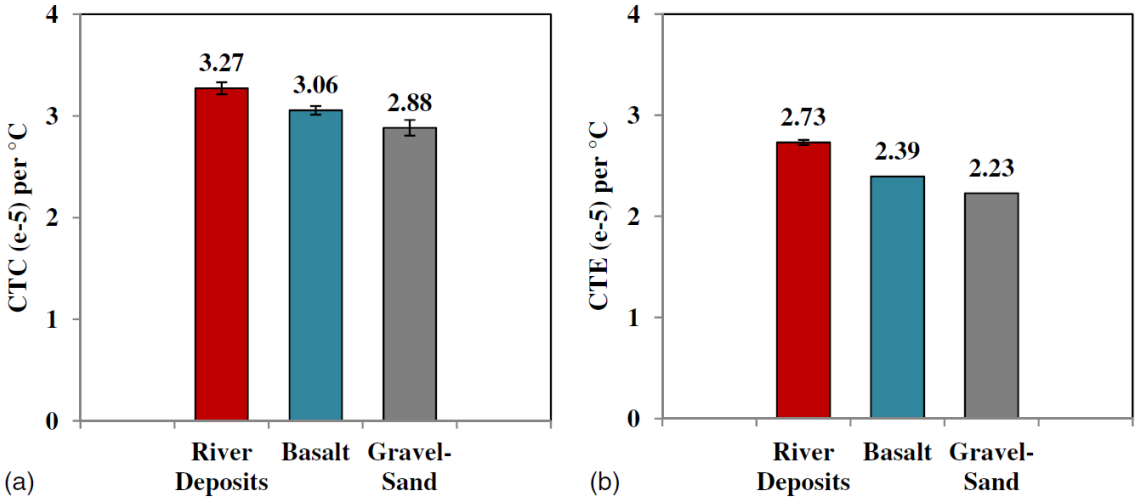

Figure 3.5: Influence of aggregate origin on thermal coefficient. (Islam et al. [9])

3.2.2 Temperature and frequency dependent stiffness

The bitumen in asphalt causes visco-elastic behaviour [10, 11, 12]. In general, higher temperatures lead to softening of the bitumen and thus to a lower Youngs modulus of the asphalt. H.Leaderman [13] found that the relation between Youngs modulus and temperature is similar to the relation between Youngs modulus and time. This is also known as the TTSP: Temperature-Time Superposition Principle. This effect was clearly illustrated by Anupam [14] in figures 3.6 and 3.7. This indicates that asphalt stiffness is thus temperature ánd loading-frequency dependent.
TTSP can be used to obtain asphalt properties for temperature-frequency combinations that are difficult to test directly. For instance creep is difficult to test due to time limitations in a laboratory. Another limitation may be the frequency range of the test equipment. Using TTSP it is possible to test the specimen within a limited loading frequency range, but at different temperatures. It is then possible to shift the test results from different temperatures over the frequency axis until they line up and form a so called master curve.
In figure 3.7 the green curve with test temperature T_2 is left in its original position, and thus this temperature is now also called the reference temperature. The other curves are moved along the x-axis, which is renamed from "frequency" to "reduced frequency", indicating the frequencies are now based on a shifting procedure. The frequencies f_1 and f_2 are determined by the capabilities of the test device and the available laboratory time.
During laboratory testing Zhang et al have found [11] a master curve for some typical Dutch mixtures as shown in figure 3.8. It is noted that the tests were performed on unaged asphalt in laboratory conditions, and thus the exact stiffness may not be representative for asphalt that has undergone a few years of seasonal and operational loading.

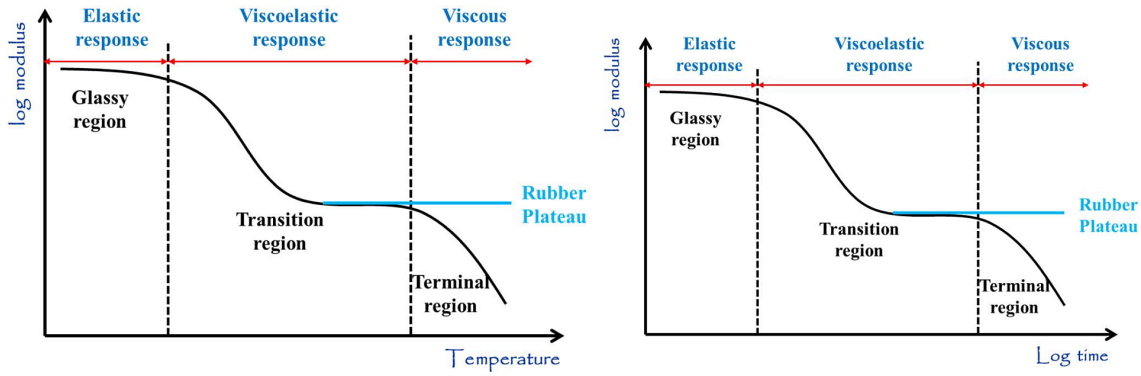

Figure 3.6: Interchangeability between temperature and frequency. (Anupam, [14])

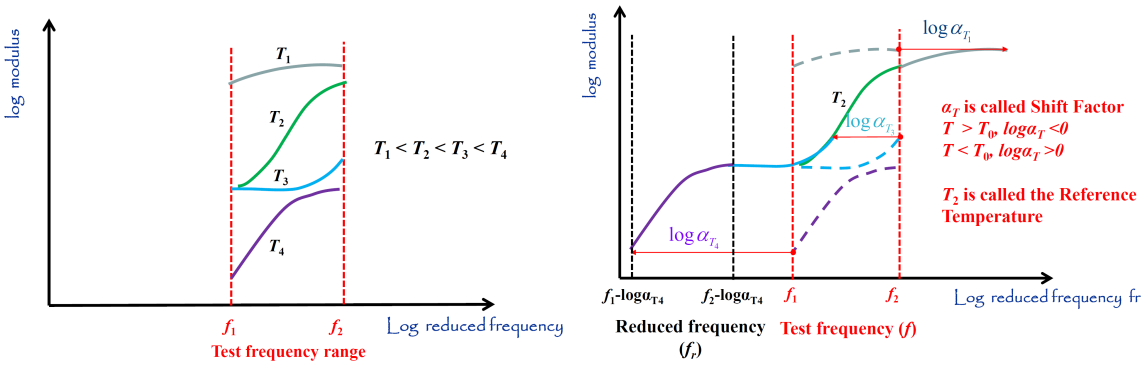

(a) Test apparatus with limited frequency range, at different temperatures

(b) Shift to create master curve

Figure 3.7: Creation of master curve (Anupam, [14])

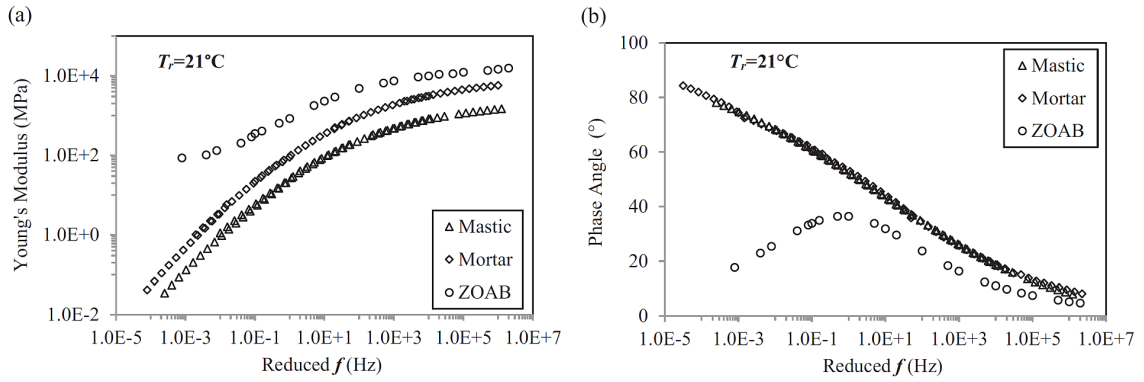

Figure 3.8: Master curves of typical Dutch Mixtures (Zhang 2018 [11])

3.3 Theory: Dynamics of beams and plates.

Some basic theory on column and plate dynamics is presented. Both as a refresher and a reference. In chapter 7 the influence of temperature induced stress on the vibrations of some bridge components is calculated using the equations below.

3.3.1 Column under compression, ODE approach

The ODE for a static prismatic beam under compression is derived according to [15] and figure 3.9

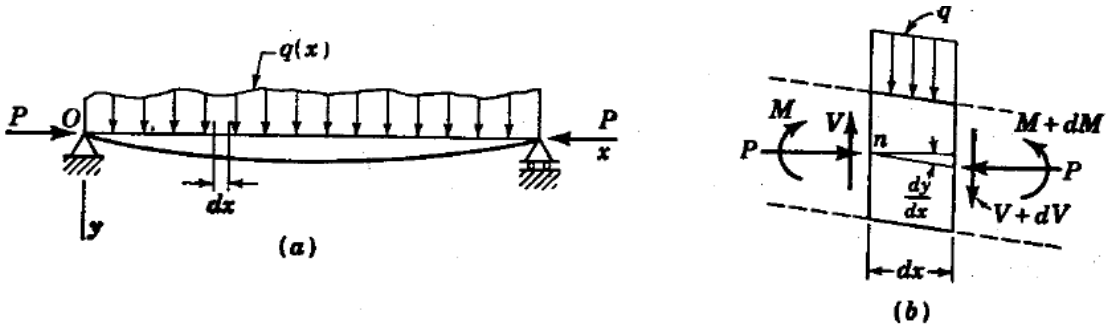

Figure 3.9: beam geometry, taken from Timoshenko [15]. In this thesis F is used as compressive force instead of P.

$$\mathrm{d}V = -q \cdot \mathrm{d}x \tag{3.3}$$

$$\sum M_{point\,n} = -M + M + \mathrm{d}M - V\mathrm{d}x - dV\mathrm{d}x - F\frac{\mathrm{d}y}{\mathrm{d}x}\mathrm{d}x - q\mathrm{d}x\frac{\mathrm{d}x}{2} = 0 \tag{3.4}$$

$$\mathrm{d}M = V\mathrm{d}x + dV\mathrm{d}x + F\frac{\mathrm{d}y}{\mathrm{d}x}\mathrm{d}x + \frac{q}{2}\,\mathrm{d}^2x = 0 \tag{3.5}$$

Dividing everything by $\mathrm{d}x$:

$$\frac{\mathrm{d}M}{\mathrm{d}x} = V + dV + F\frac{\mathrm{d}y}{\mathrm{d}x} + \frac{q}{2}\mathrm{d}x \tag{3.6}$$

One can take the limit $\mathrm{d}x \to 0$ while using eq:3.3

$$\begin{aligned} \lim_{\mathrm{d}x\to 0}\frac{\mathrm{d}M}{\mathrm{d}x} &= V + dV + F\frac{\mathrm{d}y}{\mathrm{d}x} + \frac{q}{2}\mathrm{d}x \to \\ \frac{\mathrm{d}M}{\mathrm{d}x} &= V - q\cdot 0 + F\frac{\mathrm{d}y}{\mathrm{d}x} + 0 \\ \frac{\mathrm{d}M}{\mathrm{d}x} &= V + F\frac{\mathrm{d}y}{\mathrm{d}x} \end{aligned} \tag{3.7}$$

The kinematic and constitutive relations for an Euler-Bernoulli beam are well known as:

$$\begin{aligned} \varphi &= -\frac{\mathrm{d}y}{\mathrm{d}x} \\ \kappa &= \frac{\mathrm{d}\varphi}{\mathrm{d}x} \\ EI\cdot\kappa &= M \end{aligned} \tag{3.8}$$

Assuming EI is constant along x for prismatic beams this results in the ODE:

$$EI\frac{\mathrm{d}^4y}{\mathrm{d}x^4} + F\frac{\mathrm{d}^2y}{\mathrm{d}x^2} = q \tag{3.9}$$

Generalising this to the dynamic case in which $q = -\rho A \frac{\mathrm{d}^2 y}{\mathrm{d}t^2}$:

$$EI\frac{\mathrm{d}^4 y}{\mathrm{d}x^4} + F\frac{\mathrm{d}^2 y}{\mathrm{d}x^2} + \rho A\frac{\mathrm{d}^2 y}{\mathrm{d}t^2} = 0 \tag{3.10}$$

Assuming the solution of the first mode has the form of eq:3.11 and substituting this in eq:3.10:

$$y(x,t) = f(t) \cdot sin\frac{\pi x}{l} \tag{3.11}$$

$$\frac{\mathrm{d}^2 f(t)}{\mathrm{d}t^2} + \frac{1}{\rho A}\frac{\pi^2}{l^2}\left(EI\frac{\pi^2}{l^2} - F)\right) f(t) = 0 \tag{3.12}$$

Which can be further simplified to

$$\frac{\mathrm{d}^2 f(t)}{\mathrm{d}t^2} + \omega^2 f(t) = 0 \tag{3.13}$$

in which ω is the angular frequency in rad/s and:

$$\omega^2 = \frac{\pi^2}{\rho A l^2}\left(\frac{\pi^2 EI}{l^2} - F\right) \tag{3.14}$$

Equation 3.14 shows that if the compression force increases up to the Euler Buckling force $F_{buckling} = \frac{\pi^2 EI}{l^2}$ for an increasing compression force F, the eigenfrequency lowers, and vice-versa.

3.3.2 Column under compression, energy approach

For a prismatic beam the free vibration $y(x)$ of a beam with hinged ends can be described as follows:

$$y = \sum_{i=1}^{\infty} q_i sin\frac{i\pi x}{l} \tag{3.15}$$

In which q_i is the excitation (modal coordinate) of mode i with shape $sin\frac{i\pi x}{l}$.
In [16] the effect of axial forces on lateral vibrations is discussed using an energy approach. The increase of the length of the center line can be expressed as [16]

$$\int_0^l (\mathrm{d}s - \mathrm{d}x) \approx \frac{1}{2}\int_0^l \left(\frac{\mathrm{d}y}{\mathrm{d}x}\right)^2 \mathrm{d}x \tag{3.16}$$

Assuming a compression force F, the corresponding diminishing energy is [16]

$$\frac{F}{2}\int_0^l \left(\frac{\mathrm{d}y}{\mathrm{d}x}\right)^2 dx = \frac{F}{2}\int_0^l \left(\sum_{i=1}^{\infty} q_i \frac{i\pi}{l} cos\frac{i\pi x}{l}\right)^2 = \frac{F\pi}{4l}\sum_{i=1}^{\infty} i^2 q_i^2 \tag{3.17}$$

If the ends were free to move, this would have been the work of force F, if the ends are hinged, it's the change in stored compression energy. Adding this to the bending energy of a beam this results in the following potential energy [16]

$$P = \left(\frac{EI\pi^4}{4l^3} - \frac{F\pi}{4l}\right)\sum_{i=1}^{\infty} i^2 q_i^2 \tag{3.18}$$

The kinetic energy of the beam is [16]

$$K = \frac{\rho A l}{4}\sum_{i=1}^{\infty} \dot{q_i}^2 \tag{3.19}$$

Using Lagrange's equations and making use of the notations

$$a^2 = \frac{EI}{\rho A} \qquad \alpha^2 = \frac{Fl^2}{EI\pi^2} \tag{3.20}$$

we obtain:

$$q_i = C\cos\left(\frac{a\pi^2 i^2}{l^2}\sqrt{1-\frac{\alpha^2}{i^2}}\right)t + D\sin\left(\frac{a\pi^2 i^2}{l^2}\sqrt{1-\frac{\alpha^2}{i^2}}\right)t \tag{3.21}$$

This shows that the frequency of each mode is influenced by the compression force F through the term:

$$\sqrt{1-\frac{\alpha^2}{i}} = \sqrt{1-\frac{Fl^2}{EI\pi^2 i}} \tag{3.22}$$

For the first mode with $i = 1$ one can see the similarity to Euler's buckling formula.

$$F_{buckling} = \frac{\pi^2 EI}{l^2} \tag{3.23}$$

If the compression force F approaches the buckling force $F_{buckling}$ from below, the angular frequency ω turns to 0. Increasing compression force thus results in lower frequencies.

For parts that are in tension, one should look carefully at eq 3.20 and note that α^2 can become negative. It might be more intuitive to rewrite the equations 3.21and 3.20 for a tension force T to:

$$\alpha^2 = \frac{Tl^2}{EI\pi^2} \tag{3.24}$$

$$q_i = C\cos\left(\frac{a\pi^2 i^2}{l^2}\sqrt{1+\frac{\alpha^2}{i^2}}\right)t + D\sin\left(\frac{a\pi^2 i^2}{l^2}\sqrt{1+\frac{\alpha^2}{i^2}}\right)t \tag{3.25}$$

This shows that a higher tension force T results in higher frequencies.

The result from eq 3.21 can also be compared to the one from eq: 3.14, for the first mode:

$$\left(\frac{a\pi^2 i^2}{l^2}\sqrt{1-\frac{\alpha^2}{i^2}}\right) = \sqrt{\frac{EI\pi^4}{\rho A l^4}\left((1-\frac{Fl^2}{EI\pi^2}\right)} = \sqrt{\frac{\pi^2}{\rho A l^2}\left(\frac{EI\pi^2}{l^2}-F\right)} = \sqrt{\omega^2} \tag{3.26}$$

This shows that both approaches lead to the same result.

3.3.3 Plate dynamics

Timoshenko has written about plate dynamics in [16] and applied the Ritz procedure for the free vibrations of rectangular isotropic plates. Bassily and Dickinson [17],[18] used the same Ritz approach to estimate the natural frequencies of isotropic rectangular plates under in-plane shear (N_{xy}) or compression (N_x , N_y) forces. First they write the displacement field as a multiplication of beam vibration shapes having identical edge fixity as the plate.

$$W = \sum_{m=1}^{p} \sum_{n=1}^{p} A_{mn} \cdot \phi_m(x) \cdot \psi_n y \tag{3.27}$$

In which A_{mn} is an undetermined amplitude coefficient, and $\phi(x)$ and $\psi(y)$ are the beam functions.

$$\begin{aligned} \phi_m(x) &= A_m sin(\epsilon_m x) + B_m cos(\epsilon_m x) + C_m sinh(\epsilon_m x) + D_m cosh(\epsilon_m x) \\ \psi_m(x) &= \overline{A}_n sin(\eta_n y) + \overline{B}_n cos(\eta_n y) + \overline{C}_n sinh(\eta_n y) + \overline{D}_n cosh(\eta_n y) \end{aligned} \tag{3.28}$$

The strain energy of the plate at the maximum amplitude may then be written as:

$$\begin{aligned} P = \frac{1}{2} \int_0^b \int_0^a \Bigg(D \cdot \left[(\frac{\mathrm{d}^2 W}{\mathrm{d}x^2})^2 + (\frac{\mathrm{d}^2 W}{\mathrm{d}y^2})^2 + 2\nu \frac{\mathrm{d}^2 W}{\mathrm{d}x^2} \frac{\mathrm{d}^2 W}{\mathrm{d}y^2} + 2(1-\nu)(\frac{\partial^2 W}{\partial x \partial y})^2 \right] \\ + N_x (\frac{\mathrm{d}^2 W}{\mathrm{d}x^2})^2 + N_y (\frac{\mathrm{d}^2 W}{\mathrm{d}y^2})^2 + 2N_{xy} \frac{\mathrm{d}W}{\mathrm{d}x} \cdot \frac{\mathrm{d}W}{\mathrm{d}y} \Bigg) \mathrm{d}x \, \mathrm{d}y \\ with: \; D = \frac{Et^3}{12(1-\nu^2)} \end{aligned} \tag{3.29}$$

And the kinetic energy as:

$$K = \frac{1}{2} \rho t \omega^2 \int_0^b \int_0^a W^2 \mathrm{d}x \, \mathrm{d}y \tag{3.30}$$

By using the Lagrange equation the solution may the be searched using:

$$\frac{\partial P}{\partial A_{ik}} - \frac{\partial K}{\partial A_{ik}} = 0 \; with \; i = 1, 2, 3, ..., p \; and \; j = 1, 2, 3, ..., q \tag{3.31}$$

This is a set of linear homogeneous equations that can be solved for ω.

If, for instance, one would like to know the influence of external tension and/or shear forces N_x, N_y, N_{xy} on a plate with a size of 0.3 x 2.192 m that's hinged on all edges. The result for the first mode would be: (evaluated with Maple for $\nu = 0.3$):

$$\omega_{1,1} = \frac{\sqrt{3.063 N_{xy} + 12026 N_y + 4.219 N_x + 17368 D}}{\sqrt{\rho t}} \tag{3.32}$$

Here $\omega_{1,1}$ implies that this is the shape that has one half wave in both the x and y directions.

Again the similarity with equations 3.14 and 3.26 can be seen. The natural frequency has a square root dependency on the ratio between the buckling- and the applied-loads.

4 Case: the Haringvlietbrug

The Haringvlietbrug is a multi-span continuous steel box-girder bridge in the south of the Netherlands. It has 10 spans of 106 meter each. The deck cantilevers on both sides of the box-girder, and consists of a 10 mm thick steel deck plate with longitudinal ribs. On top of the deck plate is a multilayer system comprising of two 30 mm thick layers of asphalt and two waterproofing membranes. A picture of the bridge can be seen in 4.1.

Figure 4.1: Haringvlietbrug. The first span left of the tower is the opening bascule. The third span left of the tower is the area of interest

4.1 Geometry and materials

Cross-section & frames
Along the length of the bridge, frames are placed every 2167 mm center to center. These frames include the cantilever- and crossbeams. Not all frames are equal, there is a type C frame with struts, and Type A and B frames without struts. The B frame is identical to the A frame, except the cross member at the bottom of the box is omitted. They can be seen in figures 4.2 and 4.3. The frames alternate in a C-B-A-B-C scheme with a 2167 mm center-to-center spacing, resulting in 1 strut every 4 frames. This can also be seen in figure 4.4.

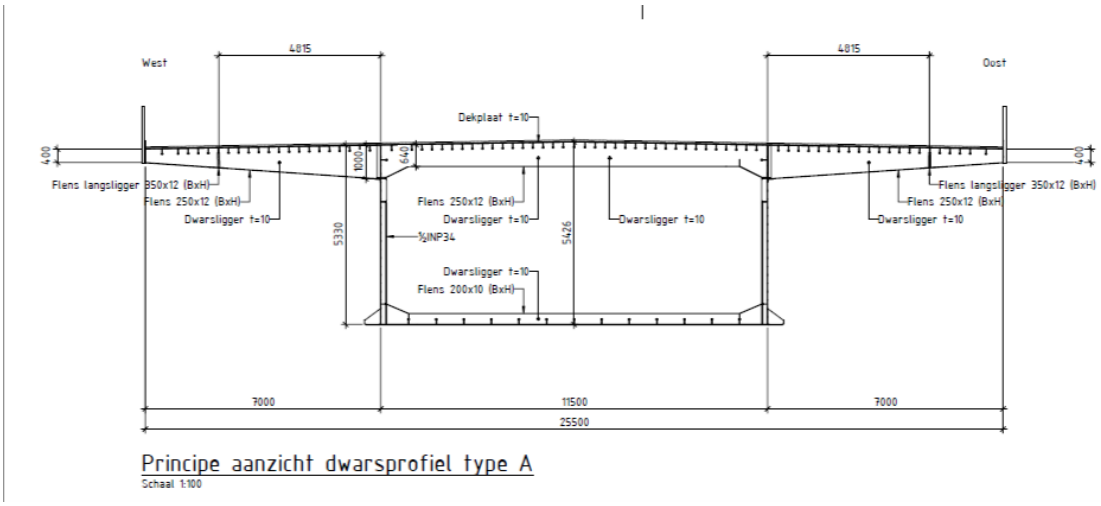

Figure 4.2: Frame type A

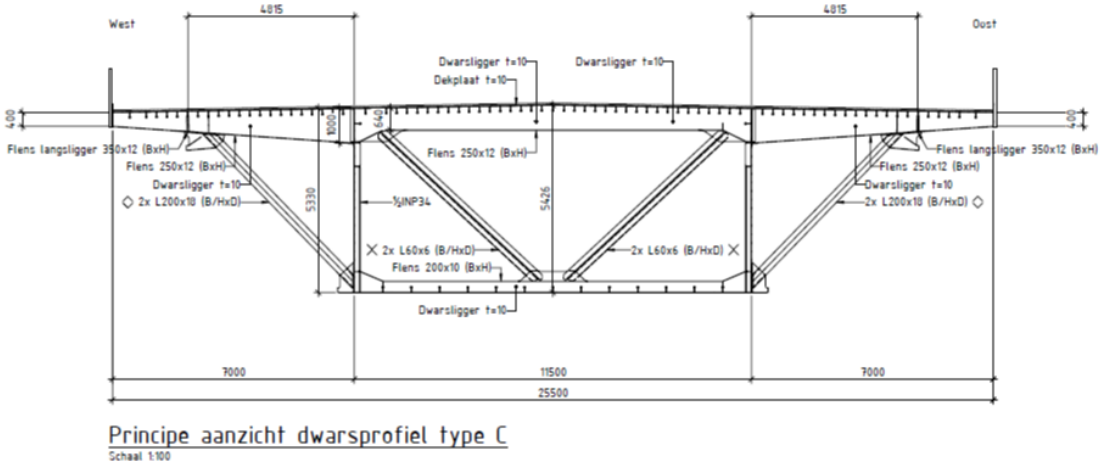

Figure 4.3: Frame type C

Deck
The deck is reinforced with longitudinal ribs made out of bulb-profiles. These stiffeners are mainly spaced 300 mm center-to-center, as can be seen in figure 4.5

Deck Surfacing
The deck surface consists of a 10 mm steel plate, on which two 30 mm layers of asphalt are placed. All layers are separated by a waterproofing membrane. The configuration is as seen in table 4.1 in which the parameters of the asphalt are given by the contractor.

(a) inside (b) outside

Figure 4.4: Main Box girder

(a) Photo of ribs (b) Detail of rib geometry

Figure 4.5: Longitudinal ribs as deck stiffeners

Table 4.1: Deck Layers

Layer [–]	Thickness $[mm]$	Material [–]	Density $[kg/m^3]$	Youngs Modulus at 20°C $[GPa]$
5	30	ZOAB	2000	5.1
4	4	Parafor Ponts	1500	0.2
3	30	Asphalt	2360	9.0
2	4	Mistral C	1500	0.2
1	10	steel	7850	210

4.2 Measurement campaign

The Haringvlietbrug is outfitted with a significant amount of sensors. Strain sensors were already in place, for a recalculation of prediction of remaining structural lifetime. Some of the strains sensors were also equipped with temperature sensors for temperature compensation of the sensor. In addition to these existing sensors, additional sensors were placed: 16 temperature sensors on the deck and inside the asphalt, 1 displacement sensor at one of the supports, and 32 acceleration sensors on two localized areas below the cantilever deck.

Strain sensors

Two types of strain sensors were used: Fibre optics from the Fibre Bragg Grating (FBG)type and discrete strain gages (DSG). A description of the positions is found in table 4.2. Strain sensor positions are also shown in figures 4.6 through 4.15. The FBG strain sensors (labelled: s,c,d,w,o,x) also have a FBG temperature sensor next to them. The DSG sensors (labelled: b) do not have their own temperature sensors.

Table 4.2: Strain sensor type, direction and location

Amnt	Type	Location	Direction	Description
18	FBG	s	Strut axis	Strut, Top and bottom, 3 sides.
02	FBG	c	Beam axis	Crossbeam Cantilever, bottom Flange
04	FBG	d	Beam axis	Crossbeam, bottom Flange
03	FBG	o	Longitudinal	Bottom plate of Box-girder
06	FBG	w	Longitudinal	Web of Box-girder, top and Bottom
20	FBG	x	Beam axis	Joint Strut-Cantilever
08	DSG	b	Beam axis	Bulb = Bottom of Ribs
28	DSG	b	Beam axis	Crossbeam Cantilever, web next to rib opening
02	DSG	b	Longitudinal	Bottom of deck plate

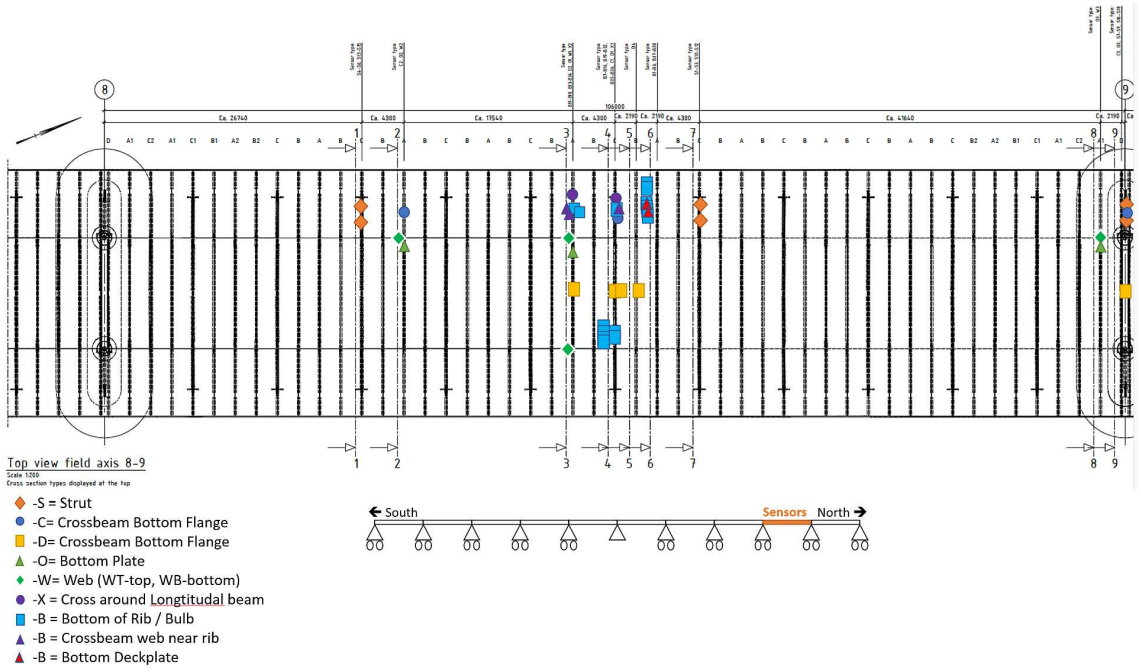

Figure 4.6: Sensor overview

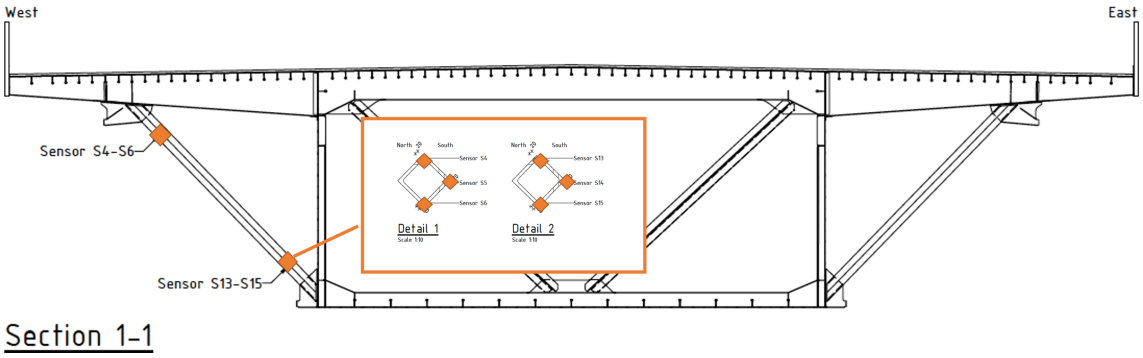

Figure 4.7: Section 1: s04 to s06, s13 to s15

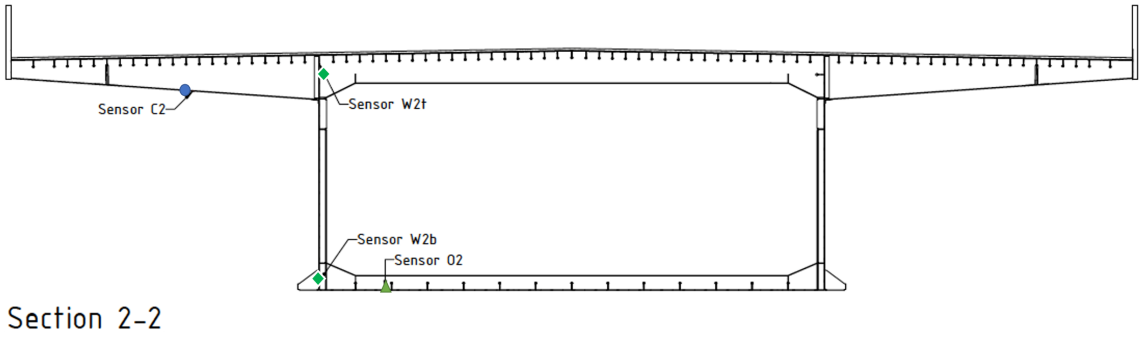

Figure 4.8: Section 2: c2, w2t, w2b, o2

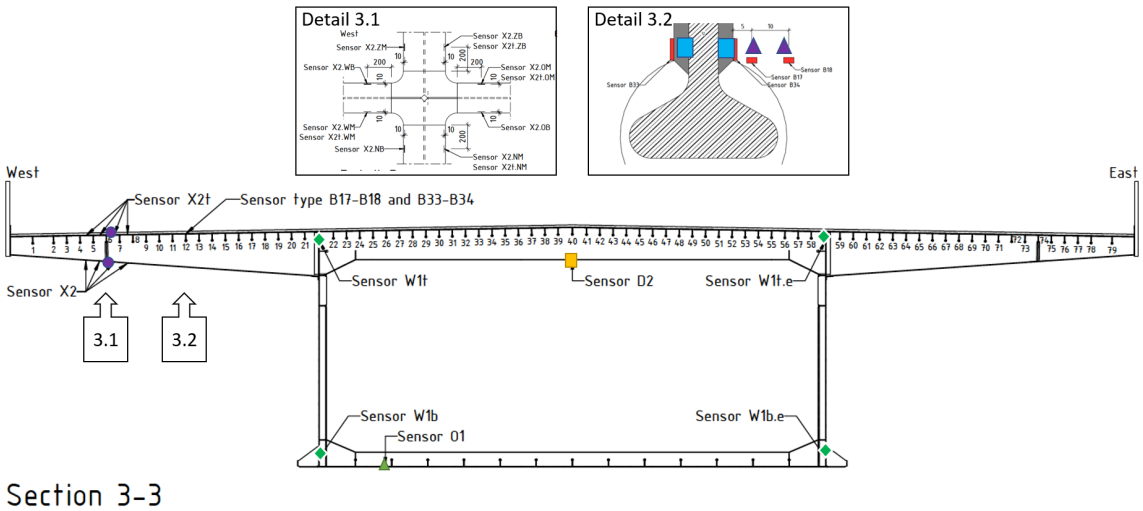

Figure 4.9: Section 3: x2.., w1t, w1b, w1te, w1be, o1, d2

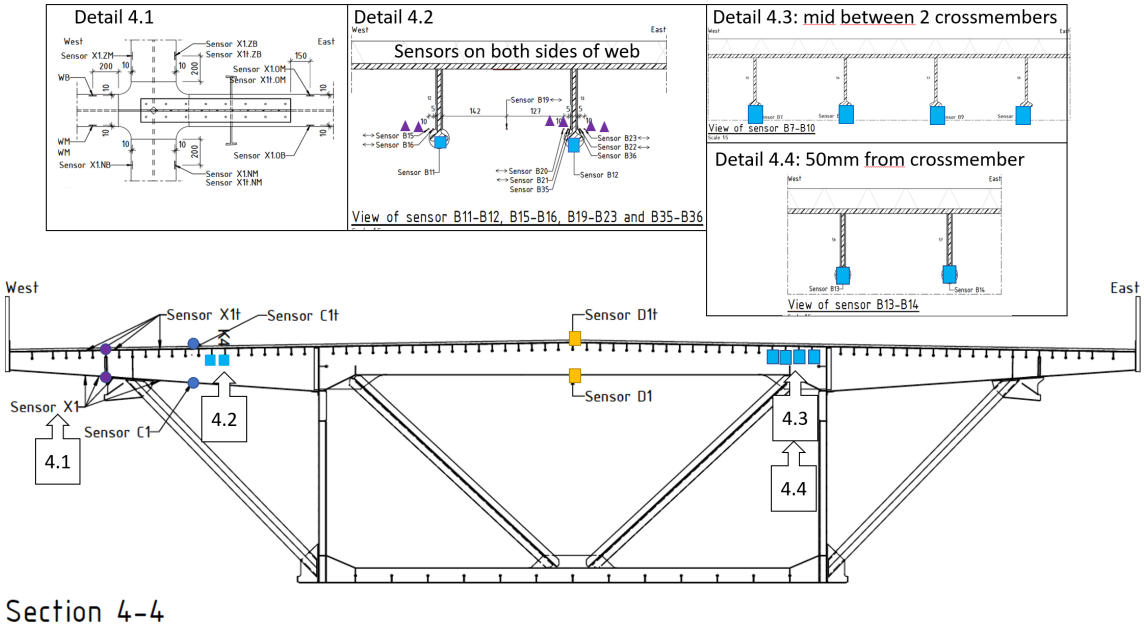

Figure 4.10: Section 4: x1.., c1, d1, b7 to b10, b13 to b14

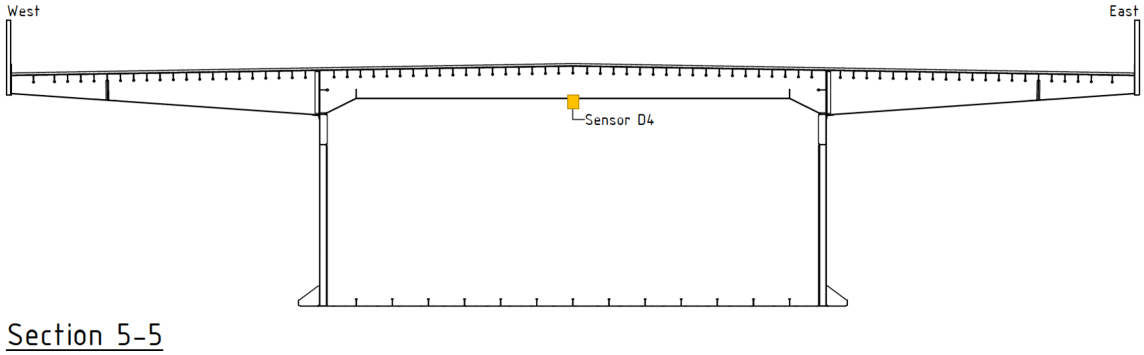

Figure 4.11: Section 5: d4

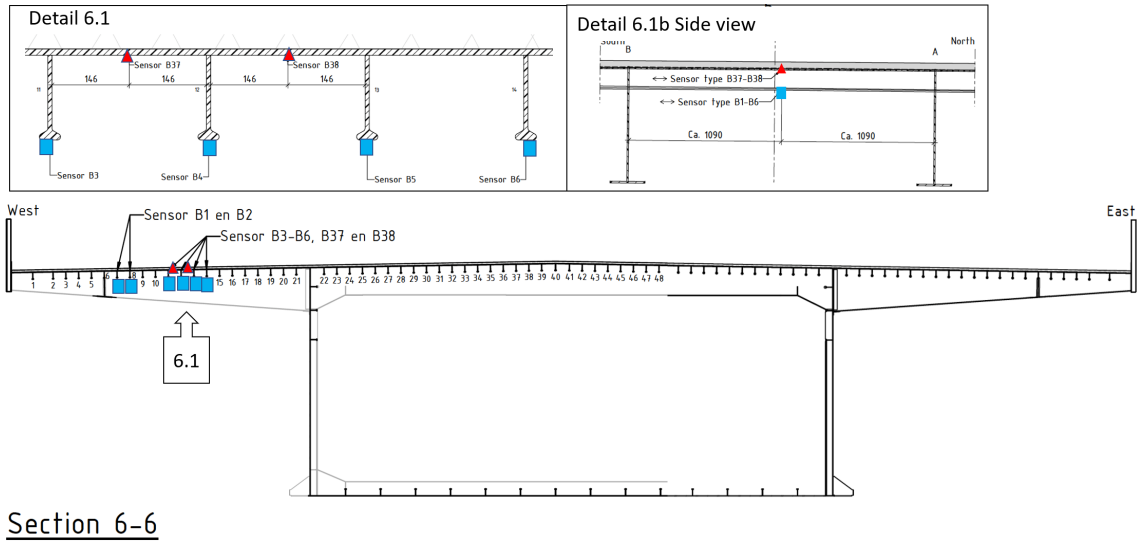

Figure 4.12: Section 6: b01, b02, b03 to b06, b37,b38

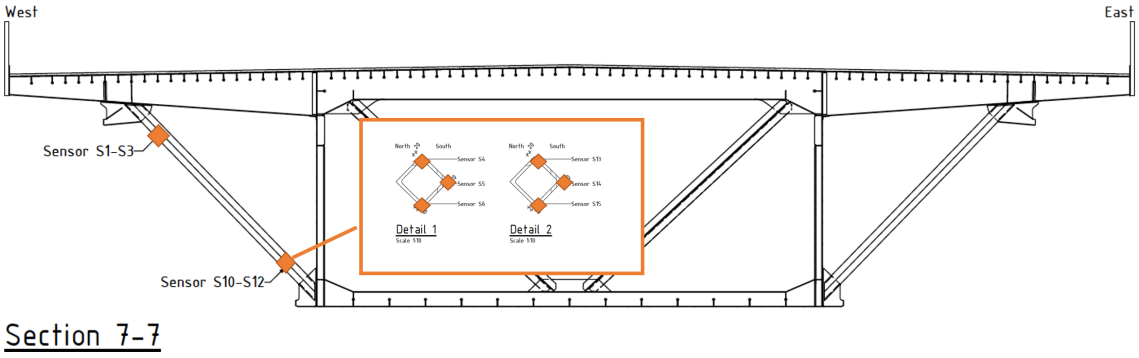

Figure 4.13: Section 7: s01 to s03, s10 to s12

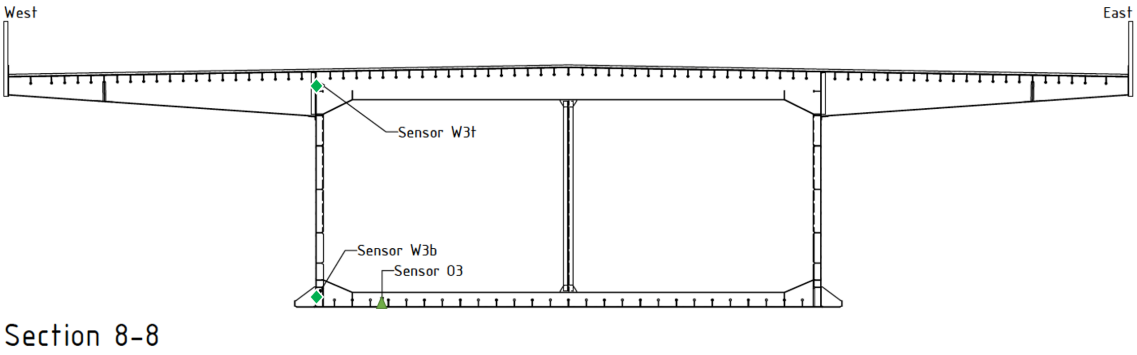

Figure 4.14: Section 8: w3b, w3t, o3

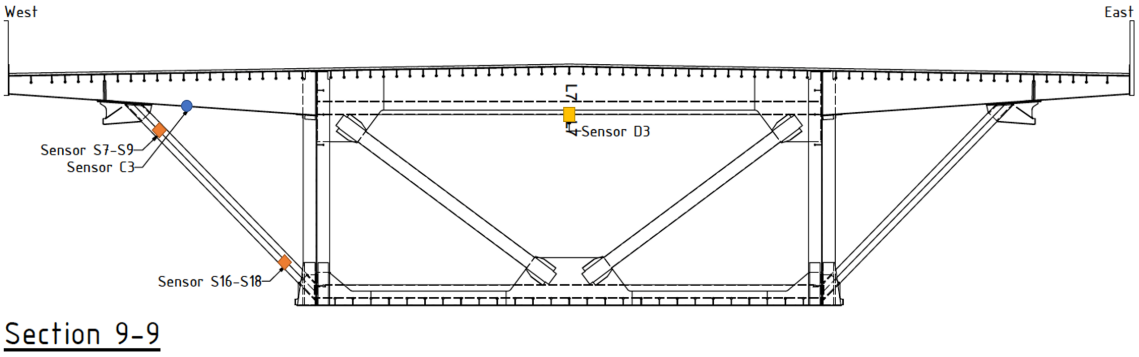

Figure 4.15: Section 9: s07 to s09, s16 to s18, c3, d3

Temperature sensors

All FBG strain sensors are equipped with a FBG temperature sensor as well, to account for temperature drift. In addition, 16 discrete PT1000 temperature sensors are added to obtain a better overview of the temperature distribution in the bridge. Their positions are shown in figure 4.16

Table 4.3: Temperature sensor type and location

Location	type	Amount	description
S	FBG	18	Strut, Top and bottom, 3 sides
C	FBG	02	Crossbeam Cantilever, bottom Flange
D	FBG	04	Crossbeam, bottom Flange
O	FBG	03	Bottom plate of Box-girder
W	FBG	06	Web of Box-girder, top and Bottom
X	FBG	20	Joint Strut-Cantilever.
at	PT1000	6	Asphalt top & Bottom
at	PT1000	5	Deck plate
at	PT1000	2	Bottom of Rib
at	PT1000	2	Crossbeam
at	PT1000	1	Strut, next to a FBG for cross-calibration

Acceleration sensors

The bridge was equipped with 32 acceleration sensors. These were mainly used for research in damage detection by a fellow student [19]. Therefore they were split in 2 groups of 16 sensors, one group for a *healthy* section of the bridge, and one group for a *damaged* section of the bridge.

Displacement sensor

The bridge is supported on 11 pylons, of which the center one is pinned, while the others are rollers. The 10th pylon is equipped with a LVDT measuring the axial displacement of the bridge relative to the support. The support is shown in figure 4.17. There are 4 spans between the fixed support and the LVDT, resulting in a distance of $4 * 106 = 424$ m.

4.2.1 Sensor specifications overview

The specification of the sensors are displayed in table 4.4.

Table 4.4: Sensor and sampling specifications

Parameter	FBG_pd	FBG_t	DSG	at	Acc	LVDT
Name and/or type	Atgrating	Atgrating	Vishay	Atal-TEP102B	KAE-005-5-1	LDI-128-400
Measured unit	$\mu\epsilon$	°C	$\mu\epsilon$	°C	g	mm
Resolution	unknown	0.1°C	unknown	0.3 °C	unknown	0.1 mm
Accuracy	unknown	1.0°C	unknown	1.0 °C	unknown	1.0 mm
Sample rate	≈100 Hz	≈25 Hz	300 Hz	1/5min	1 kHz	1/min
Sample schedule *)	cnt	cnt	cnt	cnt	int	int

*) sample schedule:
cnt = continuous
int = interval 20 minutes per hour

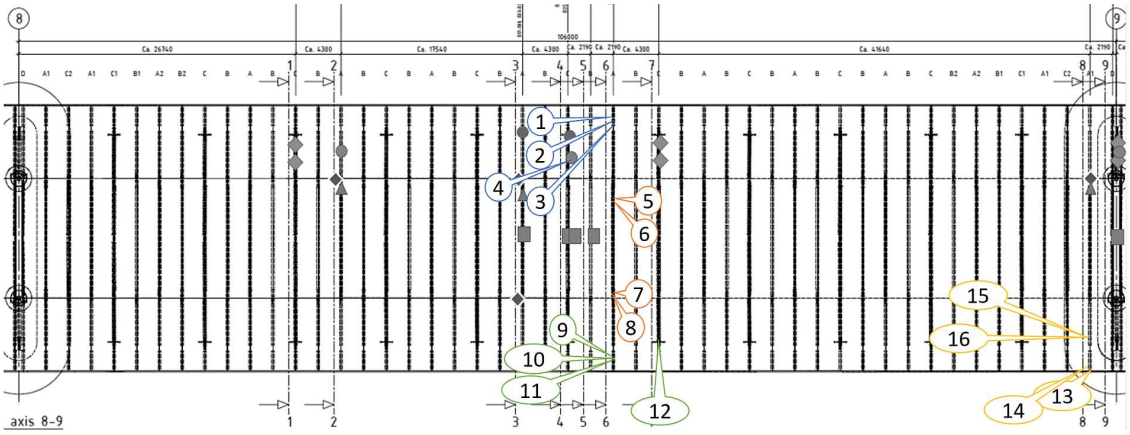

(a) Overview of the at01..at16 sensors

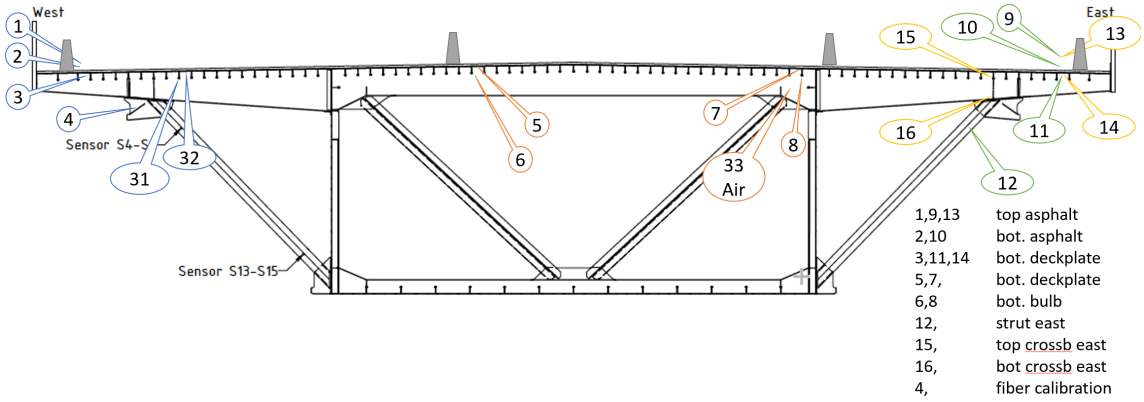

(b) Principal cross section with at01..at16, sensors at30..at32 were added later.

Figure 4.16: PT1000 Temperature sensor positions

(a) Pinned support at center of bridge

(b) Roller support (view from east)

(c) Roller support with LVDT (view from west)

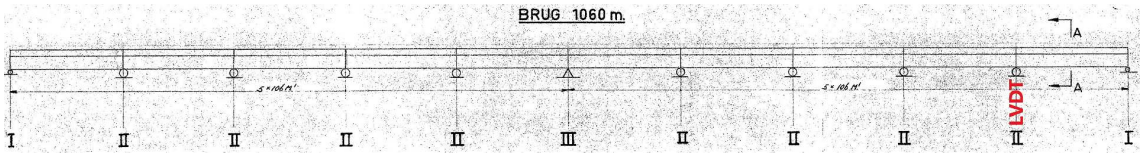

(d) Support scheme

Figure 4.17: Bridge Supports and LVDT

4.3 Data processing

Data from all sensors was gathered by 4 different systems, from different suppliers. In total more than 1TB of data was obtained, in different formats, at different sample-rates and from different time zones.
For each type of sensor the input data was indexed to Amsterdam summertime, re-sampled to $\frac{1}{60}$ Hz, filtered with a low-pass Butterworth filter and, if needed, a temperature correction was applied. For strain sensors, the mean strain of each sensor was removed in order to calculate daily strain amplitudes.
The down sampling, low-pass filtering and sensor temperature corrections are explained in the following paragraphs.

4.3.1 Downsampling

Temperature induced stress and strain in a bridge are gradually developing effects that can be characterised as low-frequent. The characteristic period could be up to a whole day, or even more if we account for seasonal fluctuation. This means no high frequency content is required in the dataset, and thus the size of the dataset can be reduced by downsampling, which also speeds up further computations.
The signals are downsampled to 1/60Hz by averaging all data points of each minute. The result is visually checked for computing artefacts. An example of this visual check can be seen in figure: 4.18.

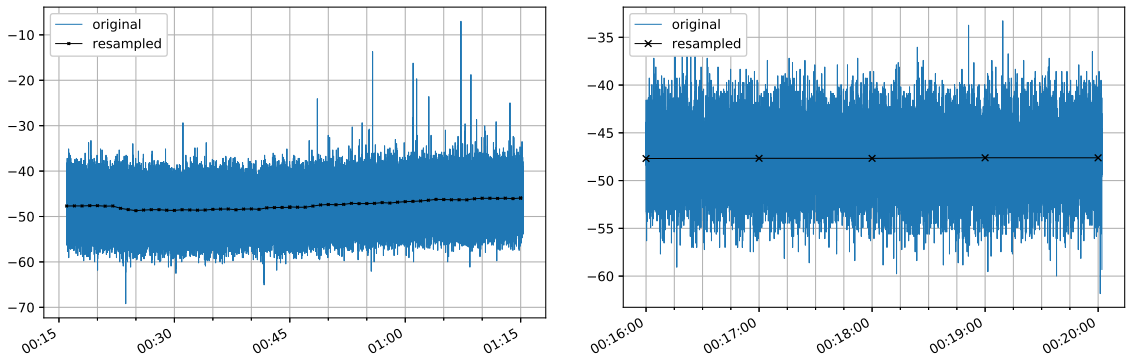

(a) 1 hour timeframe

(b) 4 minute timeframe

Figure 4.18: Strain signal with and without downsampling

4.3.2 Lowpass Filtering

The main purpose of the downsampling is reducing the size of the dataset. This downsampling also acts as a rudimentary lowpass filter, but does not perform as well as a real filter. The downsampled signal still shows a significant amount of noise, which needs to be filtered out. The signal was passed 6 times through a 2nd order Butterworth Filter. Resulting in a computationally efficient 12th order filter with very limited phase shift. A cut-off frequency of $\frac{1}{30}$ times the Nyquist rate was chosen, resulting in a $\frac{1}{30} * \frac{1}{60} * 0.5 = 0.28 * 10^{-3}$ Hz $= 0.28$ mHz cut-off frequency.
Examples of the filter results are shown in figures 4.19 and 4.20. Before filtering, one can clearly see large spikes at the whole hours during the day. If the bascule bridge opens, it's nearly always the first 10 minutes of a whole hour, which correlates to this significant jump in strain for most sensors. The lowpass cut-off frequency was chosen as a compromise between filtering this jump and obtaining a realistic variation for the temperature induced strains.

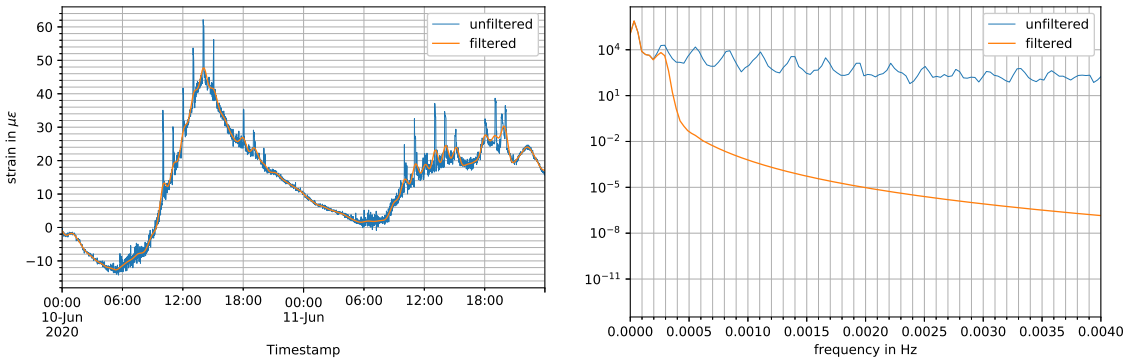

(a) Time domain (b) Frequency domain

Figure 4.19: FBG filtering of sensor w1b, at the bottom of the West box wall.

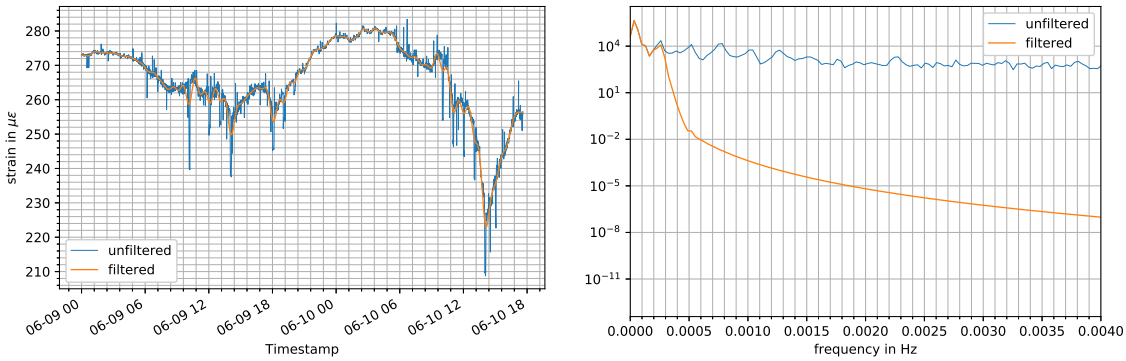

(a) Time domain (b) Frequency domain

Figure 4.20: DSG filtering of sensor b04, at the bottom of a West cantilever rib.

4.3.3 Sensor Temperature Compensation

Both the FBG strain sensors and the discrete strain gages suffer from temperature induced measuring errors. This might result in a gain-change (the ratio between readout and applied strain changes), as well as a drift (the readout shifts). To re-mediate these errors various procedures for sensor temperature compensation (STC) exist.
There is a distinct difference between the reported strains from the FBG measurements and those from the discrete strain gages. After correct temperature compensation, the FBG sensors show total-strain, while the discrete strain gages show only the stress-induced strain component after compensation.
$\varepsilon_{total} = \varepsilon_{stress} + \varepsilon_{temperature}$.

FBG sensors

The FBG sensors are temperature compensated by the supplier through additional temperature sensors at each location. The supplier states[1] that he uses the following formula for calculation of temperature-corrected stress:

$$\varepsilon(t)_{purified\ deformation} = \frac{\Delta\lambda(t)_{strain\ sensor} - \Delta\lambda_{temperature\ sensor}}{k_\varepsilon \cdot \lambda_{0,strain_sensor}} \cdot 10^6\ \mu\varepsilon \tag{4.1}$$

with:

$k_\varepsilon = 0.78$ For all sensors
$\lambda_{0,strain\ sensor} =$ Calibration wavelength of strain sensor
$\Delta\lambda_{temperature\ sensor} =$ Change of wavelength in temperature sensor
$\Delta\lambda_{strain\ sensor} =$ Change of wavelength in strain sensor
(t) denotes time dependent variable

And the formula for the temperature:

$$\Delta T = \frac{\lambda_{temperature\ sensor}(t) - \lambda_{0,temperature\ sensor}}{k_t} \tag{4.2}$$

with:

$\lambda_{0,temperature\ sensor} =$ Calibration wavelength of temperature sensor
$\Delta\lambda_{temperature\ sensor} =$ Change of wavelength in temperature sensor
$k_t =$ Sensor specific temperature sensitivity
(t) denotes time dependent variable
$T =$ Temperature in °C

The sensor specific temperature sensitivities k_t were supplied in a table, and vary between 0.0093 and 0.011, a difference of 18%. Equation 4.2 shows the temperature sensors have unique sensor specific temperature sensitivities varying up to 18%, while equation 4.1 shows that no account was made for these specific sensitivity deviations: formula 4.1 has no variable named k_t. This implies there is at least 18% uncertainty in the temperature correction of the supplied strains.

Discrete strain gages

The discrete strain gages were not fully compensated for temperature drift, because the original measurement campaign did not require this. First the original compensation will be shown, followed by the new approach to add temperature compensation.

[1] by internal email

Original compensation
In total 5 additional DSG strains sensors of the same type as the normal DSG sensors were placed in similar positions to function as compensation sensors. Therefore they were not glued in place, but positioned with a slightly flexible compound normally used for mounting semiconductors on a heat sink. The supplier assumed that this flexible compound would not allow strain in the bridge elements to transfer to the compensation sensor, and thus this compensation sensors should only measure temperature induced sensor drift. By subtracting the compensation strain from the measurements, this should have resulted in temperature compensated strain measurements. The large peaks in the compensation measurements during the bridge openings, see figure 4.21, indicate that significant amounts of strain were applied to the compensation sensor. There is no reason to assume that the temperature of the compensation strain gage could change so abruptly during a bridge opening. The compensation sensor shows about -25% of the strain on the strain sensors. Knowing the compensation sensor is positioned orthogonally to the strain sensors, a full mechanical bond between reference sensor and steel would account for -30% due to Poisson ratio. A rudimentary calculation shows the bond between reference sensor and steel is not flexible as promised by the contractor, but actually transfers $\approx \frac{25}{30} \approx 83\%$ of the applied strain.

New compensation
For the new compensation the following approach was used:

- Add the compensation channel to the strain channel. This removes the original compensation.
- Use the manufacturer's specsheets to obtain the STC-curve of the sensors.
- Use the discrete temperature measurements to obtain a prediction of the strain sensor temperature.
- Apply the STC using the temperature and STC Curve.

Two different sizes of Vishay strain gages were used, each with their own STC-curve. The STC has 2 components: a gain factor which is approximately 1.5% per 100 °C , which is neglected, and a thermal output polynomial. An example data-sheet is shown together with the polynomials for both sensor types in figure 4.22. The application of the new STC raises significant doubt on the accuracy of the strain measurements, see figure 4.23. The supplied "compensated" signal is sometimes completely out of phase with the uncompensated signal, while the new compensated signal is usually somewhere in between. One should note that neither the original compensation nor the new compensation is based on a temperature sensor directly besides the strain gage. This sensor may be metres away, but with a comparable vertical position relative to deck. This might result in a small temperature difference, which results in a significant compensation error.

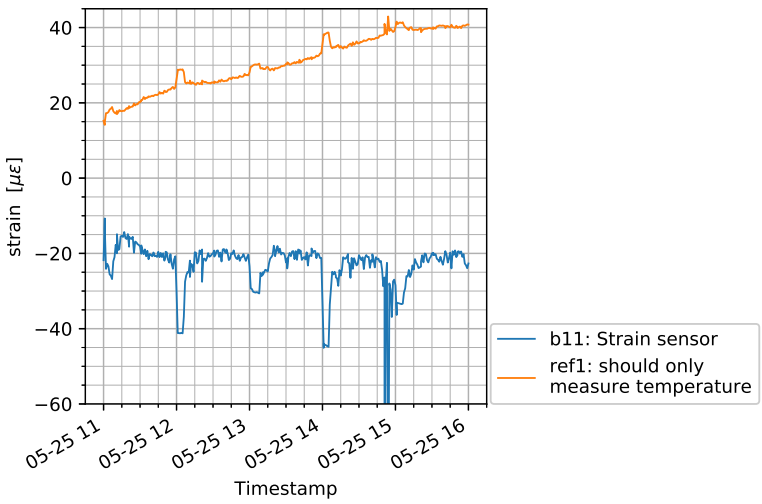

Figure 4.21: Example of unfiltered DSG STC-reference sensor measuring bridge strain instead of temperature effects

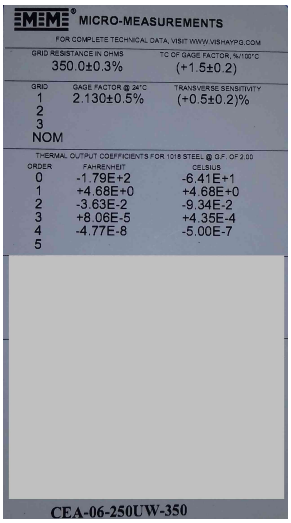

(a) Specsheet for type 250UW

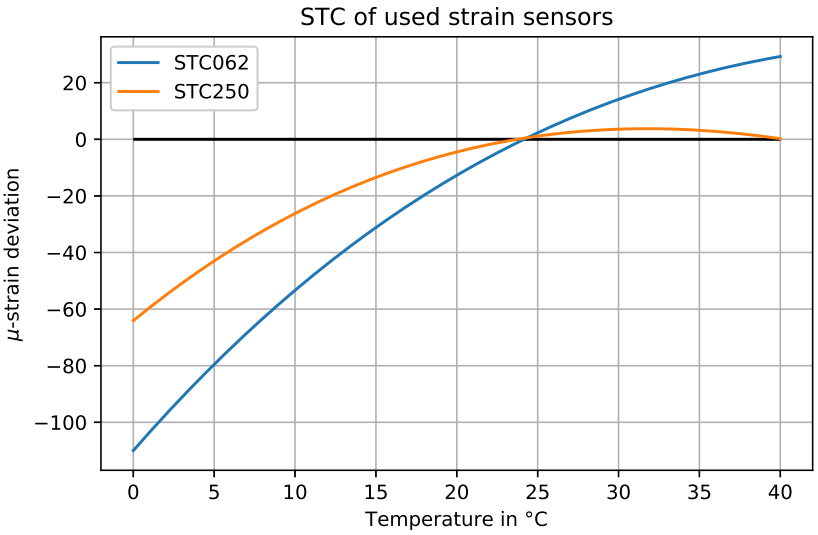

(b) STC polynomial for both types

Figure 4.22: STC for discrete strain gages.

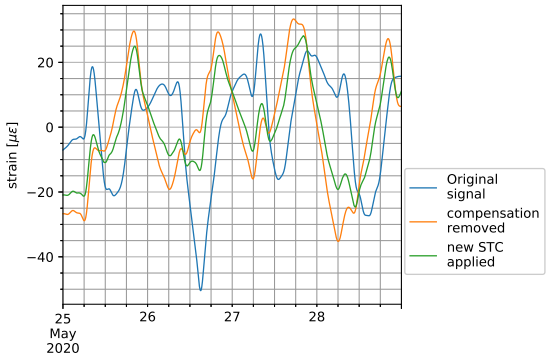

(a) Sensor b02: Bulb West Cantilever

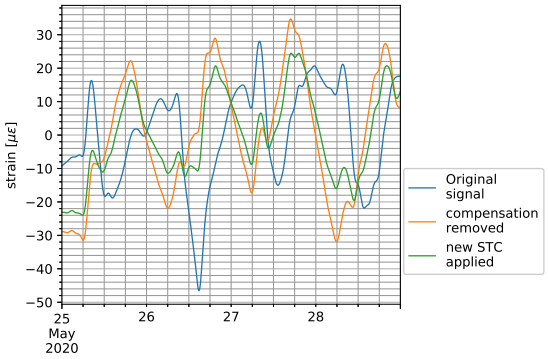

(b) Sensor b05: Bulb West Cantilever.

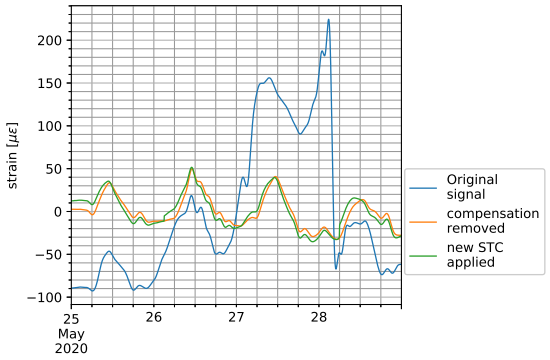

(c) Sensor b08: Bulb Eastside above the Box.

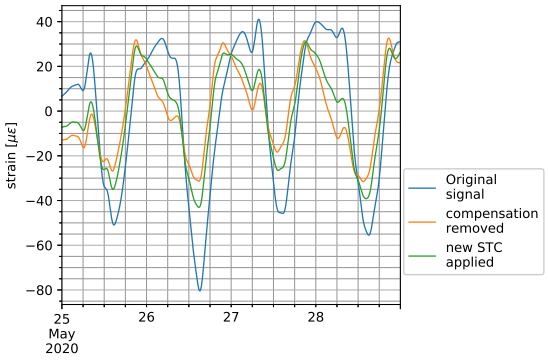

(d) Sensor b37: West Deck plate. (Next to b05)

Figure 4.23: Influence of sensor temperature compensation on discrete strain gages.

Table 4.5: Offset added to each FBG channel in ° C

c2	5.21	w1b	5.40	s01	3.31	s10	3.68
c3	5.61	w1be	5.61	s02	3.69	s11	3.56
d1	7.43	w1t	4.69	s03	3.12	s12	3.61
d2	5.95	w1te	5.36	s04	3.55	s13	2.91
d3	7.62	w2b	5.41	s05	4.16	s14	2.89
d4	6.63	w2t	5.28	s06	3.94	s15	3.27
o1	3.75	w3b	8.90	s07	5.16	s16	5.96
o2	3.18	w3t	8.61	s08	5.07	s17	5.56
o3	4.67			s09	2.25	s18	5.57

4.3.4 FBG Temperature offset

One of the analogue temperature sensors (at04) was placed right next to three FBG temperature sensors(s01,s02,s03) at the top of a West strut. The measurements of a few cool days for these sensors are shown in figure 4.24, while figure 4.25 shows the difference between each of the FBG strut sensors and the analogue temperature sensor at the same position. From this figure it is clear that the FBG sensors deviate significantly from the analogue temperature sensors. The analogue temperature sensors were compared against each other before installation, and they matched up to within 0.5 °C from each other. The analogue temperature sensors also show a plausible temperature in relation to the KNMI ambient temperature. This implies that the FBG temperature sensors have a significant offset, ranging from -2 to -5 °C for the strut sensors.
Figure 4.26 shows the temperatures of all analogue sensors mounted to a steel element. Between 03:00 and 09:00 all temperatures drop to a minimum of 13.0 ± 0.2°C. This implies the bridge cools down to a nearly homogeneous temperature state at night. The same period is shown for the FBG sensors in figure 4.27, here the temperatures drop to $7.5°C \pm 3.0$°C. No physical cause can be found for these large differences at night, implying this is just a sensor deviation. Therefore the FBG sensors have been manually offset: over a period of 3 cool days, the 0.005 quantile of the analog strut sensor and the FBG temperature measurements was calculated. The difference between each FBG quantile and the analog strut sensor quantile was then added to each FBG sensor. Values of the calculated offsets are shown in table 4.5. As can be seen in figure 4.28 the FBG channels now drop to 13.2 ± 0.2°C , similar to the analog temperature channels.

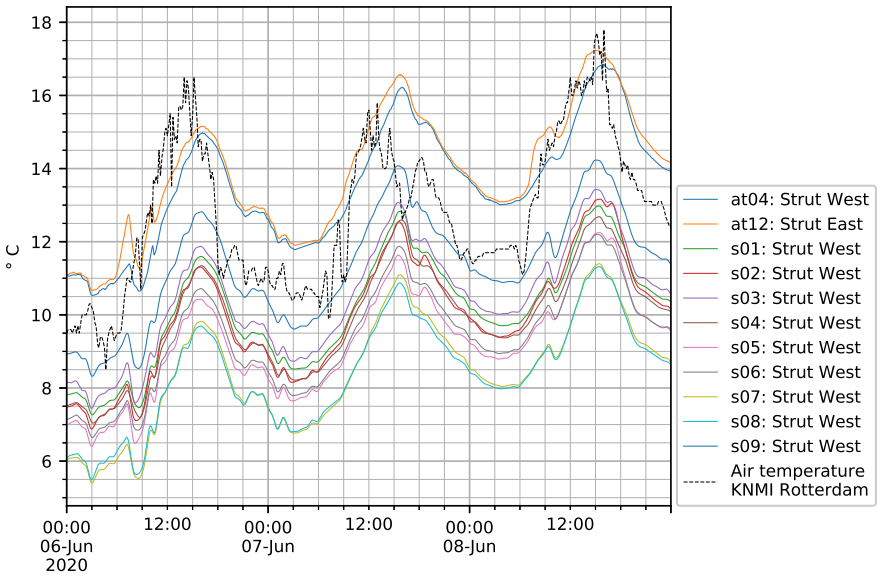

Figure 4.24: Strut temperatures from FBG and analogue temperature sensors.

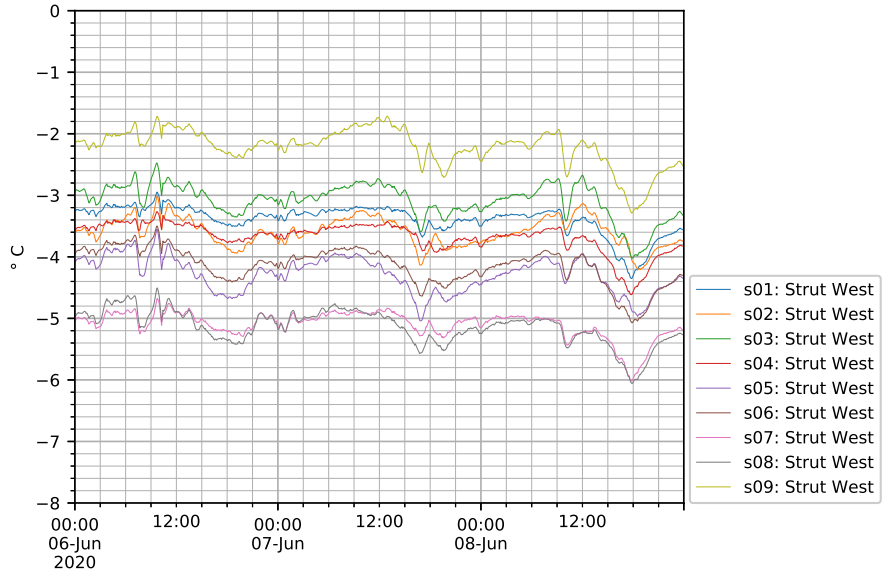

Figure 4.25: Difference between FBG strut temperature sensors, and the analogue strut temperature sensor at04.

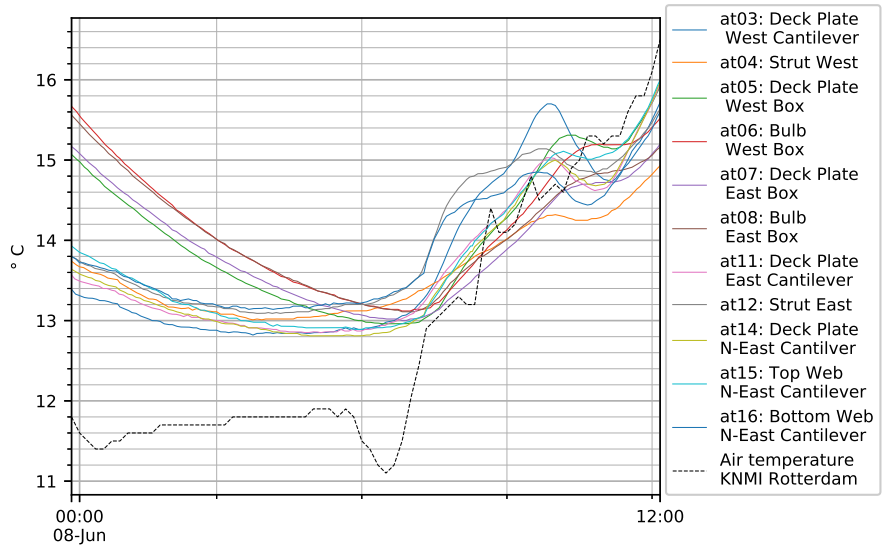

Figure 4.26: Analogue temperature sensor readings for steel elements on a cool night

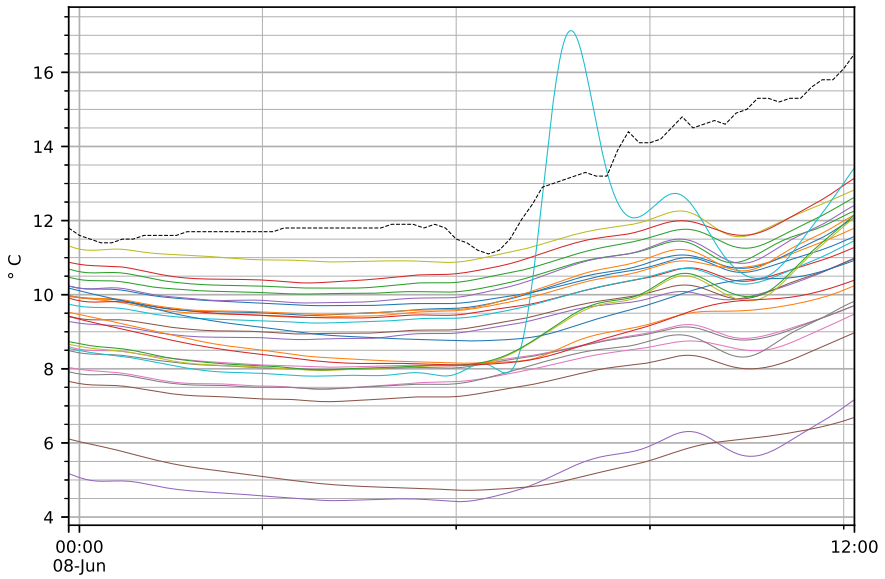

Figure 4.27: FBG temperature sensor readings for steel elements temperatures on a cool night

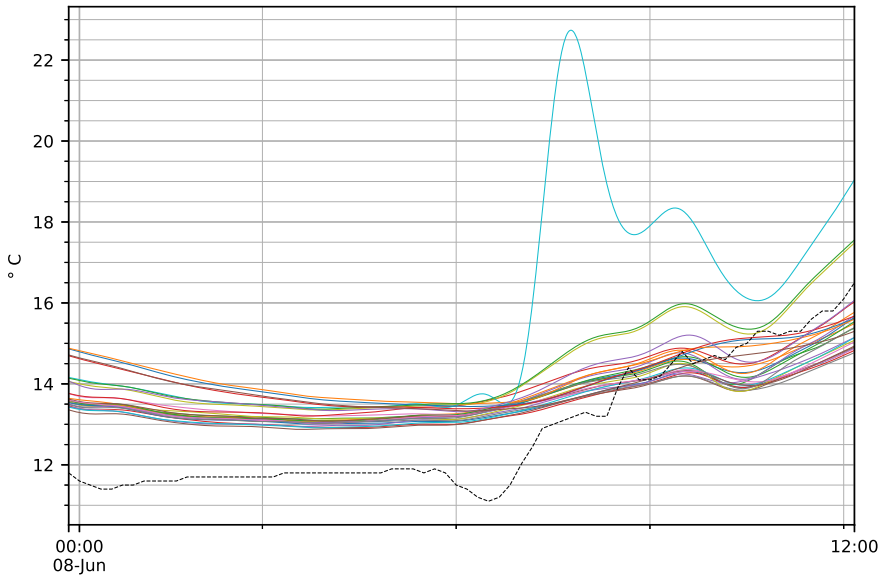

Figure 4.28: FBG steel temperatures on a cool night after offset

4.4 Case summary

The characteristics of the Haringvlietbrug, the measurement campaign and the post-processing of the measurements are summarized below.

Bridge Geometry:

- The bridge is a continuous static indeterminate steel box-girder bridge, containing 10 spans of 106 meter each.
- The 25.5 m wide deck consists of a 10 mm steel plate, with two 30 mm layers of asphalt on top, separated by waterproofing membranes.
- The deck is reinforced using longitudinal ribs with a 300 mm center-to center spacing.
- The frames encompassing the main crossbeams are positioned 2192 mm center-to-center.
- There is one set of struts in every 4 Frames.
- The box-girder is approximately 11.5 m wide and 5.3 m high.

Measurement campaign:

- The bridge was equipped with various brands and types of strain gages. Amongst others, in the following positions:
  - Discrete strain gages at the bottoms of various ribs
  - Discrete strain gages in the longitudinal direction underneath the deck plate.
  - FBG strain gages in the longitudinal direction near the top and bottom of the box-girder walls.
  - FBG strain gages at the bottom of the cross-beam flanges. Centered above the box, and halfway underneath the cantilever.
  - FBG strain gages at the top and bottom of the struts.
- The bridge was equipped with various brands and types of temperature sensors. Amongst others:
  - FBG temperature sensors at all FBG strain gage positions
  - Analogue sensors inside the top- and bottom asphalt layers, at the shoulder of the driving lane. These are near the outer edges of the cantilever.
  - Analogue sensors underneath the deck plate, below the asphalt sensors.
  - Analogue sensors underneath the deck plate and on the bottom of the ribs. Approximately at the shoulders of the center lane, above the box.
- The bridge was equipped with a Linear Variable Differential Transformer (LVDT) measuring support displacement, 424 m apart from the fixed support.

Data Processing:

- All data was downsampled to 1 sample per minute, and a low-pass filter was applied.
- The Sensor Temperature Compensation (STC) of the discrete strain gages induces significant uncertainty. The supplier did not correctly compensate for STC [2], thus the original compensation was removed. A new compensation was applied using manufacturer-supplied sensor specifications and the best available sensor temperature. There are significant differences between the compensated and the uncompensated strain signals. The result is very sensitive to both the sensor temperature and the compensation formula.
- After STC compensation, FBG strain sensors measure total strain, while discrete strain gages measure stress-induced strain. $\varepsilon_{total} = \varepsilon_{stress} + \varepsilon_{temperature}$.
- FBG temperature sensors show significant offsets between each other. Sensors that are know to be just 10 mm apart, show differences of up to 2.9°C relative to each other.
- All FBG temperature sensors show temperatures significantly lower than the ambient temperature from KNMI, and also lower than calibrated analogue sensors right next to them. Therefore all FBG temperature sensors are given an offset to match their temperatures in a cold night when, based on the analogue sensors, the temperature of the bridge is assumed homogeneous.

[2] The deficiency in the compensation was insignificant for the original sensor purpose

5 Measurement Data

The different sensor types were all operational in different periods. For a comprehensive analysis it's preferred to have all measurements at the same point in time. Unfortunately this was only partially possible.
The LVDT only became available after the strain sensors were dismantled. Table 5.1 shows that the period between 2020-05-21 and 2020-06-12 should have data for both strain and temperature sensors. Unfortunately multiple days show significant data loss. This might be due to a shutdown of the acquisition system, or due to a poor network connection.

Table 5.1: Available periods

Supplier	Start Measurements	Stop Measurements
DSG	2019-11-14	2020-06-11
FBG	2020-05-19	2020-06-12
Analogue	2020-05-21	ongoing
LVDT	2020-09-30	ongoing

From the set a few hot days are usable however. For instance the period from 2020-05-30 00:00 until 2020-06-01 23:59 shows 3 warm and sunny days with acceptable data quality. The period from 2020-06-06 00:00 until 2020-06-08 shows 3 cool days with acceptable data quality. The shown periods are exactly one week apart, and both periods shows Saturday, Sunday and Monday. This presents similar traffic conditions for the first 2 days. Unfortunately Monday June 1 is Whit Monday, a national holiday. This implies the 3rd day may not have similar traffic conditions.

The LVDT is not available in this period. Use of the LVDT will thus be limited to FE-model validation based on the remaining temperature sensors available in October 2020.

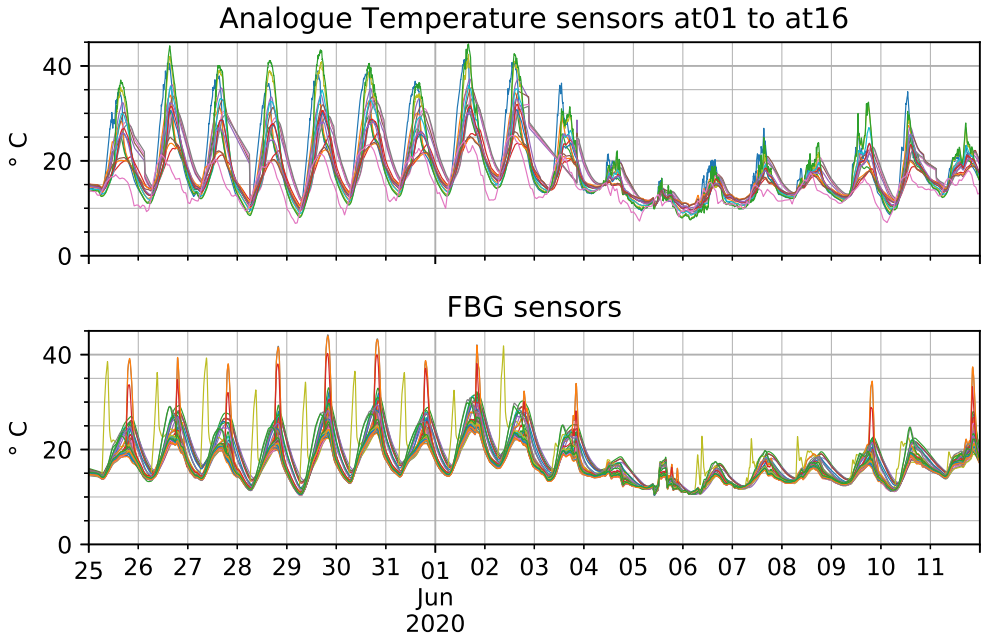

Figure 5.1: Temperatures full measured period

5.1 Measured temperatures

This section will show a subset of the measured temperatures. Not all measured temperature distributions are intuitive, in appendix B an ordinary differential equation (ODE) is used to create a heat flow model of the asphalt deck plate composite. This model is studied to explain the effects of solar radiation, ambient temperature, barrier induced shade and, finally, trapped air inside the box. For the full analysis please see appendix B. For the exact positions of all sensors see figures 4.6 to 4.16.

Figure 5.2 shows all analogue sensors in the warm period. In this period the largest simultaneous temperature difference between 2 sensors is approximately 20°C and occurs on June 1st around 16:00. The minimum simultaneous temperature differences usually occur between 06:00 and 06:30, just before sunrise. The ΔT at this time can be as low as 3 °C on June 1st. The Dark green line that obtains the highest temperature is the North-East top asphalt sensor.
Figure 5.3 shows the FBG temperature sensors of interest for the same period. Both figures show a similar pattern: just after sunrise the bridge starts heating up, reaching it's peak temperature between 14:00 and 16:00. After sundown the bridge slowly cools down to just above ambient temperature. This cooling process continues until sunrise, when the ambient temperature rises again. The bridge, with it's large thermal inertia, then follows again.

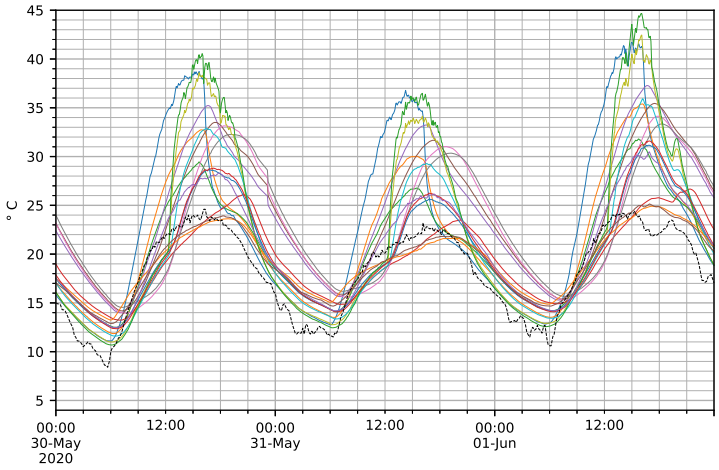

Figure 5.2: Analogue temperature measurements for 3 warm days.

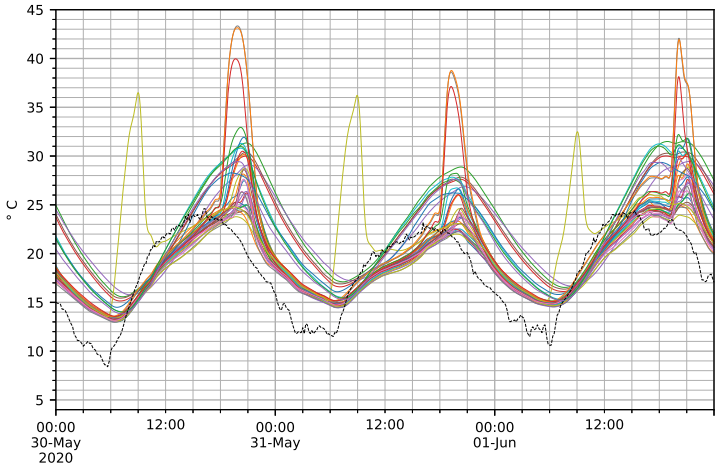

Figure 5.3: FBG temperature measurements for 3 warm days.

Figure 5.5 shows the temperature distribution of the main box girder, using sensors on both the East and West wall, positioned 200 mm above or below the corners. The red line shows short but large temperature peaks on the lower side of the East wall just before 09:00. The orange lines shows similar peaks on the lower side of the West wall starting just after 18:00. These peaks might be caused by a low sun shining underneath the cantilever. With the strong drop after 09:00 being caused by shade from the cantilever. The cantilever is approximately 7 meter wide, and the bottom box wall sensors are approximately 4.7 meter below the lower edge of the cantilever. A solar inclination below $\approx 34^{\circ}$ would then allow sun to hit the box wall at the sensors position. Figure 5.4 shows the solar inclination for June. The inclination crosses the 34° line at approximately 09:30 and 17:30. This confirms the assumption that the peaks are caused by sun shining underneath the cantilever. Small differences in the calculated times are caused by not including the bridge- and solar azimuth in the shade calculation.

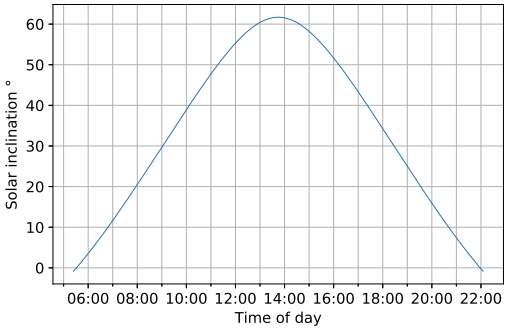

Figure 5.4: Solar inclination

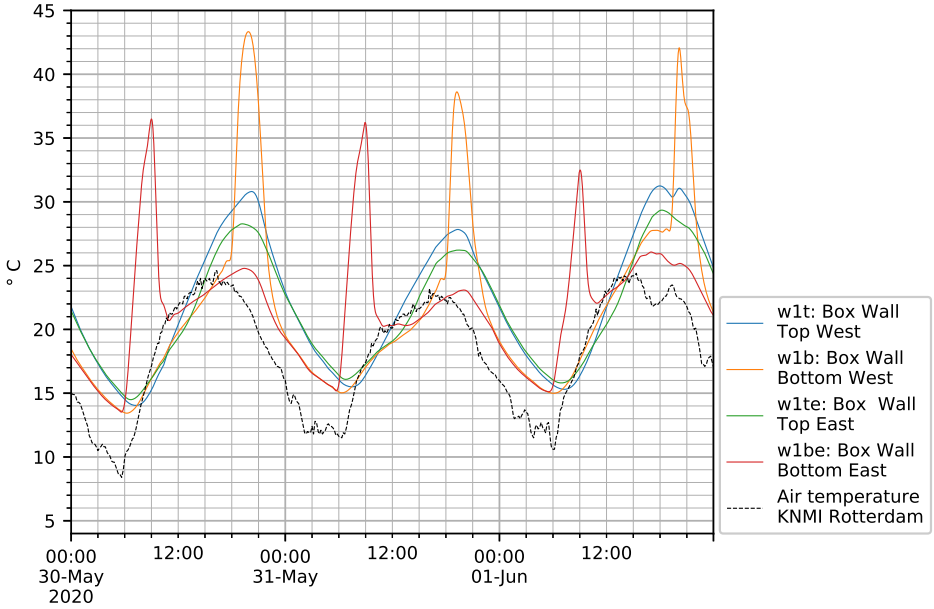

Figure 5.5: Temperature of the Box Walls.

The bridge is oriented in North-South direction, with an Azimuth of 21.1°. With the sun predominantly moving in the East-West direction, the assumption is that there is no significant temperature gradient along the North-South direction. The measurements from figure 5.6 do confirm this. The North asphalt and deck plate sensors, (at13, at14) are 50 meter further North than the normal sensors (at09, at11), and show very similar temperatures. The largest temperature difference is only 2°C, which may be attributed to local effects such as shade.

Looking at the temperature distribution between the top of the asphalt and the bottom of the deck plate, figures 5.7 and 5.8 show a large vertical gradient. The sensors for the top and bottom of the asphalt are only 40 mm apart, but still show temperature differences of over 6°C between each other. Asphalt temperature reaches 44.5°C in the period shown, the absolute maximum temperature for the entire measurement period was 54.86 °C for the North-East top asphalt sensors on Aug 15 2020 15:44. The distance between the bottom asphalt sensor and the deck plate sensor is only 20 mm and shows temperature differences of 4°C. The total difference between the top of the asphalt and the bottom of the deck plate reaches over 10°C . The deck plate obtains temperatures of 31°C, which is approximately 8°C warmer than the ambient air temperature in Rotterdam.

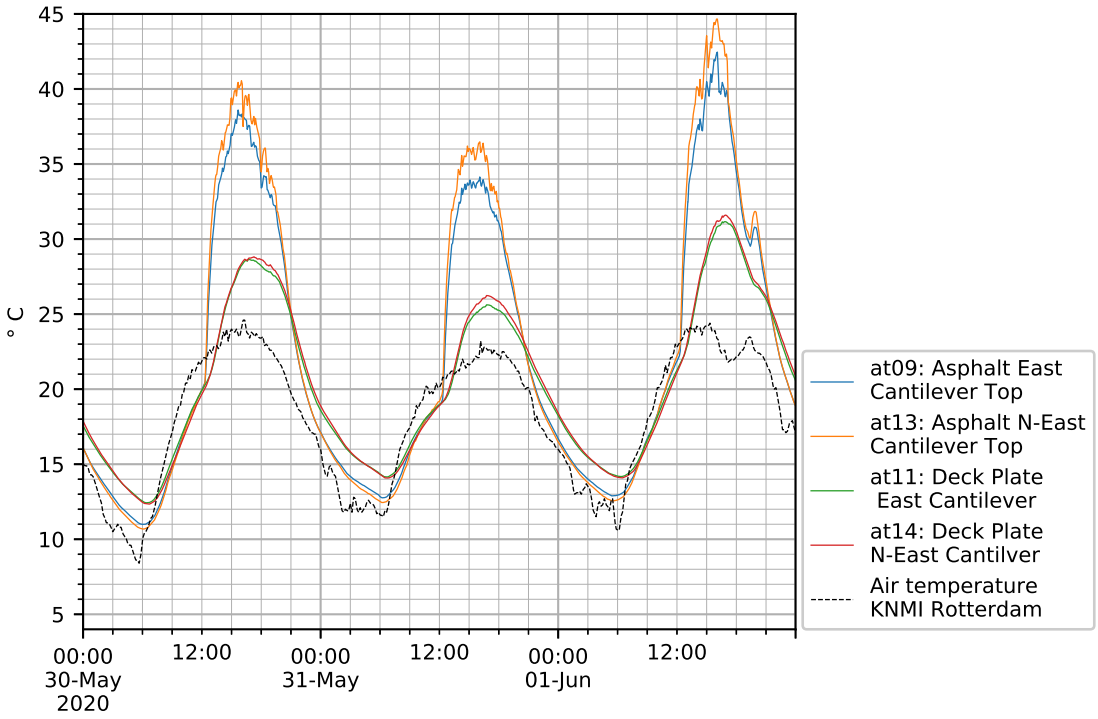

Figure 5.6: Temperature distribution in the North-South direction.

Figure 5.9 shows the temperature distribution of the deck plate along the West-East Axis.
For the days shown in figure 5.9, the sensors on the West side of a (driving) lane show a strong temperature rise in the morning, while the sensors on the East side of a lane lag behind. Just after 12:00 the East side of the lanes suddenly shows a fast temperature rise. This effect can be explained by shade. The sensors are on the shoulder of the lane, while the lanes are separated by 80 cm high steel barriers. Depending on the solar inclination, these barriers cast a shade on the asphalt containing the sensors. A full study of this effect was done in appendix B, with figure B.3 showing the effects of the daily solar cycle on the barrier induced shade.
Figure 5.9 also shows different behaviour between the cantilever and the parts above the box. In the morning the East cantilever heats up faster than the East deck above the box. They obtain the same solar radiance, but the cantilever is also heated by the warm ambient air underneath it. The box however is filled with cool air, and thus the deck above it shows a small lag in temperature rise. During the day the air inside the box heats up, to well above ambient temperature, allowing the deck above the box to reach higher temperatures than the cantilever. In the evening the temperatures of the cantilevers quickly drop, while the deck above the box stays warm due to the trapped hot air. For the shown period no air temperature measurements are available in the box. In September some additional sensors were placed, confirming this hypothesis. Figure 5.10 shows a few warm days in September, following a cooler period. Early in the morning of 13 Sept all temperatures are similar to the ambient temperature. Around 09:00 the air temperature in the box rises, due to the morning sun heating the East box wall. Between approximately 10:00 and 11:00 no direct sunlight hits any of the box walls or the deck above it. The air temperature inside the box rises slowly during this period. After 12:00 the solar inclination is high enough to reach the entire deck (in September solar inclination is much smaller than in June), and the temperature rises strongly. After the sun lowers again, the air temperature inside the box lowers significantly, mainly due to heat-loss to the deck plate. The air temperature inside the box does not drop all the way to the outside temperature. In the night of 13-14 September, a temperature difference of 5°C between inside and outside air temperature remains. This temperature difference was not present the night before.

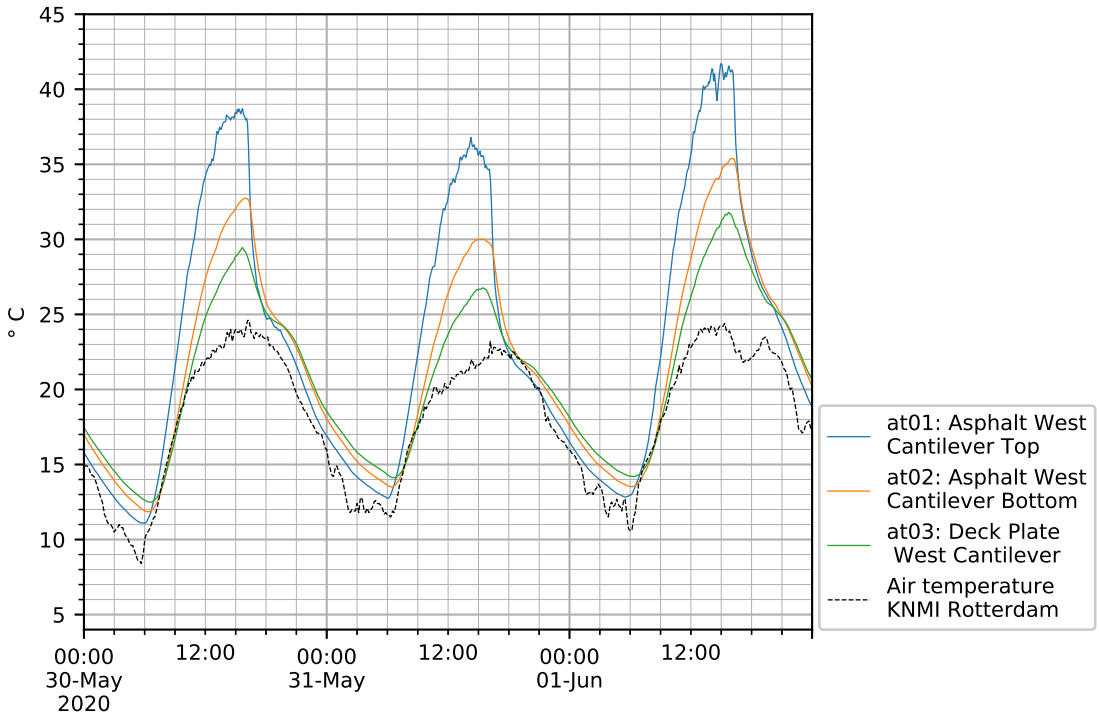

Figure 5.7: Temperature distribution inside the West cantilever deck.

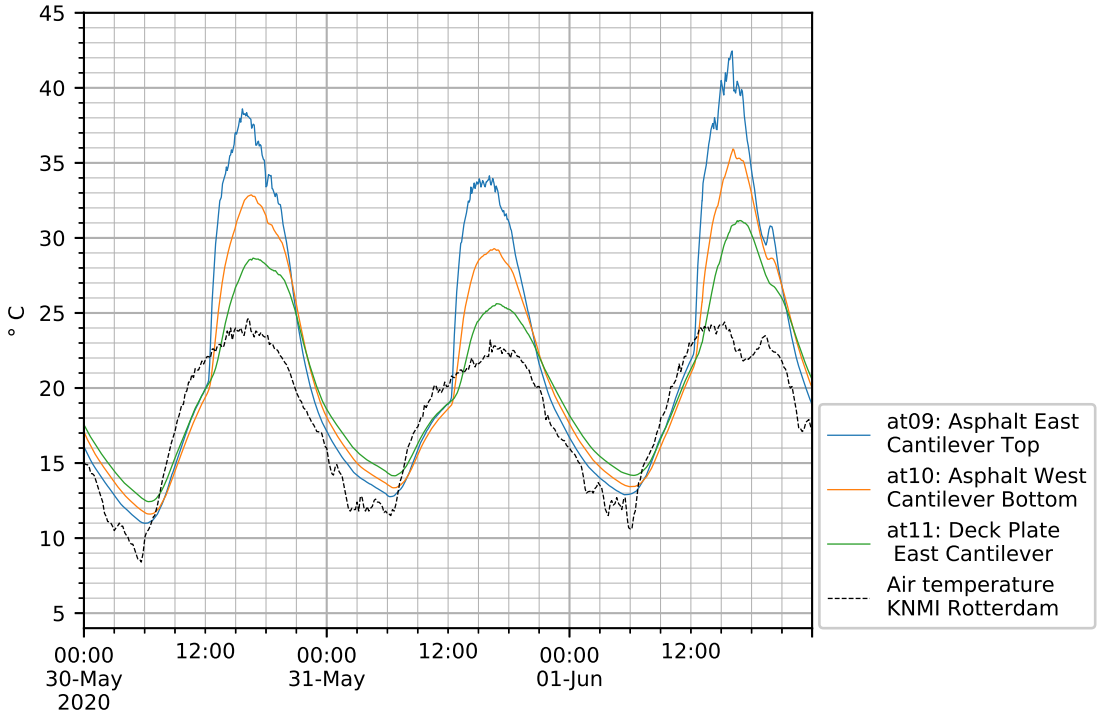

Figure 5.8: Temperature distribution inside the East cantilever deck.

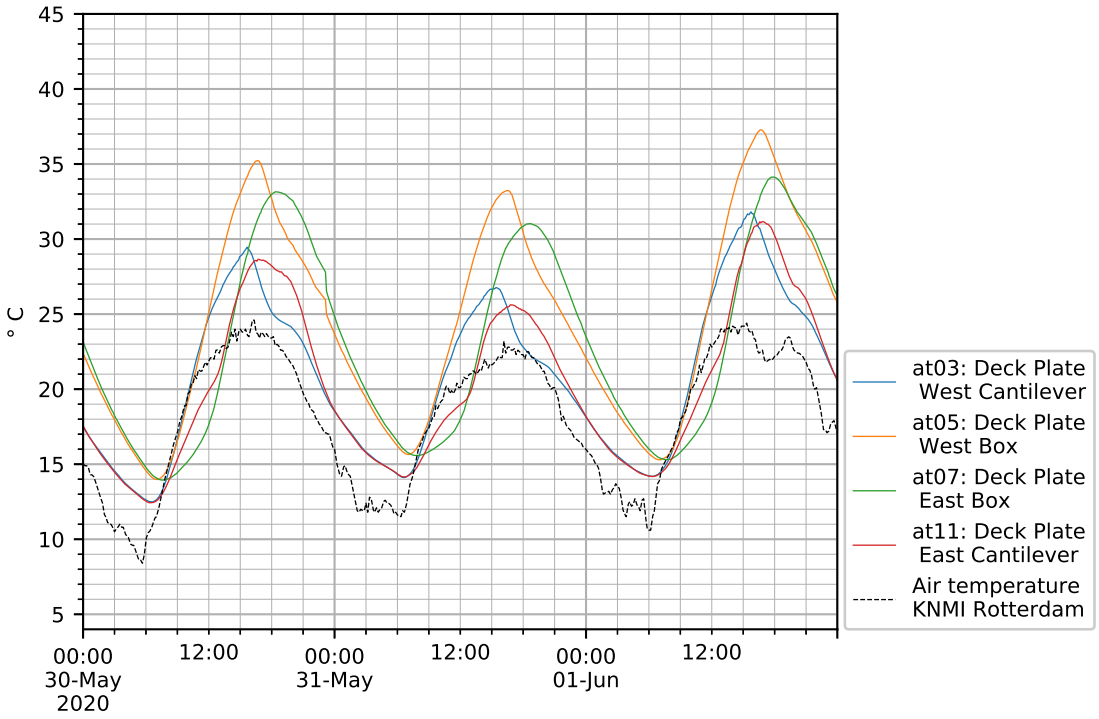

Figure 5.9: Temperature distribution of the deck plate in the West-East direction

The vertical temperature gradient between asphalt and deck plate was shown to be over 10°C in figures 5.7 and 5.8. This temperature gradient occurred over a height of just 60 mm. Figure 5.11 shows the vertical temperature gradient between deck plate and the bottom of the ribs. The steel rib is made of 160 mm high profiles having a 40x12 mm bulb at the bottom. The temperature difference between deck plate and bulb is usually within 2°C over 160mm height. This implies the total vertical temperature gradient is strongly non-linear. This is in agreement with the codes, as shown in chapter 3.1, where the temperature gradient along the height of the bridge is piecewise linear with 3 segments, each 100 mm high, in the top 300 mm of the bridge.

Three struts on the West side are equipped with a total of 19 temperature sensors. Each strut has three FBG sensors near its top (s01 to s09) and three FBG sensors near its bottom (s10 to s18). An extra analogue temperature sensor (at04) was placed right next to sensors s01 to s03, in order to compare the two types of sensors. For each strut a top and bottom sensor is shown in figure 5.12.
All West struts undergo similar daily temperature cycles, indicating there is no significant temperature gradient along the longitudinal bridge axis. In the evenings the sun hits the lower part of the struts, causing short but distinct temperature rises, as was also shown in figure 5.5 for the box walls.

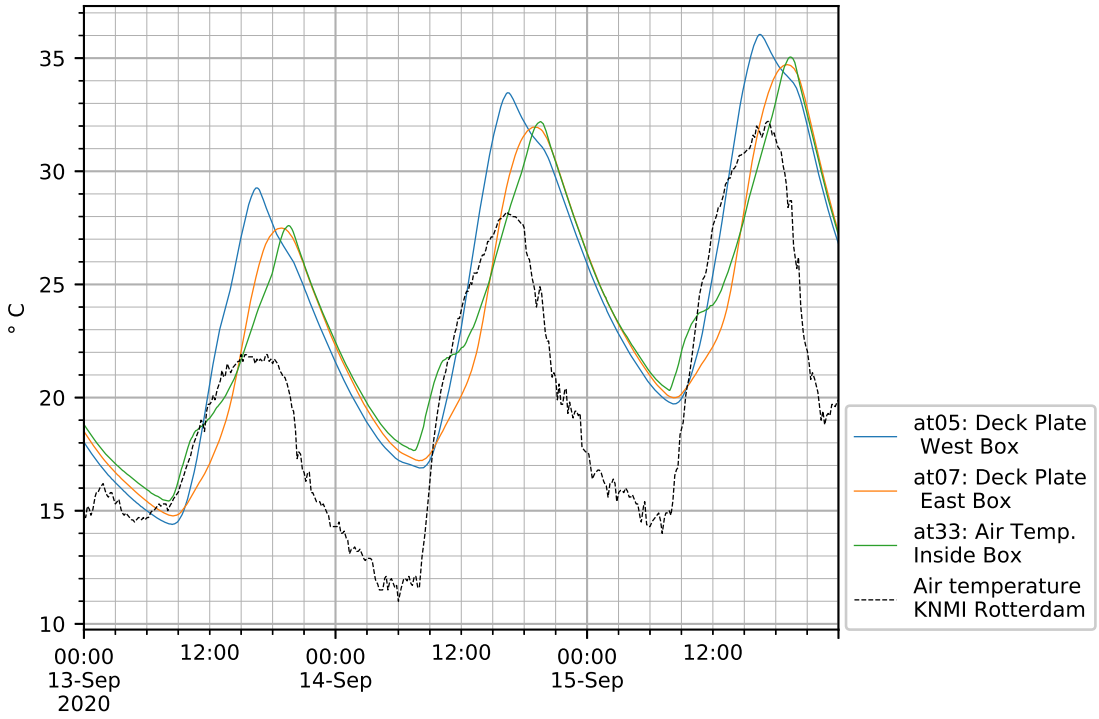

Figure 5.10: Air temperature inside the box influencing the deck plate above it

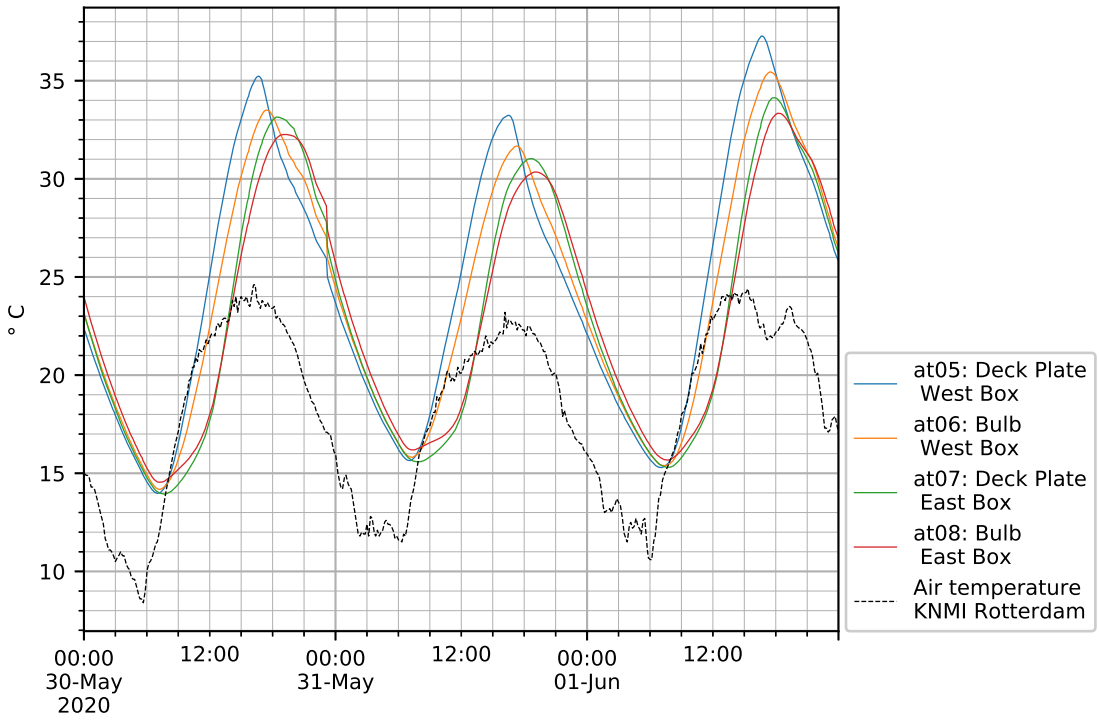

Figure 5.11: Temperature of deck plate and bulb above the box.

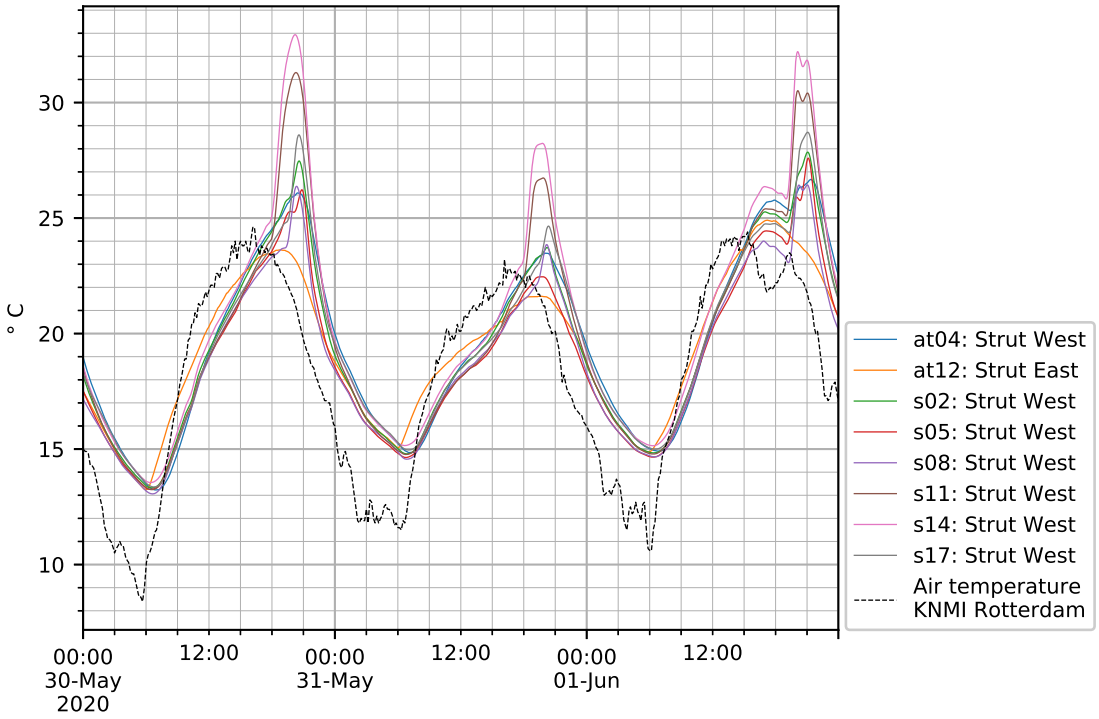

Figure 5.12: Temperatures of the struts.

5.2 Measured support displacement

By measuring the axial displacement of the bridge, the average axial strain in the bridge can be approximated. The LVDT is in operation since Sept 30. The warmest days available in October were found to be Oct 16 and Oct 17, so this period is included in figure 5.13. The asphalt reaches temperatures of just over 20°C, while the deck plate reaches temperatures of 16 °C. The daily temperature amplitude is approximately 9°C for steel elements. During this period the axial displacement of the bridge varies between -32 and +2 mm. An amplitude of 34 mm. In figure 5.13 the curves of the LVDT displacement and the sensor temperatures look similar.
To verify if the bridge is free to move along it's roller support a comparison is made between:

- The average axial strain in the bridge, based on the displacement of the LVDT divided by the distance between the LVDT and the fixed support:
  $\varepsilon_{LVDT} = \frac{\text{Displacement}}{\text{Distance}} = \frac{0.001}{4 \cdot 106} = 2.36\mu\varepsilon$ per mm displacement.
- Using the temperature coefficient of steel, and each of the temperatures measured by the shown sensor, a prediction of axial strain can be made. Assuming the entire bridge has a homogeneous temperature, the axial strain would be:
  $\varepsilon_{TemperatureSensor} = \alpha_{T,Steel} \cdot \Delta T = 12 \cdot 10^{-6} \cdot DeltaT = 12\mu\varepsilon$ per $\Delta^{\circ}C$

The predictions of the average axial strain based on the LVDT and three temperature sensors are shown in figure 5.14. The figure shows that a single well placed temperature sensor is to some extent capable of predicting the average axial bridge strain and the support displacement. The standard deviation between the strain expected based on the web temperature of the west cantilever, and the strain based on the support displacement is only 5.4 $\mu\varepsilon$, while the daily amplitude is $80\mu\varepsilon$. For the highest temperatures the LVDT shows a slightly smaller strain. This could indicate an inhomogeneous temperature distribution in the bridge. The temperature measurements 5.1 show that higher temperatures also result in larger temperature gradients inside the bridge. At night a single sensor might be representative of the average bridge temperature, but during a warm and sunny day the complex 2D or even 3D-temperature distribution inside the bridge cannot be captured by a single sensor.

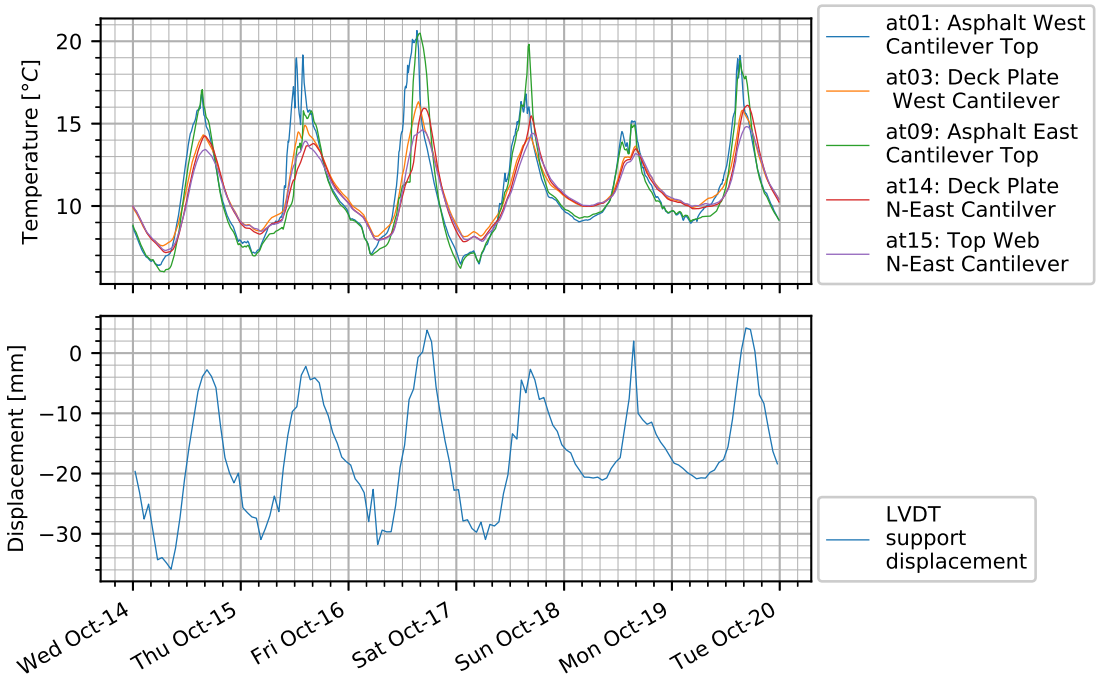

Figure 5.13: Axial support displacement compared to temperatures.

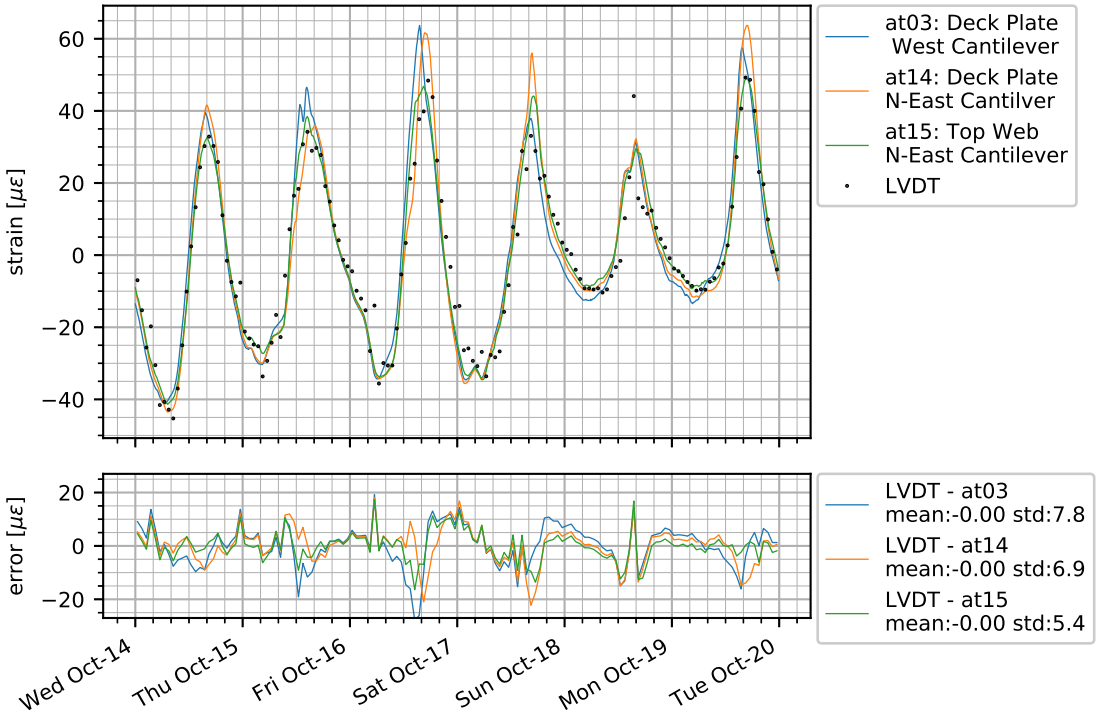

Figure 5.14: Average axial strain in the bridge, and deviation between LVDT and Temperature predictions

5.3 Measured traffic

Traffic load was not measured on the Haringvlietbrug itself, but Rijkswaterstaat provides traffic intensity data at 2 points near the bridge, see figure 5.15 for exact locations. The most northern point measures South-Bound traffic, while the Southern point measures North-Bound traffic. Traffic is reported in intervals of one hour, e.g. total vehicles between 12:00 and 13:00. The distance between the measurement locations and the bridge is relatively small compared to the distance travelled by a car or truck in this interval. Therefore no correction for distance is applied. Each one hour interval is converted to a data point at the half hour. For instance the interval between 12:00 and 13:00 is shown as a single point at 12:30.

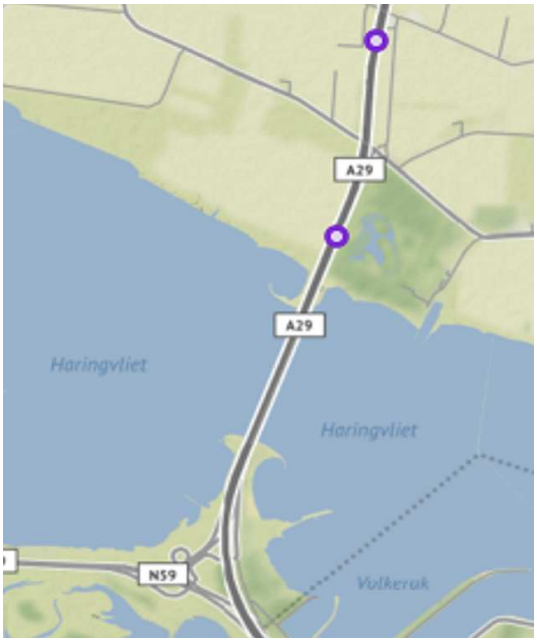

Figure 5.15: Traffic measurement system locations

An overview of the amount of passing vehicles for the periods of interest is shown in figure 5.16. Traffic intensity is split out per vehicle length class, and some weights have been assumed in table 5.2. Measured average vehicle speed is also reported. Based on vehicle amount, mass and speed, the traffic load can be simplified to an Uniformly Distributed Load (UDL) on the bridge. Strains are downsampled to 1 sample per minute, and with over 1500 passing vehicles per hour, each sample contains approximately 25 passing vehicles per direction. Therefore conversion to UDL seems a justifiable simplification.
UDL per vehicle category is calculated using equation 5.1, and shown in figure 5.17.
On Saturday, freight traffic starts increasing at 03:00 and rises till 10:00. At 12:00 it starts decaying linearly until midnight. Total traffic weight on Saturday May 30 reaches $0.55 + 0.45 \approx 1.0\text{kNm}^{-1}$, with large trailers contributing over 50% of total load.
On Sunday May 31 there is little freight traffic, this may be due to the general ban on Sunday freight traffic in France and Germany. Traffic from light weight vehicles starts increasing after 06:00. Total traffic reaches 0.45kNm^{-1}, with freight traffic contributing less than 25%.

Monday June 1 is Whit Monday, and a national holiday. Traffic rises again at 03:00 until approximately 12:00, reaching a total of 0.7kNm^{-1}.

$$q_{UDL\ Vehicle} = \frac{\text{Vehicles/hr} \cdot \text{Vehicle Mass [Ton]} \cdot 9.81}{3600 \cdot \text{Vehicle speed [m/s]})}\ [\text{kNm}^{-1}] \tag{5.1}$$

Traffic load is split into 3 categories: car, truck and trailer. For application in the FE-model, simplified assumptions on distribution over the lanes are needed: Trucks and trailers use the right lane, cars use the left lane. In reality some cars may use the right lane, and some trucks may overtake each other. But during rush hours, when traffic loading is dominant, the simplification seems justified.

Table 5.2: Assumed vehicle weights based on reported length.

Length m	Type -	Weight Ton	Speed m/s
2.4 to 5.6	Car	1	31.9
5.6 to 11.5	Truck	8 Ton	27.8
12.2 and above	Trailer	30 Ton	23.6

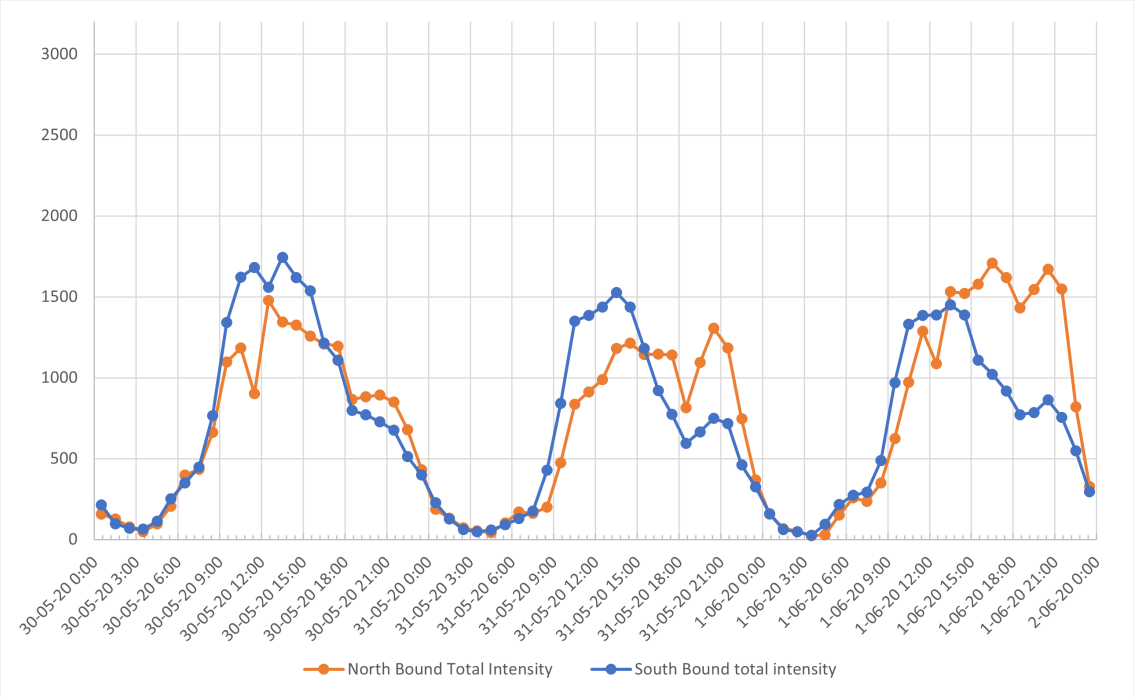

(a) Sat May 30 to Mon June 01

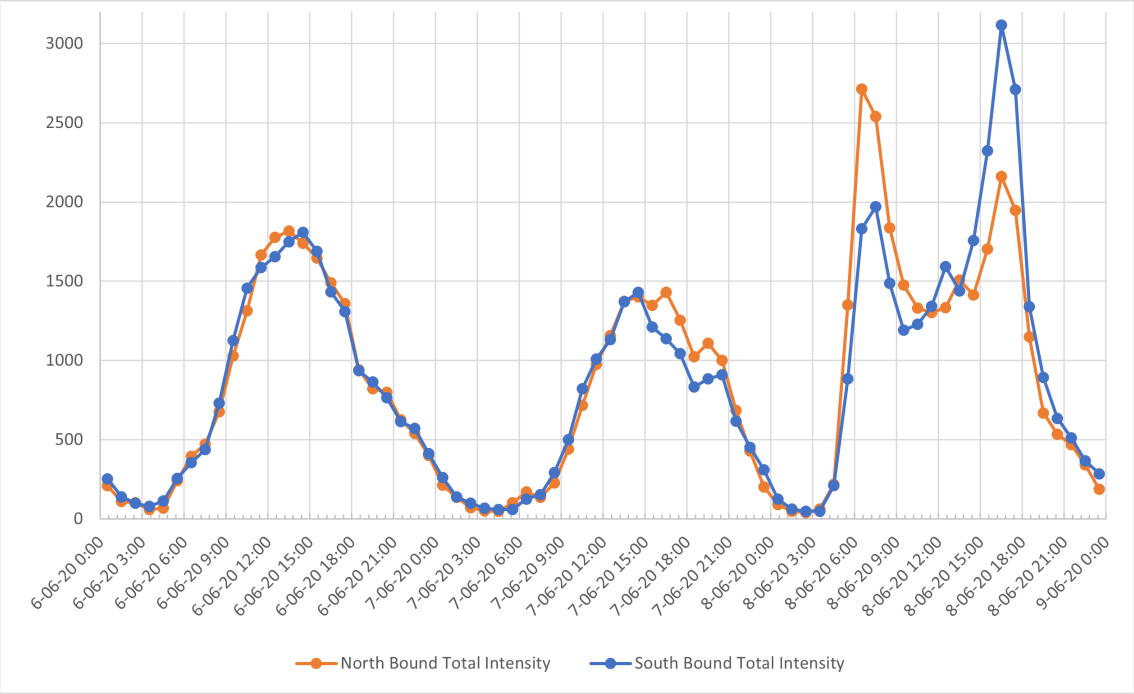

(b) Sat June 06 to Mon June 08

Figure 5.16: Total passing vehicles per hour

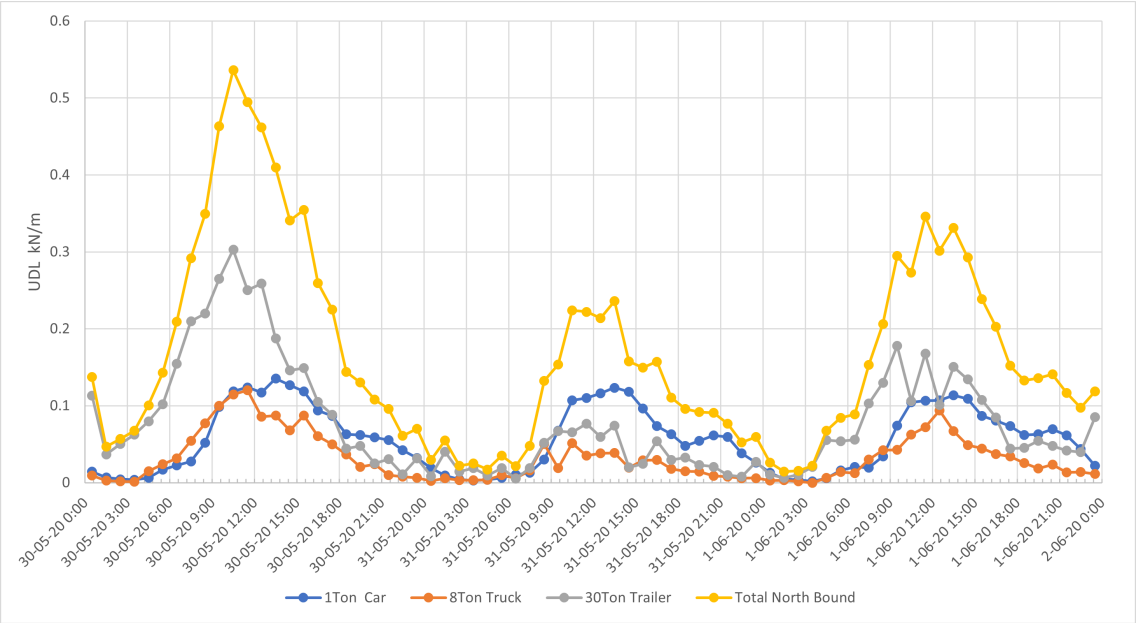

(a) Northbound

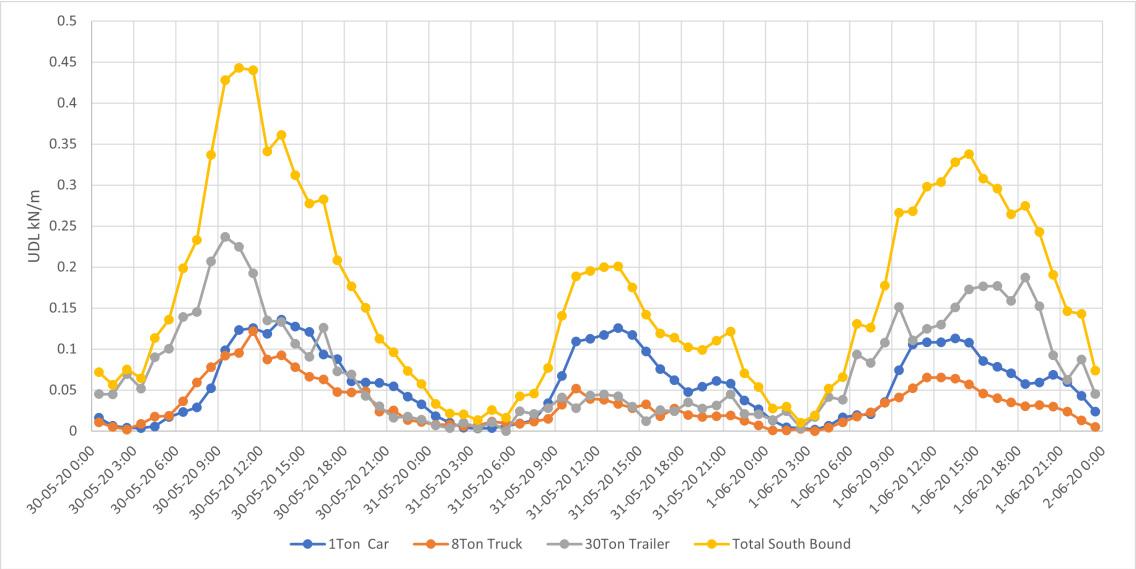

(b) Southbound

Figure 5.17: Traffic intensity converted to UDL loads in kN/m

5.4 Measured strains

There is a plethora of strain measurements available because the original measurement campaign focuses on peak stress near some specific connections. The research questions in this thesis mainly cover the dynamic behaviour of the deck and bulbs, so only a few subsets are used. See figures 4.6 to 4.15 for detailed drawings of sensor positions.

- The w... FBG sensors of the box wall for verification of the global bridge elongation and curvature.
- Sensors b01 to b06, b11, b12 for bulb stress in the cantilever.
- Sensors b07 to b10, b13, b14 for bulb stress above the box.
- Sensors b36, b37 for deck plate stress in the west cantilever.

Before the measured strains are shown, the reader is reminded of the sensor temperature compensation discussed in paragraph 4.3.3. The reported strains are either compensated by the FBG supplier or by the author, but contain significant uncertainty.

Strain sensors are glued to the structure while it is already loaded with self weight and traffic. It is therefore only possible to measure a change of strain since commissioning of the measurement system. This is, however, an arbitrary point in time. Temperature measurements have shown that, for the periods shown, internal temperature differences are smallest between 06:00 and 06:30 in the morning. While each day the temperature distribution in the bridge may significantly vary due to environmental influences, between 06:00 and 06:30 the same nearly homogeneous internal temperature distribution is reached. With the only remaining variable being the average homogeneous bridge temperature, which does not induce significant stress as will be shown by the FE-model explained in section A. This implies that this period could also serve as a reliable reference point for temperature induced stress. Therefore the strains are given an offset in order to have the mean strain between 06:00 and 6:30 equal to zero for one of the shown days. The area that is used for this zero-offset is indicated with black lines.
All strains are shown as total Δ-strain, according to equation 5.2, which for 1D-linear elasticity results in equation 5.3.

$$\varepsilon_{total} = \varepsilon_{temperature} + \varepsilon_{stress} \tag{5.2}$$

$$\Delta\varepsilon_{total} = \alpha_T \Delta T + \frac{\Delta\sigma}{E} \tag{5.3}$$

The strains in the box walls are shown in figure 5.18. Unfortunately data corruption has occurred on one of the channels for May 30th and 31st. The strains are offset in such a way that mean strain on May 30 between 06:00 and 06:30 equals zero. The top of the West and East box wall show similar strain behaviour, with 10 to 13% difference at the daily peaks around 18:00. The West bottom box wall deviates significantly from the other parts. No cause for this has been found yet. The short drops in strain of the West bottom box wall just after 18:00 coincide with the large temperature spike at that time, see figure 5.5 for the temperature plot. At this time the local temperature rises strongly. A few possible explanations for this downward spike are evaluated:

1. If this part of the box wall was free to deform, then the increase in temperature should result in an elongation. This should show up as a positive strain peak. This does not correspond to figure 5.18.
2. If this part of the box wall is not free to deform, then there would be no change in total strain. Therefore no peak should be visible just after 18:00.
3. If the FBG-sensor were temperature-compensated in such a way that it measures stress induced deformation instead of total deformation as stated by the supplier, then a partly prevented elongation should result in a compression spike. This is in accordance with the graph. The 20°C temperature rise could result in $20 \cdot \alpha T = 20 \cdot 12 \cdot 10^{-6} = 240\mu\varepsilon$. The 30 $\mu\varepsilon$ drop on May 31st 18:00 could indicate approximately $\frac{1}{8}$ of total strain is prevented. However, if only stress induced strain were shown by the FBG sensors, the other strains should all be close to 0. The LVDT has shown that the axial bridge elongation is in agreement with what would normally be expected if the bridge was free to elongate. This implies that daily temperature variations should not induce significant global axial stress in the box walls.
4. This part of the box wall is close to the center of the 106 meter bridge span. Therefore the assumption is that this part is both under tension in the axial direction, and that shear forces are relatively low. Non-linear effects such as partial plate buckling are thus deemed unlikely to occur during the day. If the local plate temperature significantly rises, extra compression stress might occur however. If this were to result in buckling, the strain should still show a positive spike, because the plate would be free to expand sideways, and not a negative one.
5. If the FBG Sensor temperature compensation were applied incorrectly (see chapter 4.3.3), then a large change of temperature might result in significant sensor drift, resulting in false readings.

Explanations 1 to 4 are not in agreement with the measurements shown. Explanation 5 might explain the shown measurements. Therefore it is concluded that the small drops in strain at the West bottom box wall at the time of the large local temperature rise, are most likely caused by incorrect sensor temperature compensation.

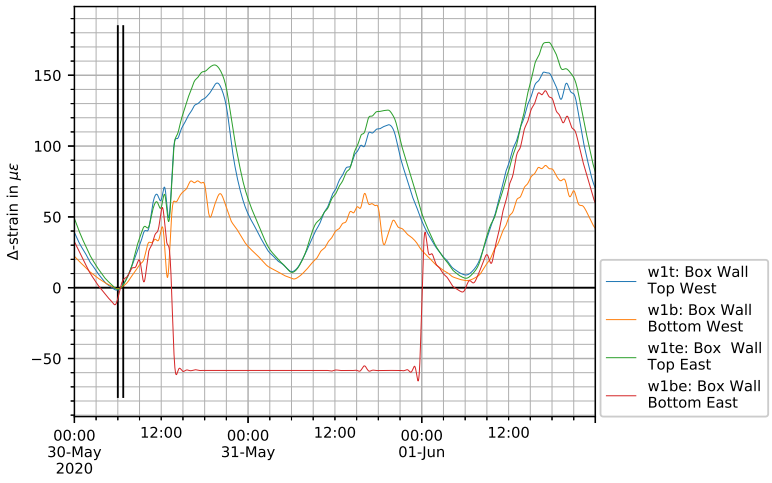

Figure 5.18: Strains in the box wall.

The strains in the bulbs of the cantilever as shown in figure 5.19 show a significantly smaller daily amplitude than was shown for the box walls. The box walls show a daily strain amplitude of approximately 150 $\mu\varepsilon$, while the bulbs show a daily strain amplitude of approximately 40 to 50 $\mu\varepsilon$. Figures 5.9 and 5.5 have shown the daily temperature amplitude is in the order of 10°C for the deck plate and box walls. If bridge elongation is not prevented, then this should result in a daily strain amplitude of $\varepsilon = \Delta T \cdot \alpha_T \approx 10 \cdot 12 \cdot 10^{-6} = 120\mu\varepsilon$. The asphalt has a much larger daily temperature amplitude, and has a higher temperature coefficient. Therefore if the asphalt temperature is also accounted for, then the daily strain amplitude should be even larger. This discrepancy remains unexplained.
Another striking detail is what looks like either a sudden spike in strain between 06:00 and 11:00, or a sudden drop in strain between 08:00 and 12:00 on May 30 and 31. The exact is also unknown. Traffic rises strongly at that time for May 30 (figure 5.17), but on May 30 the traffic intensity is half of that the day before, while the drops seem to have an equal magnitude.
At the same time of the the spike, the East box wall temperature shows a large temperature spike. It is however unclear how that could result in tension strain in the West bulb, without also inducing this strain in the bulbs above the box, or the West box wall. The drop and/or spike remain unexplained.
The bulb strains also deviate from each other. The largest difference of approximately 16$\mu\varepsilon$ between b01 and b06, which are both West cantilever bulbs, occurs at 21:00 on May 30. Figure 5.9 has shown that the largest temperature deviation of a cantilever deck due to barrier induced shade occurs at 12:00 and 18:00, and not at 21:00. Therefore barrier induced shade is an unlikely cause of the strain deviation between bulbs b01 and b06. Figures 5.20 and 5.21 show the strains for 2 bulbs, with sensors b05 and b06 at mid-span of the bulb, while sensors b11 and b12 are positioned next to the web of the cantilever cross beam acting as the support. The sensors are not on the same span, but they are positioned along the same bulb-axis. See figures 4.6, 4.10and 4.12 for detailed sensor position drawings. The sensors clearly show a difference between mid-span and the support. This is indicative of curvature. For a clamped-clamped beam loaded with a q-load the mid-span bottom shows tension and positive strain, while the bottom near the support shows compression and negative strain. A continuous static indeterminate beam on multiple supports shows little curvature due to inhomogeneous temperature, and the curvature has a similar size on cold days (figure 5.21), so it's likely this curvature is traffic induced, and not caused by temperature change.

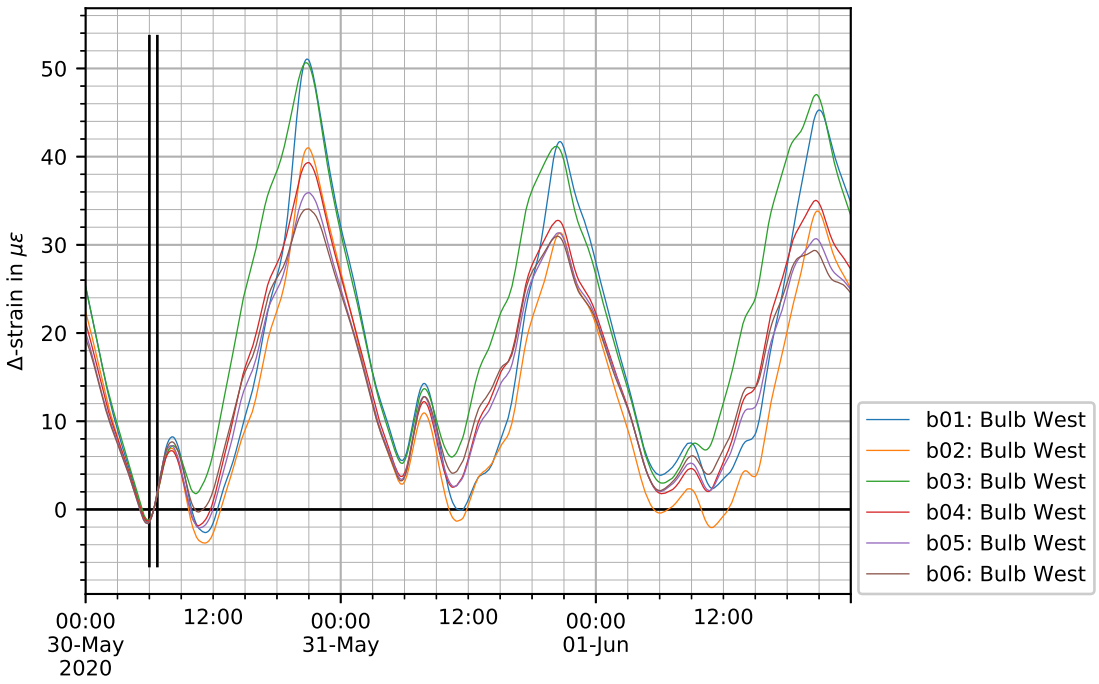

Figure 5.19: Mid-span strains in the cantilever bulbs.

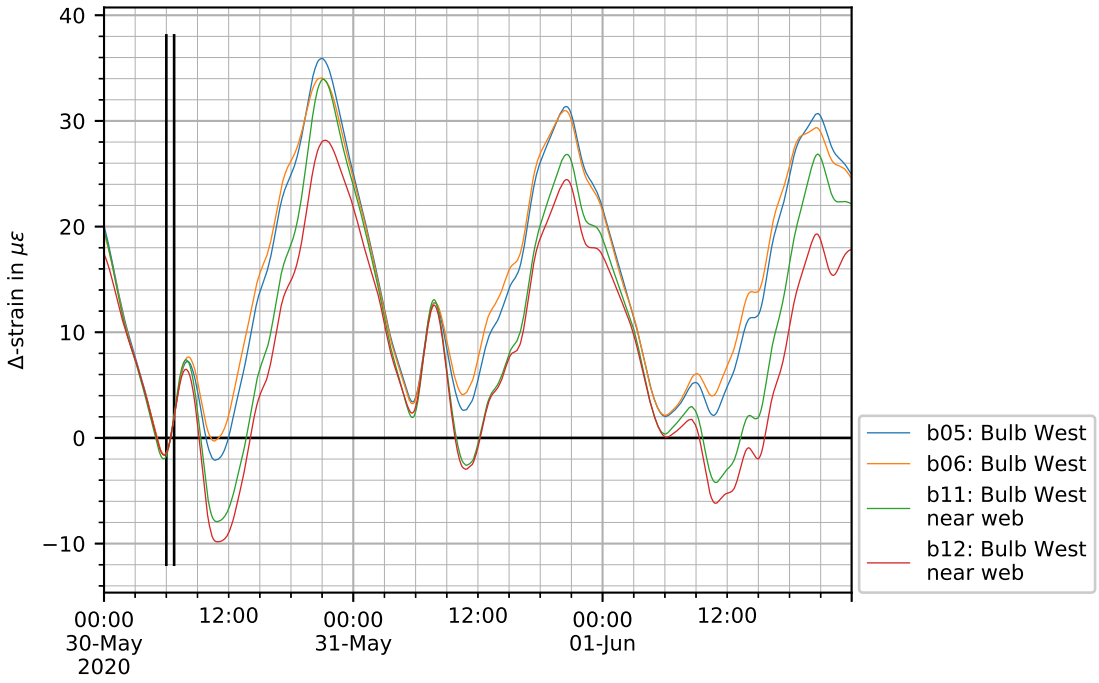

Figure 5.20: Cantilever bulb strains. Mid-span versus near a support.

For the bulbs above the box a large difference in the strains is shown. This might partially be explained by the proximity of b10 to the box wall. The wall and deck plate are relatively thin compared to the wall height. A common effect for thin-walled sections is an effect known as shear lag. Only a part of the top and bottom flanges, close to the web, contributes to the effective bending stiffness, while other parts of the top and bottom shear relative to the effective parts. The bulb closest to the wall (b10) might contribute more to the bending stiffness than the bulb over 1 meter away (b07). Another difference may be that the box wall contributes significantly to the local deck stiffness, and vehicle load is transferred directly to the wall, instead of the neighbouring bulb.
Figure 5.23 shows that the bulb, containing b08 mid-span and b13 near a support, shows a large curvature during the day. The mid-span strain is larger (more positive) than the support-strain, indicative of a curvature similar to what would be expected due to a traffic load on the deck.
The bulb containing b09 and b14 actually shows an inverted curvature. The midspan strain (orange) is smaller(more negative) than the support strain(red), indicating the bulb bends upwards between supports. This is counter-intuitive, and not yet explained.

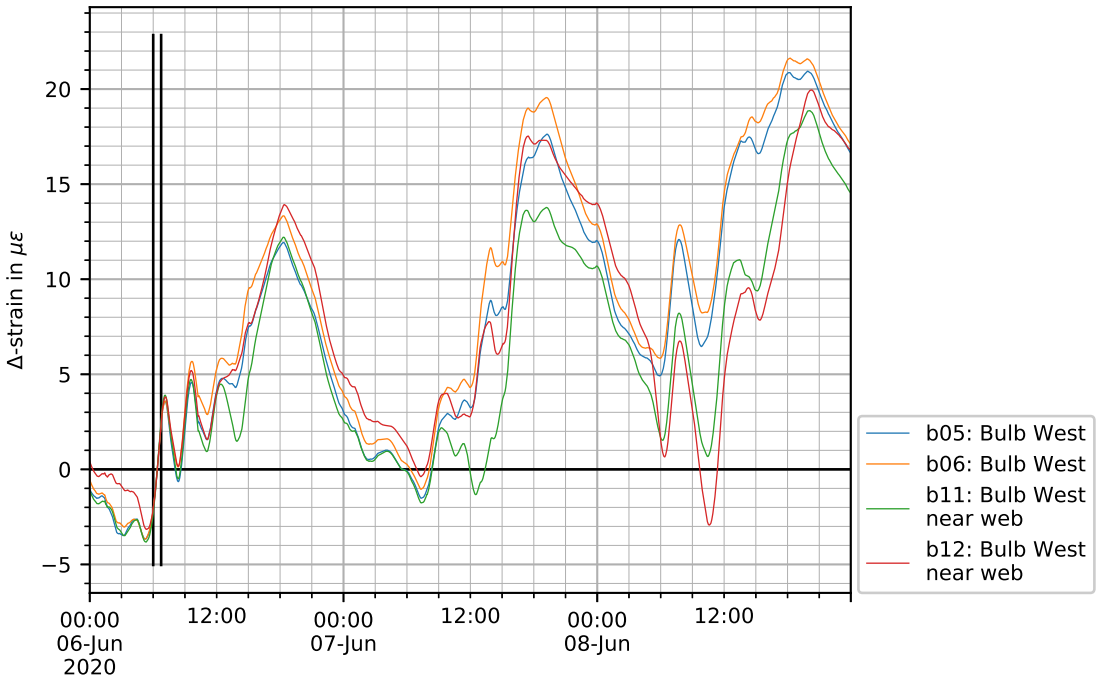

Figure 5.21: Cantilever bulb strains in a cold period. Mid-span versus near a support

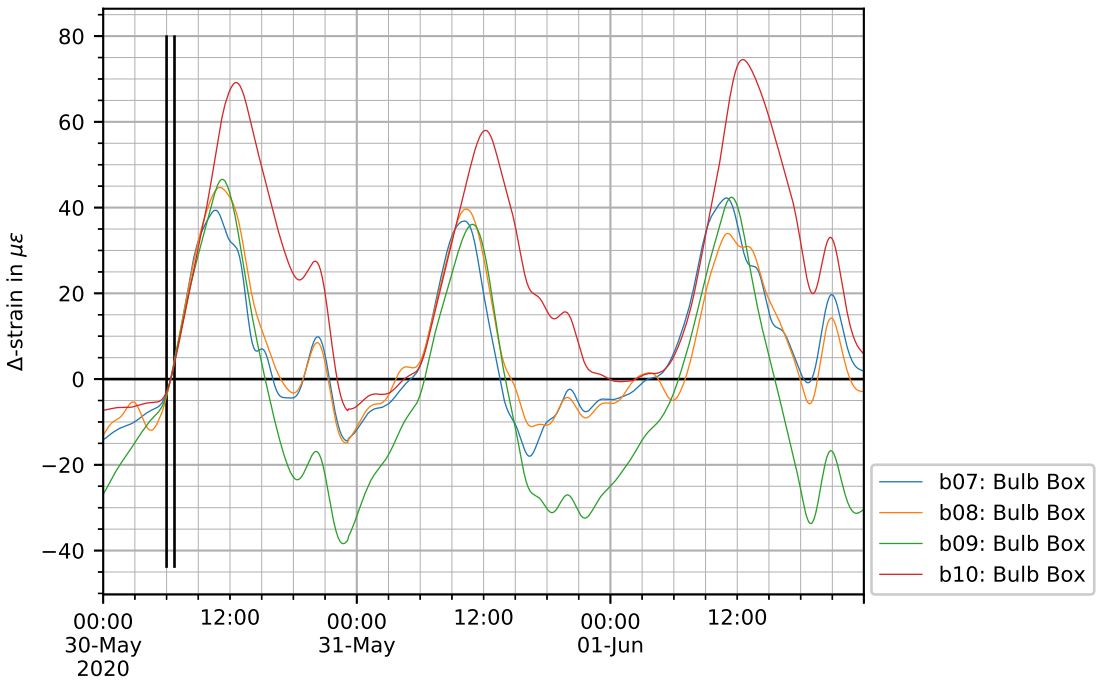

Figure 5.22: Mid-span strains in the bulbs above the box.

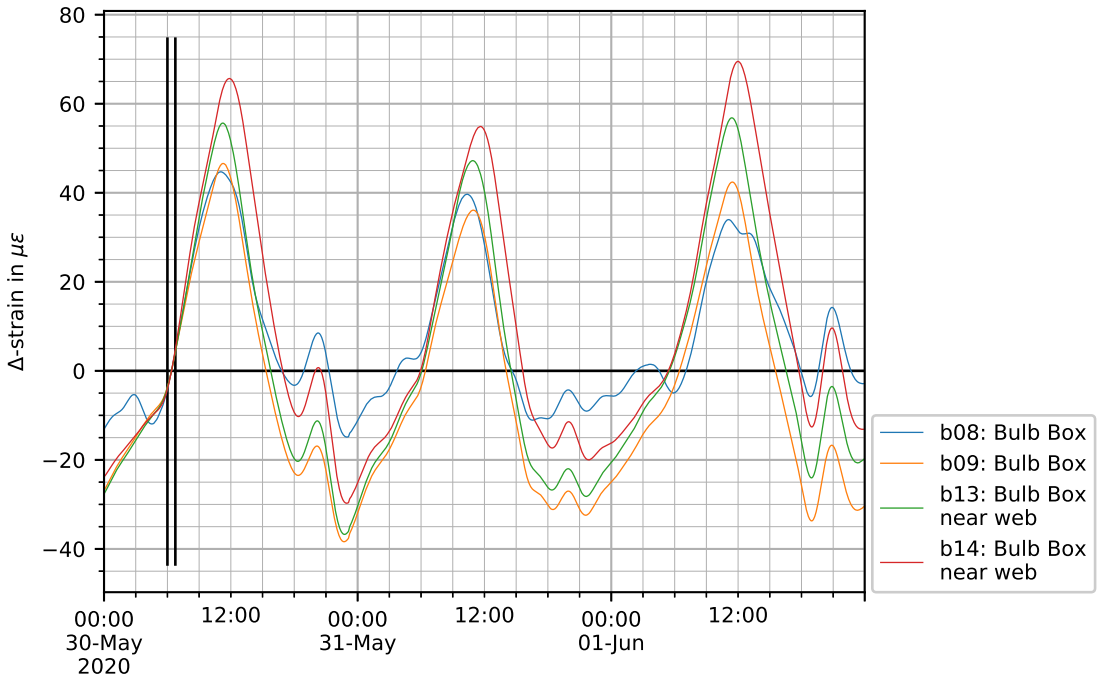

Figure 5.23: Strains in the bulbs above the box. Mid-span versus near a support.

5.5 Measurements summary

The majority of the measurements are shown for two 3-day periods. A warm period from Saturday May 30 to Monday June 1[1], and a cooler period from Saturday June 6 to Monday June 8 2020.

Temperature Measurements.

- On an average warm day, the maximum simultaneous temperature difference between 2 points of the bridge is approximately 20°C at approximately 16:00.
- The top of the asphalt reaches the highest temperatures, up to 45°C for the periods shown. The absolute maximum temperature was 54.86°C for the top North-East asphalt sensor on Aug 7 2020 15:44.
- There is a large temperature difference of up to 6°C between the top and bottom asphalt sensors, which are placed just 40 mm apart.
- There is a large temperature difference of up to 4°C between the bottom asphalt sensor and the bottom deck plate sensor. These sensors are just 20 mm apart.
- The deck above the box girder warms up slightly slower than the cantilever deck. It also reaches higher temperatures and cools down significantly slower in the evenings. This is due to the trapped air inside the box.
- There are significant temperature differences between the East- and West sides of the driving lanes. This is due to barrier induced shade.
- The lower part of the East box wall heats up significantly in the early morning, just after sunrise. This is due to the sun shining underneath the cantilever. At the end of day, before sunset, the lower part of the West box wall heats up significantly.
- The temperature of the asphalt and deck plate is explained using a heat-flow model in appendix B. There is insufficient data to determine whether or not traffic induced friction has a significant influence on deck plate temperature.

Support displacements.

- The LVDT measurements show that the bridge moves relative to one of the roller supports.
- During the measurement period in October a daily axial elongation of 32 mm was observed for a 424 m section of bridge.
- The support displacement is in line with what would be expected based on the average bridge temperature. Only a small subset of the temperature sensors was still available in October however.

Traffic counts.

- Vehicle counts, lengths and average speeds were obtained from Rijkswaterstaat.
- Using assumed weights, vehicle counts were converted to an UDL of approximately 0.55 kN/m for North-bound traffic and 0.45 kN/m for South-bound traffic. This was on a Saturday.

[1] Monday June 1, 2020 is Whit Monday, a national holiday

Strain Measurements. For strain measurements the values are reported. For discussion and evaluation of the strains, see chapter 6.4.1. The FBG sensors measure total strain (ε_{total}), the discrete strain-gage sensors measure only stress-induced strain (ε_{stress}).
$\varepsilon_{total} = \varepsilon_{Stress} + \varepsilon_{Temperature}$

- The total longitudinal strains in the box-wall show a daily variation with a nearly sinusoidal shape. The difference between crest and trough is approximately 150 $\mu\varepsilon$, except for the West bottom box wall where it is only 70 $\mu\varepsilon$.
- The stress-induced longitudinal bulb strains are significantly smaller with daily the daily difference between trough and crest of only 40 to 50 $\mu\varepsilon$.
- Stress-induced longitudinal bulb strains for the cantilever show a difference between mid-span and near a support. This could indicate that the bending moment along the axis varies. In the warm period this variation is larger than in the cool period.
- Stress-induced longitudinal bulb strains above the box show a difference between trough and crest is approximately 70 $\mu\varepsilon$.
- Stress-induced longitudinal bulb strains above the box also show a difference between mid-span and near a support, indicating a possible variation in the magnitude of the bending moment. Above the box this difference is opposite to that of the cantilever. Indicating the displacement and/or loading is in the opposite direction.

6 Effect of Temperature on Stress & Strain

In chapter 4 the positions of the temperature sensors were shown, including some plots of the measurement results. In this chapter temperatures at discrete sensor positions will be translated to gradients that can be put in a Finite Element Model (FE-Model) to calculate stress and strain. Then finally an attempt will be made to verify those strains against the measured strains.

6.1 Finite Element Model of the Haringvlietbrug

A part of the Haringvlietbrug was modelled using a 3D-FEM package. A summary of the model is given below, but for a full description of the FE-Model, including model verifications, one is referred to Appendix A.
The first 3, out of 10, spans of the Haringvlietbrug were modelled. One end was clamped to simulate the remaining 7 spans, while the other supports were assumed as rollers. The sensors are mounted on the second span of the Haringvlietbrug, and thus the center span of the FE-Model.
The deck plate was modelled using isotropic plate elements of 10 mm steel, asphalt was not included. Chapter 8 will show that this is a valid simplification.
The longitudinal ribs below the deck plate are constructed out of plate elements, with a beam element for the bulb at the bottom of the rib. The web of the crossbeams is modelled using plate elements, while the crossbeam bottom flanges are modelled as a beam. The box girder walls and bottom are modelled with plate elements. Struts are modelled as beams.
For each load case (e.g. self weight, traffic weight, differential temperature load) an individual linear static calculation was carried out. The resulting stress and strain for each sensor position was exported to the tables shown in Chapter A.8.

For a full description and validation of the FE-Model please see chapter A.

6.2 Measured temperatures to load cases

As was shown in chapters 3.1 and 4 the temperature distribution in the bridge is not homogeneous, but varies over the different structural components. Due to the North-South orientation of the bridge no significant temperature gradient was found along the length of the bridge. For the vertical gradient a few sensor positions are available:

- Asphalt temperature.
- Deck plate temperature.
- Bulb temperature.
- Bottom Flange of crossbeam temperature.
- Box wall temperature at top and bottom.

The Eurocode assumes the largest gradient is in the upper 30 cm of the bridge. It is allowed to apply this in a piecewise linear fashion along the the height of the bridge, matching up at points 0, 10, 20, 30 and x cm from deck level, where x is the height of the bridge. The available sensor positions allow a similar representation of this piecewise linear gradient, with points at approximately 0, 15, 60 and x cm from deck level.

In the East-West direction the following gradients were found in the measurements:

- The deck and bulbs above the box have different temperatures than the cantilevers
- The East and West cantilever have different temperatures due to shade
- The bottom of the East and West box walls show distinct temperature differences during sunrise and sundown.

Based on the available sensor positions and the observed gradients a set of temperature interpolation functions was added to the FEM model that define temperatures of the following elements respectively. A simplified graphic representation of these temperature distributions is shown in figure 6.1.

- LC1: Homogeneous.
  Homogeneous bridge temperature. All elements are included.
- LC11: West Deck.
  The entire deck plate west of the cantilever has a $+10°C$ temperature. A small 60 cm wide transition strip is included above the web of the main box girder.
  All vertical planes (web of bulb profiles, web of longitudinal beams, web of main box) have a triangular temperature load with $+10°C$ at deck level, and $+0°C$ at the height of the bulbs (approx 150 mm below deck level).
- LC12: West Bulb.
  Below the west side cantilever deck, all bulbs of the bulb-profiles obtain the $+10°C$ temperature. All vertical planes (web of bulb profiles, web of longitudinal beams, web of main box) have a triangular temperature load with $+10°C$ at bulb level, and $+0°C$ at either deck-level or flange-level of the crossbeams.
- LC13: West Bottom Flange.
  Below the west side cantilever deck, all bottom flanges of the cross-members and longitudinal beams obtain a $+10°C$ temperature. All vertical planes (web of cross-members, web of longitudinal beams, web of main box) have a triangular temperature load with $+10°C$ at flange-level, and $+0°C$ at either bulb-level or bottom box girder level.
- LC14 to LC16 are similar to LC11 to 13, but above the box girder.
- LC17 to LC19 are similar to LC11 to 13, but on the east cantilever side.
- LC20 West Box Wall Bottom.
  The lower west side of the box girder (including the strut) obtains $+10°C$ which linearly decays to the level of either the bottom cross member or the east side of the box girder
- LC21: East Box Wall Bottom is similar to LC21, but on the east side.

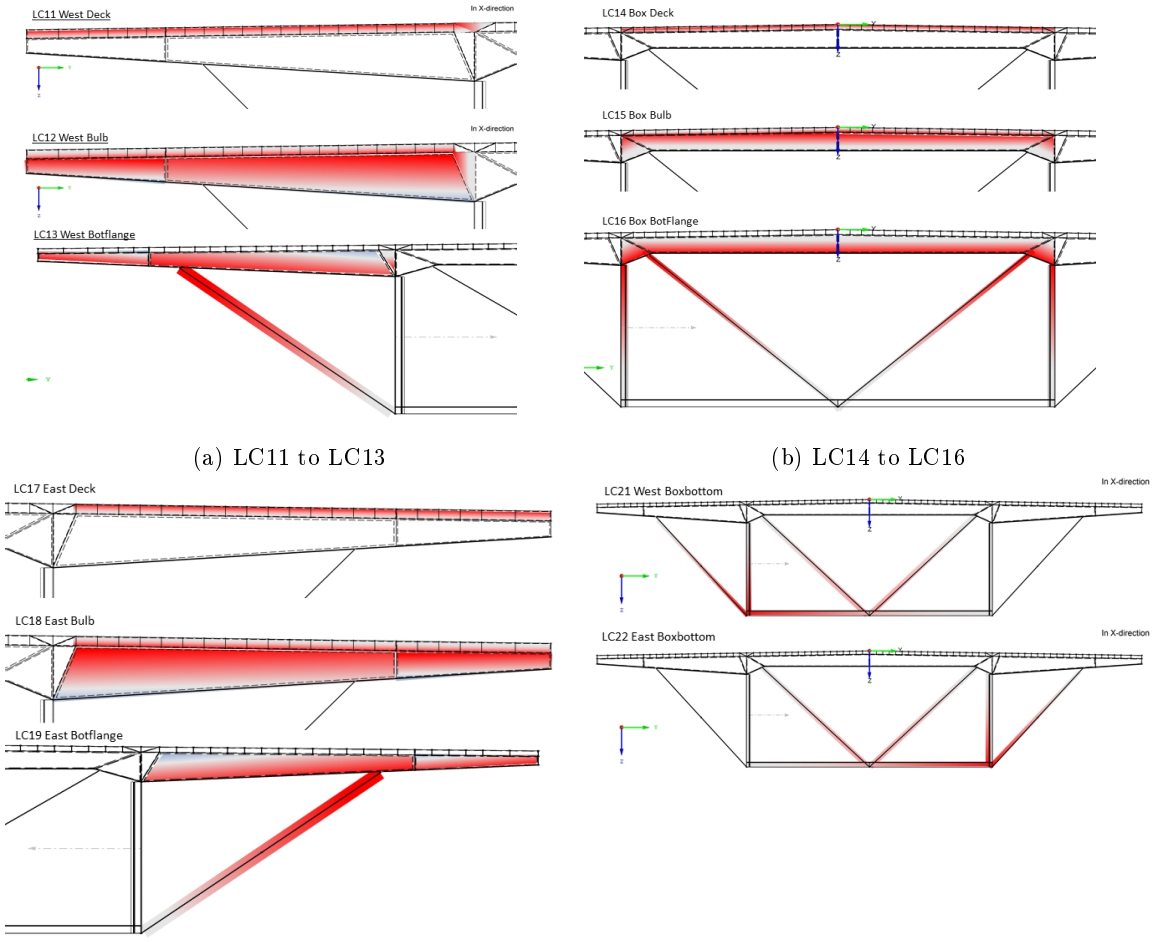

(a) LC11 to LC13

(b) LC14 to LC16

(c) LC17 to LC19

(d) LC21 and LC22

Figure 6.1: Temperature load cases. Dark red is $+10°C$, White is no load, Blue is a small negative temperature artefact due to RFEM's linear gradient restriction

6.3 FEM load case solicitation and post-processing

The solicitations of each of the load cases are calculated as follows:

LC1, A homogeneous component:
The average homogeneous temperature of the bridge can be determined on 4 areas with significant area and temperature. These areas are the box bottom, the West and East Box walls, the deck including ribs above the box, and the cantilever decks including ribs. For the total deck area including the upper half of the box walls, the median of the 4 available deck plate sensors is taken. These are at03 west cantilever deck plate, at06 west deck plate above the box, at08 East deck plate above the box and at11 East cantilever deck plate. By taking the median local shade induced temperature effects don't skew the results.
For the total area of the box bottom and the lower half of the box walls, the minimum temperature of the East(w1be) and West(w1b) bottom box wall sensors is taken. By taking the minimum, the very local temperature rises due to morning and evening sun that were seen in figure 5.5 don't influence the average bridge temperature.
The median of the deck and the minimum of the box bottom are averaged, where the deck area has a weighing factor 2, to account for the extra material there. Resulting in the following equation:

$$\begin{aligned} LC1a &= \frac{2 \cdot \text{median}(at03, at06, at08, at11) + \text{minimum}(w2b\_t, w2be\_t)}{3} \\ LC1 &= LC1a - \text{offset} \end{aligned} \tag{6.1}$$

This method for calculating the average homogeneous bridge temperature deviates from Eurocode, where average bridge temperature is described as the temperature at the bottom of the bridge.
The exact definition of LC1(a) has no physical meaning. LC1a is subtracted from all other temperature load cases. It exists merely to give a sense of an average bridge temperature, and to compare this with displacement along the supports. Once LC1a is subtracted from all other cases, one can now define LC1, with an arbitrary offset. This allows shifting of the calculated stress and strains to have their zero at the same point in time as those of the measurements.

All other temperature load cases are defined as a ΔT to the average bridge temperature LC1a, and therefore LC1a is subtracted from the absolute element temperature to obtain differential temperatures.

LC11: West Deck:
The West deck is influenced by local shade. This shade line moves during the day. Early in the morning the entire cantilever deck is covered with shade due to the East barriers. Once the sun rises shade then slowly diminishes towards the East. In the afternoon shade starts on the West side, and increases to once again cover the entire deck.
Assuming the deck only has significantly different temperature from the mean bridge temperature when fully exposed to solar, shade is of no significance for this load cases. Therefore the medium temperature between a cantilever deck plate sensor just West of a barrier (at03) and a sensor just East of a barrier (at11) is taken.

$$LC11 = \text{mean}(at03, at11) - LC1a \tag{6.2}$$

LC12, West Bulb:
There is no temperature sensor at any cantilever bulb in the given period. Temperature sensor at31 was placed on a West bulb in September however, and shows a reasonable match with sensor at15 ($\Delta T \leq 2^{\circ}C$), which is a sensor at the top of the East cantilever crossbeam web. Therefore the East cantilever crossbeam web temperature is taken as the temperature of the West cantilever bulbs.

$$LC12 = at15 - LC1a \tag{6.3}$$

LC13, West Bottom Flange:
The available FBG sensors positioned at the bottom of the west crossbeam flange are used.

$$LC13 = \text{mean}(c2\_t, c3\_t) - LC1a \tag{6.4}$$

LC14, Deck above box:
For load case 14, the temperature of the deck above the box, the same shade applies as explained in LC11. The mean is taken of at05(West deck plate above the box) and at07(East deck plate above the box)

$$LC14 = \text{mean}(at05, at07) - LC1a \tag{6.5}$$

LC15, Bulb above box:
For load case 15 the same as LC14 applies. The mean is taken from a sensor at a bulb in the West side of the box (at06) and one sensor from a sensor at a bulb in the East side of the box(at08).

$$LC15 = \text{mean}(at06, at08) - LC1a \tag{6.6}$$

LC16, Bottom flange crossbeam above the box:
Sensors d1,d2 and d4 are positioned at the center of the bottom flange of the crossbeam above the box. The mean of these sensor readings is taken.

$$LC16 = \text{mean}(at06, at08) - LC1a \tag{6.7}$$

LC17 to LC19, East cantilever:
The West cantilever temperature measurements have shown that each lane has significant internal temperature differences between it's East- and West-side due to barrier induced shade. There are not enough measurements available to state with certainty that the East cantilever as a whole has a similar temperature distribution as the West cantilever. However the heat transfer equations in appendix B have shown that deck temperature is strongly dependent on solar radiation on top, and ambient temperature on the bottom. Those 2 environmental variables are assumed equal for the East and West cantilever. This implies there is no reason to assume the West cantilever as a whole has a significantly different temperature than the East cantilever. Therefore the load cases for the East cantilever are taken to be equal to those of the West cantilever.

$$\begin{aligned} LC17 &= LC11 \\ LC18 &= LC12 \\ LC19 &= LC13 \end{aligned} \tag{6.8}$$

LC21 and LC22, Box Wall Bottom: For the bottom of the box walls the East side has only 1 sensor (w1be). The West side has multiple, but only the one in the same cross-section as the East sensor is used (w1b).

$$\begin{aligned} LC20 &= w1b\_t - LC1a \\ LC21 &= w1be\_t - LCa \end{aligned} \tag{6.9}$$

The solicitation of each load case in the period of interest is shown in figure 6.2 for the warm period and figure 6.3 for the cool period . Load-cases LC17 to LC19 are identical to LC11 to lC13 and are thus omitted. LC1 has been offset to obtain zero average temperature on May 31 between 06:00 and 06:45, as indicated by black lines. The average temperature denoted by LC1 has an amplitude of approximately 15 degrees and shows a smooth sine-shape with a period of one day, with the minimum occurring just after 06:00. All other temperature loads show erratic behaviour. LC20 and LC21 containing the bottom of the box wall show large spikes. These spikes are identical to the ones shown in figure 5.5. The spikes recorded by the local sensors are reflected through the shape function in a significant part of the box wall and -bottom. Based on the available measurement data, it could not be validated whether this is correct, which introduces uncertainty in the model.

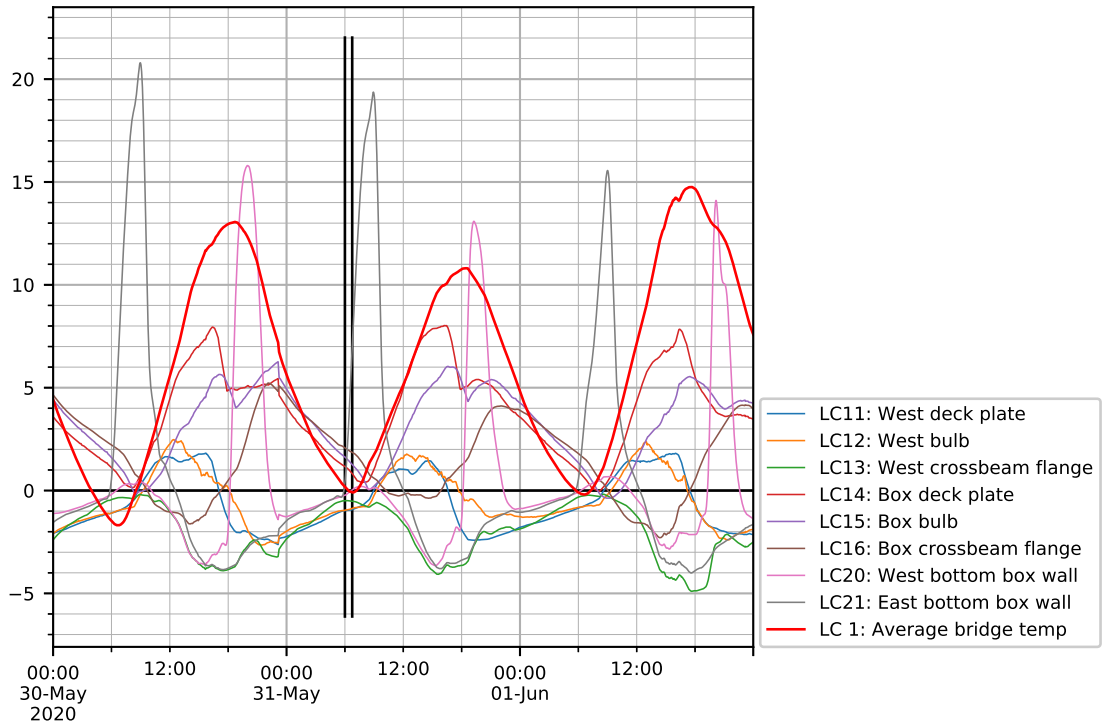

Figure 6.2: Load case solicitation, warm period

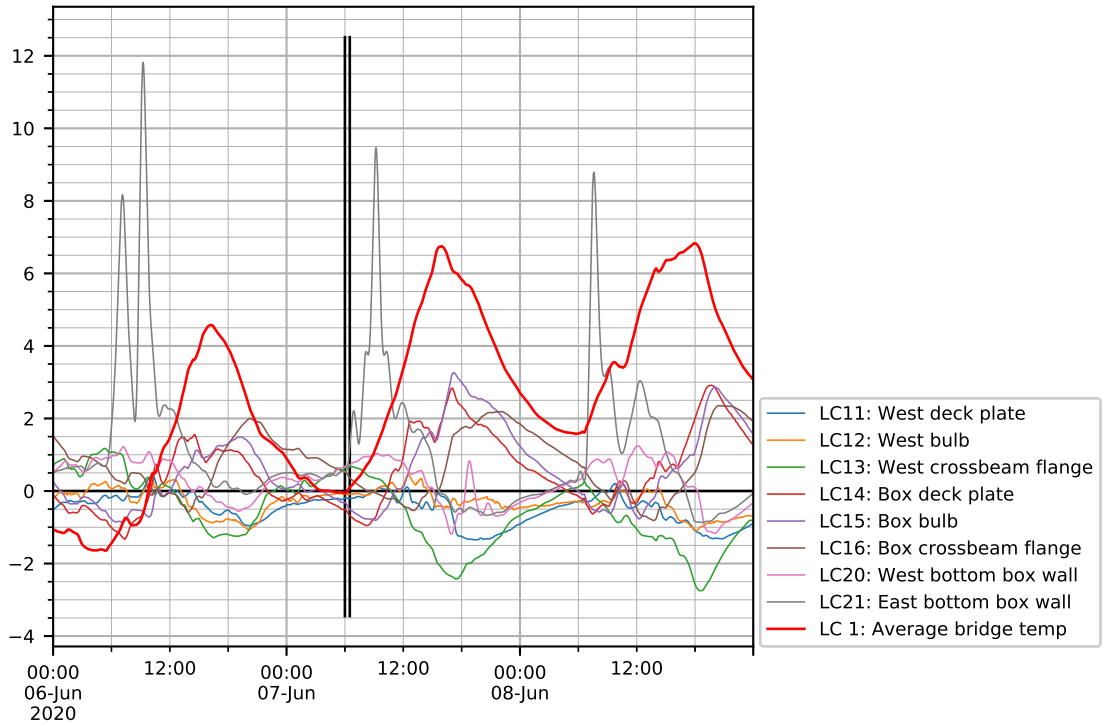

Figure 6.3: Load case solicitation, cool period

6.3.1 Post-processing

For each of the individual load cases (e.g. self weight, traffic weight, temperature load) a static linear calculation was carried out using the FE-Model. The stress and strain at the sensor positions are exported for each load case. These results are stored in matrices, as shown in tables A.4 to A.7, that convert each load case into stress and strain at the sensor positions.
Figures 6.2 and 6.3 show the solicitation of each load case, for each time step in the periods of interest. This load case solicitation over time is also stored as a matrix. Calculation of the stress and strain, for each time step in the periods of interest, is now a matrix operation, rather than a full FEM calculation.

$$\varepsilon = LCS \cdot A \tag{6.10}$$

$$\sigma = LCS \cdot B \tag{6.11}$$

Where:

$\mathscr{E}$ = Matrix containing the strains of all sensors for all points in time

σ = Matrix containing the stress of all sensors for all points in time

A = Matrix relating load case solicitation to sensor strain

B = Matrix relating load case solicitation to sensor stress

LCS = Matrix containing LoadCaseSollicitation at each point in time

6.4 FEM Strain

For the period of interest the strains are shown in figure 6.4. This strain was given an offset to obtain average strain at May 30 between 06:00 and 06:30 equal to zero, similar to what was done for the measured strain in the previous chapter. From the graph it's clear that all points have similar strain, as would be expected for a continuous bridge beam. There is little to no curvature in both direction, so the main strain component is that of the axial elongation of the bridge. See also appendix A, where a continuous beam is subjected to a temperature load, inducing a nearly constant bending moment along the beam. Constant bending moment implies constant curvature. Because the continuous beam has multiple supports, the only constant curvature that kinematically fits, is zero curvature. Hereby proving that the entire cross-section should obtain a similar strain due to temperature change in a geometrically linear calculation.
Traffic data from RWS was used to obtain a simplified UDL-traffic load. See chapter 5.3 for details on obtaining traffic loading. Effect of traffic on strain is shown in figure 6.5, and the combined effect is shown in figure 6.6. Traffic load shows very little influence on the global strain distribution. The daily variation of temperature based strain is approximately 200 $\mu\varepsilon$ from crest to trough, while the daily variation due to traffic is only 0.7 to 1.5 $\mu\varepsilon$. A strain of 1.5 $\mu\varepsilon$ due to an applied force, relates to 0.3 MPa.

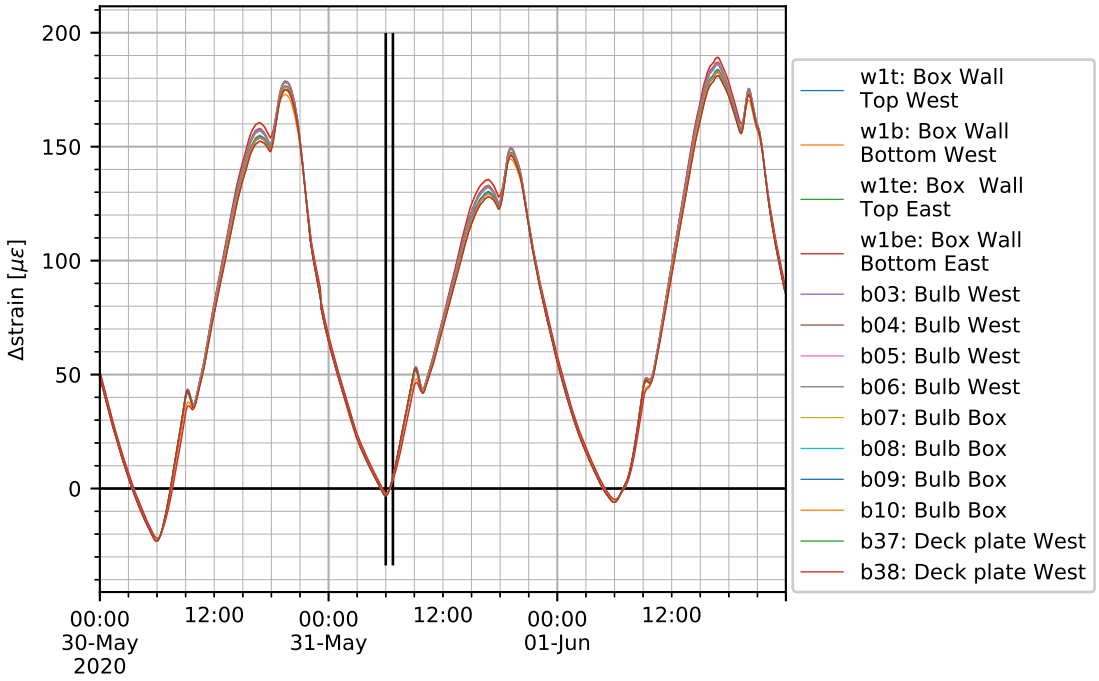

Figure 6.4: FEM strains due to temperature measurements only

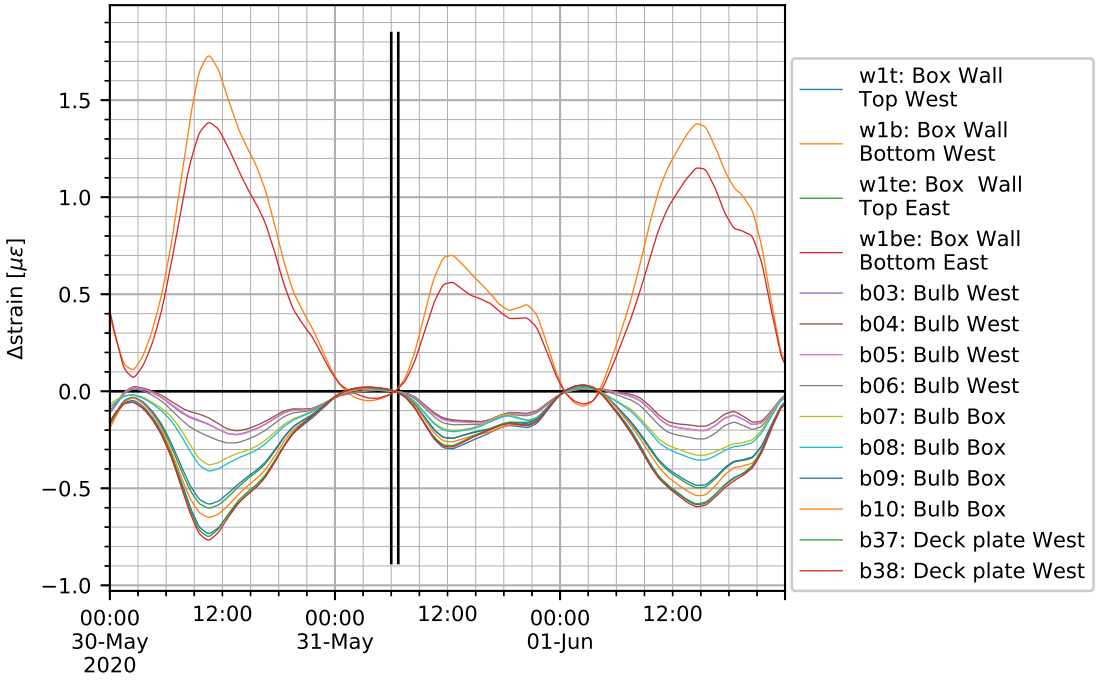

Figure 6.5: FEM strains due to traffic load only

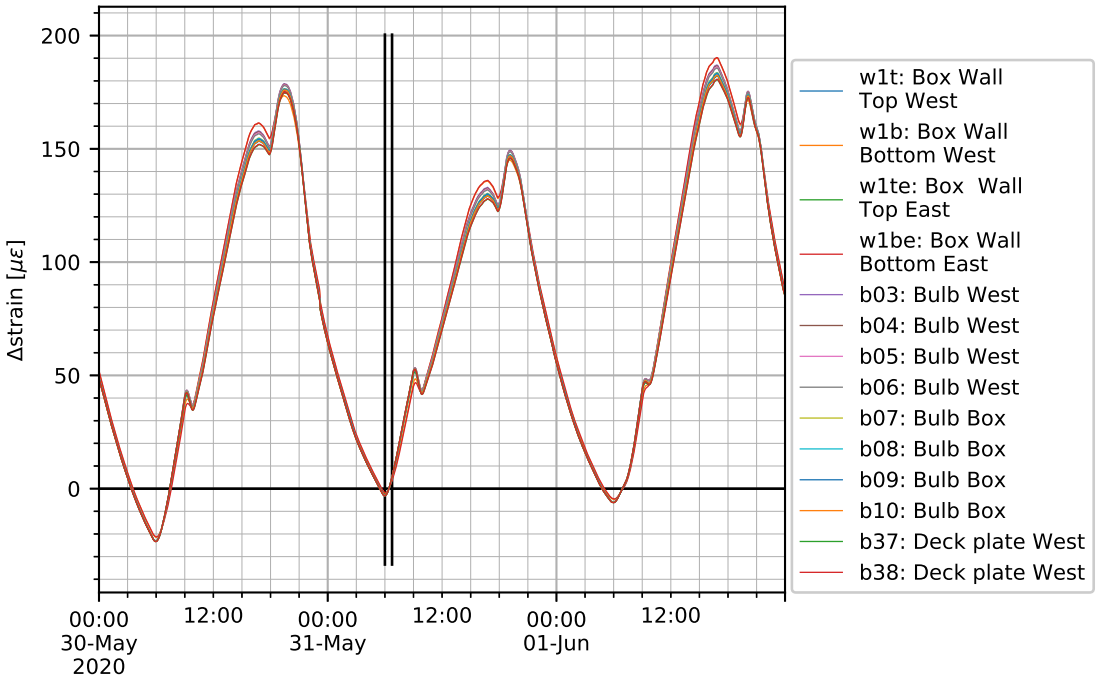

Figure 6.6: FEM strains due to temperature and traffic

6.4.1 FEM Strain validation

In section 5.4 the measured strain was reported, while in section 6.4 the FEM strain was reported. It is therefore possible to compare the measured strain with the simulated strain, to verify the model against the measurements. The FE-model has already been verified with simplified hand calculations and with measurements obtained from the LVDT, see section A.7.4, and shows good results there. Keeping in mind that section 4.3.3 has shown that the FBG strain sensors show significant influence on the sensor accuracy due to temperature change, the model itself also contains some uncertainty due to the following assumptions and simplifications:

- Asphalt material and -temperature are not included in the model. Based on table 8.7 the contribution of asphalt to the axial stiffness of the deck plate is small .
- Not all temperature distributions are as linear as assumed, it is however the best approximation based on the available sensors. The alternative would be a full heat-flow analysis, which is beyond the scope of this study.
- The Deck temperatures are assumed piecewise homogeneous. In reality this may not be true because of e.g. shade, wind, traffic friction.
- The calculations are made geometrically linear. Second order effects like additional curvature/buckling are unaccounted for. The full analysis of stress and strain over time is executed using linear combinations of the separate temperature gradients. If second order effects were to be included, each step in time (every minute) would require a full non-linear computation, which is infeasible due to time and computational constraints.
- Traffic is simplified to two 1.2 meter wide UDL loads per lane. This adds significant uncertainty, but is deemed reasonable considering the existing uncertainty about exact vehicle weights and positions.

Figure 6.7 shows the predicted and measured strains in the box walls. The top of the box walls align with the predictions within 30%, while the bottom of the box walls show significant deviations, especially on the West side. The verification with the LVDT in section A.7.4 has shown that the measured strains from the FBG do not match with the measured displacement at the supports. For a few cooler days, the results are shown in figure 6.8. The daily amplitude for FEM strains is halved, and the same goes for the measured strains. The difference between West bottom wall and West top wall is now 25 $\mu\varepsilon$, while it was approximately 50$\mu\varepsilon$ for warm days. Three possible causes for the deviation of the bottom west wall relative to the other box wall sensors are evaluated:

- The difference is caused by traffic load. Figure 5.16 shows June 7 actually has more passing vehicles than May 31. If traffic caused the difference, then this difference should be bigger on June 7, not smaller.
- The difference is caused by temperature gradients not accounted for in the FE-model. Figure 5.1 shows the internal temperature differences on June 6 are almost 3 times smaller than those on May 30, while the deviation on cool days is only a factor 2 smaller. Figure 5.2 has shown the largest temperature differences occur close to 15:00 except for some very local peaks. This period coincides with the period with the maximum deviations between FEM and measured strains. Based on the temperature measurements one would expect however that on cooler days, the gradients are orders of magnitude smaller, and be much smoother than on warm days. Also a significant deviation of local strain due to a temperature gradient is implausible, due to the static indeterminate nature of the bridge with 10 supports.
- The deviation is caused by poor STC of the sensor. The deviation scales almost perfectly linear with the total strain. STC for the FBG sensor is applied in a linear way, and the supplier has stated that each temperature sensor has it's own temperature coefficient. There is up to 18% variation between the reported temperature coefficients of the installed sensors. A typing or administration error is easily made and could account for the shown error. Looking at the early morning on May 30 06:00, the sensor shows a more positive strain than all other sensors. At this time both traffic loading and temperature gradients are insignificant, but the night temperature is a bit lower. An error in the STC could account for this.

The last cause is deemed most plausible. This is further confirmed by the FE-Model validation in section A.7.4, which shows that the measured support displacement is not in agreement with the

measured strain of the West bottom box wall. This leads to the conclusion that the deviations in the West bottom box wall strain are caused by sensor STC.

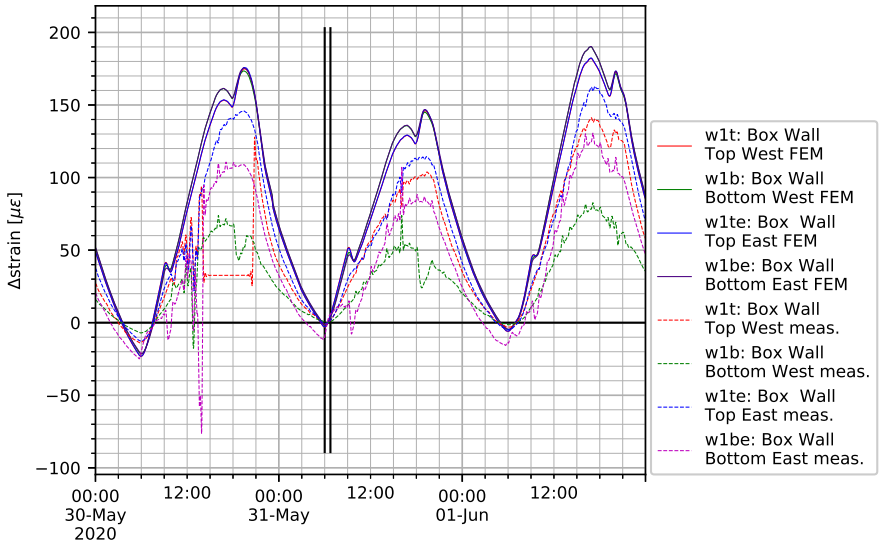

Figure 6.7: Strain FEM versus Measured, box walls

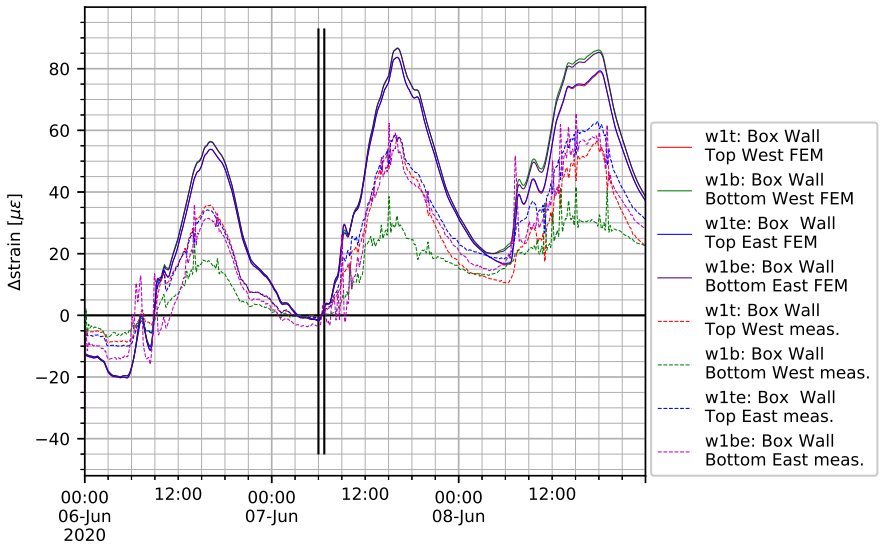

Figure 6.8: Strain FEM versus Measured, box walls. Cold days.

6.5 FEM stress

The stress was calculated, as shown in figure 6.9. While the strains are similar for each point, the stress is not. This can be explained by the temperature difference:

$$\varepsilon_{total} = \varepsilon_{force} + \varepsilon_{temperature} = \frac{\sigma}{E} + \alpha\Delta T \tag{6.12}$$

Similar total strains but with a different temperature should thus result in a different stress for each point.

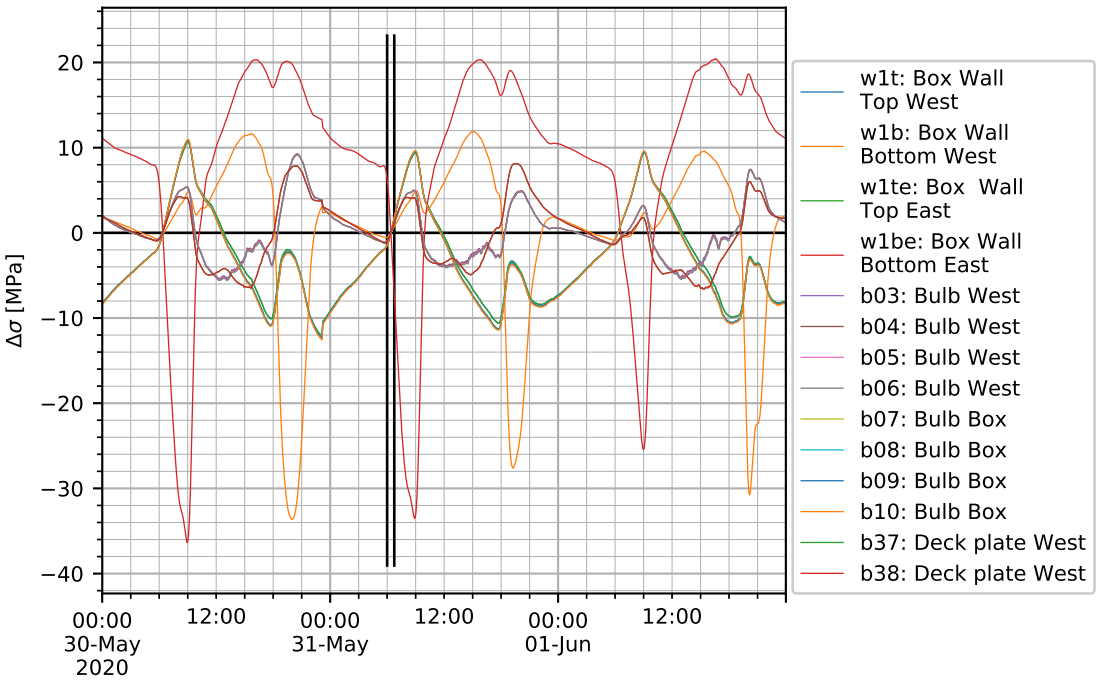

Figure 6.9: FEM stress based on temperature measurements

Figure 6.10 shows the stress in the box wall due to temperature. The local temperature peaks of the bottom box wall induce a large compression stress of 35MPa at the sensor positions. This is a plausible result. The local temperature rise can not induce global bridge curvature, while the other parts of the bridge also constrain axial elongation of the bridge to some extent. A constrained temperature induced positive strain of the box wall, will therefore induce compression. All other parts of the bridge undergo a small tension stress at the same time, due to force equilibrium.

Figure 6.11 shows the results for the bulbs of the cantilever. The tension peaks in the morning between 08:00 and 09:00, and the evening between 20:00 and 21:00 coincide with the compression peaks of the bottom box wall. This is considered plausible, since the bridge supports are rollers and the LVDT has shown the bridge is free to move with little friction. Therefore all axial elements of the bridge need to share a global axial force equilibrium. Compression in the box wall, should result in tension somewhere else.
Between 12:00 and 15:00 the stress at mid-span (b05, b06) is higher than near the supports (b11, b12). Assuming the temperature along the bulb axis is homogeneous, this is indicative of curvature with a downward deflection. However no traffic load is applied in this figure. A possibility is that a vertical temperature gradient in the cantilever beams, with the top warmer than the bottom, forces the tips downward. The crossbeams that don't contain a strut are free to deform, but the strut prevents this deformation for 1 in 4 crossbeams. Crossbeams could therefore have unequal height, forcing curvature in the deck and ribs. As has been stated before, the mid-span sensors are

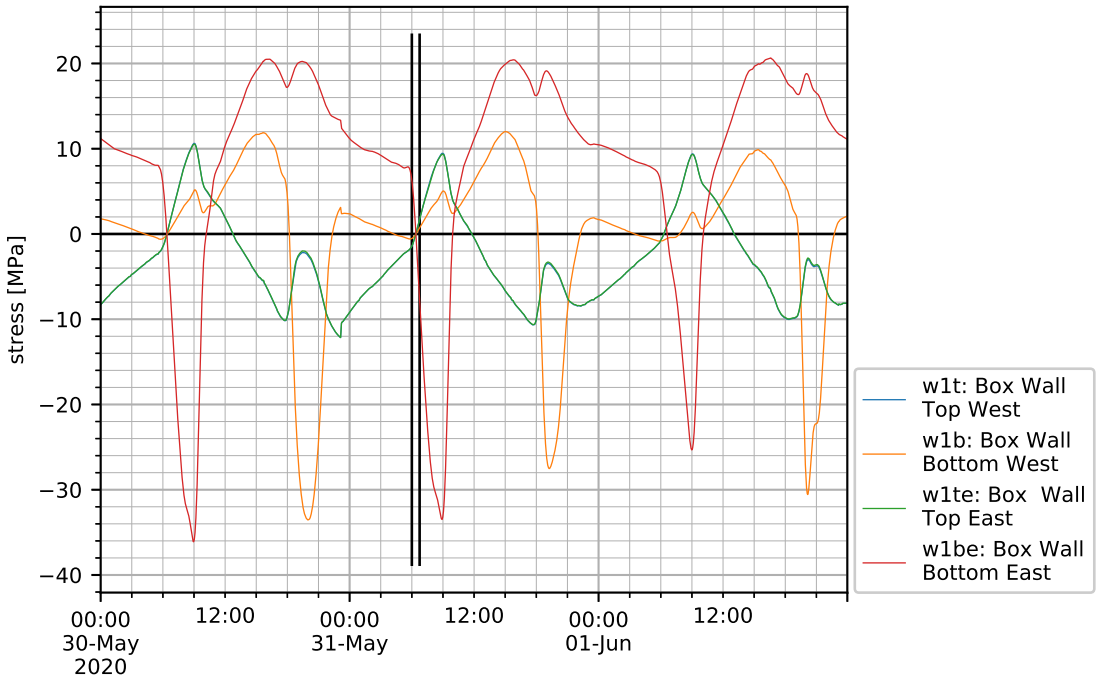

Figure 6.10: Box wall FEM stress based on temperature measurements

not in the same span as the sensors near a web. Therefore no exact curvature can be determined based on the combined stresses.

The stress in the bulbs above the box is shown in figure 6.12. While the cantilever showed curvature, the bulbs above the box do not. The same peaks due to the temperature rise in the bottom box walls are visible.
As expected, for the West cantilever bulbs the stress peak is largest during the West box wall temperature rise. For the bulbs above the box, which are on the East-side, the peak is largest during the East box wall temperature rise.

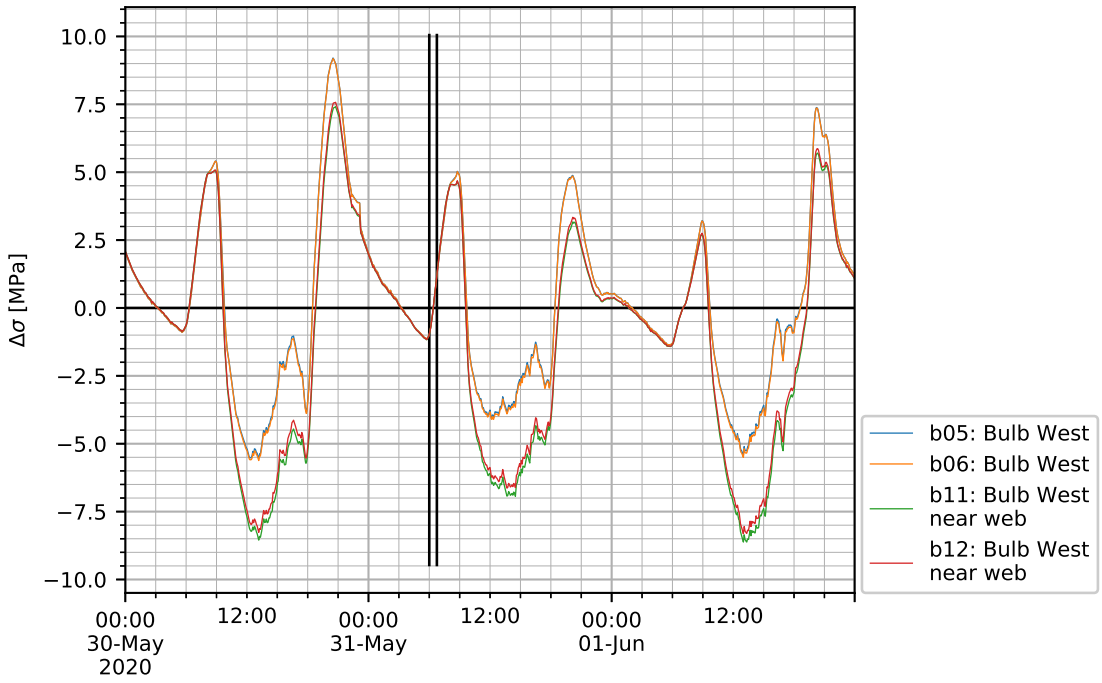

Figure 6.11: Cantilever bulb FEM stress based on temperature measurements

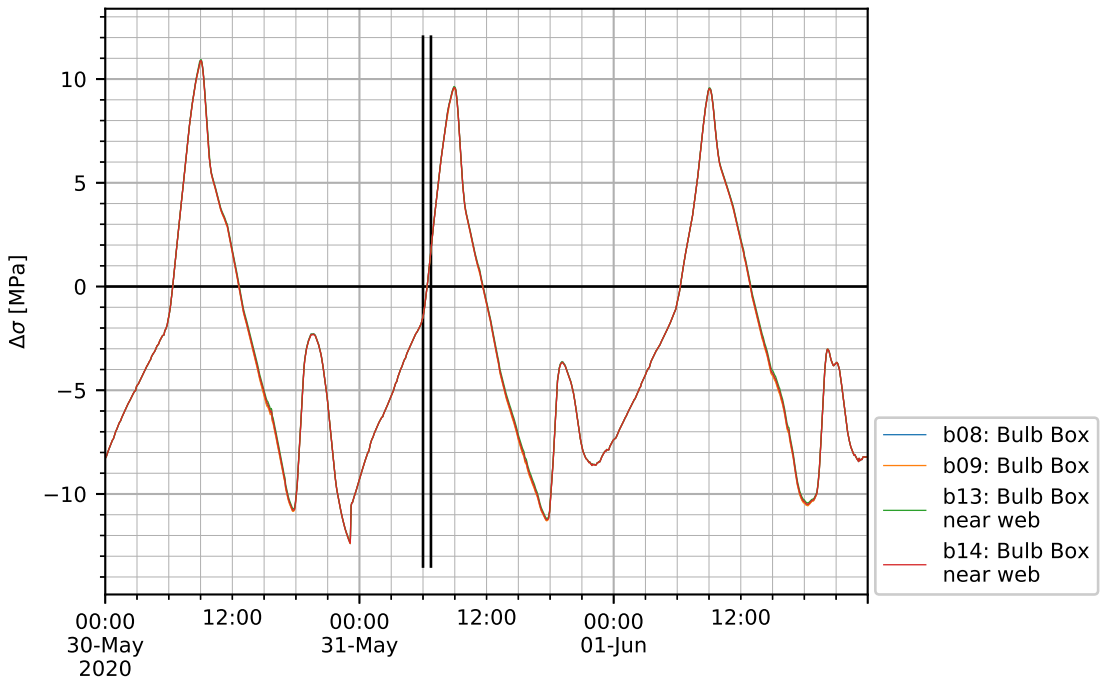

Figure 6.12: Box bulb FEM stress based on temperature measurements

Using the time histories of the stress as presented in figure 6.9, three specific points in time are selected for a full FEM calculation[1]. On May 31 08:55 the East box wall bottom obtains the maximum compression stress, while at 19:00 the West box wall bottom that obtains the maximum compression stress. Lastly 14:00 is chosen as a time-step to investigate the difference in stress between the mid-span of a rib, and the stress near a supporting web, as shown in figure 6.11. For these 3 time-steps, the resulting longitudinal stress σ_x in the box- and deck-plates is shown in figure 6.13. Note that a zero-offset was applied to the time-histories in figure 6.9, and thus the reported absolute stress in the time-histories is not identical to 3D-FEM figure 6.13, where no offset is applied.
At 08:55, figure 6.13a shows the asymmetrical stress distribution due to the heating of the lower part of the East box wall, resulting in compression stress at the bottom East side of the main box girder, and a small tension stress in the deck. At 14:00, figure 6.13b shows that the stress distribution is almost symmetrical, but the deck above the box is under axial tension, with the cantilevers under compression. This is due to the higher temperature of the cantilever deck compared to the deck above the box. At 19:00, figure 6.13c shows both effects. The Lower West side of the box is under compression, due to its high temperature in comparison to the rest of the bridge. The temperature difference between the deck above the box and the cantilever deck is clearly visible. Above the box a compression stress is shown, with a tension stress in the cantilevers.

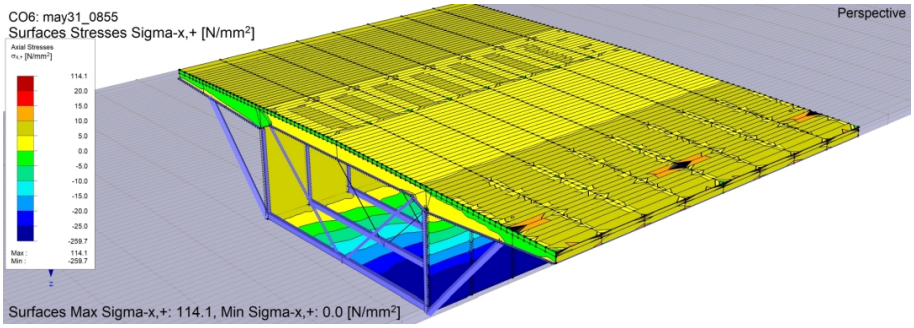

(a) Time 08:55. Maximum temperature at bottom of the East box wall.

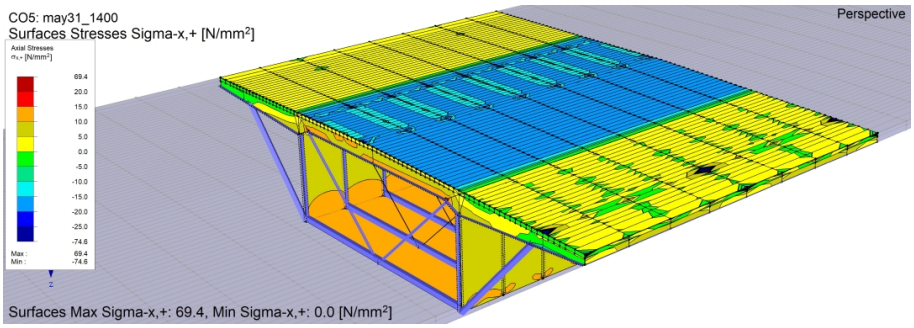

(b) Time 14:00. Mid afternoon.

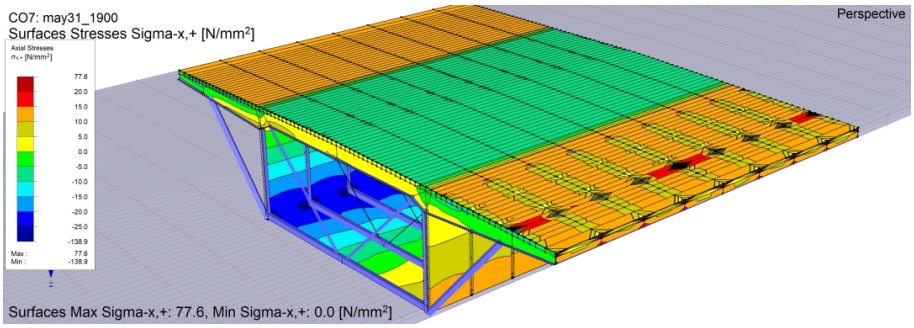

(c) Time 19:00. Maximum temperature at bottom of the West box wall.

Figure 6.13: May 31 2020, Stress σ_x. West side is on upper left, East side is on lower right.

[1] A slightly simplified one-span model with a course mesh was used in order to reduce computational complexity.

The stress time-histories in figure 6.11 also indicated curvature during the afternoon. A full FEM calculation was made using the load-case solicitation of May 31 14:00, and the results are shown in figures 6.14 and 6.15. Figure 6.14 shows a top-view of the deck, with the North-side of the bridge on the right side of the figure. A section spanning 3 struts is shown, and it's clear that the cantilevers with a strut show smaller deflection than the cantilevers without a strut. Figure 6.15 shows the West cantilever, below the deck plate, looking from the West side towards the bridge. The cantilever crossbeam-webs between 3 struts are shown, together with the longitudinal edge-beam in front, the rib (containing b05 and b11) in the mid-plane, and the top part of the West box wall in the back. Figure 6.15a shows the end of the cantilever moves downwards. The deck plate acting as the top flange of the crossbeam is warmer than the bottom flange, resulting in curvature. The struts partially restrain this curvature, resulting in a 50.4kN compression Force in the struts. Struts are only present in 1 in 4 frames, resulting in different deflections for the supported cross-members compared to the unsupported cross-members. This also results in curvature in the rib. Figure 6.15b shows that the curvature in the ribs also results in differential strains, and with a homogeneous temperature distribution in the longitudinal direction, also implying stress. A compression strain in the bottom of the rib near a supported cross-member, and a tension strain in the bottom of the rib near the middle unsupported cross-member. This is in agreement with figure 6.11.

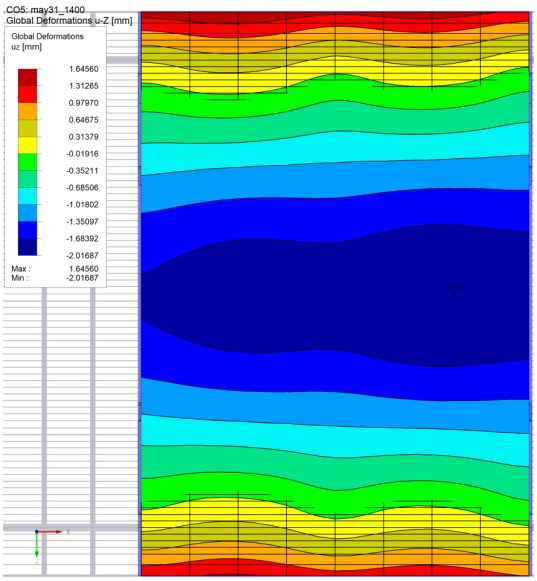

Figure 6.14: Top-view of vertical deck displacement u_z, May 31 14:00.

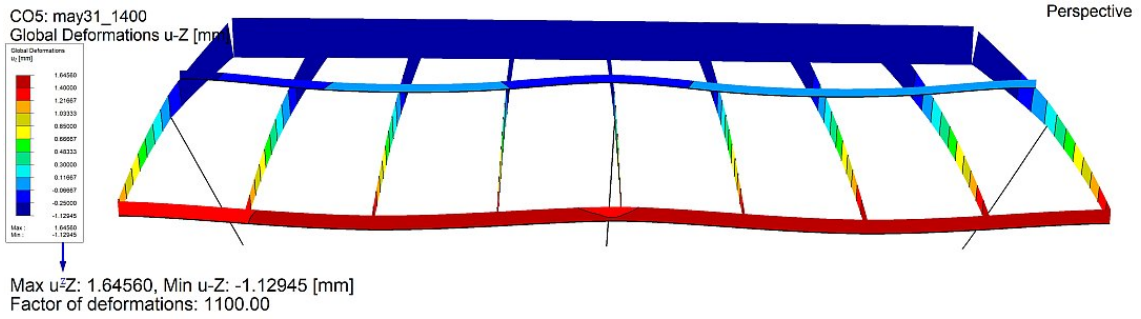

(a) Deformation u_z

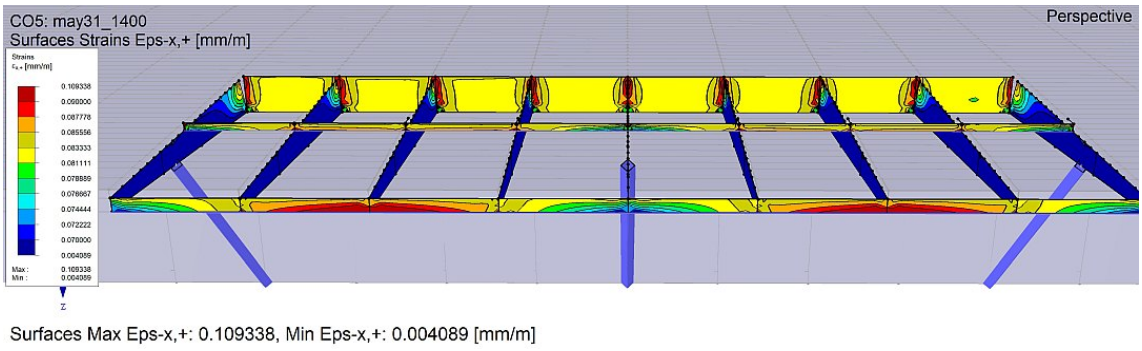

(b) Strain ε_x

Figure 6.15: West cantilever crossbeams, as seen from Westside, May 31 14:00.

6.5.1 FEM stress validation

Chapter 6.4.1 compared the total strains from the FE-Model with the total strains measured by the FBG sensors, and did not include the strains from the discrete strain gages at the bulbs. The results from the discrete strain gages are reported below.
The discrete strain gage's are matched to the temperature coefficient of steel. Applying the STC procedure as described in chapter 4.3.3 does not result in total strain measurements, but in measurement of stress-induced strain:
$\varepsilon_{total} = \varepsilon_{stress} + \varepsilon_{temperature}$.
Multiplying the measured stress-induced strain in a material with the material's Youngs modulus results in a "measured" stress. This allows a direct comparison between the calculated FEM stress and the "measured" stress. In the following figures the FEM and measured stress are shown for the West cantilever bulbs, and for the bulbs above the box.

Figure 6.16 shows the stress in the West cantilever bulbs for a warm period, and figure 6.17 shows the same positions for a cool period. FEM stress is shown with a solid line, measured stress with a dashed line. The warm period in figure 6.16 shows clear daily stress peaks at approximately 09:00 and 21:00. At these times, the lower part of the box walls heat up due to the low standing sun. Heating of the lower part of the box walls results in positive temperature-induced strain there. The static indeterminate supports of the bridge limit curvature, and so only axial bridge elongation remains. This results in tension in other parts of the bridge. This tension stress is overestimated by the FE-Model: the calculated stress peaks are larger and steeper than the measured stress. The temperature gradient incorporating the bottom of the box wall is assumed linear and inferred from a single temperature sensor at the bottom of the box wall. This single sensor thus influences a large part of the cross-sectional area. There are no sensors in place to determine the exact temperature gradient, but the assumed linear gradient might be an oversimplification, inducing significant uncertainty in the temperature distribution, and thus also in the strain and stress.

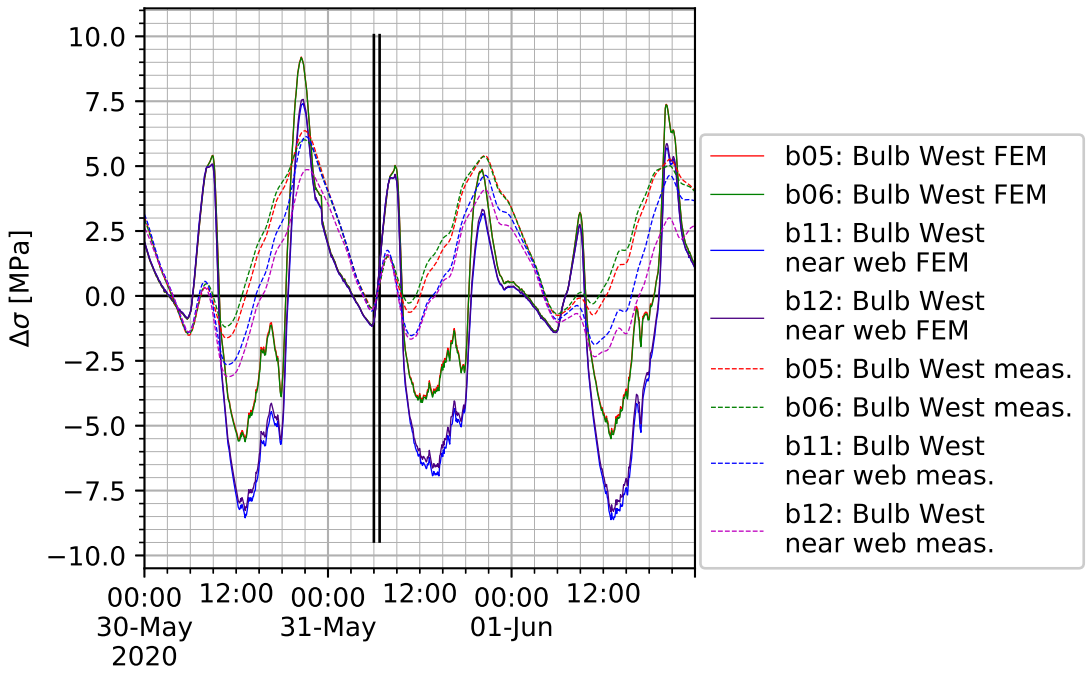

Figure 6.16: Stress FEM vs Measured, West cantilever bulbs.

The FEM- and measured strains shown in figure 6.16 also indicate a stress difference between mid-span of the bulb, and near a support. This indicates that the bending moment varies along the bulb axis. The measurements show a difference of approximately 1.5 MPa between mid-span and near the supporting web, while the FE-model show a difference of approximately 2.5 MPa, an overestimation of 67%. Between 09:00 and 18:00, the FE-model indicates a larger compression stress than the measurements show. This might be caused by the zero-offset at 06:00 to 06:30, where the strain has already risen due to the bottom box wall temperature.

In the cool period shown in figure 6.17, the FE-model is in agreement with the measurements on June 6 until 23:00. After 23:00 erratic fluctuations occur, and for most of June 07 the model is off. Weather data shown in figure 6.18a indicates rainfall in this period. The water on the bridge might add weight and change local sensor temperature, causing model uncertainty.

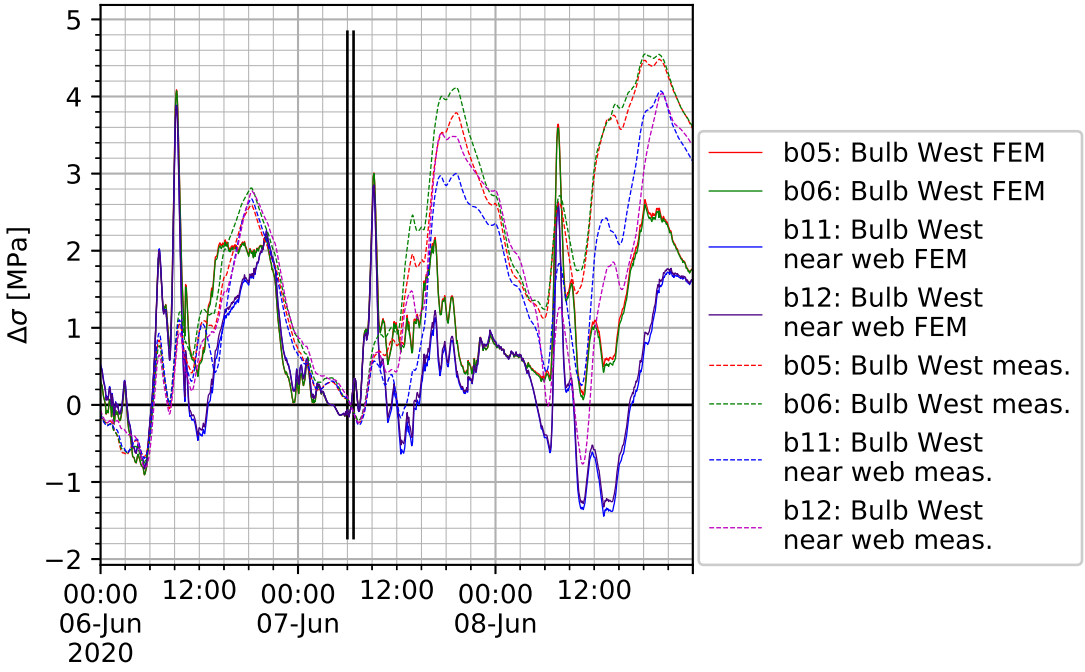

Figure 6.17: Stress FEM vs Measured, West cantilever bulbs. Cool period.

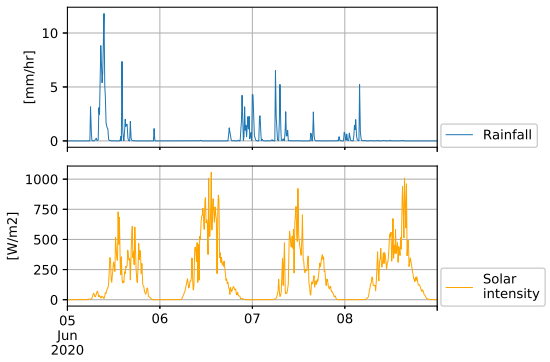

(a) KNMI Weather data

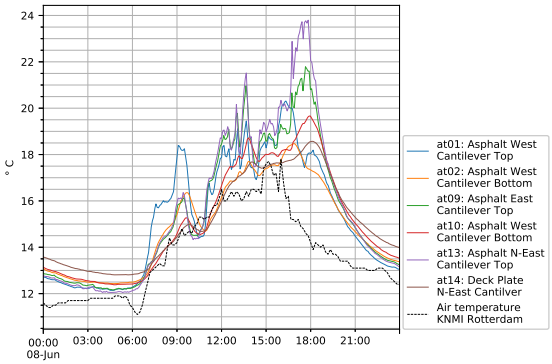

(b) Temperature drop 10:00 to 11:00

Figure 6.18: June 08, possible rainfall and temperature drop.

The bulbs above the box are shown in figures 6.19 and 6.20. Again FE-Model stress is shown with a solid line, while the measurements are shown with a dashed line. In the warm period (figure 6.19) the FE-model is in agreement with the measurements. The total daily variation from trough to crest is approximately 24 MPa for the FE-Model and 19 MPa for the measurements, an error of 23%.
In the cool period the FE-model shows sensitivity to local temperature changes. In the morning of June 6, both the measurements and the FE-model show oscillations, but the FE-model overestimates these with a factor 2. The sudden drop in stress on June 8 at approximately 10:30 is captured. For the bulbs above the box this is a drop, implying compression stress. The bulbs in the cantilever (figure 6.17) also show a small drop at the same time, but it is preceded by the much larger daily spike from the bottom box walls heating up, masking the effect. Figure 6.18 shows rain in Rotterdam early in the morning of June 08, and the temperature drop of the asphalt at 10:00. It is possible the rain from Rotterdam travelled 30km South, and reached the bridge a few hours later, causing this temperature drop, and the resulting stress-change. The influence of rain on the bridge and the FE-model is not fully understood, therefore rain might be the cause of these spikes, but it can't be stated with certainty, but no other likely causes were found.

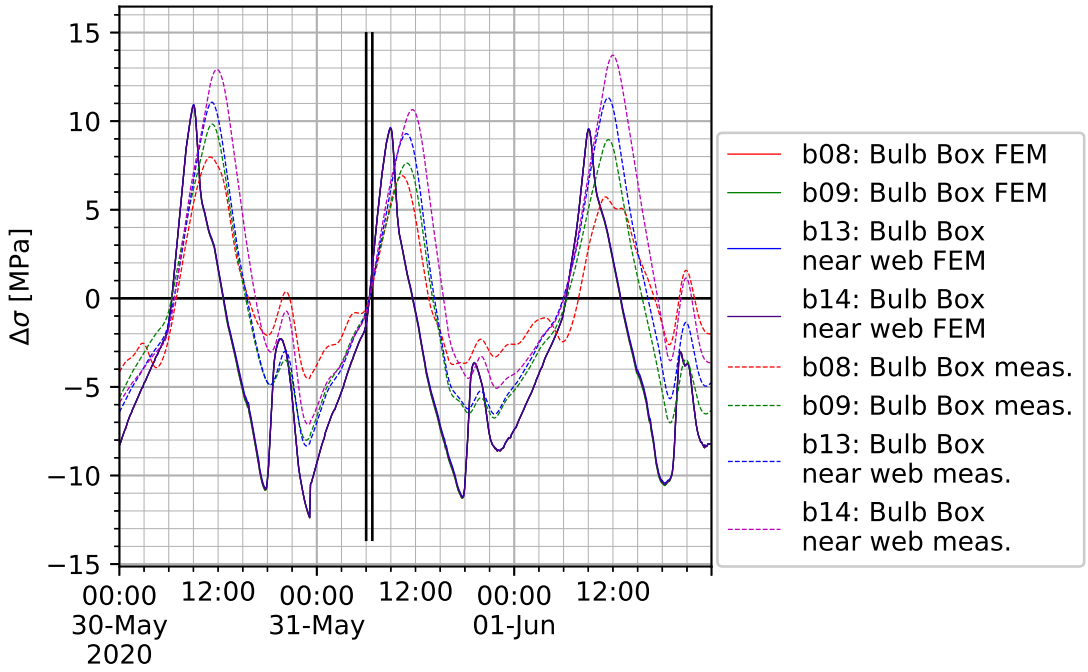

Figure 6.19: Stress FEM vs Measured, bulbs above the box.

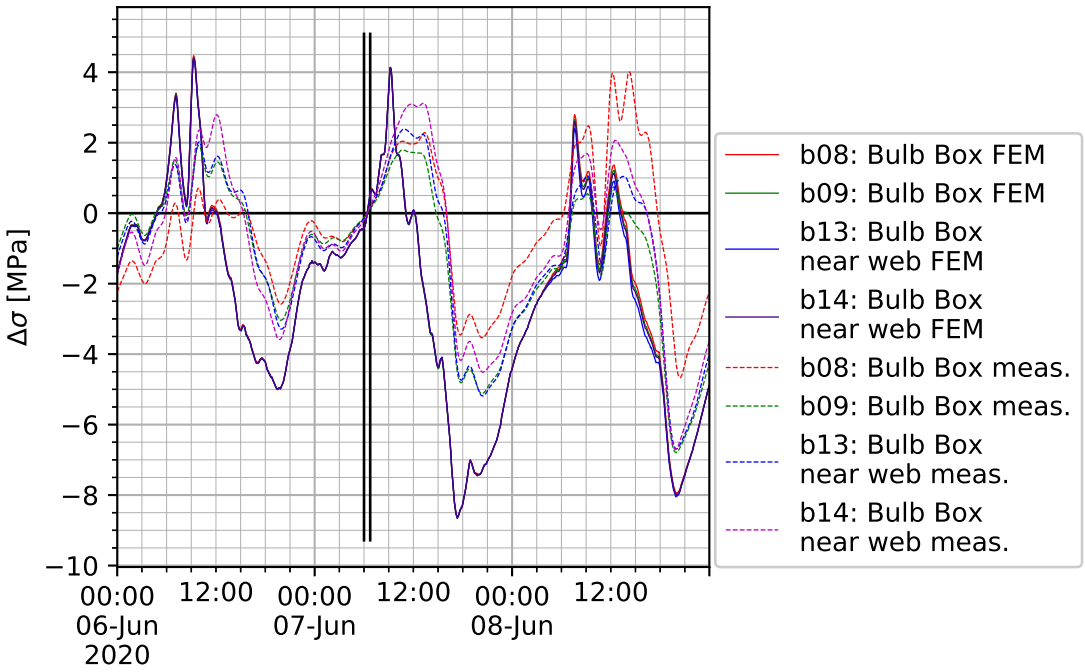

Figure 6.20: Stress FEM vs Measured, bulbs above the box. Cool period.

6.6 Summary: Temperature induced stress and strain

FE-Model of bridge and temperature

- The first three spans of the bridge were modelled in a 3D-FEM package. One end was clamped to simulate the 7 remaining spans, the other supports were assumed as rollers. The span containing sensors is the second span of the Haringvlietbrug, and thus at the center of the FE-Model. Asphalt was not included in the 3D FE-Model.
- One temperature load case was created resembling the average bridge temperature.
- To account for the inhomogeneous temperature distribution, an additional 11 temperature load cases were constructed as interpolation functions. This allows setting the temperatures of each individual element type and/or location, creating a piecewise linear temperature distribution across the bridge cross-section. Examples of the created load case are: "West cantilever deck plate","Bottom of the ribs of the West cantilever deck" and "Bottom West corner of the box-girder".
- Additional load cases were created for self weight and traffic load.
- For each load case an independent geometrically and physically linear calculation was made, and the resulting stress and strain at the sensor locations were exported to the tables shown in Appendix A.8.
- Temperature measurements were converted to load cases solicitation. Using the solicitation, linear combinations of the load case results (e.g. stress and strain) have been calculated for each minute of the measurement period.

FE-strain

- In the warm period the daily FEM-strain variation due to temperature changes, has an amplitude of approximately 200 $\mu\varepsilon$ for all observed sensors.
- The FEM-strain due to temperature variation was validated against support displacement, using the LVDT, and shows good correspondence.
- The daily FEM-strain variation due to and UDL resembling traffic, has an amplitude of 0.8 to 1.7 $\mu\varepsilon$ for the different sensors.
- The Measured strains in the box wall match the FEM-strains to within 30%, except for the bottom West box wall. There the deviation is over 50%. The cause is unknown, but sensor STC may be a contributing factor.

FE-stress

- The lower parts of the box walls undergo compression stress peaks of approximately 40 MPa due to morning- or evening sun, heating the plate locally.
- Other parts of the bridge show tension stress peaks at the same times as the compression peaks in the lower parts of the box walls. Elements closer to the box wall show larger peaks than those further away.
- The stress in the bulbs of the cantilever show a daily amplitude of 16MPa. Difference in stress between mid-span positions and positions close to the web of the cross-beam show the bending moment in the rib is not constant along its axis.
- The stress in the bulbs above the box shows no difference between the mid-span and near the supporting cross-members. The daily stress variation is approximately 23 MPa from trough to crest, and is mainly caused by the tension peak from the lower parts of the East box wall part heating up.
- The discrete strain gages measure stress-induced strain only. This stress-induced strain is converted to stress by multiplying with the Youngs Modulus.
- FEM-stress was verified against measured stress-induced strain. Stress variation due to local temperature rise of the bottom box walls is severely overestimated. The assumed

linear temperature gradients from load cases LC21 and LC22, and the availability of just a single sensor for the calculation of these load case solicitations are suspected causes for this uncertainty.

- On June 7 the FEM-stress deviates from the measured stress. Weather data suggests this might caused by rain.
- A large stress change was found on June 8, 10.30. This change was found in both the FEM-model and the measurements, for all the bulbs shown. Weather data and temperature measurements suggest this might be caused by rain.

7 Effect of Stress on dynamic characteristics

Chapter 6.5 has shown that the internal temperature distribution of the bridge may induce significant internal stresses. The FE-model has shown that the bottom box wall may undergo a daily stress cycle with an amplitude of up to 55 MPa due to these temperature differences. For the bulbs in the cantilever and the ones above the box the amplitudes are 16 and 22 MPa respectively.
The literature discussed in chapter 3.3 has shown that the eigenfrequencies of a beam or plate are strongly affected by externally applied forces. The simplest example is a column under compression. Using equation 7.1 the force-frequency relation is shown in figure 7.1a. Taking the derivative of this function ($\frac{\mathrm{d}\omega}{\mathrm{d}F}$ shown in figure 7.1b) shows that the change of eigenfrequency due to an applied external force is dependent on the ratio between initial force and buckling load. For elements close to buckling load a small change in applied force could result in significant frequency shift, while for elements under tension, the same force could barely have an influence.

$$\omega^2 = \frac{\pi^2}{\rho A l^2}\left(\frac{\pi^2 EI}{l^2} - F\right)$$

$$\omega = \sqrt{\frac{\pi^2}{\rho A l^2}}\sqrt{\frac{\pi^2 EI}{l^2} - F} \tag{7.1}$$

$$\frac{\mathrm{d}\omega}{\mathrm{d}F} = -\sqrt{\frac{\pi^2}{\rho A l^2}}\frac{1}{2 \cdot \sqrt{F_{buckling} - F_{initial}}} \tag{7.2}$$

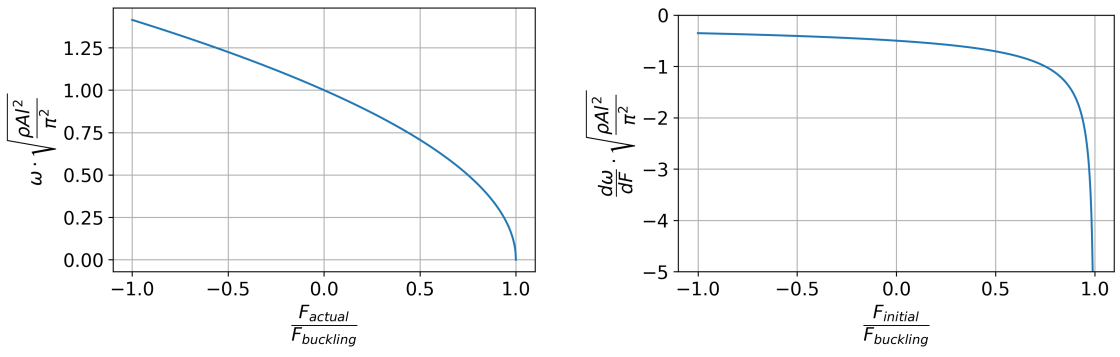

(a) ω (b) $\frac{\mathrm{d}\omega}{\mathrm{d}F}$

Figure 7.1: ω and it's derivative as a function of F, for a column under compression.

For plate dynamics a set of equations is derived in chapter 3.3.3, that needs to be solved using a computer algebra system. This set of equations requires the stress components n_x, n_y, n_{xy}. The measurement campaign only measured deck plate strain in the longitudinal direction ε_x. It follows that this equation can't be used for the deck plate dynamics based on measurements alone. The FE-model however does allow output of stress in all directions. Therefore the results from the FE-model are used to investigate the potential effect of the predicted stress variations on the dynamic characteristics.

The influence of the internal stresses on the eigenfrequencies of the bridge are studied using a few discrete subsystems. The following three discrete subsystems are evaluated, of which the first two are also used in chapters 8.2.2 and 8.2.1, to investigate influence of temperature dependent asphalt properties on dynamic characteristics. Subsystems are ordered by increasing mathematical complexity:

- A rib-deck span between 2 cross members. This model includes 1 rib, and is only supported at the ends with cross members. The long sides are assumed free, under the assumption that all ribs of this orthotropic deck spanning 2 cross-members move identically. This subsystem is modelled as a beam-column. and is also used in chapter 8.2.2 to investigate influence of temperature dependent asphalt properties on dynamic characteristics.
- A section of deck between 2 ribs and 2 cross members. The plate is thus 300x2200 mm, and thickness includes 10 mm steel and 2 x 30 mm asphalt. The rib itself is not included. This subsystem is modelled as a plate.
- A single rib in the lateral direction. The top edge of the rib is clamped by the deck plate. This subsystem is evaluated using FEM.

In the evaluations in this chapter, the asphalt properties are assumed using a fixed temperature of 20°C and a loading frequency of 100Hz. This results in Youngs moduli of 7800 MPa for guss asphalt, and 4600 MPa for ZOAB. The influence of asphalt temperature and loading frequency on effective asphalt stiffness is discussed extensively in chapter 8, while this chapter will only focus on the effect of internal stress on dynamic characteristics.
The exact boundary conditions of these subsystems are non trivial. Given that for each subsystem only the first eigenmode is evaluated, one could assume that structural elements adjacent to the defined subsystems move in the opposite direction. It's further assumed that the supports at the boundaries are usually given by a rib or cross-beam web, with a low torsional stiffness. Therefore all boundary conditions for beam elements are assumed pinned on one end, and a hinged-roller on the other end. Under this assumption, the first eigenfrequency of a beam-column in bending may be calculated as in equation 7.1, where F is the externally applied force which can be obtained by integrating the internal stress near the boundary over the cross-sectional area of the subsystem.
Only the first eigenmode of each subsystem is evaluated, but equation7.2 also shows that for a column under compression $\frac{\mathrm{d}\omega}{\mathrm{d}F}$ becomes smaller if $\frac{\pi^2 EI}{l_{eff}^2}$ increases. For the higher modes l_{eff} decreases. Therefore the percentual change of eigenfrequency due to temperature induced stress will be smaller.
The selected subsystems only contain discrete strain gages that measure stress-induced strain after applying the temperature compensation as stated in chapter 4.3.3. This stress-induced strain can easily be converted to stress, but is very sensitive to the temperature used in the STC formula. No exact temperature measurements are available at these sensor positions, and thus the measured stress contains significant uncertainty. This implies that the best results might be obtained by observing FEM-stress and not by trying to convert strain measurements to stress. A further benefit is that FEM-stress is available in all directions $(\sigma_x, \sigma_y, \tau)$ which will be needed for the plate dynamics.
The absolute eigenfrequencies presented contain significant uncertainty, due to e.g. the boundary conditions, but they indicate the part of the frequency spectrum in which stress induced change effects may be observed.

7.1 Influence of stress on discrete subsystems

7.1.1 Rib-deck span as a beam-column

The deck of the Haringvlietbrug is orthotropic. Along the longitudinal (North-South) bridge axis the bending stiffness of the primary deck structure is high due to the rib, and the span is short with only 2.2 m between the cross-members. In the lateral (East-West) direction, orthogonal to the rib, the primary deck structure stiffness is low and the span is long. For the cantilever deck the lateral span is approximately 4.8 m between longitudinal beam and box wall. For the deck above the box, the transversal span is 11.5 m. This implies that the first eigenmode of the orthotropic deck will be strongly dependent on the stress and stiffness in the longitudinal bridge direction. Therefore it is assumed that the system could be simplified to a 1D Euler-Bernoulli beam-column problem.

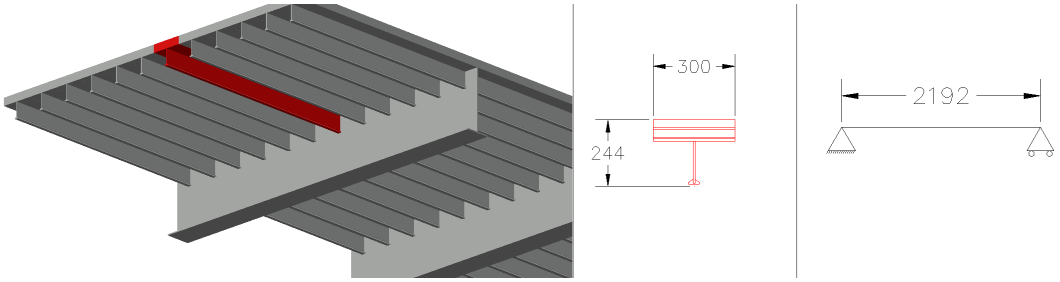

Figure 7.2: Deck section with bulb spanning 2 cross members

This beam-column subsystem, containing one rib with a bulb on the lower end, and a section of deck plate 300 mm wide, is shown in figure 7.2. Using the assumption that sections of rib-deck next to this one are moving together, the sides are assumed free. One end is assumed as a pin, the other end as hinged-roller, under the assumption that the continuous orthotropic deck spans multiple cross members and the first eigenmode will have all spans alternate between upwards and downwards displacement in the first mode-shape. The lateral stiffness of the crossbeam web is assumed small compared to the bending stiffness of the rib-deck, and therefore neglected. A compression force is applied to one end, based on the stress from the FE-model:

$$\begin{aligned} F &= -\sigma_{neutral\ axis} \cdot A_{steel} \\ &= -\{\sigma_{rib} + \sigma_{deck} \cdot \frac{z_{na} - z_{bulb}}{z_{deck} - z_{bulb}}\} \cdot A_{steel} \end{aligned} \tag{7.3}$$

Note that for stress, tension is defined as positive, while equation 7.1 defines F as a compression force. This explains the minus. A_{steel} is used to best match the internal force to that of the FE-model, which does not include asphalt. For the bending vibrations asphalt does play a role, both due to its mass and its thickness, and thus asphalt will be included for the rest of the cross-sectional properties.
Cross sectional properties are calculated using:

$$EI = \int_A E(z) z^2 \, \mathrm{d}A \tag{7.4}$$

$$\rho A = \int_A \rho(z) \, \mathrm{d}A \tag{7.5}$$

$$A_{steel} = \int_{A_{steel}} \mathrm{d}A \tag{7.6}$$

In previous chapters stress was offset to obtain mean stress between 06:00 and 06:45 equal to zero. As was shown in chapter 3.3 the first eigenfrequency of a beam-column under compression equals zero if the axial compression force is equal to the buckling load. This implies that the absolute stress and force are required. The FE-model was used to calculate the absolute stresses due to self-weight of steel (load case 101) and asphalt (load case 102). These stresses are added to the stresses due to temperature gradients and shown in figure 7.3. As can be seen the daily stress amplitude is approximately 14 MPa for both the bottom of the rib (the bulb) and deck plate. Stress due to self-weight is approximately 14 to 20 MPa for the bulb and the deck plate respectively.
Using equation 7.1 the first eigenfrequency of the system is calculated and shown in figure 7.4. The eiqenfrequency of the first eigenmode is approximately 71.65 Hz at 06:00. In the mornings and evenings the bottom box walls heat up very locally, creating a relative tension peak in the deck plate. This results in an increased eigenfrequency with peaks up to 72.05 Hz for the period shown. During the heat of the day, the deck is warmer than the bottom of the bridge, resulting in an additional compression force in the deck. Due to this additional compression force, the eigenfrequency is calculated to drop to 71.5 Hz. The total magnitude of the frequency shift for the period shown is $72.05 - 71.5 \approx 0.55$ Hz.
If lateral torsional buckling of the rib is ignored, then the buckling load of the subsystem is $\frac{\pi^2 EI}{l^2} \approx$ 7700 kN, with an applied total load of $\approx$ 100kN (see figure 7.3). Using the ratio $\frac{F_{compression}}{F_{buckling}} = \frac{\approx 100}{7700} \approx 0.01$ in figure 7.1b, it is shown that this subsystem is loaded in the region where additional loading has a relatively small influence, which is confirmed by the graphs.
The model is thus insensitive to small variations in initial loading due to e.g. self-weight.

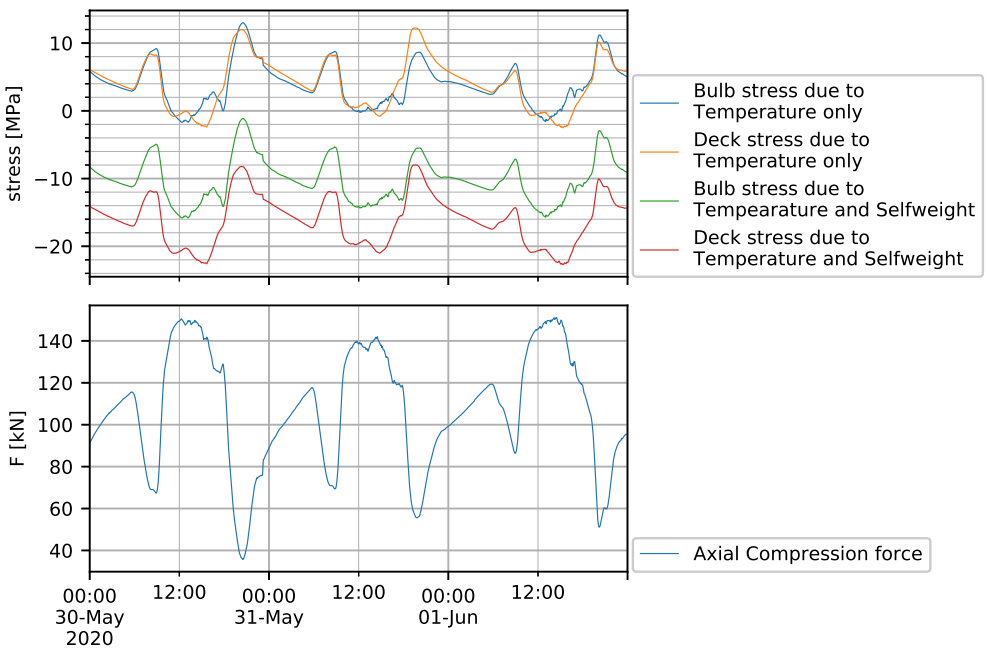

Figure 7.3: Stress in the cantilever deck-rib subsystem and resulting axial Force

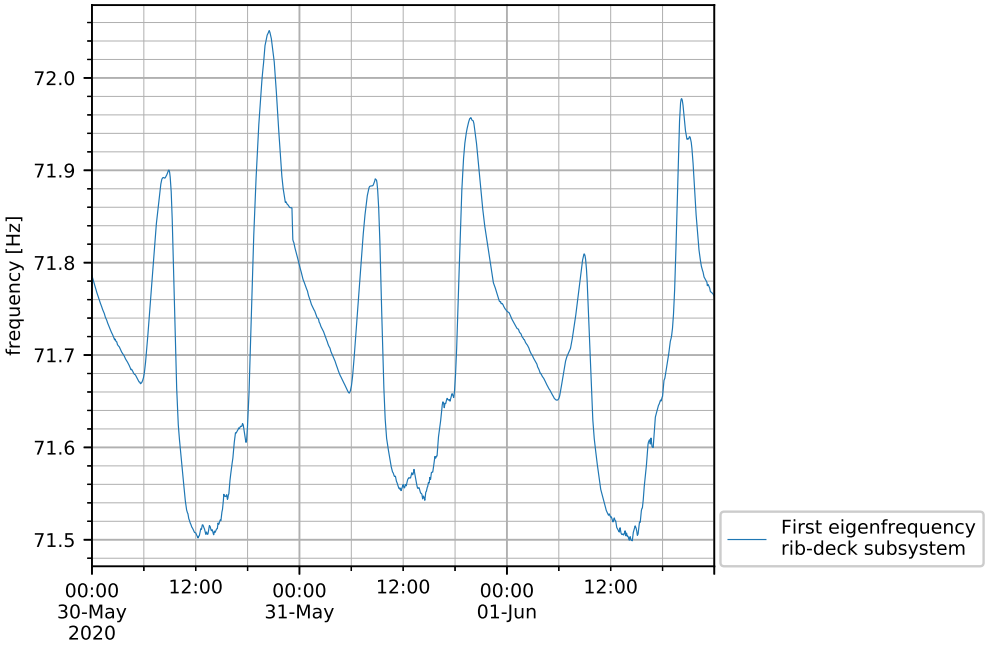

Figure 7.4: First eigenfrequency of the rib-deck subsystem

7.1.2 Deck plate with asphalt

The second subsystem is that of the deck plate including asphalt, evaluated as a plate. It is modelled to be supported on hinged-rollers on all edges, assuming the first mode has a checker-board-pattern, where all fields alternate between up and down. Again, stiffness of the supporting webs and ribs is assumed negligible. Damping is ignored. The scheme is shown in figure 7.5, and a contour plot of the first mode is shown in figure 7.6.

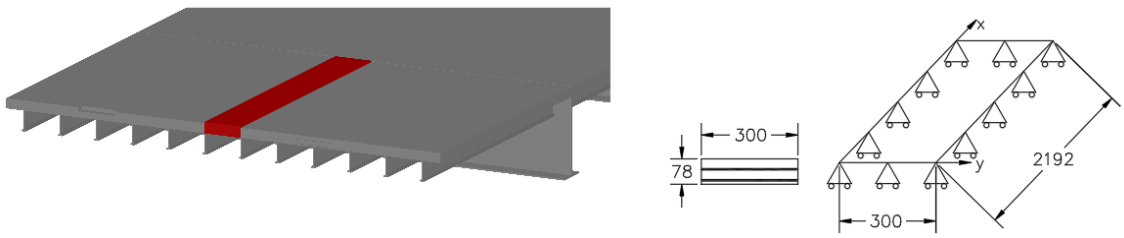

Figure 7.5: Deck plate including asphalt spanning 2 bulbs and 2 cross-members

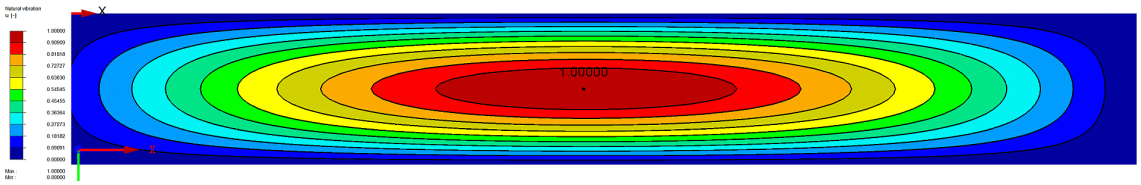

Figure 7.6: First mode of plate, FEM.

In section 3.3.3 the differential equations for plate bending have been solved using the Rayleigh-Ritz procedure, to obtain $\omega_{1,1}$ for an isotropic plate of 0.3 x 2.192 m. The result is repeated below for clarity:

$$\omega_{1,1} = \frac{\sqrt{3.063N_{xy} + 12026N_y + 4.219N_x + 17368D}}{\sqrt{\rho t}} \tag{7.7}$$

Here D and ρt are based on a solid isotropic plate. The deck plate with asphalt on top is a composite, which poses a challenge. A simplified approach is used to overcome this:

$$\begin{aligned} \rho t &= \int_t \rho(z)\,\mathrm{d}z \\ D &= \frac{Et^3}{12(1-\nu^2)} \approx \frac{1}{1-\nu^2}\int_t E(z)z^2\,\mathrm{d}z \end{aligned} \tag{7.8}$$

With:

t = composite plate thickness
z = distance to neutral axis
ν = Poisson ratio of steel

This approach is accurate for the self-weight ρt, and the bending stiffness usually denoted with D_x and D_y, while the torsion stiffness D_{xy} contains some uncertainty. Equation 7.7 does not distinguish between these different degrees of stiffness. The added uncertainty due to this simplification is deemed acceptable for the current purpose of showing whether or not the stress has a significant influence on dynamic characteristics.

Observing the numerical values in equation 7.7 the notion rises that the frequency of the first eigenmode is insensitive to stress in the x- and xy-direction. In figure 7.7 it is shown that even significant stresses of 60 MPa in the x or xy-direction influence the eigenfrequency by 0.3 Hz, or just 0.03%. Stress in the (West-East) y-direction however has significant influence. A compression stress of 60 MPa lowers the eigenfrequency by 70% to approximately 300 Hz, while a tension stress

in the East-West direction of 60MPa increases the eigenfrequency with 35% to 1350 Hz.
A verification with a small FE-Model shown in figure 7.6 shows that the Rayleigh-Ritz procedure overestimates the first eigenfrequency of this plate with approximately 30%, probably due to the high length to width ratio. Higher order modes with checker-board patterns that have cells with equal length and width (e.g. 7 half-waves of 313 mm in the x-directions, and 1 half-wave of 300 mm in the y-direction) show decreased deviations down to just a few % compared to the FE-model. The simplifications of the plate stiffness, and uncertainty in asphalt parameters and boundary conditions add further uncertainty to the model. Therefore the presented frequencies should not be interpreted as absolute values, but merely as a range of interest for further study.
The West cantilever deck plate was equipped with 2 strain sensors in the x-direction: b37 and b38. The stress and strain in these positions is already present in the FE-result tables (A.5 and A.7). The stress in the y- and xy- direction is added, and shown in figure 7.8. No significant stress in the y- or xy- direction is present in the plate. The stress in the x-direction is significantly larger, with an offset due to self-weight, and an amplitude due to differential temperatures.
While the stress in the y-direction is small with -0.1 to 1.5 MPa, it still the most dominating factor for the first eigenfrequency of the deck plate. The total magnitude of the frequency shift is approximately 12 Hz, around a center frequency of ≈1001 Hz. A deviation of plus and minus 0.6%.

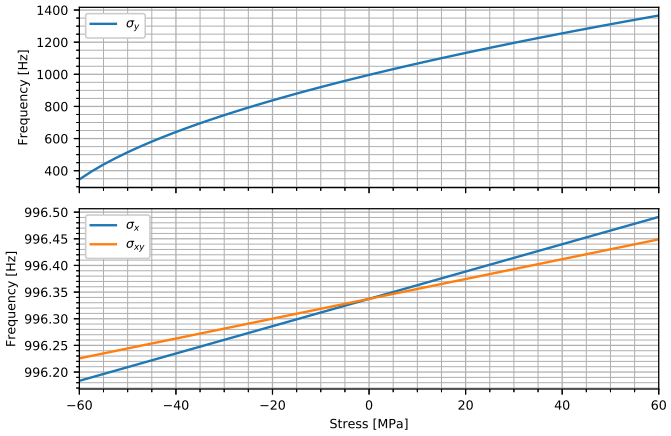

Figure 7.7: Influence of stress in a single direction on the first eigenfrequency of the deck plate - asphalt composite

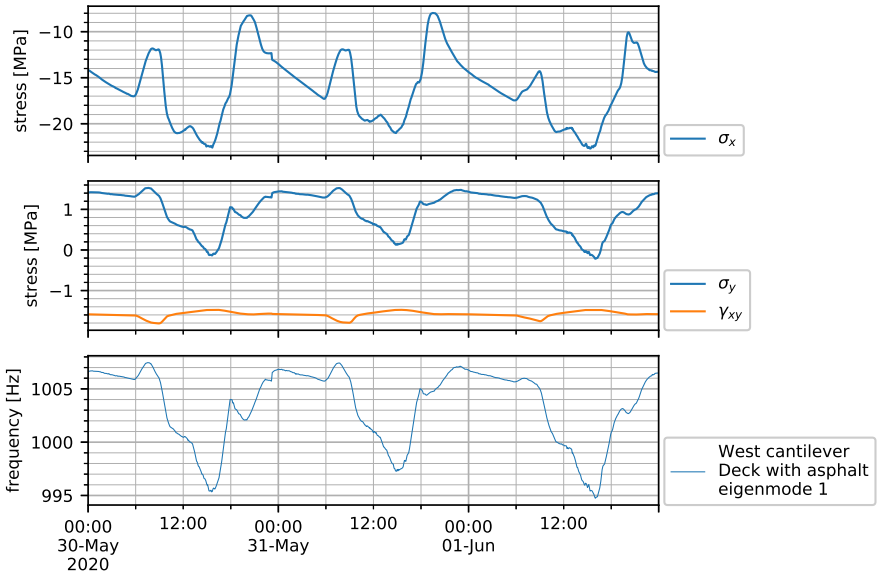

Figure 7.8: 2D-Stress and resulting eigenfrequency, West cantilever deck with asphalt.

7.1.3 Rib sideways in FEM

The third sub-model contains a rib, analysed in the weak direction. Because the deck plate adds a constraint, this can no longer be analysed as a column. Therefore a FE-model is made containing a continuous rib spanning 5 fields. Intermediate supports are assumed as hinged rollers, ignoring the lateral stiffness of the crossbeam web. Only the values for the center field are shown. For the model see figure 7.9. The web and flange of the rib are made of Mindlin-Reisner plate's of 8 and 12mm thick respectively.

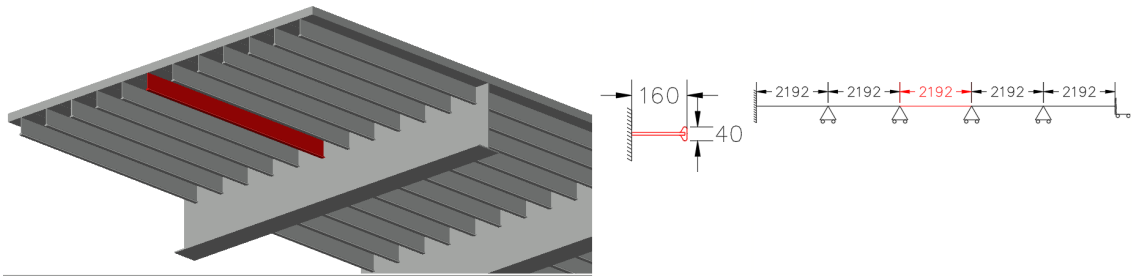

Figure 7.9: bulb sideways

The first mode is shown in figure 7.10.
To show the effect of temperature induced stress, a second analysis is run in which the right side of the model is loaded with an imposed deformation of 1.00 mm in compression on the edges. The resulting first mode is similar to the unloaded one, but with a different eigenfrequency. The comparison of the eigenfrequencies is shown in table 7.1. The 32.8 kN compression force equals an average stress of $\frac{-32800}{40 \cdot 12 + 148 \cdot 8} \approx -19.71$ MPa. This approximately 20 MPa stress change in the rib and bulb induces a frequency change of 0.475 Hz on a frequency of 189 Hz. Figure 7.3 has shown the stress in the bulb due to self-weight and temperature effects varies between -1 and -16 MPa. The expectation is that the eigenfrequency of the first sideways mode of the rib, varies between approximately 189.7 and 189.3 Hz due to daily environmental influences.

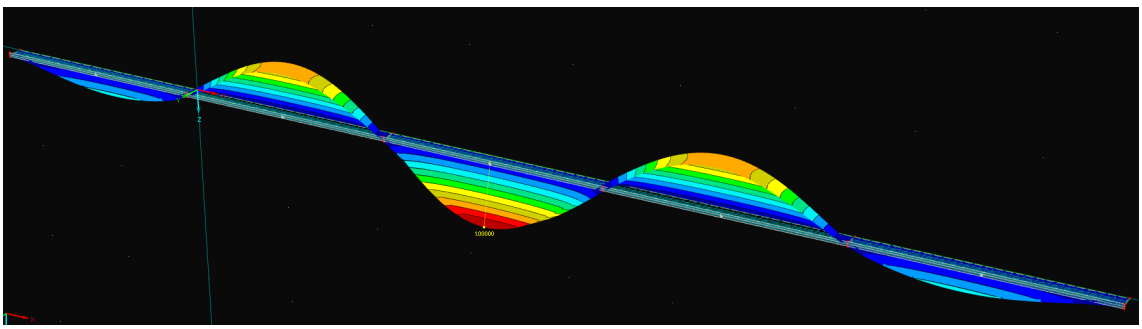

Figure 7.10: First sideways mode of the rib

Table 7.1: Eigenfrequencies for normal and compressed rib

Loadcase	Free	Compressed	unit
Force	0	32.80	[kN]
1st eigenfreq	189.679	189.204	[Hz]
Difference	-	$-14.48 \cdot 10^{-6}$	[Hz/N]

7.2 Summary: Stress to dynamic characteristics

Sub-models of the bridge are evaluated to determine influence of stress on dynamic characteristics. Using an FE-Model, combined with temperature measurements, self-weight and traffic load, the stress distribution in the sub models was determined over a three day period. To research the influence of the daily temperature variations on the sub-models, the first eigenfrequency was calculated using analytical and numerical methods. Simplifications of the model including the boundary conditions imply the determined eigenfrequencies contain significant uncertainty. However, assuming the system is linear and boundary conditions are time-independent, different boundary conditions should only influence the base eigenfrequency. The percentual change due to stress should remain similar, under the condition that compression forces are small compared to the buckling loads.

- The rib-deck spanning between two crossbeams was evaluated as an 1D-beam-column. The average axial compression force varied between 40 and 150 kN. The eigenfrequency varied between approximately 71.5 and 72.05 Hz, a shift of 0.55 Hz or 0.8%. Initial stress was well below buckling load, implying this change in eigenfrequency is insensitive to the exact determination of the initial stress.
- The asphalt- deck plate composite was evaluated as an isotropic plate using the Rayleigh-Ritz procedure. The largest stress, both the average value and the daily variance, was found in the longitudinal direction of the bridge. The transverse stress was much smaller but was shown to be the determining factor for the plate eigenfrequency. Stress varied between -0.1 and 1.5 MPa, resulting in eigenfrequencies between 995 and 1008 Hz. This is a shift of approximately 13 Hz or 1.3%.
- The sideways vibrations of a rib were studied using an FE-Model. A 20 MPa axial compression stress, results in a 0.475 Hz frequency shift, from 189.68 to 189.20 Hz. Daily stress variations are approximately 16 MPa for the warm period, just like the rib-deck, and therefore the daily frequency variation in the warm period is expected to be in the 0.4 Hz range, or 0.2%.

8 Effects of Asphalt Non-Linearity on Dynamic Characteristics

The Haringvlietbrug deck plate is covered with 2 layers of asphalt, each 30 mm thick. The top ZOAB layer, bottom guss asphalt layer and the steel deck plate are separated by waterproofing membranes. The configuration is shown in table 8.1, while the asphalt properties as given by RWS are shown in tables 8.2 and 8.3.

Table 8.1: Deck Layers

Layer [−]	Thickness [mm]	Material [−]	Density [kg/m^3]
5	30	ZOAB	2000
4	4	Parafor Ponts	1500
3	30	Asphalt	2360
2	4	Mistral C	1500
1	10	steel	7850

These tables show that the effective Youngs Modulus of asphalt is influenced by asphalt temperature and loading frequency. A brief theoretical background is given in section 3.2.2.
While the given tables seem elaborate, they don't fully cover all temperatures and loading frequencies of interest. As was shown in chapter 5.1 the asphalt reached temperatures of over 40°C , while the supplied tables 8.2 and 8.3 only supply data for up to 20°C.
In order to overcome this, asphalt material modelling is required, which will be presented in chapter 8.1.1. Chapter 8.2 will describe the potential effects of the asphalt non-linear visco-elastic behaviour on some discrete subsystems of the bridge.

Table 8.2: Youngs Modulus of Gussasphalt

Freq	-10 °C	-05 °C	00 °C	05 °C	10 °C	15 °C	20 °C
5.86 Hz	21213	17551	14207	11107	7962	5711	3745
9.77 Hz	21929	18357	15000	12023	8787	6421	4312
19.53 Hz	22842	19419	16198	13307	9992	7511	5185
25.39 Hz	23154	19792	16767	13790	10440	7922	5535
29.30 Hz	23317	19985	17037	14045	10689	8154	5732
35.16 Hz	23523	20230	17336	14378	11000	8447	5988
39.06 Hz	23621	20369	17520	14558	11180	8607	6130
50.78 Hz	23878	20658	17895	15020	11608	8995	6508
58.59 Hz	24000	20802	18119	15244	11812	9110	6683

Table 8.3: Youngs Modulus of ZOAB

Freq	-10 °C	-05 °C	00 °C	05 °C	10 °C	15 °C	20 °C
5.86 Hz	10756	8575	7431	5856	4440	3443	1988
9.77 Hz	11196	9077	7959	6389	4969	3916	2344
19.53 Hz	11774	9752	8672	7133	5724	4631	2916
25.39 Hz	11979	9991	8924	7404	6005	4897	3144
29.30 Hz	12081	10121	9059	7551	6160	5044	3270
35.16 Hz	12217	10289	9228	7736	6355	5236	3441
39.06 Hz	12285	10380	9320	7837	6465	5342	3535
50.78 Hz	12461	10608	9572	8101	6747	5626	3796
58.59 Hz	12540	10707	9695	8223	6880	5763	3927

8.1 Asphalt material modelling

8.1.1 Asphalt master curve

Asphalt is usually tested in a device with a limited frequency range, but under different temperatures. The first step in processing the laboratory measurement data into asphalt model properties is plotting this available test data on a log-log scale, as shown in figure 8.1. Each test temperature is shown as a separate line. Figure 8.1a also shows that different circumstances may lead to an identical Youngs modulus, for example: a Youngs modulus of 6000 MPa may be reached at 15 °C and ≈ 8 Hz, but also at 20 °C and ≈ 35 Hz. This implies loading frequency and temperature might be interchangeable, which is known as the Time-Temperature-Superposition-Principle (TTSP). More details of the principle are explained in section 3.2.2.

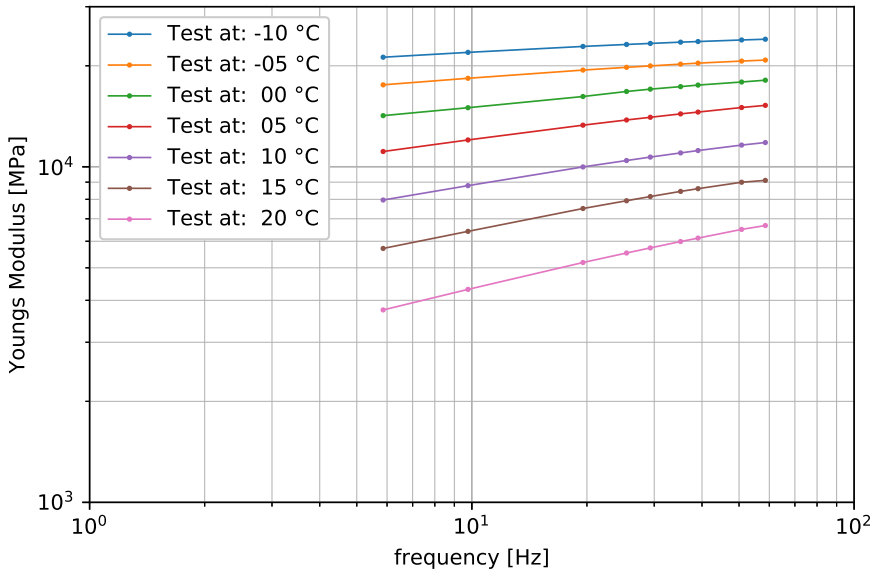

(a) Guss Asphalt

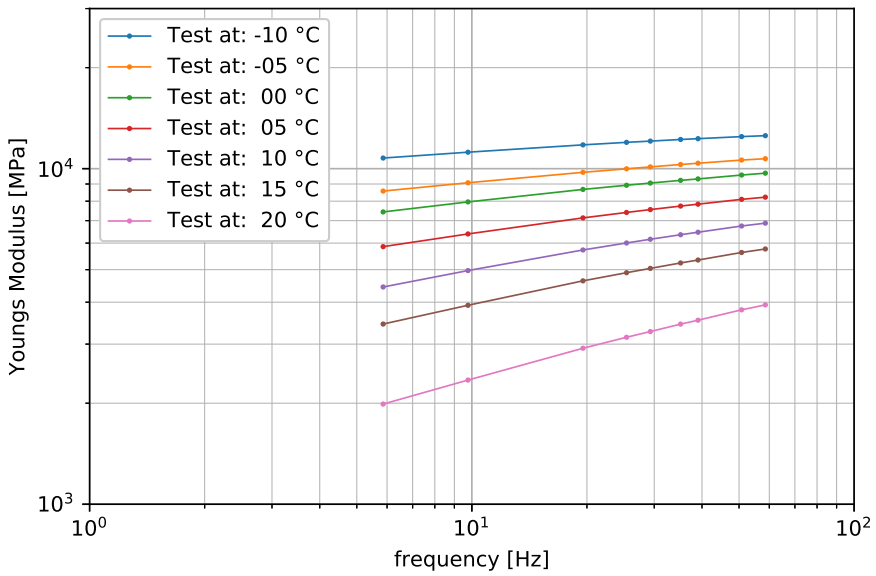

(b) ZOAB

Figure 8.1: Asphalt properties as given by RWS

Using TTSP the separate curve sections for each test temperature may be shifted horizontally until they align and form a master curve. This manual process is purely based on visual appearance. Figure 8.2 shows the individual sections line up nicely after applying this shift. The x-axis is renamed to "reduced frequency", as is common in pavement engineering. This indicates the x-axis does not denote actual test frequencies, but that frequencies are derived from tests at other temperatures.
The measured curve of one of the test frequencies is not shifted along the frequency axis, in this case the one for 15°C. For the following plots, 15°C is now called the reference temperature. The choice of this reference temperature and thus the unmoved test curve is up to the user, as long as this reference temperature is clearly stated. All other sections were moved using equation 8.1 with the shift factors from table 8.4. Table 8.4 shows that because 15°C is the reference temperature, the shift factor $\log(\alpha_T) = 0$ for $T = 15°C$.

Table 8.4: Shift factors $\log(\alpha_T)$

	Guss Asphalt	ZOAB
T= 20°C	-0.699	-0.767
T= 15°C	0.000	0.000
T= 10°C	0.653	0.447
T= 5°C	1.447	1.021
T= 0°C	2.176	1.681
T= -5°C	3.021	2.161
T= -10°C	4.097	3.190

$$f_{reduced} = 10^{(\log(f_{test})+\log(\alpha_T))} \tag{8.1}$$

Once the master curve is assembled the data points are used to fit a sigmoid function (eq:8.2), in which a, b, c, d are arbitrary constants. The parameters obtained from curve fitting are shown in equations 8.3 and 8.4. RMS errors between the available data points and the sigmoid curve are 60.9 and 40.3 MPa for Guss asphalt and ZOAB respectively, indicating a good match.
The resulting sigmoid function is shown in figure 8.3, where the minimum and maximum frequency are chosen such that the global shape of the sigmoid is visible. Care should be taken that a significant amount of extrapolation is shown, and even small changes in the fit, may lead to significant deviations at the ends of these functions.
In chapter 8.2 frequencies between 10^{-3} Hz and 10^3 Hz are used at temperatures between 15 and 40°C . Due to the change of temperature and TTSP a larger section of the presented sigmoid curve will be used than the 10^{-3} to 10^3 Hz range. These values should therefore be used as an indication only.

$$\log(E) = a + \frac{b}{1 + e^{-c(\log(frequency)-d)}} \tag{8.2}$$

$$\log(E_{Guss}) = 1.13 + \frac{3.35}{1 + e^{-0.42(\log(f)+2.27)}} \tag{8.3}$$

$$\log(E_{ZOAB}) = 0.50 + \frac{3.71}{1 + e^{-0.47(\log(f)+2.44)}} \tag{8.4}$$

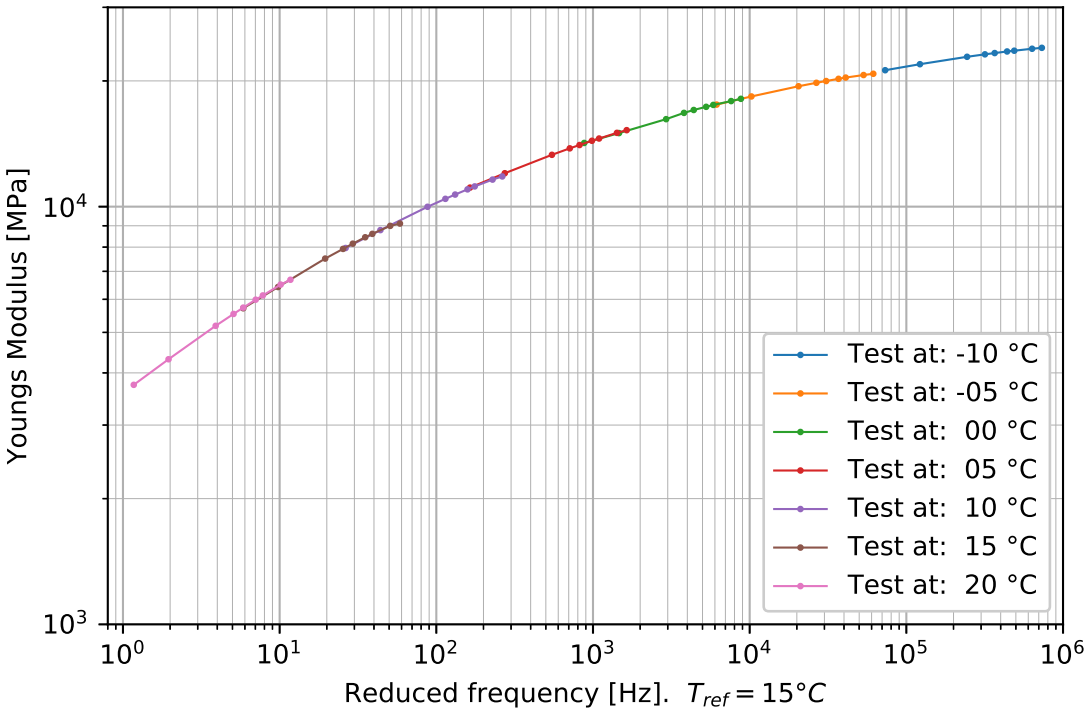

(a) Guss Asphalt

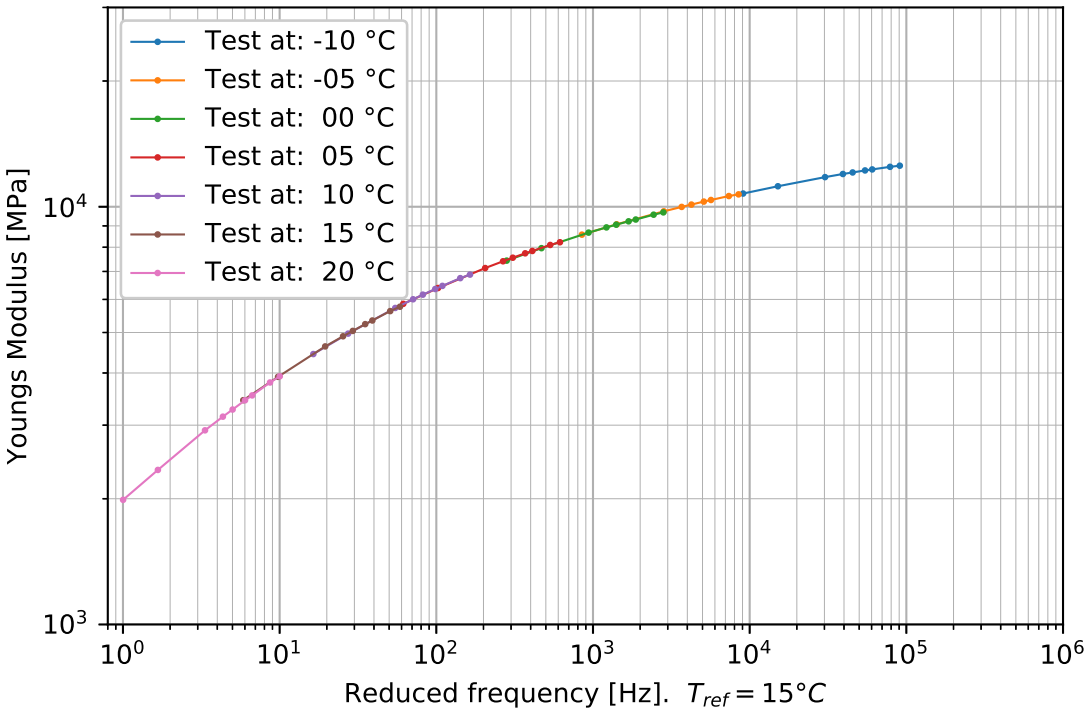

(b) ZOAB

Figure 8.2: Mastercurves of Asphalt

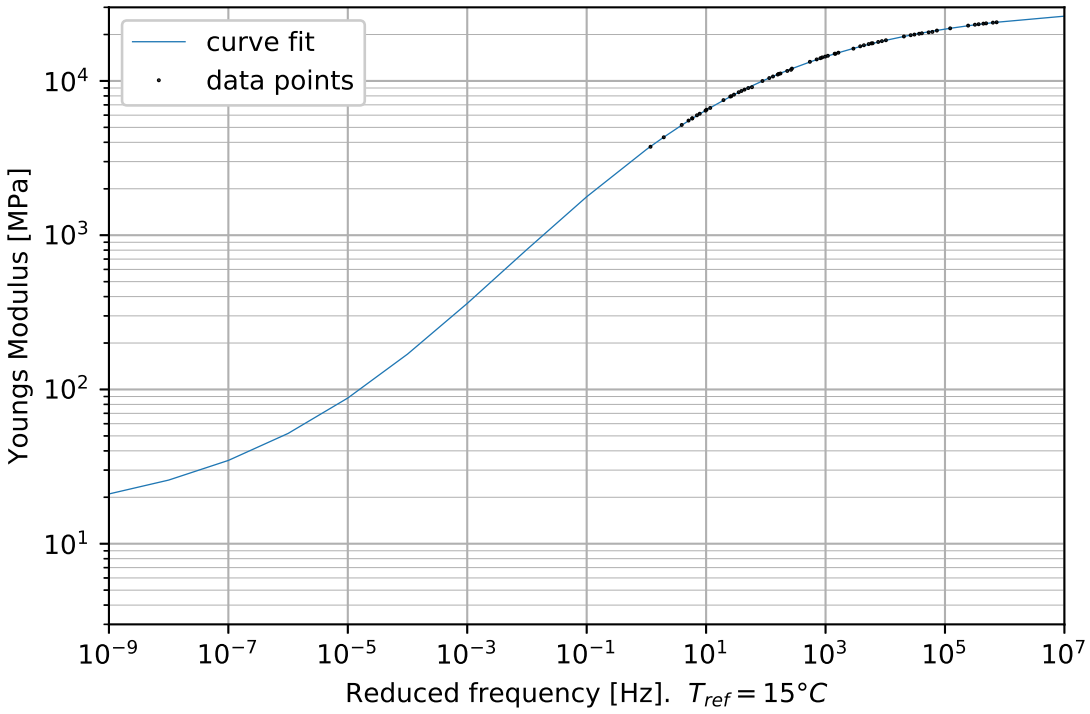

(a) Guss Asphalt

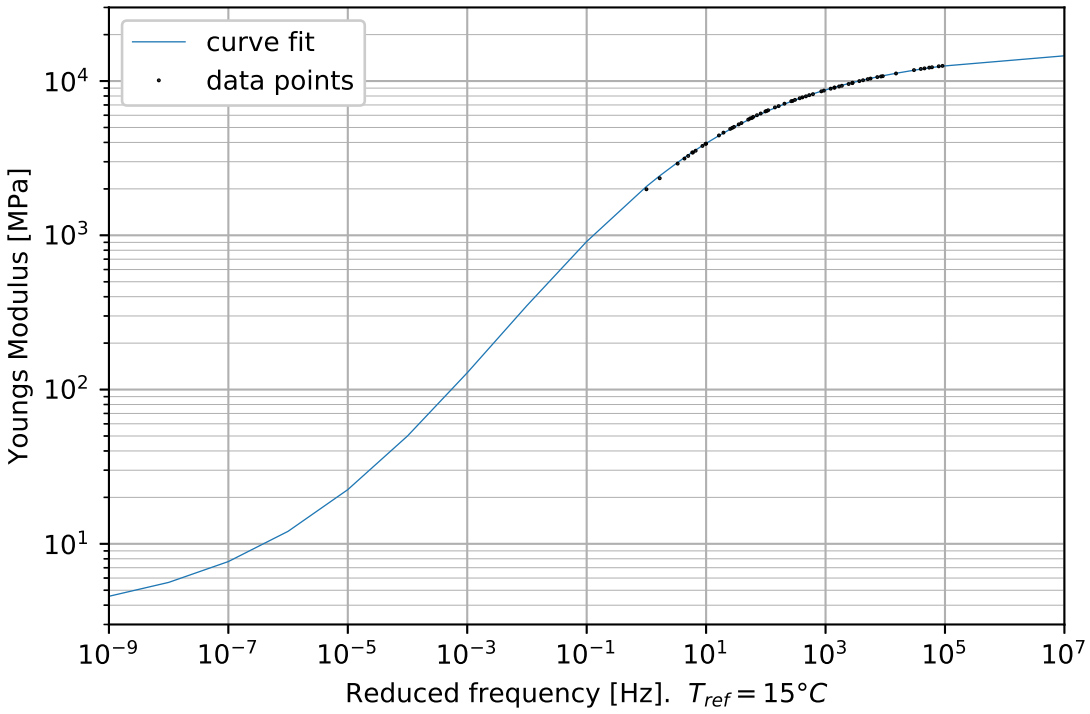

(b) ZOAB

Figure 8.3: Sigmoid fit on asphalt mastercurves

The obtained sigmoid functions from figure 8.3 are based on a reference temperature of 15 °C. Using the shift factors from table 8.4 it is possible to create copies of this curve for each test temperature. The temperature measurements of the bridge show the ZOAB reaches temperatures of 40 °C and above, for which no asphalt test data is available. Various methods exist to obtain shift factors for untested temperatures. Alrashydah and Ado-Qudais [20] compared various methods and found the Williams-Landel-Ferry (WLF)-equation to yield accurate results. The WLF-equation is shown in equation 8.5.
For both asphalt types T_0 was initially set to 15°C, forcing the curve through zero at 15°C. C_1 and C_2 are then obtained by curve-fitting. In order to adjust the fit and be more accurate for the temperatures of interest (> 20°C), below zero temperatures were neglected in the fitting procedure for ZOAB. The resulting curve is shown in figure 8.4.

$$log(\alpha_t) = \frac{-C_1(T - T_0)}{C_2 + T - T_0} \tag{8.5}$$

$$log(\alpha_{t,Guss}) = \frac{-16.04(T - 15)}{123.98 + T - 15} \tag{8.6}$$

$$log(\alpha_{t,ZOAB}) = \frac{-9.45 \cdot 10^6(T - 14.0)}{7.98 \cdot 10^7 + T - 14.0} \tag{8.7}$$

Finally the WLF-curves from figure 8.4 are used to shift the sigmoids from figure 8.3 from their reference temperature of 15°C to the required temperatures. Based on the measured temperatures in May and June 2020, the temperatures 10, 15, 35 and 40°C are chosen, together with the original test temperatures to show the quality of the fit. See figure 8.5 for course plots, and figure 8.6 for a close-up.
It is important to note that the values for temperatures above 20°C are a double extrapolation. First the master curve was extrapolated with a sigmoid function, and then the sigmoid function was shifted with a WLF-extrapolation. This introduces uncertainty in the modelled temperature-frequency stiffness dependence.

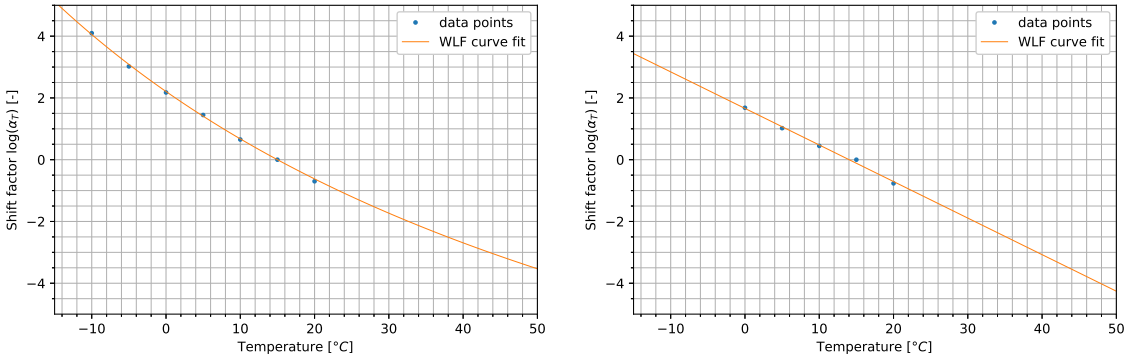

(a) Guss asphalt

(b) ZOAB

Figure 8.4: WLF-Curve for shift factors

8.1.2 Asphalt temperature-strain relation

There is no universal temperature coefficient α_T for asphalt ($\varepsilon = \alpha_T \cdot \Delta T$), as there is for steel. For the Haringvlietbrug no specific temperature coefficients were supplied, so an assumption is made based on table 3.1. This table shows that the Coefficients of Thermal Contraction (CTC) and Expansion (CTE) are similar between 10 and 55°C . This temperature range also covers the observed temperatures of the Haringvlietbrug, so the average of the CTC and CTE between 10 and 55 degrees is taken in equation 8.8. The obtained asphalt temperature coefficient of $27 \cdot 10^{-6}$ differs significantly from the temperature coefficient of steel, which is only $12 \cdot 10^{-6}$. A difference of a factor 2.25.

$$\frac{(2.94 + 3.11 + 2.57 + 2.38 + 2.56 + 2.63) \cdot 10^{-5}}{6} = 27 \cdot 10^{-6} \varepsilon^{\circ} C^{-1} \tag{8.8}$$

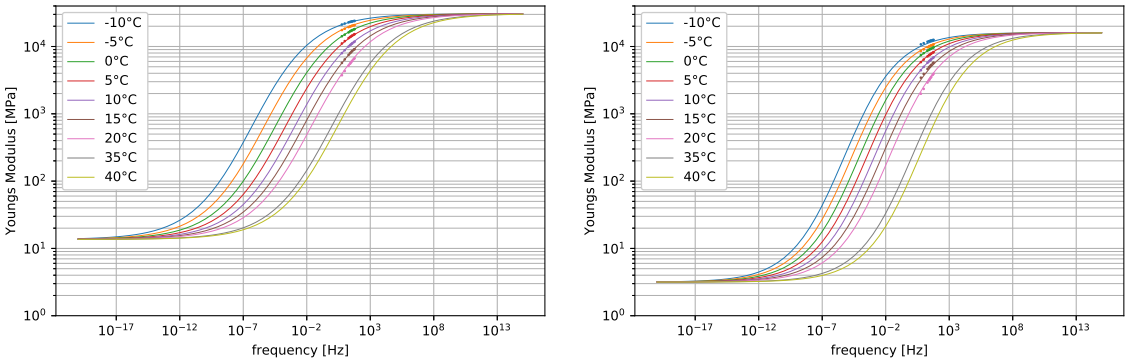

(a) Guss Asphalt (b) ZOAB

Figure 8.5: Master curves for asphalt at multiple temperatures

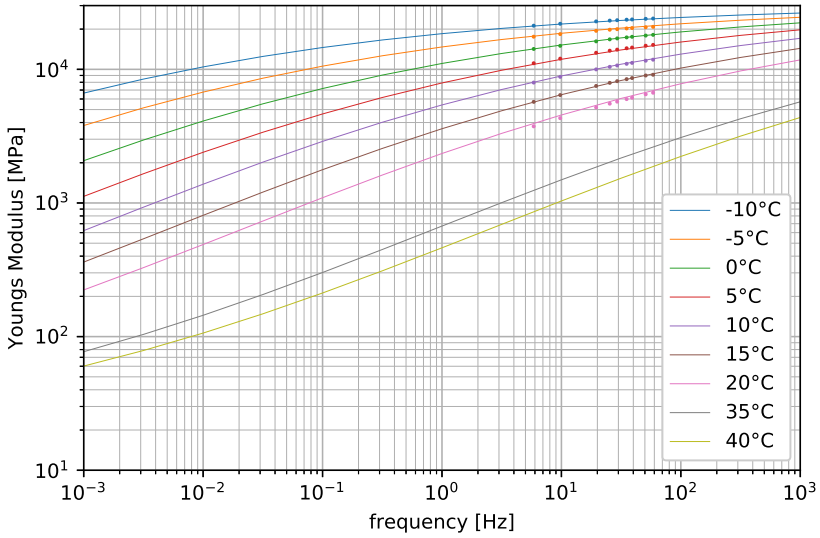

(a) Guss Asphalt

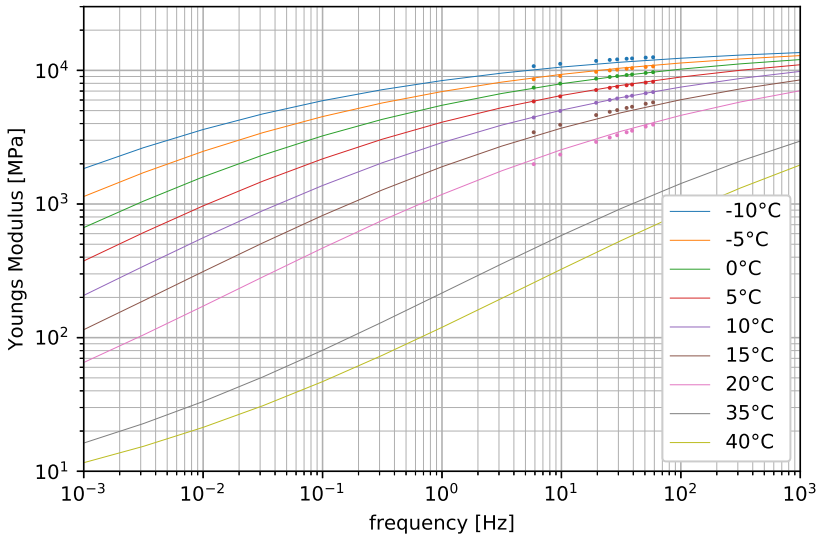

(b) ZOAB

Figure 8.6: Master curves for asphalt at multiple temperatures, close-up

8.2 Influence of asphalt on subsystems

The influence of asphalt on dynamic behaviour of the bridge due to temperature loads is evaluated in order to compare this influence to other environmental effects like differential stresses and strains in the steel structure. This evaluation is performed both for an entire bridge span and for smaller scale subsystems. The following systems are considered:

- Asphalt (2 layers of 30 mm), Deck plate (10 mm).
- Asphalt (2 layers of 30 mm), Deck plate (10 mm), ribs 300 mm c-t-c.
- Entire bridge: Asphalt, Deck plate, ribs, box wall, box bottom.

For each of the subsystems the following parameters are calculated:

- Composite axial stiffness EA, unit weigth ρA, composite bending stiffness EI
- Unrestrained axial elongation due to 1 °C homogeneous temperature rise.
- First eigenfrequency of the subsystem.

Rigid bonds between asphalt and steel is assumed. Slip or shear that might exist due to the flexible membranes is ignored, resulting in upper-bound stiffness results. Recently multiple studies were performed on multilayer asphalt with waterproofing membranes, see [21, 22, 23], showing this might have a significant influence in specific deck sections. Calculated values should only be evaluated relative to each other, not as stand-alone values.
For tables 8.5, 8.6 and 8.7 the parameters are calculated as in equations 8.9 through 8.13. Each line starts with a description of the system, followed by the parameters that were used to obtain asphalt stiffness: the temperatures of ZOAB and Guss Asphalt respectively, and a reference loading frequency. The parameters of the asphalt at these different temperatures and loading frequencies are then obtained from the shifted master curves as explained in section 8.1.1.

$$EA = \int_A E(z)\,\mathrm{d}A \tag{8.9}$$

$$EI = \int_A E(z)z^2\,\mathrm{d}A \tag{8.10}$$

$$\rho A = \int_A \rho(z)\,\mathrm{d}A \tag{8.11}$$

$$\varepsilon = \frac{1}{EA}\int_A E(z)\alpha_T(z)\,\mathrm{d}A \tag{8.12}$$

$$\omega_1 = \sqrt{\frac{\pi^4 \cdot EI}{\rho A l^4}} \cdot \frac{1}{2\pi} \tag{8.13}$$

with: z = vertical distance to neutral axis.

All calculations of the dynamic properties should be read as an approximation of the frequency range in which a change might occur, and the size of the frequency shift that follows from it. The small sub-models are strong simplifications of the full bridge, and defining correct boundary conditions for these sub-models is a daunting task. All models are assumed pinned on one end, with a hinged roller on the other end, based on the assumption that the supporting ribs and/or crossbeams have a low torsional stability in comparison to the bending stiffness of the sub-model under consideration. Effects of axial force due to self weight and/or temperature gradients is ignored.
Effects of damping could be significant, especially due to the viscous nature of asphalt. However the high sensitivity of the Youngs modulus to temperature is considered to have a much larger influence. Given that no accurate information about the exact damping properties is available, the focus here is on Youngs Modulus and the effect of damping is neglected.

8.2.1 Deck plate with asphalt

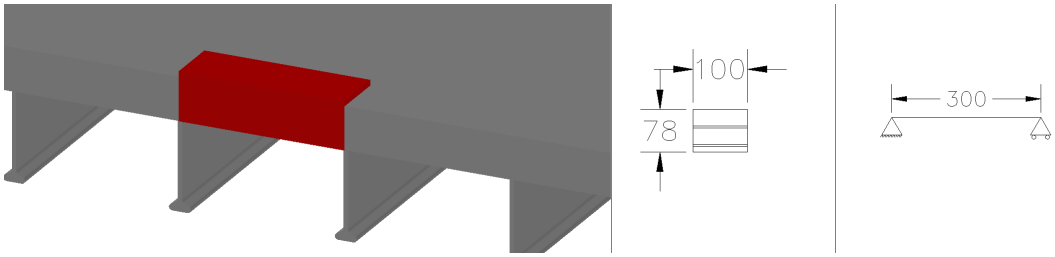

Figure 8.7: Deck section spanning 2 bulbs

Stress and Strain

As can be seen in table 8.5 the asphalt has significant influence on the deck plate subsystem behaviour. The axial stiffness EA changes between $6.3 \cdot 10^8$ and $8.36 \cdot 10^8$ for no asphalt versus cold asphalt at high frequency loading. This is a change of 36%. This axial deck plate stiffness mostly plays a role in loads in the East-West direction of the bridge. Near the crossbeams the deck is part of the upper flange, and here some influence might be found. For low frequency loading such as temperature induced stress, the asphalt already plays a much smaller role. Assuming a significant temperature change could develop in 15 minutes, this could be approximated with a $\frac{1}{15 \cdot 60} = 0.001$ Hz loading frequency. At 0.001Hz even cold asphalt only contributes $\frac{6.34}{6.30} = 0.6\%$ to the axial stiffness.

The influence on bending stiffness is very significant, with almost 2 orders of magnitude between a steel deck plate only versus a cold 15°C asphalt at 1 kHz loading. Even at a loading frequency of 0.001Hz, cold asphalt still almost doubles the bending stiffness of the steel plate only.

The asphalt might also influence static stress and strain due to temperature change. In this subsystem the effect is most pronounced in the W-E direction (for the N-S direction see section 8.2.2, which includes the ribs). The daily temperature cycle is low-frequency, so looking at the ε for 0.001 Hz, even at the 15 °C the asphalt contributes $\frac{1.21}{1.2} - 1 = 0.8\%$ to the unrestrained elongation, which is small. In table 8.5 it is assumed that asphalt and steel have the same temperature. The measurement data show asphalt warms up to over 40°C , while the steel deck plate remains at approximately 30°C (figures 5.7 and 5.8). The effect may thus be larger than 0.8%, but due to the low Youngs Modulus of asphalt at these temperatures and low loading frequencies, the influence will still be small.

Table 8.5: Influence of asphalt on deckplate

	E_{zoab} MPa	E_{guss} MPa	EA N	ρA kg/m	EI Nm^2	Elongation $\varepsilon°C^{-1}$	ω_1 Hz
Deck, Asphalt absent	0	0	6.30e+08	23.5	5.25e+03	1.20e-05	260.59
Deck, Asphalt 15|15°C|0.001Hz	115	361	6.34e+08	62.8	9.44e+03	1.21e-05	213.97
Deck, Asphalt 40|35°C|550Hz	1604	4932	6.89e+08	62.8	5.97e+04	1.33e-05	538.38
Deck, Asphalt 40|35°C|1000Hz	1960	5717	6.99e+08	62.8	6.99e+04	1.35e-05	582.29
Deck, Asphalt 15|15°C|1000Hz	8486	14353	8.36e+08	62.8	2.14e+05	1.57e-05	1019.43

Influence of asphalt on deck plate dynamics

Table 8.5 also shows the first eigenmode of the subsystem at different temperatures, assuming a simple Euler Bernoulli beam on pin and roller supports. At night, when temperatures are approximately 15°C, the first eigenfrequency of the deck plate subsystem with cold asphalt is 1019Hz. On hot days, the asphalt warms up to 40 and 35°C for ZOAB and Guss asphalt respectively, and thus the EI of the composite drops. The first eigenfrequency is recalculated to be 582 Hz. Assuming the eigenfrequency coincides with the loading frequency, this drop from 1019 to 582Hz also changes the asphalt behaviour. If this drop in loading frequency is also taken into account by setting the loading frequency to 550Hz, the first eigenfrequency drops further to 538 Hz. More iterations of this process could be carried out, but this will only result in a false sense of accuracy. There are many other parameters that have a much larger influence, for example: exact asphalt properties, the membrane stiffness, boundary conditions or damping.
The global change in behaviour is potentially significant. Due to the temperature rise at a warm day with asphalt temperatures of up to 40°C, the first eigenfrequency of the subsystem drops with 481 Hz, and is only 52% of the eigenfrequency at 15°C.

8.2.2 Deck plate with rib and asphalt

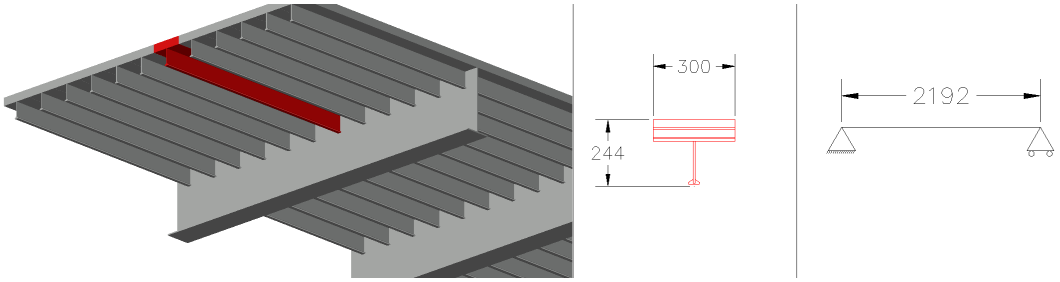

Figure 8.8: Deck section with bulb spanning 2 cross members

Stress and Strain

Table 8.6 shows the influence of asphalt on a rib-deck plate span between 2 cross members. The change in axial stiffness for low frequency loads is small with only $\frac{9.82}{9.78} - 1 = 0.4\%$. The change in axial elongation due to temperature change is also small with $\frac{1.21}{1.20} - 1 = 0.8\%$. This confirms the assumptions that were made during construction of the FE-model: for the global quasi-static behaviour of the bridge due to temperature changes, ignoring the asphalt contribution to the stiffness seems to be a justified simplification.

Influence of asphalt on rib-deck plate dynamics

The previous section (8.2.1) has shown that a stiffness change of asphalt might induce a 48% drop in the eigenfrequency of the deck plate subsystem. Once the bulb is included, the influence of asphalt is significantly smaller, because the steel plate with rib already has a large EI compared to the deck plate only.
At 15°C the subsystem's first eigenfrequency is 73.17Hz. On a warm day this first eigenfrequency drops to 68.63 Hz, a change of -6.2%, which is well within the measurement resolution of a SHM-campaign. This implies that the temperature dependent behaviour of the asphalt is a factor to be considered in vibration based SHM campaigns.

Table 8.6: Influence of asphalt on deckplate including bulb

	E_{zoab} MPa	E_{guss} MPa	EA N	ρA kg/m	EI Nm^2	Elongation $\varepsilon°C^{-1}$	ω_1 Hz
Deck, bulb, Asphalt absent	0	0	9.78e+08	36.5	3.21e+06	1.20e-05	96.94
Deck, bulb, Asphalt 15|15°C|0.001Hz	115	361	9.82e+08	75.8	3.23e+06	1.21e-05	67.51
Deck, bulb, Asphalt 40|35°C|70Hz	739	2777	1.01e+09	75.8	3.34e+06	1.25e-05	68.63
Deck, bulb, Asphalt 15|15°C|70Hz	5651	9596	1.11e+09	75.8	3.80e+06	1.38e-05	73.17

8.2.3 Full bridge with asphalt

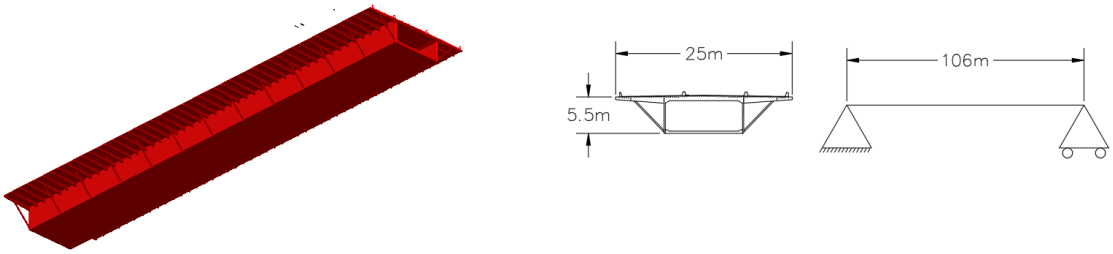

Figure 8.9: One full bridge span

Stress and Strain

On the scale of a full bridge span, the contribution of the asphalt to axial stiffness is small. The same applies to the bending stiffness. Even when asphalt is assumed to be 15°C and loaded at 1.3Hz, it only contributes $\frac{6.8}{6.68} - 1 = 1.8\%$ to the global bending stiffness. For passing traffic this might be noticeable, but for the much lower frequency temperature loading, the stiffness drops and the contribution is less than 0.2%.

Influence of asphalt on full bridge dynamics

The variation in the first eigenfrequency of the 106 m long single span subsystem due to asphalt temperature is 0.01Hz. The influence of other factors (i.e. weight of traffic on bridge) might be much larger, possibly masking the effects of the asphalt property change.

Table 8.7: Influence of asphalt on full bridge

	E_{zoab} MPa	E_{guss} MPa	EA N	ρA kg/m	EI Nm^2	Elongation $\varepsilon°C^{-1}$	ω_1 Hz
Bridge, Asphalt absent	0	0	1.31e+11	4908.1	6.68e+11	1.20e-05	1.63
Bridge, Asphalt 15|15°C|0.001Hz	115	361	1.32e+11	8243.5	6.69e+11	1.20e-05	1.26
Bridge, Asphalt 40|35°C|1.3Hz	134	737	1.32e+11	8243.5	6.69e+11	1.21e-05	1.26
Bridge, Asphalt 15|15°C|1.3Hz	2069	3868	1.36e+11	8243.5	6.80e+11	1.25e-05	1.27

8.3 Asphalt Summary

With regard to the material modelling, a summary of the findings is presented in this chapter is presented:

- The asphalt parameters as obtained from RWS do not fully cover all required temperatures and loading frequencies. Therefore master curves have been constructed in order to study potential effects at higher temperatures and frequencies.
- After shifting the individual test curves, a master curve was obtained. A sigmoid function was fitted with RMS error of 60.9 and 40.3MPa for guss asphalt and ZOAB respectively over the tested frequency-temperature range.
- Using the WLF equations, the master curves were shifted to the required temperatures of 35 and 40°C.
- The calculated asphalt properties are based on dual extrapolation which introduces uncertainty in the models.
- The temperature coefficient of asphalt was found to be $\approx 27 \cdot 10^{-6}\mathrm{K}^{-1}$, which is over twice as large as the temperature coefficient of steel $\approx 12 \cdot 10^{-6}\mathrm{K}^{-1}$.

With regard to the influence of asphalt on discrete subsystems, a summary of the findings is presented in this chapter is presented:

- In the smallest subsystem including only asphalt and deck plate, the influence of asphalt is significant. The first eigenfrequency might vary by 53% compared to its original value, based on observed temperature changes in May and June 2020.
- For the subsystem including asphalt, deck plate and rib, asphalt temperature is a significant factor for the eigenfrequencies. The first eigenfrequency might vary by 6.2 % compared to its original value, based on observed temperature changes in May and June 2020.
- For a single bridge span, the asphalt influences the first eigenfrequency by $\approx 1\%$ compared to its original value. This may seem insignificant, but is still measurable in a SHM-campaign. It could therefore overshadow small damage.

9 Conclusion & Discussion

The Haringvlietbrug was used to study the influence of temperature on natural vibrations of steel bridges. Chapter 4 describes the Haringvlietbrug geometry and measurement campaign, while chapter 5 shows the obtained measurement data. Chapter 6 describes the procedure used to obtain FEM stress and strain, with the influence of temperature induced stress investigated in chapter 7. Finally the temperature dependent material properties of asphalt are studied in chapter 8. Using these chapters, the research questions may be answered.

9.1 Conclusion

The conclusions are presented using the structure of the research questions:

Question 1: What are the temperature distributions that occur in the bridge due to environmental influences?
Measurements have shown that the bridge obtains a complex 2D-temperature distribution over its cross-section. No significant temperature differences were found along the longitudinal axis of the bridge. Struts at different positions along the length of the bridge showed no significant temperature differences between each other. Local temperature differences might exist, e.g. for a rib the temperatures at mid-span and near the supporting cross-beam might differ from each other.
The initial expectation that the bridge would heat up from the top, has proved to be only partially correct. In the morning, the lower East side of the box wall heats up due to the small inclination of the morning sun hitting a vertical surface. For a short period the bottom of the box wall is significantly warmer than the top of the bridge. In the evening the lower part of the West box wall shows the same behaviour.
European design codes only prescribe a vertical temperature gradient, with a linear horizontal temperature gradient if the engineer finds it necessary. The measurements have shown 3 significant horizontal temperature gradients:

- The deck above the box has a different temperature than the cantilevers. Measurements show that the air inside the box has a different temperature than the ambient air, and thus this air might act as a heat buffer and isolator.
- Each driving lane shows a horizontal temperature gradient during the day, caused by barrier induced shade in the morning and evening. The shape of this gradient could not be determined due to insufficient temperature sensors. Using the heat-flow equations a reasonable approximation of this gradient could be obtained however.
- The walls of the box show significant local temperature rise if the solar inclination is small. Due to insufficient sensors the exact determination of the influenced area was impossible.

Question 2: To what extent can these complex 3D temperature distributions be simplified in order to obtain homogeneous or linear-varying component temperatures?

For gradients in the vertical direction:

- Asphalt, deck plate, rib and crossbeam have different temperature distributions, which are strongly influenced by their exposed surfaces in relation to solar radiation and convective heat transfer. A linear interpolation between temperatures at discrete element boundaries seems justified, e.g. top of the asphalt, bottom of the deck plate, bottom of the rib, bottom flange of the crossbeam.
- Non-linear gradients are expected in vertical surfaces connected to surfaces that are exposed to significant solar radiation, e.g. the web of the crossbeam below the deck. Additional control points should be measured. Eurocode prescribes 0, 100, 200 and 300 mm from the deck surface for vertical temperature gradients, and these values could be used for uniform flat surfaces. If the geometry is not uniform, then additional control points should be placed at points where a structural connection, boundary or interface changes the materials thermal properties, the cross-section or the surface area that's exposed to environmental influences such as solar radiation or wind.
- The lower parts of the walls of the box girder show significant temperature deviations during the morning (East side) and evening (West side) on days with significant solar radiation. The prescribed piecewise linear vertical temperature gradient of the Eurocode does not capture this.

For gradients in the horizontal direction:

- The East and West cantilever deck show similar average temperatures relative to each other. The deck above the box deviates from the cantilevers.
- The driving lanes all show a significant temperature difference between their West- and East- edges. The heat-flow model has shown that this is not a linear gradient, but that the temperature distribution is strongly dependent on the position of the shade-line. A linear interpolation between these West and East shoulders of the road does not capture the average temperature and the differential stresses in the deck.
  In order to reduce computational- and modelling- complexity, the FE-model did not include this gradient in any way, assuming a homogeneous temperature instead. If an accurate representation of the stress distribution in the deck is required, then a better method should be developed. Either by manually drawing shade-lines for each time of day, or by automating this process in a heat-flow model.
- Hollow sections that contain trapped air show different temperature behaviour than beam- and plate elements which are exposed to the environment on both sides.
- Non-linear gradients are expected in surfaces connected to surfaces that are exposed to significant solar radiation, e.g. the bottom plate of the box between the box walls. Additional control points should be measured to capture these non-linear gradients. The Eurocode prescribes 0, 100, 200 and 300 mm from the deck surface for vertical temperature gradients, but does not cover non-linear horizontal gradients. Horizontal temperature gradients may have a different distribution, because the convective heat transfer coefficient significantly differs between vertical and horizontal surfaces. The current measurement set-up did not provide enough data to study this influence, and thus the values of 0, 100, 200 and 300 mm from the exposed surface are used as a starting point for horizontal surfaces as well. However, an additional control point at 600 mm is advised. With this set-up, the first points (0, 100, 200, 300 mm) are close enough to make sure temperature uncertainty only covers a small amount of material, while the extra point at 600 mm can be used to verify that the full non-linear part of the gradient is captured and the rest of the material has a linear temperature distribution. If the geometry is not uniform, then additional control points should be placed at points where a structural connection, boundary or interface changes the materials thermal properties, the cross-section or the surface area that's exposed to environmental influences such as solar radiation or wind.

Question 3: Which altered strain distributions in structural components occur due to environmental changes?
The FE-model has shown that the average homogeneous temperature of the bridge is dominant in the daily strain variation. Due to the static indeterminate nature of the bridge, there are no significant global curvatures due to temperature gradients.
The ribs show local temperature induced curvature due to the geometry of the bridge, where only one in four cantilever crossbeams is supported by a strut. The cantilever crossbeams that are not supported by a strut are free to curve downwards if the deck plate, which is also the upper flange, is warmer than the bottom flange. This creates height differences between adjacent crossbeams, inducing curvature in the ribs.

Question 4: How do these altered strain distributions influence the dynamic characteristics of the structural components of interest?
The influence of strain distributions on dynamic characteristics was not evaluated. In general, stress-free elongation results in lower eigenfrequencies. Daily strain variations due to temperature change were found to be in the order of 100 $\mu\varepsilon$. For a beam $\omega^2 = \frac{\pi^2 EI}{\rho A L^4}$, indicating a $+100\mu\varepsilon$ strain results in a frequency change of $\frac{1}{1.0001^2} - 1 = 0.02\%$. Compared to other effects studied, this is considered insignificant.

Question 5: Which altered stress distributions in structural components occur due to environmental changes?
The bridge is free to elongate and thus the average bridge temperature has no significant influence on global stress. Asphalt has a different temperature expansion coefficient than steel, which could induce internal stress on a smaller scale. The largest temperature variations are on a hot day, with the asphalt obtaining temperatures of over 40°C. At these temperatures and with temperature changes occurring gradually, resembling a low-frequency loading, the asphalt stiffness is very low. Therefore the local stress induced due to differences between temperature coefficients is also low.
Due to sun, shade and trapped air inside the box-girder significant temperature gradients occur over the bridge cross-section. These temperature gradients have significant influence on the stress distribution. Warm components obtain axial compression stress, while cool components obtain tension stress.
The lower parts of the box wall heat up significantly if the solar inclination is low and the solar intensity is high. This induces stress in the entire cross-section of the bridge, including the deck.
The bridge geometry with 1 strut every four frames complicates the analysis of the stress distribution. Unsupported cantilever crossbeams are free to deform due to vertical temperature gradients, while the supported ones are restrained by the struts. This induces curvature in the deck and the ribs, resulting in additional stress distributions.

Question 6: How do these altered stress distributions influence the dynamic characteristics of the structural components of interest?
Sub-models of the bridge were evaluated both analytically and numerically using FEM. Stress variations over the warm period from May 30 to June 2 2020 were applied to the sub-models and their effect on eigenfrequencies is calculated. The eigenfrequency contains significant uncertainty due to simplifications in the model and, especially, the boundary conditions. However, given that each sub-model is loaded well below the buckling load, the relative influence of stress on eigenfrequency can be assumed to be linear. This implies uncertainty about the exact eigenfrequency, but it induces only limited uncertainty in the relative change of this eigenfrequency.
Compression forces between 50 and 150 kN in the rib-deck composite beam influenced the fundamental eigenfrequency of this subsystem by ≈ 0.55 Hz or 0.8%.
Local segments of deck plate between ribs and crossbeams have significant stress in the longitudinal direction of the bridge, but this stress has no significant influence on the first eigenfrequency of the subsystem. The transverse stress, of which both the mean and daily variation are much smaller, is the dominating influence for the deck-plate vibrations. The fundamental eigenfrequency of the subsystem was shown to vary between ≈ 995 and ≈ 1008 Hz, a shift of ≈ 13 Hz or 1.3%.

Lateral vibrations of the rib were evaluated using an FE-model, and show a daily variation of 0.4 Hz for the warm period. An influence of 0.2%.

Question 7: Which material properties change due to temperature distributions?
Asphalt Youngs Modulus has shown to be strongly influenced by temperature change. Based on the available data, master curves were created and extrapolated to the temperatures and frequencies of interest. At low frequency loading of 1.3 Hz the Youngs Modules of ZOAB varied between 2069 MPa at 15°C, and 134MPa at 40°C. For guss asphalt the Youngs modulus varied between 3868 MPa at 15°C and 737 MPa at 35°C. The ZOAB difference is over 1500%. The values are based on dual extrapolation and contain significant uncertainty.
The Youngs Modulus of asphalt was shown to have significant influence on the dynamic characteristics of the bridge, especially when focussing on local subsystems that include asphalt material. No other parameters were evaluated, as the change of asphalt Youngs modulus appears to be the dominating factor.
The condition and typical properties of asphalt vary per bridge. The uncertainty about the exact Asphalt parameters progresses through the model into the results. If an analysis requires these parameters, then an asphalt sample should be obtained and tested in a lab, in order to obtain the master curves.

Question 8: How do these changing properties influence the dynamic characteristics of the structural components of interest?
For local vibrations where the asphalt contributes significantly to the stiffness, the influence was significant. Three simplified subsystems were evaluated using asphalt properties based on temperature measurements and extensive extrapolation of asphalt master curves. Verification based on measurements is required.

- In the warm period shown, the fundamental eigenfrequency of the deck plate subsystem could vary by 53% due to asphalt stiffness change.
- For the rib-deck composite beam, the asphalt contribution to bending stiffness is smaller than for the deck plate only. Due to asphalt stiffness change, the first eigenfrequency shows a 6.2% change of it's original value over the warm period shown.
- The first eigenmode of the 106 meter bridge span is also influenced by asphalt stiffness, the first eigenfrequency varies by $\approx 1\%$ due to asphalt temperature variations observed in the warm period.

Question 9: What is the relation between the expected dynamic properties of the system and the measured temperature data?
For local modes of the deck plate, the asphalt temperature is the dominating parameter in dynamic characteristics variance, allowing for frequency shifts of over 53%. The asphalt stiffness is strongly influenced by temperature, lowering the stiffness of the asphalt deck plate composite. Lower stiffness leads to lower eigenfrequencies: $\omega = \sqrt{\frac{k}{m}}$.
Homogeneous temperature change does not have significant influence on internal stress distribution in the bridge cross-section. Therefore no stress-induced influence on the dynamic characteristics was found due to homogeneous temperature change.
The temperature gradients were shown to induce significant internal stress distributions. The observed locations were loaded well below buckling frequency and therefore the influence of temperature induced stress on the fundamental eigenfrequency of the subsystem was small with only 1.3% for the asphalt deck plate composite.

Question 10: Which temperature sensor layout is required in order to predict this change of dynamic characteristics?
For local deck vibrations, asphalt temperature has shown to be the dominant factor in frequency change. The Haringvlietbrug geometry induced significant temperature differences in the asphalt layer due to the barriers inducing shade, and the box girder isolating parts of the deck from below. In order to accurately cover the temperature effects for this subsystem, one would need to place enough sensors to accurately predict asphalt temperature of the region of interest, including asphalt that contributes to boundary conditions of the subsystem under consideration.
Depending on the support scheme and geometry of the bridge, vertical- and horizontal temperature gradients may or may not induce significant internal stress. The static indeterminate global system of the Haringvlietbrug results in significant stress due to vertical and horizontal temperature gradients. Expected temperature gradients that may induce stress in the structural components of interest should be captured. Depending on bridge geometry the amount of sensors required for this may differ. Temperatures of asphalt, deck plate, bottom rib, crossbeam flange and bottom of the box should be measured at a minimum in order to account for the temperature dependent asphalt properties, and the non-linear vertical gradient as prescribed by the Eurocode.
Direct sunlight has a significant influence on local temperature rise. Before designing a temperature sensor network, the size and position of areas that are hit by direct sunlight should be estimated, including the variation of these positions over the day and the seasons. The influence of seemingly insignificant elements such as 60 cm high steel barriers should not be underestimated. The sensor network should be able to capture local temperature gradients due to sun- and shade.
Sections that contain air isolated from the environment (e.g. hollow sections, box girder) show different temperature distributions than I-beam and plate elements which are exposed to the environment on both sides. All walls, including top and bottom, of these sections should be measured separately.
It is advised to have multiple sensors per typical location, in order to verify assumptions of identical temperatures at similar positions. Assumed linear gradients with significant height ($>$0.1 m) should be captured with multiple sensors, to verify the linearity.

9.2 Discussion

Temperature gradients

The temperature sensor layout was determined based on temperature gradients expected from literature and engineering judgement. No full 3D-heat-flow model of the bridge was created prior to the design of the measurements set-up. There is a risk that the sensor layout imposes a bias on the modelled gradient shape and direction: If no gradient is expected, then no sensor is placed to measure it, implying unexpected gradients could be missed. This induces uncertainty about the actual temperature distribution. The measurements have actually shown gradients that were not expected, due to added redundancy in the sensor layout. Positions that were assumed to have equal temperatures have shown differences, inviting further research into possible gradients.
In the transverse direction uncertainty remains about the temperature distribution due to the barrier induced shade. Based on the initial measurements, additional sensors along the W-E axis of the the deck plate were preferred. A single sensor below the cantilever deck plate was added later to overcome part of this uncertainty. The added sensor illustrated the temperature gradient between West- and East side of a driving lane was not linear, although for this period no direct comparison to strain measurements could be made, and the sensor only covered a cooler period.
The buffer- and insulation effect due to air inside the box was underestimated during sensor-layout design. Initial assumptions of equal bulb temperature inside and outside the box were therefore invalid. Again one sensor was added later, with the same comments as above.
The significance of the effect of sunrise and sunset on the temperature of the lower parts of the box wall was unknown at the time of the sensor layout design. Based on the measurements a more dense layout would have been preferred on both the bottom plate of the box girder, the box wall and the strut.
The purpose of the presented research is to determine if and how temperature influences the natural vibrations of steel bridges. The exact determination of the occurring temperature gradients is not necessary to achieve this purpose. Despite the stated uncertainties, the conclusions about the influence of shade, and the dominance of non-linear asphalt properties still hold.

Asphalt parameters

Asphalt parameters were provided for a limited time and frequency range. This required extensive material modelling and extrapolation, introducing uncertainty. Even with this asphalt parameter uncertainty, the expectation is that asphalt is still the most dominant factor for local deck plate vibration frequency. With the current parameter set, asphalt influence was $\approx 6\%$ for the rib-deck plate subsystem, while temperature induced stresses for a similar sub-model induced a 0.7% frequency change. The difference is a factor 8.5, implying that even with significant uncertainty about the exact temperature dependent asphalt stiffness, it is still the dominant parameter for local deck-plate vibrations.

Temperature compensation

Both strain sensor types, analogue and fibre-optic, were temperature compensated by the supplier. The purpose for the sensors was to measure high frequency strain variations due to traffic loading. Initial analysis is usually carried out on independent 1 or 10 minute blocks, where each block is normalized to obtain zero mean stress. Temperature change in those short intervals is relatively small, so deviations in the temperature compensation remain unnoticed. For the purpose of this thesis, being longer period temperature effect modelling, these limitations have proven critical. Where the performed measurements turned out to be of sufficient quality for analysis of traffic passage effects, for an evaluation of long term temperature induced strains and stresses this does not hold. It is very clear that the requirements to the sensor set-up are directly dependent on the analysis objectives. For vibration based SHM it is concluded that strict high end requirements to the sensor set-up apply, which were not met at the Haringvlietbrug. Due to timing of the measurement campaign no additional measurements could be requested to obtain better temperature measurements and sensor compensation.
The Strain sensor measurements of the Haringvlietbrug are used to validate the FE-model, and have shown to be fit for this purpose. No model updating was carried out using the strain mea-

surements. The uncertainty in the measurements due to poor STC therefore does not progress into the FE-Model, and does not harm the conclusions drawn from this FE-Model.

Strain validation

The FE-model was validated against the LVDT measurements of the support displacement, which confirmed the validity of the FE-model. This was in a cooler period, with limited sensor availability, and smaller daily temperature variations. The FE-model was further validated with manual calculations of deflection due to gravity loading, and those results also matched.
The FE-model was further validated against the FBG strain measurements, and showed deviations of approximately 30 to 50%, depending on the sensor position. The West bottom box wall showed the largest deviation, no cause has been found.
While the match is not perfect, the global pattern matches and does not harm the conclusions.

Stress validation

The FE-model was further validated against the discrete strain gages measuring stress-induced strain. By multiplying stress-induced strain with the Youngs modulus, stresses were obtained. In general the measurements confirm the validity of the FE-model, with some specific exceptions, as stated below.
The FE-Model overestimated the effect of local temperature gradients in the lower parts of the box walls. The assumption of linear temperature gradients in load cases 21 and 22, containing the lower box walls and using 1 temperature sensor each, introduces significant uncertainty. It is expected that the gradients are not linear, but no sensors were available to verify this.
The effect of rain is not fully captured. Added mass of water is not included in the model, and the sudden introduction of cold liquid on the deck might induce temperature gradients that are not captured by the sensor layout. The influence of rain is not in the scope of thesis, but does invite further research.

Eigenfrequency calculation

Temperature effects on eigenfrequencies were studied based on simplified sub-models. The evaluations have focussed on sub-models representing isolated parts of the overall bridge structure.
For sub-models from chapter 8 that focus on asphalt stiffness change, the angular velocity of the first mode is calculated with the following formula:

$$\omega_1 = \sqrt{\frac{\pi^4 \cdot EI}{\rho A l^4}} \tag{9.1}$$

It is possible to factor out the term relating to EI:

$$\omega_1 = \sqrt{\frac{\pi^4}{\rho A l^4}} \cdot \sqrt{EI} \tag{9.2}$$

This implies that a change of EI will result in the same fractional difference for systems of all lengths and thus also for various undamped linear boundary conditions. In these sub-models the exact frequency contains uncertainty, but the magnitude of the change due to change in EI is well determined using the simplified models with boundary conditions as specified above. Note here that a model assessment based on vibration measurements was not carried out, but could be performed to evaluate the absolute values of the frequencies obtained from simplified models.

This does not fully apply for the sub-models including both initial- and temperature induced stress:

$$\omega = \sqrt{\frac{\pi^2}{\rho A l^2}} \sqrt{\frac{\pi^2 EI}{l^2} - F} \tag{9.3}$$

In this formula it is not possible to factor out the Force. If stiffer boundaries result in higher buckling load, then the influence of the Force reduces. The calculated frequency changes might

therefore be an overestimate of the actual frequency change. This does not harm the conclusion that temperature dependent asphalt properties are the dominant parameter for local deck plate vibrations.

9.3 Recommendations

The Haringvlietbrug was studied by using measurement data in combination with analytical and numerical methods. The knowledge gained is directly applicable in future vibration based Structural Health Monitoring (SHM) campaigns. Recommendations for these SHM-campaigns are given in section 9.3.1.
Some of the observations based on the measurements remain unexplained and require further research based on a dedicated measurement set-up. Recommendations for future research are given in section 9.3.2.

9.3.1 Recommendations for application in SHM applications.

- From just after sunrise until just before sunrise the next morning, no steady-state temperature distributions were found for the Haringvlietbrug. This implies dynamic characteristics vary continuously during this period.
- Just before sunrise the bridge temperature approaches a steady state and obtains an almost homogeneous temperature distribution. This implies no significant variations due temperature induced stress occurs, which makes this period crucial for vibration based SHM. If this short period contains enough observations with adequate excitation, then the complexity of the temperature gradients is reduced, relaxing the requirements on the measurement set-up stated below. If measurement data of other periods is required, then this short period can be used as a reference point to calibrate the equipment and the model.
- Rain was found to have a significant influence on internal temperature, strain and stress distributions. This influence was not accurately captured by the FE-Model. It is advised to exclude measurement data that contains rain, including a period afterwards where it's expected that voids in the asphalt are still saturated with water.
- Influence of temperature dependent asphalt material properties requires absolute temperatures. Influence of temperature induced stress, however, is based on relative temperatures. A single element temperature is useless in predicting temperature induced stress, only when temperature differences across the entire cross-section are taken into account, an accurate prediction of temperature induced stress is possible.
- Temperature dependent asphalt properties are a determining factor in the frequencies of free vibrations of the deck plate. If an analytical prediction of the dynamic characteristics is required, then the temperature- and frequency dependent stiffness of asphalt samples, taken from the bridge, should be obtained in a laboratory.
- Asphalt temperature is a determining factor in the frequency of free vibrations of the deck plate. It's advised to use multiple temperature sensors to capture the temperature distribution in the asphalt, taking into account local effects such as shade.
- Investigate which areas of the bridge are exposed to direct solar radiation, including when and where shade might occur. Incorporate this knowledge in the design of a temperature sensor layout. For further advice on sensor layout requirements see also the answer to research question 10 in chapter 9.
- Before using and/or specifying strain sensor measurements, thoroughly investigate the sensor temperature compensation required, and implement methods to verify the accuracy of the measurements after compensation. Analysis of temperature induced stress sets stricter requirements on the sensor temperature compensation procedure than commonly requested for strain based vibration analysis. These requirements are easily underestimated. Require raw data, instead of being dependent on black-box compensation implemented by a supplier.
- Start a thorough validation of the measurement data before the installation is decommissioned. Continuously monitor the measurement data, swiftly investigate deviations and adjust the set-up accordingly.

9.3.2 Recommendations for future research.

- Uncertainty about the stiffness of multilayer steel-asphalt-membrane composites, at different temperatures and loading frequencies remains. Further studies investigating the bending stiffness of these composites, including the waterproofing membranes, at different temperatures could provide useful insights in the dynamic characteristics of the asphalt deck-plate composite at different temperatures.
- Asphalt stiffness is usually tested under single frequency excitation at different temperatures and frequencies, and the master curves are based on these tests. Further testing of asphalt under multi-frequency excitation could be carried out to validate the applicability of these master curves for the dynamic stiffness of asphalt under operational multi-frequency excitation.
- The piecewise linearity of the temperature gradients has not been positively confirmed. Further research on these temperature gradients, either numerically or using measurement data, could provide insights in the most optimal sensor positions, and possible non-linear interpolation functions.
- Investigate the usability of thermal imaging cameras, in order to obtain temperature measurements of the bridge with a high spatial resolution.
- The FE-model of the Haringvlietbrug did not account for temperature jumps at the boundary between sun and shade. Research on the influence of local temperature jumps in large plate elements, including possible second order effects, could improve the understanding of these local influences.
- The calculated change in dynamic characteristics has not been validated using acceleration measurements. It is advised to carry out such a validation, in order to validate the thesis conclusions.
- Research the influence of rain on the natural vibrations of steel bridge. Incorporating effects such as added mass, change of temperature and influence of asphalt saturation.

10 Terms and definitions

CTC	Coefficient of Thermal Contraction.
CTE	Coefficient of Thermal Expansion.
Dynamic characteristics	The set of Eigenvectors, Eigenfrequencies and damping for all eigenmodes of a system at a given time under a given temperature distribution
DSG	Discrete Strain Gage.
Environmental influences	Changes due to day/night, Sun/Shade, Wind & Ambient temperature.
FE-Model	A computer model of a structure, making use of FEM.
FEM	Finite Element Method.
FBG	Fibre Bragg Grating. A fibre-optic sensor that can be used to measure strain and/or temperature. It measures at a discrete position, where a small grating has been etched in the fibre.
KNMI	The Royal Netherlands Meteorological Institute. [1]
LC	Load Case. A set of imposed loads, be it temperature, force or displacement, that is applied to the FE-Model.
LVDT	Linear Variable Differential Transformer. A linear displacement sensor.
ODE	Ordinary Differential equation.
RFEM	A computer program for FEM modelling and analysis made by Dlubal. `www.dlubal.com`
RWS	RijksWaterStaat is the executive agency of the Dutch ministry of Infrastructure and Water Management.[2]
STC	Sensor Temperature Compensation. The actions that are taken to reduce temperature induced sensor deviations.
SHM	Structural Health Monitoring.
TTSP	Time Temperature Superposition Principle.
UDL	Uniformly Distributed Load.
WLF-equation	Williams-Landel-Ferry-equation. An equation to extrapolate shift factors for asphalt master curves.
ZOAB	Zeer Open Asfalt Beton. A typical Dutch asphalt mixture which is very porous.

[1] Description taken from https://www.knmi.nl/over-het-knmi/about
[2] Description taken from www.rijkswaterstaat.nl/english/about-us

Bibliography

[1] Nen. *Eurocode 1: Belastingen op constructies - Deel 1-5: Algemene belastingen - Thermische belasting.*

[2] Nen. *Nationale bijlage bij NEN-EN 1991-1-5+C1: Eurocode 1: Belastingen op constructies - Deel 1-5: Algemene belastingen - Thermische belasting.*

[3] J. Římal and D. Šindler. "Comparison of Temperature Loadings of Bridge Girders". In: *Acta Polytechnica* 48.5 (5 Jan. 5, 2008). ISSN: 1805-2363. DOI: 10.14311/1049. URL: https://ojs.cvut.cz/ojs/index.php/ap/article/view/1049 (visited on 04/08/2020).

[4] You-liang Ding and Gao-xin Wang. "Estimating Extreme Temperature Differences in Steel Box Girder Using Long-Term Measurement Data". In: *Journal of Central South University* 20.9 (Sept. 2013), pp. 2537–2545. ISSN: 2095-2899, 2227-5223. DOI: 10.1007/s11771-013-1766-6. URL: http://link.springer.com/10.1007/s11771-013-1766-6 (visited on 04/08/2020).

[5] Q.-X. Zhu et al. "Investigation of Temperature Effects on Steel-Truss Bridge Based on Long-Term Monitoring Data: Case Study". In: *Journal of Bridge Engineering* 25.9 (2020). DOI: 10.1061/(ASCE)BE.1943-5592.0001593.

[6] Thaksin Thepchatri, C Phillip Johnson, and Hudson Matlock. "Prediction of Temperature and Stresses in Highway Bridges by a Numerical Procedure Using Daily Weather Reports". In: (), p. 165.

[7] Atalay Yargicoglu and C Phillip Johnson. *Temperature Induced Stresses in Highway Bridges by Finite Element Analysis and Field Tests*, p. 196.

[8] M. Tong et al. "Numerical Modelling for Temperature Distribution in Steel Bridges". In: *Computers & Structures* 79.6 (Feb. 2001), pp. 583–593. ISSN: 00457949. DOI: 10.1016/S0045-7949(00)00161-9. URL: https://linkinghub.elsevier.com/retrieve/pii/S0045794900001619 (visited on 04/06/2020).

[9] Md Rashadul Islam and Rafiqul A. Tarefder. "Coefficients of Thermal Contraction and Expansion of Asphalt Concrete in the Laboratory". In: *Journal of Materials in Civil Engineering* 27.11 (Nov. 2015), p. 04015020. ISSN: 0899-1561, 1943-5533. DOI: 10.1061/(ASCE)MT.1943-5533.0001277. URL: http://ascelibrary.org/doi/10.1061/%28ASCE%29MT.1943-5533.0001277 (visited on 10/20/2020).

[10] S Erkens. "Asphalt Concrete Response -Determination, Modelling and Prediction". Delft: TU Delft, 2002.

[11] H. Zhang et al. "Comparison of Different Micromechanical Models for Predicting the Effective Properties of Open Graded Mixes". In: *Transportation Research Record* 2672.28 (2018). ISSN: 0361-1981. DOI: 10.1177/0361198118794713. URL: https://repository.tudelft.nl/islandora/object/uuid%3A8e2f1040-1317-42e3-9f11-94869dddcd9d (visited on 04/22/2020).

[12] Guanghai Zhang, Yuanxun Zheng, and Haigui Kang. "Effect of Loading Condition and Temperature on Dynamic Properties of Asphalt Mixtures". In: *Journal of Wuhan University of Technology-Mater. Sci. Ed.* 28.2 (Apr. 2013), pp. 309–313. ISSN: 1000-2413, 1993-0437. DOI: 10.1007/s11595-013-0684-7. URL: http://link.springer.com/10.1007/s11595-013-0684-7 (visited on 04/22/2020).

[13] Herbert Leaderman. "Elastic and Creep Properties of Filamentous Materials". Thesis. Massachusetts Institute of Technology, 1941. URL: https://dspace.mit.edu/handle/1721.1/45989 (visited on 10/20/2020).

[14] K. Anupam. "CIE4353 Lecture on Visco-Elasticity".

[15] Timoshenko and Gere. *Theory of Elastic Stability*. International student edition, second edition. McGraw-Hill, 1985. 2580 pp.

[16] S.P. Timoshenko. *Vibration Problems in Engineering*. 2th ed. New York: D. Van Nostrand Company, Inc., 1937.

[17] S. F. Bassily and S. M. Dickinson. "Buckling and Lateral Vibration of Rectangular Plates Subject to Inplane Loads-a Ritz Approach". In: *Journal of Sound and Vibration* 24.2 (Sept. 22, 1972), pp. 219–239. ISSN: 0022-460X. DOI: 10.1016/0022-460X(72)90951-0. URL: http://www.sciencedirect.com/science/article/pii/0022460X72909510 (visited on 04/15/2020).

[18] S. F. Bassily and S. M. Dickinson. "Corrigendum: Buckling and Lateral Vibration of Rectangular Plates Subject to Inplane Loads—A Ritz Approach: (S. F. Bassily and S. M. Dickinson 1972 Journal of Sound and Vibration24, 219–239)". In: *Journal of Sound and Vibration* 29.4 (Aug. 22, 1973), pp. 505–508. ISSN: 0022-460X. DOI: 10.1016/S0022-460X(73)80066-5. URL: http://www.sciencedirect.com/science/article/pii/S0022460X73800665 (visited on 04/15/2020).

[19] Marie-Louise Greijmans. "Vibration-Based Damage Detection of the Haringvlietbrug". TU Delft, 2020.

[20] Esraa Alrashydah and Saad Abo-Qudais. "Hot Mix Asphalt Time-Temperature Shifting and Fitting Techniques: A Comparative Study". In: *Construction and Building Materials* 146 (Aug. 1, 2017), pp. 514–523. DOI: 10.1016/j.conbuildmat.2017.03.213.

[21] G. Tzimiris. "Experimental Investigation of Membrane Materials Used in Multilayer Surfacing Systems for Orthotropic Steel Deck Bridges". In: (2017). DOI: 10.4233/uuid:503a9595-508b-4901-86ab-c6ce7429fb67. URL: https://repository.tudelft.nl/islandora/object/uuid%3A503a9595-508b-4901-86ab-c6ce7429fb67 (visited on 04/22/2020).

[22] J. Li et al. "Finite Element of Multilayer Surfacing Systems on Orthotropic Steel Bridges". In: *2013 International Highway Technology Summit IHTS, (also called: 6th China Highway Technology Summit), Beijing, China, April 16-18, 2013* (2013). URL: https://repository.tudelft.nl/islandora/object/uuid%3A5d9468d2-a745-426c-9db9-58cee8ae4f2e (visited on 02/18/2020).

[23] X. Liu et al. "Modelling of Five-Point Bending Beam Test for Asphalt Surfacing System on Orthotropic Steel Deck Bridges". In: *The International Journal of Pavement Engineering* (2019). ISSN: 1029-8436. DOI: 10.1080/10298436.2019.1697440. URL: https://repository.tudelft.nl/islandora/object/uuid%3Ae01344c1-79f5-4a10-9398-ae143bfda089 (visited on 04/22/2020).

[24] Byong Chol Bai et al. *Thermal Properties of Asphalt Mixtures Modified with Conductive Fillers*. July 2, 2015. DOI: 10.1155/2015/926809. URL: https://www.hindawi.com/journals/jnm/2015/926809/ (visited on 09/21/2020).

[25] *Www.Sunearthtools.Com*. URL: https://www.sunearthtools.com/dp/tools/pos_sun.php?lang=en.

A FEM Model of the Bridge

To analyse the measurements, a FE-Model of the Haringvlietbrug was created. In order to be able to fully simulate the temperature induced stress & strain, the following requirements were set:

1. Global behaviour of the 9 span continuous structure should be captured.
2. The model should be detailed enough to be able to input temperatures and temperature gradients for specific elements.
3. The model should allow for temperature load cases that can be based on discrete temperature measurements.
4. It must be possible to obtain simulated stress and strain at the position of the discrete strain sensors.

To reduce computational complexity the following simplifications were made:

5. There will be no heat-flow analysis.
6. The asphalt on the deck is not modelled in the large model. The deck is a steel plate only. Due to the low Youngs modulus of asphalt compared to steel, and the low influence compared to the full box beam, this is deemed an acceptable simplification. See section 8.2 for further justification of this choice.

A.1 Size of model

The Haringvlietbrug has 10 spans, all strain sensors are installed in the second to last span. At first a FE-Model was constructed that contained half of this span, applying symmetry conditions on both ends. After a few tests this model was deemed unfit, because it did not accurately capture the global behaviour of the bridge. For the half-span-model a vertical temperature gradient did not induce curvature, while a 10-span beam did. To correct this, a few simplified beam models were studied. A beam with arbitrary cross section was loaded with a vertical temperature gradient in the following configurations:

- A half span. Left end fully clamped, right end rotations prevented.
- A set of 3 spans. Left end fully clamped. Other supports hinged rollers.
- The whole 10 spans.

These model size variants with their respective boundary conditions are shown in figure A.1

The results, shown in figure A.2, imply that a 3 span model captures the global behaviour correctly, while the half-span model does not. Therefore 3 spans of the Haringvlietbrug will be modelled.

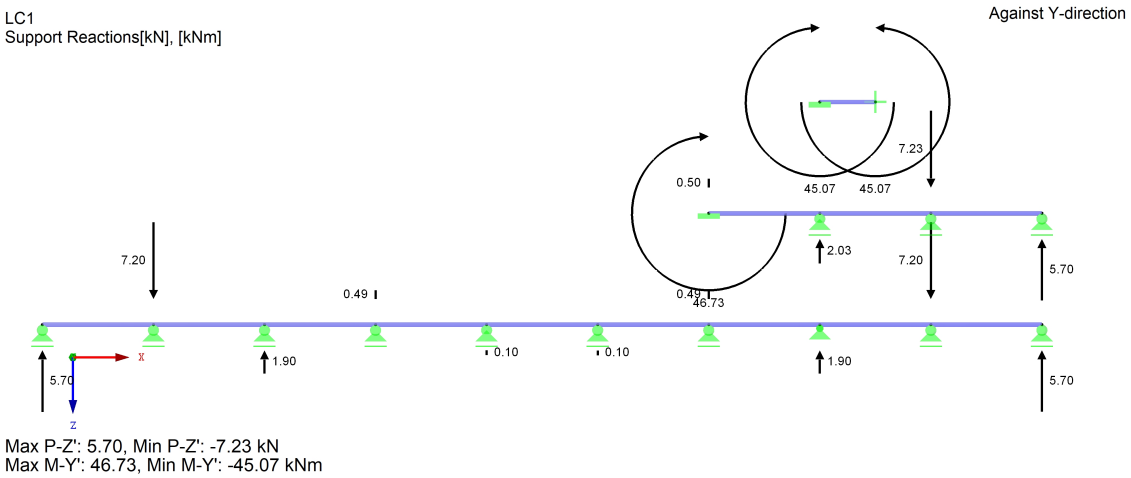

Figure A.1: model variants with boundaries & support reactions.

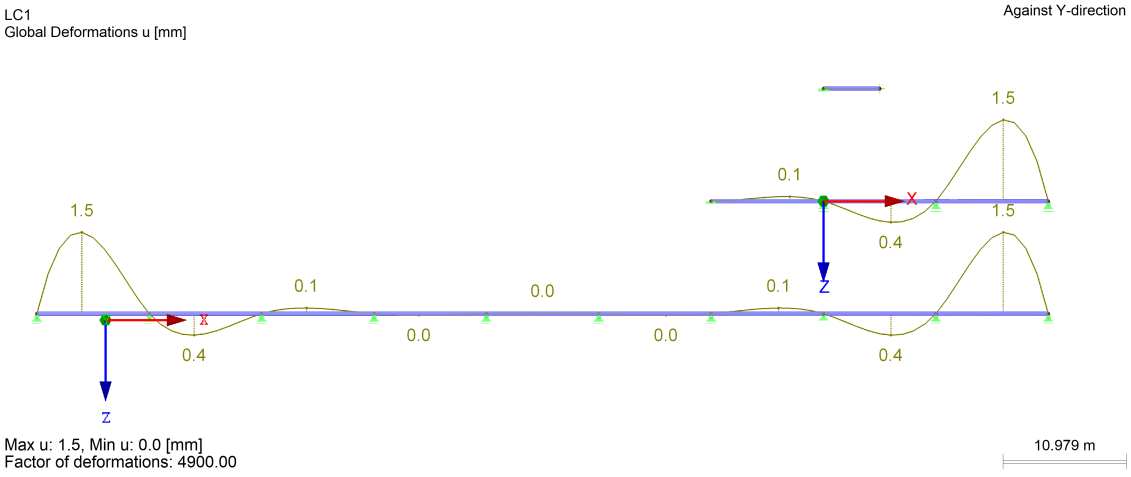

(a) Deflection

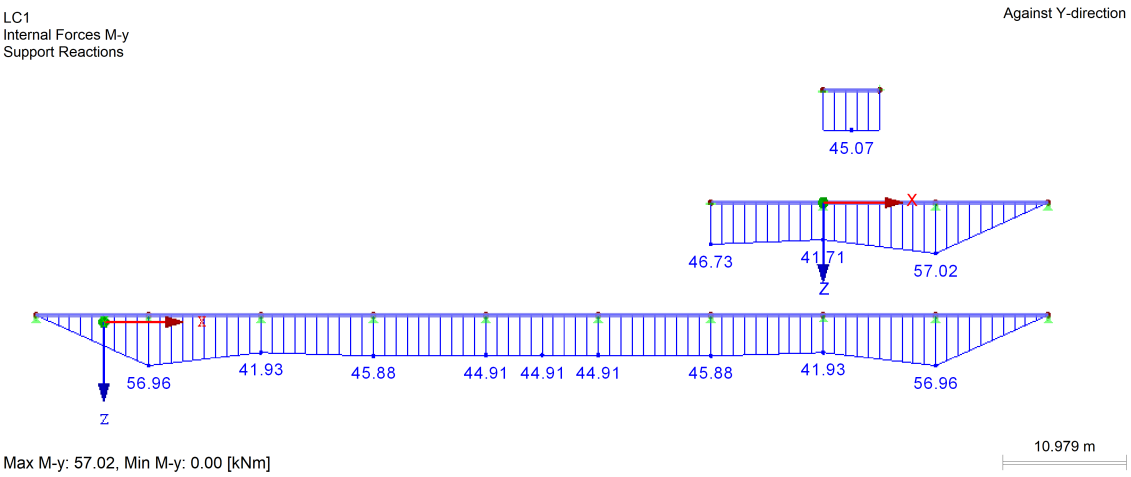

(b) Bending Moment

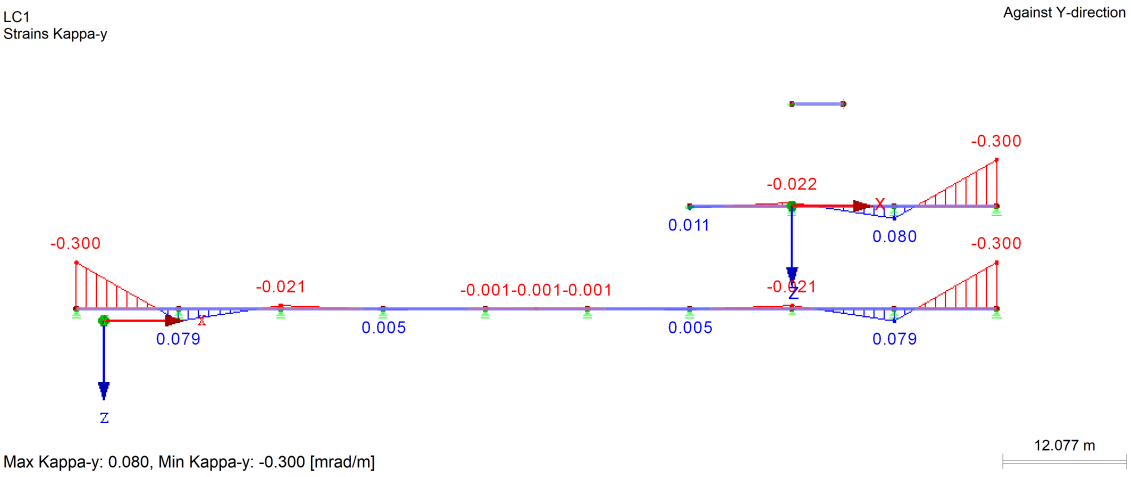

(c) Curvature

Figure A.2: Comparison of results for 3 simplified beam models. Each subfigure shows, from top to bottom: half span with symmetry conditions, 3 span model with 1 symmetry condition, full 9 span model. All beams are loaded with a temperature gradient where the top is hotter than the bottom.

A.2 Geometry and cross section

The cross-section of the bridge is modelled according to the supplied drawings, especially the ones shown in figure 4.3. This cross section including struts is modelled including a section of deck 2167 mm long. After applying all loads, an array copy is used to create the whole 3 spans. After which supports are added, and superfluous struts are deleted.
The bulb profiles underneath the deck are modelled as a plate $t = 8, h = 147$ mm for the web, and a beam 40×12 mm for the bulb. Flanges of the cross members are modelled as beams 350×12 mm, while the web is made of plate elements. The bottom plate includes bulb profiles as well, but because this area is of less interest, the bottom plate with ribs is reduced to a slightly thicker isotropic plate without ribs. The defining parameter for this new thickness is the axial stiffness along the longitudinal bridge axis.

$$\begin{aligned} t_{new} &= \frac{\text{total crossection area of plate and bulbprofiles}}{\text{width of bottom plate}} \\ &= \frac{11500 * 10 + 13 * (147 * 8 + 40 * 12)}{11500} \\ t_{new} &= 11.8 \text{ mm} \end{aligned} \tag{A.1}$$

Span 1 and 3 are not outfitted with sensors, they exist merely to allow proper boundaries on span 2. To reduce complexity in spans 1 and 3, the crossbeams are omitted. This allows for a much larger mesh size in those spans, while still imposing the correct boundaries for span 2. To still allow application of self weight and traffic loads, the stiffness matrix of the deck plate is modified to increase the bending stiffness (and ónly the bending stiffness) of the deck plate by a factor 1000. This is similar to the stiffness that the crossbeams would have added. Because the axial stiffness is unmodified, the boundaries still match for the global behaviour.

A.3 Supports

At the left end of the model all nodes and lines are restrained along the x direction. This implies a fully clamped end.
The vertical supports are nodal supports at the node where box-bottom, box-wall and strut node meet. They only constrain movement in the vertical (Z) direction.
Additional constraints in the sideways (Y) direction are placed above each pier, at a node in the center of the bottom plate where the struts join.
The supports are shown in figure A.3

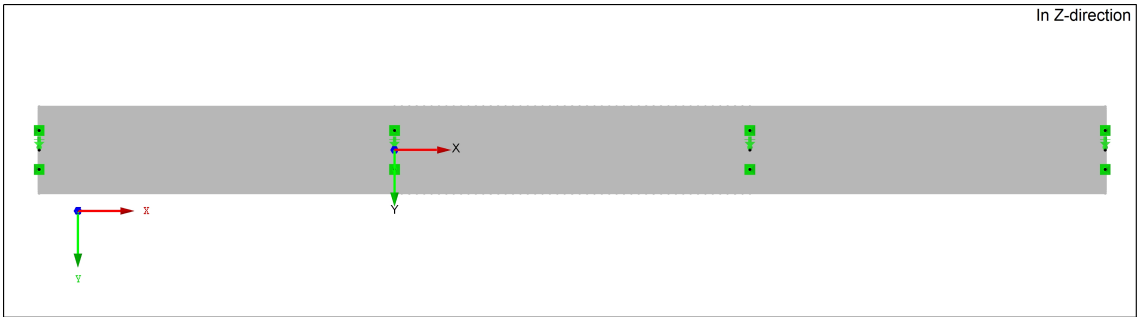

(a) Top View of nodal supports

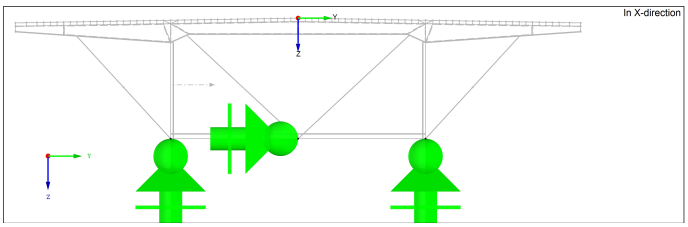

(b) Cross-section of nodal supports

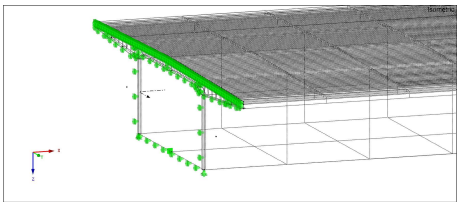

(c) Isometric view of Symmetry condition for spans 4..10

Figure A.3: Overview of supports

A.4 Loads

A.4.1 Temperature loads

One of the challenges in modelling the temperature induced stress & strain, is in applying the temperature distribution inside the bridge. A full heat-flow analysis of the bridge is well beyond the scope of this project, so a pragmatic approach is chosen.
Based on the available temperature measurements and the Codes [1], assumptions are made about the temperature gradients through the bridge:

- The temperature is constant along the longitudinal X-axis of the bridge.
- There is linear Z-gradient between deck and bulb.
- There is linear Z-gradient between bulb and bottom of cross-member.

- There is a linear Z-gradient between bottom cross-member and bottom of the box.
- The deck and corresponding bulbs above the box, behave differently from the cantilevered deck, due to trapped hot air inside the box.

Based on these assumptions the temperature load was split in a "homogeneous" average bridge temperature, and a set of load cases that contains a $+10°C$ temperature change of 1 element group, which linearly decays to $+0°C$ at the nearest other element group. Each load case can then be multiplied with a measured temperature to obtain a piecewise linear temperature distribution throughout the bridge.
The temperature load cases are shown graphically in figure A.4, and explained below.

- LC1: Homogeneous.
  Homogeneous bridge temperature. All elements are included.
- LC11: Deck out West.
  The entire deck plate west of the cantilever has a $+10°C$ temperature. A small 60 cm wide transition strip is included above the web of the main box girder.
  All vertical planes (web of bulb profiles, web of longitudinal beams, web of main box) have a triangular temperature load with $+10°C$ at deck level, and $+0°C$ at the height of the bulbs (approx 150 mm below deck level).
- LC12: Bulbs out West.
  Below the west side cantilever deck, all bulbs of the bulb-profiles obtain the $+10°C$ temperature. All vertical planes (web of bulb profiles, web of longitudinal beams, web of main box) have a triangular temperature load with $+10°C$ at bulb level, and $+0°C$ at either deck-level or flange-level of the crossbeams.
- LC13: Bottom flange out west.
  Below the west side cantilever deck, all bottom flanges of the cross-members and longitudinal beams obtain a $+10°C$ temperature. All vertical planes (web of cross-members, web of longitudinal beams, web of main box) have a triangular temperature load with $+10°C$ at flange-level, and $+0°C$ at either bulb-level or bottom box girder level.
- LC14:LC16 are similar to LC11:13, but above the box girder.
- LC17:LC19 are similar to LC11:13, but on the east cantilever side.
- LC20 Box bottom west.
  The lower west side of the box girder (including the strut) obtains $+10°C$ which linearly decays to the level of either the bottom cross member or the east side of the box girder
- LC21: Box bottom east is similar to LC21, but on the east side.

Care has been taken to avoid double temperature loads at overlapping area's. If element sets overlap, i.e. part of the west web of the box-girder is influenced by both LC12 and LC15, their amplitude is adjusted accordingly.

A.4.2 Generic loads

The bridge contains a highway in 2 directions, and a small side road that's barely wide enough for 2 vehicle to pass each other.
This results in 5 lanes of traffic. Eurocode defines 2 ULS & SLS loads:

1. A uniform load across the entire length & width of each "theoretical"-lanes.
2. A set of small rectangular loads with the size of a wheel.

For the model a different approach is chosen. The drawings and inspection reports show that each lane has 2 approx 1.2 m wide strips where the wheel loads dominate. For each lane a load case is created where those two 1.2 m wide strips are loaded with a 1kNm^{-2} load along the entire length of the bridge. This results in LC31:LC35, which can be seen in figure A.5.
Self-weight of steel is calculated automatically in LC101, while self-weight of the asphalt layers is added manually in LC102.

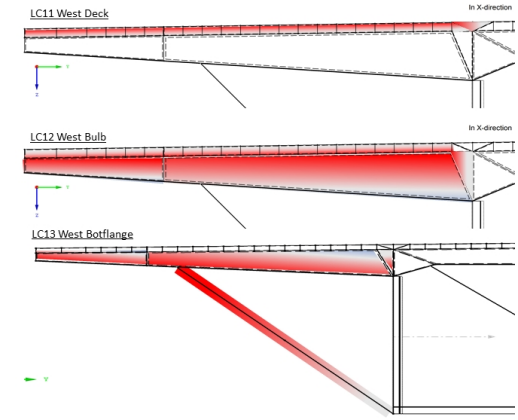

(a) LC11..LC13

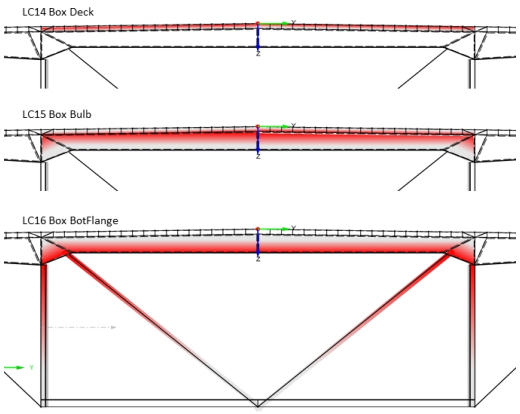

(b) LC14..LC16

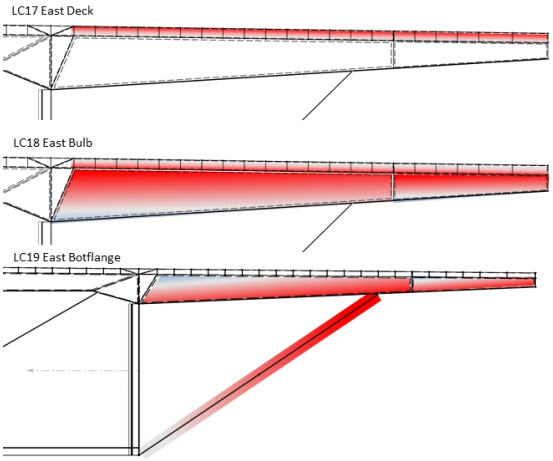

(c) LC17..LC19

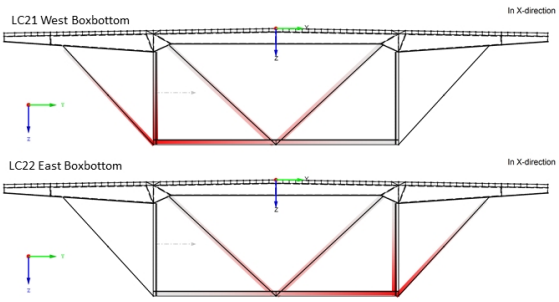

(d) LC21..LC22

Figure A.4: Temperature load cases. Dark red is $+10°C$, white is no load, blue is a small negative temperature artefact due to RFEM's linear gradient restriction.

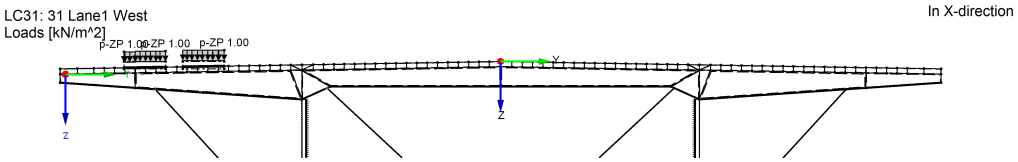

(a) LC31 West Highway Lane.

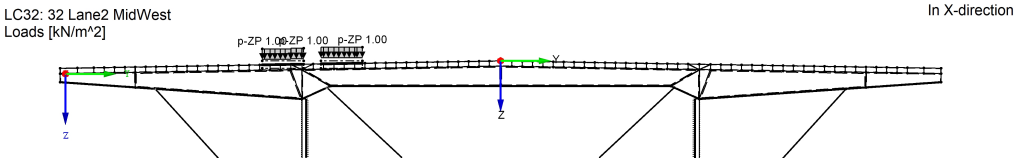

(b) LC32.

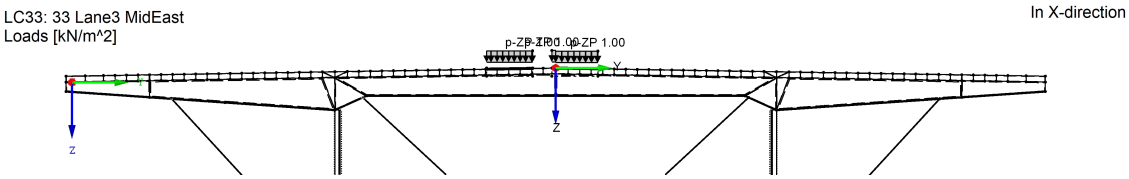

(c) LC33.

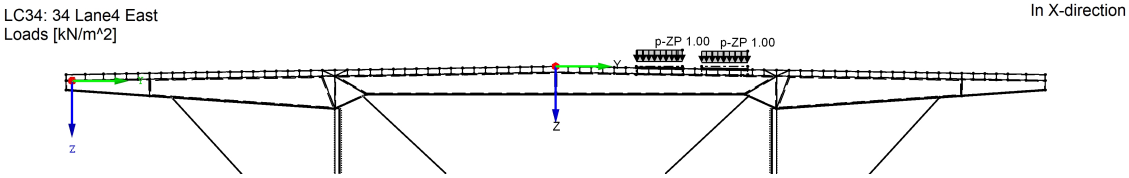

(d) LC34 East Highway lane.

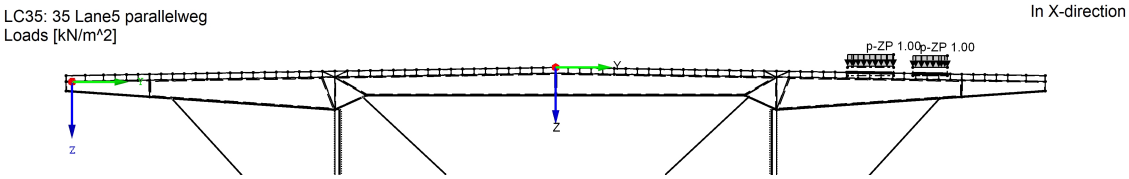

(e) LC35 East Side road.

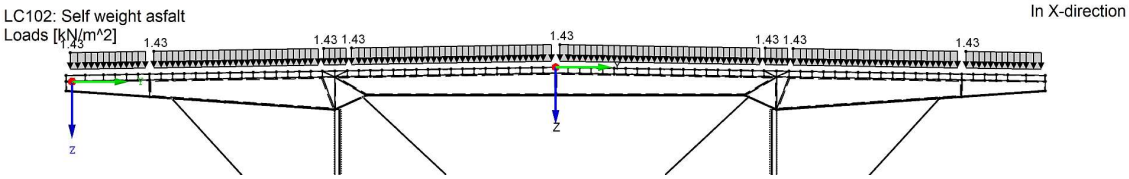

(f) LC102 Self weight Asphalt.

Figure A.5: Generic load cases for traffic and self-weight

A.5 Sensor positions

To compare the model with the measurements, specific points of the model are exported to .csv files for further processing in python.

- Beam elements: An additional node is placed, splitting the beam of interest. The results for one of the connecting beams at this node are exported. Exported are nodal displacement, internal forces, and internal strains.
- Plate elements: RFEM does not support imprinting a node on a surface for this purpose. It does however allow drawing a grid [1], and the results at these grid points can be exported to .csv. Exported are grid point displacement, internal forces and strains. Care is taken to use the correct side of the plate.

Stress is calculated manually with python, by dividing the force over the area.

A.6 Mesh

While RFEM does not allow explicit element type definition, in the global settings shear deformation has been accounted for in Beams, and the plate theory is set to Mindlin Reissner.
The mesh size is set to $100mm$ for the areas where sensors are placed. While a courser mesh of approximately $600mm$ is used for the rest of span 2. This allows for 4 elements between subsequent cross-members.
In spans 1 and 3, no cross-members are present, and the mesh-size is increased to $5000mm$.

[1] This grid is not to be confused with the mesh, or the integration points

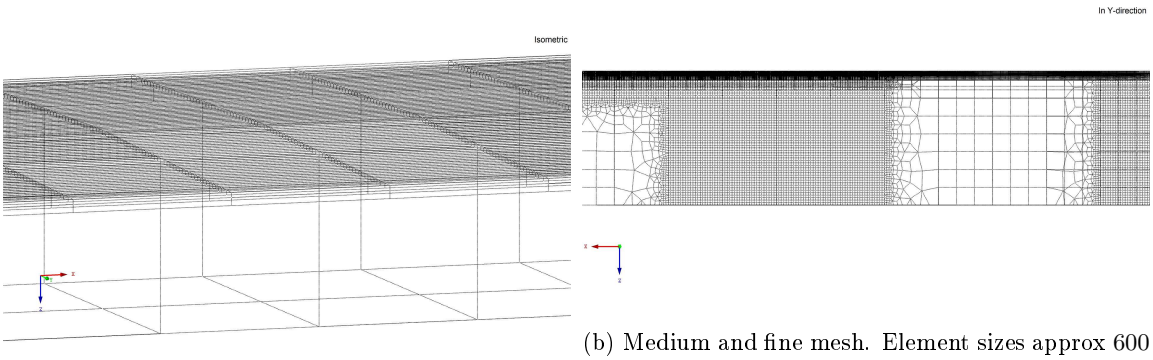

(a) course Mesh. Element size approx 5000mm

(b) Medium and fine mesh. Element sizes approx 600 and 100mm respectively

Figure A.6: Mesh size

For each load case a geometrical- and physical-linear result is calculated.

A.7 Model checking

A.7.1 Deflection

The deflection of an analytical beam is compared to the displacement of the FE-Model. Using a small python script the Moment of Inertia of a bridge span is calculated to be 3.179×10^{12} mm^4 and the shear area of the box walls to be 106.6×10^3 mm^2. A simple 3 span beam model with 1 side clamped was given these parameters and a load of 25.5m $\times$ 1.43 kNm^{-2} = 36.465 kNm^{-1}, which is identical to the asphalt self weight of LC102.
In tables A.1 and A.2 a comparison is made for the maximum deflection and the distribution of the support reactions. The deflection deviates 9%, which is acceptable: No shear lag in the deck is included in the beam model, and the geometry of the beam model is simplified [2]. The support reactions are within 1%, which is good.

Comparison of deflection	Field 1 [mm]	Field 2 [mm]	Field 3 [mm]
Euler	18.65	10.66	43.05
Timoshenko	24.39	16.82	49.29
Full FEM	27.02	19.33	52.11
FEM corrected	26.02	18.33	51.12
Difference FEM vs Timoshenko	7 %	9 %	4%

Table A.1: Deflection check. "Full FEM" is nodal displacement at center of span. "FEM corrected" is after correction due to the the singularity near the supports.

Comparison of support reactions	Supp. 1 [kN]	Supp. 2 [kN]	Supp. 3 [kN]	Supp. 4 [kN]
Euler	1954	3688	4352	1512
Timoshenko	1948	3703	4336	1518
FEM	1938	3718	4332	1519
Difference FEM vs Timoshenko	-1 %	0 %	0 %	0 %

Table A.2: support reaction check

A.7.2 Summation of temperature loads

The individual temperature loads LC11 through LC21 should add up to the same result as the global average temperature of LC1. For the sensor positions of interest the resulting strains of LC11:LC21 are summed, and then compared to LC1. See table A.3 for the results.
As can be seen the accuracy is good for most sensors, with a deviation $< 1\%$. The sensors with a deviation $> 1\%$ are the result of small temperature jumps in LC13, LC16 and LC19. This occurs at the bottom flange of the cantilever: The web of the crossbeam is not rectangular but tapered. A temperature load with a linear gradient only allows 1 edge of this web to have a constant temperature. The other edge will deviate. Therefore the web is split in 2 shorter sections, to reduce this deviation. Unfortunately this also induces a jump, which occurs exactly at those sensor positions.

A.7.3 Elongation due to temperature change

The FE-Model contains 3 spans, with 1 end restrained in x-direction and the other free. The model boundaries are at -105.191 m and $+210.391$ m, for a total length of 315.582m. The $10°C$ homogeneous temperature change in LC1 should result in 315582 $mm \times 10°C \times 12 \cdot 10^{-6}/°C = 37.87$mm deformation at the free end. This is identical to the displacement of one of the end-nodes in the FE-model, which is also 37.87mm.

[2] amongst others: the deck is a horizontal flat instead of pitched

Table A.3: Comparison of LC1 with the sum of LC11:21, all values are in μ-strain

	LC1	LC11:21	diff.	err.%
b01	12.00	12.01	0.01	0.08 %
b02	12.00	11.98	-0.02	-0.19 %
b03	12.00	11.99	-0.01	-0.09 %
b04	12.00	11.99	-0.01	-0.07 %
b05	12.00	11.99	-0.01	-0.06 %
b06	12.00	11.99	-0.01	-0.04 %
b07	12.00	11.98	-0.02	-0.14 %
b08	12.00	11.98	-0.02	-0.13 %
b09	12.00	11.99	-0.01	-0.11 %
b10	12.00	11.98	-0.02	-0.15 %
b11	12.00	12.02	0.02	0.19 %
b12	12.00	12.02	0.02	0.17 %
b13	12.00	12.00	-0.00	-0.02 %
b14	12.00	12.00	-0.00	-0.02 %
b37	12.00	12.02	0.02	0.14 %
b38	12.00	12.01	0.01	0.10 %
c1_pd	12.00	13.49	1.49	12.44 %
c2_pd	12.00	13.31	1.31	10.92 %
d1_pd	12.00	11.90	-0.10	-0.79 %
d2_pd	12.00	11.90	-0.10	-0.81 %
d4_pd	12.00	11.91	-0.09	-0.78 %
o1_pd	12.00	11.93	-0.07	-0.57 %
o2_pd	12.00	11.94	-0.06	-0.46 %
s0103	11.97	11.99	0.03	0.21 %
s0406	11.97	11.99	0.02	0.19 %
s1012	11.97	11.99	0.03	0.22 %
s1315	11.97	11.99	0.02	0.19 %
w1b_pd	12.00	12.00	-0.00	-0.00 %
w1be_pd	12.00	12.00	-0.00	-0.03 %
w1t_pd	12.00	11.99	-0.01	-0.06 %
w1te_pd	12.00	11.99	-0.01	-0.08 %
w2b_pd	12.00	12.00	0.00	0.01 %
w2t_pd	12.00	11.99	-0.01	-0.08 %
x1n_pd	12.00	12.13	0.13	1.05 %
x1o_pd	12.00	13.49	1.49	12.44 %
x1w_pd	12.00	12.48	0.48	3.96 %
x1z_pd	12.00	12.13	0.13	1.05 %
x2n_pd	12.00	12.04	0.04	0.36 %
x2o_pd	12.00	13.74	1.74	14.49 %
x2w_pd	12.00	12.45	0.45	3.73 %
x2z_pd	12.00	12.04	0.04	0.36 %

A.7.4 Elongation compared to LVDT measurements

The FE-model can also be verified against the LVDT measurements. The LVDT was placed at a roller support 424 meter away from the fixed support. This LVDT measures the axial elongation of the bridge. Using this LVDT the FE model might also be validated, using the following procedure:

1. Compare the LVDT displacement against temperature measurements from specific sensors in October.
2. Compare those temperature sensors to FEM LC1 (average bridge temperature)solicitation in June.
3. Compare the FEM strains due to LC1 in June with the temperature measurements and expected strain.
4. Compare the FEM strains due to LC1 in June with the measured strains of the box wall.

Step 1: LVDT displacement in October.
The LVDT was commissioned on Sept 30, and thus not yet available during the FBG strain measurements. The only sensors that are available in both June and October are the analogue temperature sensors. Therefore they are used as a bridge between the periods. A relatively warm period in October was chosen as a starting point: 14 to 20 Oct.
The LVDT measures support displacement of a support 424 meters away from the fixed support. The average axial bridge strain can thus be calculated as follows:
$\varepsilon_{LVDT} = \frac{\text{Displacement}}{\text{Distance}} = \frac{0.001}{4 \cdot 106} = 2.36\mu\varepsilon$ per mm displacement.
Assuming the bridge temperature is homogeneous, and using the temperature of coefficient steel, a single temperature sensor could predict the average axial bridge strain :
$\varepsilon_{TemperatureSensor} = \alpha_{T,Steel} \cdot \Delta T = 12 \cdot 10^{-6} \cdot DeltaT = 12\mu\varepsilon$ per $\Delta^{\circ}C$ These 2 strains are compared against each other in figure A.7, which was also shown in chapter 5.2. The temperature of the top web of the east cantilever (at15) matches the LVDT measurements with a standard deviation of $5.4\mu\varepsilon$. The east cantilever deck plate has a slightly higher deviation of $6.9\mu\varepsilon$.

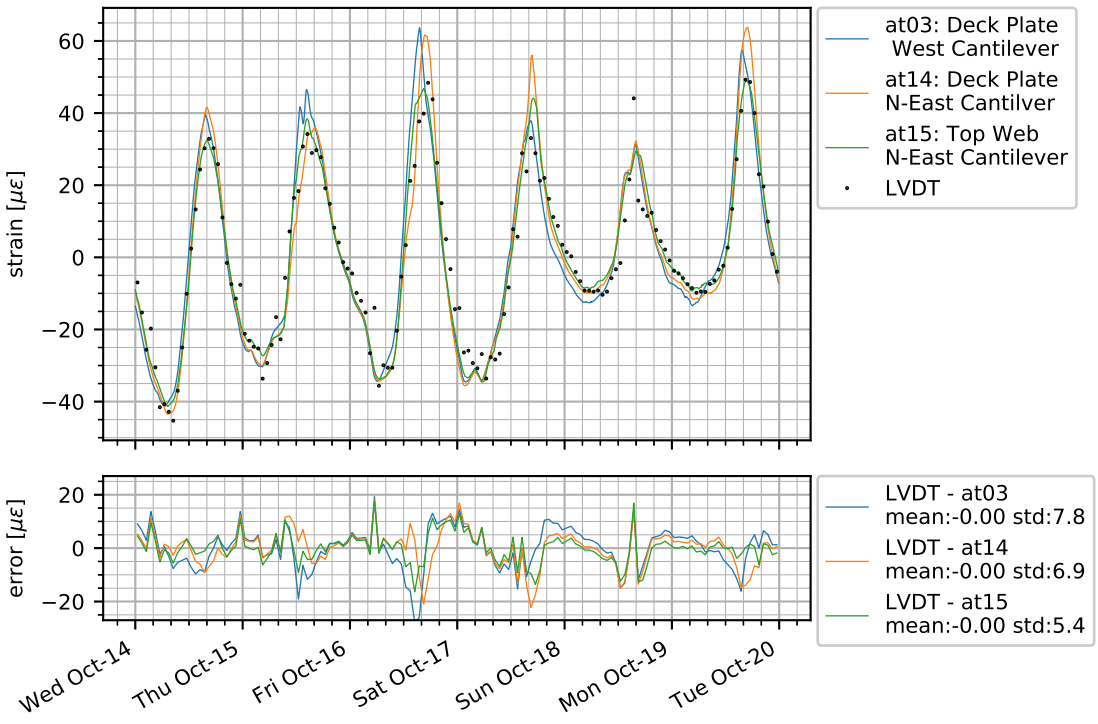

Figure A.7: predicted strains from LVDT and temperature measurements

Step 2: Comparison between temperature sensor matching LVDT and LC1.
Load case 1 is defined using both analogue and FBG temperature sensors, and thus cannot be calculated in October. Therefore the at14 and at15 sensors from step 1 are used to verify if LC1 is plausible. Figure A.8 shows the differences between load case 1 solicitation and the amplitude of the west cantilever web and deck plate. Just after midday the west cantilever web is a few degrees warmer than LC1, while in the evenings the west cantilever web is a bit cooler. An explanation for this can be found in the calculation of LC1: LC21 also uses temperature sensors of the box wall, and the box contains trapped air. For a further explanation see chapter 5.1.
The peak differences are approximately 5 °C which is a 30% of the 15°C daily temperature amplitude. The standard deviations of only 1.09 °C is pretty good however: smaller than 7% of the daily temperature amplitude.

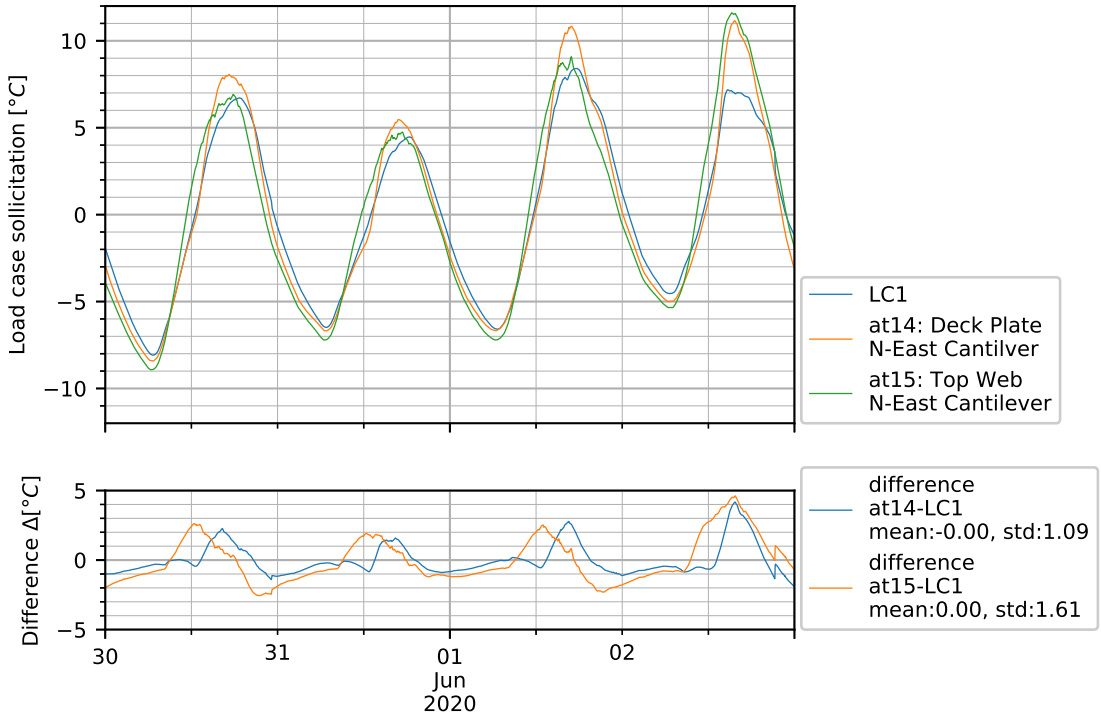

Figure A.8: Loadcase 1 solicitation versus West cantilever web temperature amplitude

Step 3: LC1 FEM strain versus temperature strain.
Table A.4 shows a 12.00$\mu\varepsilon$ strain for LC1 on almost all sensor positions. The temperature coefficient of steel is $12 \cdot 10^{-6}$ so this matches.

Step 4: FEM strain versus strain measurements.
The strain due to LC1 is compared to the measured strains in the box wall. Figure A.9 shows these strains. Just like in chapter 5.4 the strains are offset to have mean strain between 06:00 and 06:30 equal to zero. The West bottom box wall deviates significantly from the FEM strains. The bridge is assymmetric and the highway is located mainly on the West side of the bridge, and thus traffic might induce additional strains in mainly the west box wall. The other channels show of good match. With standard deviations below 10% of the daily strain amplitude.

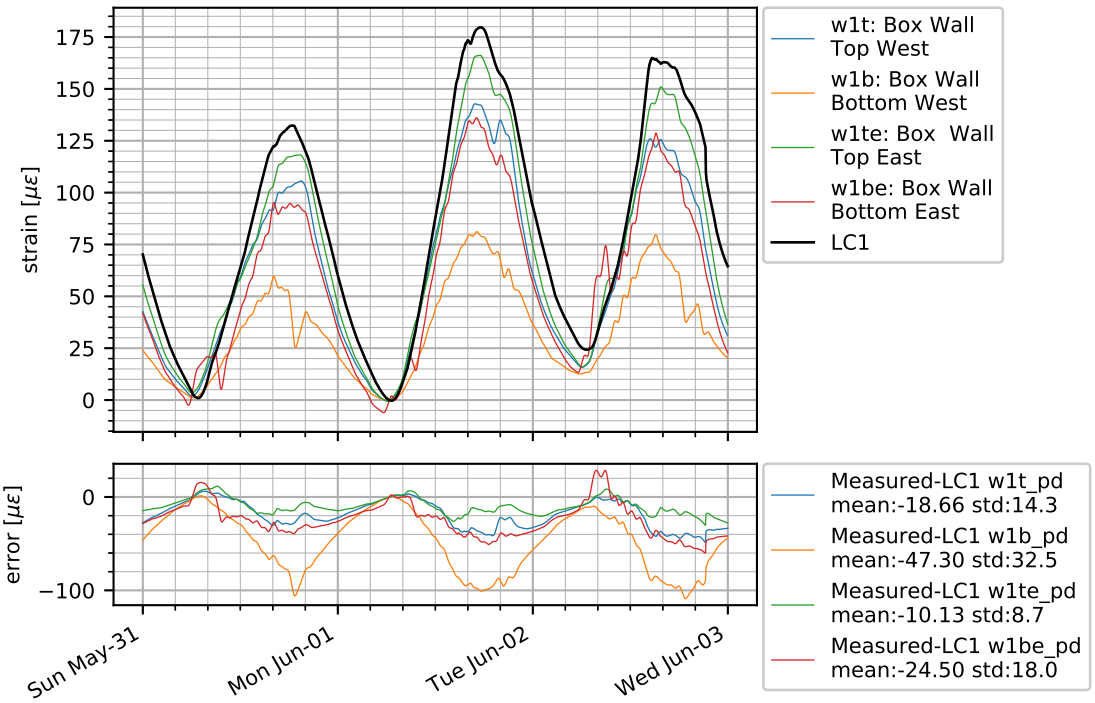

Figure A.9: Strain due to FEM LC1 versus measured strains

Conclusion

- The strain measurements in the box wall do not show a good fit with LC1-strains of the FE model. For the west bottom box wall, the difference is over 50%.
- LC1 of the FE Model shows the correct strain outputs, correlating to the temperature coefficient of steel, $12 \cdot 10^{-6} \varepsilon^{\circ} C^{-1}$, in the result tables.
- LC1 matches temperature sensors at14 and at15, both on the East Cantilever with a standard deviation below 7%
- An average strain calculation based on temperature sensors at14 and at15 matches the displacement measured by the LVDT with a standard deviation below 10%.
- Therefore the poor match between FE-Model and measurements is not due to a modelling error. Exact cause is unknown, but further investigation of traffic load and FBG sensor temperature compensation (STC) is advised.

A.8 result tables

The output of the FEM model is reduced to a few tables as shown in tables A.4 through A.7. For each sensor both the stress and strain of each loadcase is shown. See figures 4.6 through 4.15 for sensor position.

Table A.4: **Strain** due to loadcases in μ-strain

case	LC1	LC11	LC12	LC13	LC14	LC15	LC16	LC17	LC18	LC19	LC20	LC21
b01	12.00	1.43	0.32	0.05	2.98	0.71	0.58	1.63	0.52	0.18	1.80	1.80
b02	12.00	1.52	0.29	0.02	3.18	0.66	0.40	1.61	0.51	0.18	1.82	1.79
b03	12.00	1.52	0.29	0.03	3.17	0.66	0.41	1.60	0.50	0.18	1.83	1.79
b04	12.00	1.52	0.30	0.04	3.13	0.67	0.44	1.59	0.50	0.18	1.82	1.79
b05	12.00	1.51	0.30	0.05	3.08	0.68	0.49	1.59	0.50	0.18	1.82	1.79
b06	12.00	1.50	0.31	0.06	3.02	0.70	0.53	1.59	0.50	0.18	1.81	1.79
b07	12.00	1.53	0.47	0.18	2.78	0.74	0.73	1.52	0.38	0.09	1.77	1.79
b08	12.00	1.53	0.48	0.18	2.77	0.74	0.75	1.50	0.39	0.09	1.77	1.79
b09	12.00	1.54	0.48	0.18	2.73	0.75	0.78	1.49	0.39	0.10	1.77	1.78
b10	12.00	1.58	0.48	0.17	2.69	0.68	0.78	1.45	0.45	0.13	1.79	1.79
b11	12.00	1.04	0.47	0.41	1.14	1.10	2.11	1.73	0.52	0.15	1.52	1.84
b12	12.00	1.09	0.46	0.38	1.31	1.06	1.96	1.71	0.51	0.15	1.55	1.84
b13	12.00	1.42	0.49	0.22	2.87	0.75	0.68	1.67	0.30	0.06	1.75	1.79
b14	12.00	1.45	0.49	0.21	2.78	0.77	0.72	1.64	0.30	0.08	1.76	1.79
b37	12.00	1.33	0.35	0.17	2.50	0.80	0.98	1.64	0.51	0.17	1.75	1.83
b38	12.00	1.34	0.36	0.16	2.53	0.79	0.96	1.63	0.50	0.17	1.75	1.83
c1_pd	12.00	-1.93	4.13	10.84	3.60	-0.71	-2.92	-0.17	-0.00	0.05	0.66	-0.06
c2_pd	12.00	-1.89	4.52	10.21	3.58	-0.74	-2.89	-0.14	0.02	0.03	0.67	-0.06
d1_pd	12.00	1.16	-0.41	-0.75	6.12	1.17	3.81	1.16	-0.44	-0.71	0.40	0.40
d2_pd	12.00	1.13	-0.40	-0.72	5.73	1.25	4.11	1.12	-0.41	-0.68	0.39	0.39
d4_pd	12.00	1.14	-0.40	-0.73	5.96	1.20	3.95	1.14	-0.43	-0.70	0.38	0.39
o1_pd	12.00	1.58	0.48	0.20	2.78	0.95	0.77	1.76	0.54	0.15	1.35	1.36
o2_pd	12.00	1.52	0.48	0.19	2.65	0.89	0.83	1.65	0.50	0.16	1.56	1.52
s0103	11.97	-0.88	0.27	12.44	-2.56	0.60	2.26	0.21	0.02	-0.02	-0.46	0.11
s0406	11.97	-0.83	0.27	12.43	-2.55	0.62	2.24	0.18	0.01	-0.02	-0.49	0.13
s1012	11.97	-0.88	0.27	0.47	-2.56	0.60	2.26	0.21	0.02	-0.02	11.51	0.11
s1315	11.97	-0.83	0.27	0.47	-2.55	0.62	2.24	0.18	0.01	-0.02	11.48	0.13
w1b_pd	12.00	1.56	0.45	0.18	2.88	0.92	0.73	1.76	0.55	0.15	1.36	1.47
w1be_pd	12.00	1.76	0.55	0.15	2.87	0.91	0.76	1.56	0.45	0.18	1.46	1.35
w1t_pd	12.00	1.45	0.41	0.16	2.61	0.75	0.90	1.59	0.48	0.16	1.72	1.76
w1te_pd	12.00	1.59	0.48	0.16	2.61	0.75	0.89	1.47	0.41	0.15	1.76	1.73
w2b_pd	12.00	1.52	0.45	0.18	2.75	0.84	0.84	1.64	0.49	0.15	1.56	1.57
w2t_pd	12.00	1.53	0.43	0.15	2.67	0.76	0.86	1.59	0.48	0.16	1.68	1.68
x1n_pd	12.00	0.13	0.71	0.79	-1.24	1.67	4.24	1.99	0.58	0.13	1.14	1.98
x1o_pd	12.00	-1.93	4.13	10.84	3.60	-0.71	-2.92	-0.17	-0.00	0.05	0.66	-0.06
x1w_pd	12.00	-3.01	3.66	11.39	-1.28	0.33	1.20	0.16	0.03	-0.01	-0.14	0.13
x1z_pd	12.00	0.14	0.70	0.79	-1.20	1.67	4.21	1.99	0.58	0.13	1.14	1.98
x2n_pd	12.00	2.03	0.23	-0.37	5.08	0.30	-1.12	1.51	0.50	0.21	2.03	1.64
x2o_pd	12.00	-2.36	4.25	11.47	0.85	-0.13	-0.60	0.01	0.01	0.02	0.18	0.04
x2w_pd	12.00	-2.35	3.49	10.98	0.80	-0.13	-0.58	0.00	0.01	0.02	0.17	0.03
x2z_pd	12.00	2.03	0.23	-0.37	5.06	0.31	-1.11	1.51	0.50	0.21	2.02	1.64

Table A.5: **Stress** due to loadcases in MPa

case	LC1	LC11	LC12	LC13	LC14	LC15	LC16	LC17	LC18	LC19	LC20	LC21
b01	0.00	0.30	-2.45	0.01	0.63	0.15	0.12	0.34	0.11	0.04	0.38	0.38
b02	0.00	0.32	-2.46	0.00	0.67	0.14	0.09	0.34	0.11	0.04	0.38	0.38
b03	0.00	0.32	-2.46	0.01	0.67	0.14	0.09	0.34	0.11	0.04	0.38	0.38
b04	0.00	0.32	-2.46	0.01	0.66	0.14	0.09	0.34	0.11	0.04	0.38	0.38
b05	0.00	0.32	-2.46	0.01	0.65	0.14	0.10	0.34	0.10	0.04	0.38	0.38
b06	0.00	0.31	-2.46	0.01	0.64	0.15	0.11	0.34	0.10	0.04	0.38	0.38
b07	0.00	0.32	0.10	0.04	0.59	-2.36	0.15	0.32	0.08	0.02	0.37	0.38
b08	0.00	0.32	0.10	0.04	0.58	-2.36	0.16	0.31	0.08	0.02	0.37	0.38
b09	0.00	0.32	0.10	0.04	0.57	-2.36	0.16	0.31	0.08	0.02	0.37	0.37
b10	0.00	0.33	0.10	0.04	0.56	-2.38	0.16	0.30	0.09	0.03	0.38	0.38
b11	0.00	0.22	-2.42	0.09	0.24	0.23	0.44	0.36	0.11	0.03	0.32	0.39
b12	0.00	0.23	-2.42	0.08	0.28	0.22	0.41	0.36	0.11	0.03	0.33	0.39
b13	0.00	0.30	0.10	0.05	0.60	-2.36	0.14	0.35	0.06	0.01	0.37	0.38
b14	0.00	0.30	0.10	0.04	0.59	-2.36	0.15	0.35	0.06	0.02	0.37	0.38
b37	0.00	-2.32	0.14	0.04	0.48	0.18	0.25	0.35	0.11	0.04	0.36	0.39
b38	0.00	-2.32	0.14	0.03	0.48	0.18	0.25	0.35	0.11	0.04	0.36	0.39
c1_pd	0.00	-0.41	0.87	-0.24	0.76	-0.15	-0.61	-0.03	-0.00	0.01	0.14	-0.01
c2_pd	0.00	-0.40	0.95	-0.38	0.75	-0.16	-0.61	-0.03	0.00	0.01	0.14	-0.01
d1_pd	0.00	0.24	-0.09	-0.16	1.29	0.24	-1.72	0.24	-0.09	-0.15	0.08	0.08
d2_pd	0.00	0.24	-0.08	-0.15	1.20	0.26	-1.66	0.23	-0.09	-0.14	0.08	0.08
d4_pd	0.00	0.24	-0.08	-0.15	1.25	0.25	-1.69	0.24	-0.09	-0.15	0.08	0.08
o1_pd	0.00	0.39	0.12	0.05	0.70	0.24	0.21	0.45	0.14	0.04	-2.30	-0.04
o2_pd	0.00	0.38	0.12	0.05	0.67	0.22	0.23	0.42	0.12	0.04	-2.25	-0.00
s0103	0.00	-0.18	0.06	0.10	-0.54	0.13	0.47	0.04	0.00	-0.01	-0.10	0.02
s0406	0.00	-0.17	0.06	0.10	-0.53	0.13	0.47	0.04	0.00	-0.00	-0.10	0.03
s1012	0.00	-0.18	0.06	0.10	-0.54	0.13	0.47	0.04	0.00	-0.01	-0.10	0.02
s1315	0.00	-0.17	0.06	0.10	-0.53	0.13	0.47	0.04	0.00	-0.00	-0.10	0.03
w1b_pd	0.00	0.33	0.09	0.04	0.60	0.19	0.04	0.37	0.12	0.03	-2.12	0.31
w1be_pd	0.00	0.37	0.12	0.03	0.60	0.19	0.05	0.33	0.09	0.04	0.31	-2.12
w1t_pd	0.00	0.30	0.09	0.03	0.55	-2.22	0.04	0.33	0.10	0.03	0.36	0.37
w1te_pd	0.00	0.33	0.10	0.03	0.55	-2.22	0.03	0.31	0.09	0.03	0.37	0.36
w2b_pd	0.00	0.32	0.10	0.04	0.58	0.18	0.06	0.34	0.10	0.03	-2.08	0.33
w2t_pd	0.00	0.32	0.09	0.03	0.57	-2.21	0.03	0.33	0.10	0.03	0.35	0.35
x1n_pd	0.00	0.03	0.15	-2.35	-0.26	0.35	0.89	0.42	0.12	0.03	0.24	0.42
x1o_pd	0.00	-0.41	0.87	-0.24	0.76	-0.15	-0.61	-0.03	-0.00	0.01	0.14	-0.01
x1w_pd	0.00	-0.63	0.77	-0.13	-0.27	0.07	0.25	0.03	0.01	-0.00	-0.03	0.03
x1z_pd	0.00	0.03	0.15	-2.35	-0.25	0.35	0.88	0.42	0.12	0.03	0.24	0.41
x2n_pd	0.00	0.43	0.05	-2.60	1.07	0.06	-0.24	0.32	0.11	0.04	0.43	0.35
x2o_pd	0.00	-0.49	0.89	-0.11	0.18	-0.03	-0.13	0.00	0.00	0.00	0.04	0.01
x2w_pd	0.00	-0.49	0.73	-0.21	0.17	-0.03	-0.12	0.00	0.00	0.00	0.04	0.01
x2z_pd	0.00	0.43	0.05	-2.60	1.06	0.06	-0.23	0.32	0.11	0.04	0.43	0.35

Table A.6: **Strain** due to loadcases in μ-strain

case	LC101	LC102	LC31	LC32	LC33	LC34	LC35
b01	-46.41	-16.66	1.09	-1.50	-1.70	-1.49	-0.99
b02	-44.67	-15.11	1.98	-1.46	-1.89	-1.64	-1.02
b03	-47.87	-16.90	1.26	-1.61	-1.99	-1.71	-1.05
b04	-49.41	-17.81	1.56	-1.68	-2.00	-1.71	-1.06
b05	-51.05	-18.78	1.34	-1.76	-2.00	-1.71	-1.07
b06	-52.78	-19.80	0.86	-1.84	-2.00	-1.71	-1.08
b07	-66.26	-27.73	-1.50	-1.72	-2.15	-0.11	-2.08
b08	-67.09	-28.27	-1.49	-1.71	-2.16	-0.42	-2.17
b09	-67.86	-28.71	-1.49	-1.71	-2.16	-2.03	-2.26
b10	-70.29	-30.30	-1.54	-1.79	-2.19	-2.56	-2.39
b11	-78.67	-41.53	-10.28	-2.46	-0.52	-0.59	-0.95
b12	-78.08	-40.88	-9.81	-2.45	-0.69	-0.73	-0.99
b13	-70.63	-34.97	-1.23	-1.37	-2.12	-6.30	-2.02
b14	-72.45	-36.09	-1.26	-1.40	-2.10	-3.37	-2.19
b37	-67.00	-29.70	-3.28	-2.21	-1.75	-1.52	-1.12
b38	-67.84	-30.11	-3.36	-2.25	-1.80	-1.57	-1.14
c1_pd	-9.44	-9.95	3.89	1.29	-2.81	-2.30	-0.66
c2_pd	-9.43	-10.34	2.05	0.36	-2.87	-1.71	0.64
d1_pd	39.42	31.51	-0.44	0.80	9.62	3.11	-0.33
d2_pd	36.33	28.84	-0.95	0.79	9.90	3.28	-0.69
d4_pd	38.31	30.24	-0.67	0.79	9.73	3.17	-0.49
o1_pd	158.98	74.22	5.98	5.70	5.07	4.45	3.19
o2_pd	81.07	33.77	3.08	2.74	2.38	2.04	1.13
s0103	-27.49	-18.45	-6.96	-0.89	1.99	1.48	0.13
s0406	-24.65	-17.04	-5.50	-0.05	2.09	1.05	-0.87
s1012	-29.22	-18.45	-6.96	-0.89	1.99	1.48	0.13
s1315	-26.38	-17.04	-5.50	-0.05	2.09	1.05	-0.87
w1b_pd	165.42	73.39	6.51	5.86	4.92	4.18	2.82
w1be_pd	165.30	73.36	3.12	3.83	4.78	5.52	5.62
w1t_pd	-70.39	-31.81	-2.74	-2.46	-2.06	-1.80	-1.31
w1te_pd	-70.29	-31.78	-1.47	-1.68	-2.01	-2.30	-2.35
w2b_pd	91.83	35.66	3.78	3.06	2.37	1.93	0.90
w2t_pd	-41.20	-16.69	-1.81	-1.48	-1.06	-0.80	-0.39
x1n_pd	-70.99	-40.10	-12.08	-2.30	2.32	1.69	-0.18
x1o_pd	-9.44	-9.95	3.89	1.29	-2.81	-2.30	-0.66
x1w_pd	-32.28	-24.00	-3.95	-0.66	0.97	0.76	0.11
x1z_pd	-70.68	-39.90	-11.98	-2.29	2.29	1.66	-0.19
x2n_pd	-5.05	5.42	5.61	0.27	-2.54	-2.19	-0.95
x2o_pd	-10.13	-8.64	1.99	0.20	-0.66	-0.54	-0.16
x2w_pd	-10.22	-8.80	1.93	0.19	-0.63	-0.51	-0.15
x2z_pd	-5.08	5.37	5.58	0.27	-2.52	-2.19	-0.95

Table A.7: **Stress** due to loadcases in MPa

case	LC101	LC102	LC31	LC32	LC33	LC34	LC35
b01	-9.75	-3.50	0.23	-0.31	-0.35	-0.31	-0.21
b02	-9.38	-3.17	0.42	-0.31	-0.40	-0.33	-0.21
b03	-10.06	-3.54	0.27	-0.33	-0.42	-0.35	-0.23
b04	-10.38	-3.75	0.33	-0.35	-0.42	-0.35	-0.23
b05	-10.73	-3.94	0.29	-0.38	-0.42	-0.35	-0.23
b06	-11.08	-4.17	0.19	-0.40	-0.42	-0.35	-0.23
b07	-13.92	-5.81	-0.31	-0.35	-0.46	-0.02	-0.44
b08	-14.08	-5.94	-0.31	-0.35	-0.46	-0.08	-0.46
b09	-14.25	-6.02	-0.31	-0.35	-0.46	-0.42	-0.48
b10	-14.75	-6.35	-0.31	-0.38	-0.46	-0.54	-0.50
b11	-16.52	-8.73	-2.17	-0.52	-0.10	-0.12	-0.21
b12	-16.40	-8.58	-2.06	-0.52	-0.15	-0.15	-0.21
b13	-14.83	-7.35	-0.25	-0.29	-0.44	-1.33	-0.42
b14	-15.21	-7.58	-0.27	-0.29	-0.44	-0.71	-0.46
b37	-14.07	-6.15	-0.76	-0.48	-0.33	-0.29	-0.23
b38	-14.21	-6.20	-0.77	-0.49	-0.34	-0.30	-0.23
c1_pd	-1.98	-2.09	0.82	0.27	-0.59	-0.48	-0.14
c2_pd	-1.98	-2.17	0.43	0.07	-0.60	-0.36	0.13
d1_pd	8.28	6.62	-0.09	0.17	2.02	0.65	-0.07
d2_pd	7.63	6.06	-0.20	0.17	2.08	0.69	-0.15
d4_pd	8.04	6.35	-0.14	0.17	2.04	0.67	-0.10
o1_pd	42.26	18.78	1.52	1.45	1.29	1.13	0.81
o2_pd	22.63	8.62	0.79	0.70	0.61	0.52	0.29
s0103	-5.77	-3.87	-1.46	-0.19	0.42	0.31	0.03
s0406	-5.18	-3.58	-1.15	-0.01	0.44	0.22	-0.18
s1012	-6.13	-3.87	-1.46	-0.19	0.42	0.31	0.03
s1315	-5.54	-3.58	-1.15	-0.01	0.44	0.22	-0.18
w1b_pd	34.22	15.39	1.37	1.23	1.03	0.88	0.59
w1be_pd	34.19	15.38	0.66	0.80	1.00	1.16	1.18
w1t_pd	-14.82	-6.72	-0.58	-0.53	-0.44	-0.38	-0.28
w1te_pd	-14.80	-6.71	-0.31	-0.35	-0.43	-0.48	-0.49
w2b_pd	18.81	7.42	0.79	0.63	0.50	0.41	0.19
w2t_pd	-8.70	-3.54	-0.38	-0.33	-0.23	-0.17	-0.08
x1n_pd	-14.91	-8.42	-2.54	-0.48	0.49	0.35	-0.04
x1o_pd	-1.98	-2.09	0.82	0.27	-0.59	-0.48	-0.14
x1w_pd	-6.78	-5.04	-0.83	-0.14	0.20	0.16	0.02
x1z_pd	-14.84	-8.38	-2.52	-0.48	0.48	0.35	-0.04
x2n_pd	-1.06	1.14	1.18	0.06	-0.53	-0.46	-0.20
x2o_pd	-2.13	-1.81	0.42	0.04	-0.14	-0.11	-0.03
x2w_pd	-2.15	-1.85	0.41	0.04	-0.13	-0.11	-0.03
x2z_pd	-1.07	1.13	1.17	0.06	-0.53	-0.46	-0.20

B Heat flow analysis of the Asphalt-Deck plate composite

B.1 Introduction

In order to understand the measurement taken by the Analogue sensors, a small python 1D-heat flow model is created. This chapter explains the model geometry, environmental inputs, and the results. While the heat transfer equation is technically out of scope for this thesis, it was found that the measurements required some clarification:

- During the day top asphalt is warmer than bottom deck plate, but at night this is the other way round. Is this plausible?
- The asphalt temperature rises significantly during the day, can this be explained by solar radiation only?
- There is a significant temperature difference between sensor locations. What is the cause for this difference between the following locations?
  - West cantilever
  - East cantilever
  - West side above the box
  - East side above the box
  - West side cantilever, directly under the wheel area. (instead of on the shoulder)

B.2 Model definition

B.2.1 Geometry

A piece of deck including one complete bulb-profile is studied in a 1D heat flow model. The C-T-C spacing of the bulbs is $300mm$, so a $300mm$ wide deck section is modelled according to figure B.1. The input parameters are shown in table B.1.
There appears to be a large range of thermal parameters of asphalt, the current parameters are obtained from [24] table III, and seem to work well.

	Asphalt	Steel Deck	Steel Web	Steel bulb	units
no. of elements	6	2	2	1	-
width of element	300	300	8	40	mm
height of each element	10	5	74	12	mm
total height	0.060	0.010	0.148	0.012	m
density	2282	7850	7850	7850	$kgm{-}3$
specific heat	959	490	490	490	$Jkg^{-1}K^{-1}$
heat transfer coefficient	1.87	46	46	46	$Wm^{-1}K^{-1}$

Table B.1: Geometry and material properties

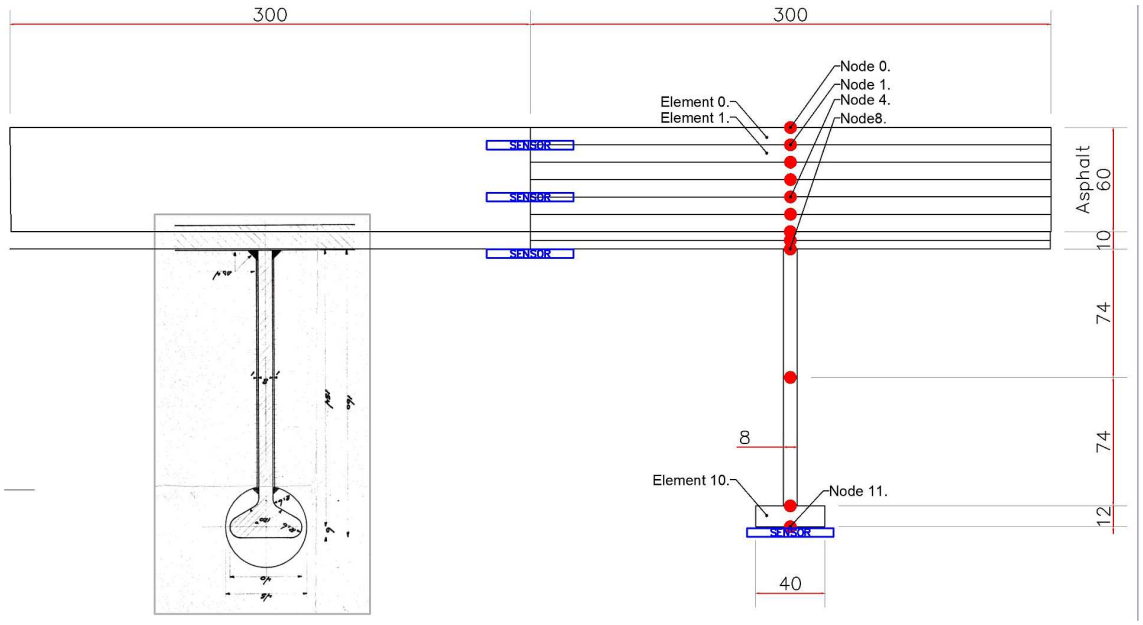

Figure B.1: Cross section of bulb and elements. Left: Original design drawings, Right: 1D model.

B.2.2 Environmental input

The Dutch weather institute KNMI provides environmental data with a 10-minute resolution for various stations in the Netherlands. Their Rotterdam station is located at Rotterdam Airport, within 27 km of the bridge. The data that is included in the model is:

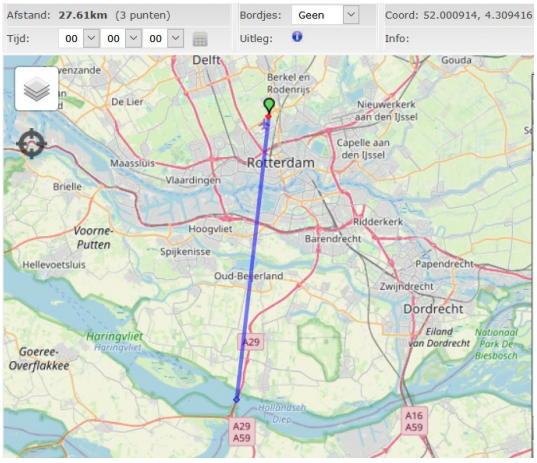

Figure B.2: Distance to Rotterdam station. (afstandmeten.nl)

- Ambient temperature in $^{\circ}C$
- Solar radiation in W/m^2 on a horizontal surface

Other data is also used for interpretation:

- Rainfall
- Wind speed

By plotting the rainfall and wind speed next to the results, specific deviations might be explained.

Radiation

Heat radiation follows Boltzmann's law. And the radiative heat transfer in the model is thus calculated as follows:

$$\dot{Q}_{1\to 2} = \sigma A_1 F_{1\to 2}(T_1^4 - T_2^4) \tag{B.1}$$

Where:

$$\begin{aligned} \sigma &= Stefan\ Boltzmann\ constant \approx 5.670373 * 10^{-8} \\ T_1 &= Temperature\ of\ the\ node\ in\ Kelvin \\ T_2 &= Air\ temperature\ in\ Kelvin \\ F &= View\ factor \\ A &= Surface\ Area \end{aligned}$$

After a few tries, a view factor of 0.8 seemed to give reasonable results, where the maximum temperature and $\frac{\mathrm{dT}}{\mathrm{dt}}$ matches during warming up.

Convection

Heat transfer due to convection is a complex phenomenon. Influencing parameters are inclination of the surface, wind speed, viscosity of the medium and others. A simplified approach is chosen, where the convective heat transfer is linear to the temperature difference:

$$\dot{Q} = hA(T - T_{air}) \tag{B.2}$$

Where:

$$\begin{aligned} h &= heat\ transfer\ coefficient \\ T &= Temperature\ of\ the\ node\ in\ Kelvin \\ T_{air} &= Air\ temperature\ in\ Kelvin \\ A &= Surface\ Area \end{aligned}$$

After some parameter tuning, a reasonable match for the maximum daily temperature was obtained with:

- $h = 23$ for the top surface of the asphalt
- $h = 26$ for the steel elements

Shade

The Model shows that Shade has a significant influence on the deck temperature. The bridge spans in a North-South direction, with an Azimuth of 21° to the North. This means the East-West movement of the sun heats different parts of the bridge during the day. See figure B.3. Using the solar azimuth and inclination from 23 June 2020 [25], the size and position of the shade is calculated. The position of the sensors relative to the barriers was taken from the installation drawings. No parameter tuning on this script was needed: The times of the distinct changes in the temperature curves for the sensors at the east- and west-cantilever deck, match up with those from the heat ODE. For an example of shade influence see figure B.4. This shows that shade has a significant influence on the deck temperature, there is a distinct curve in the temperature plot just after 12:00 in both the measured temperatures and the heat ODE with a simple shade calculation.

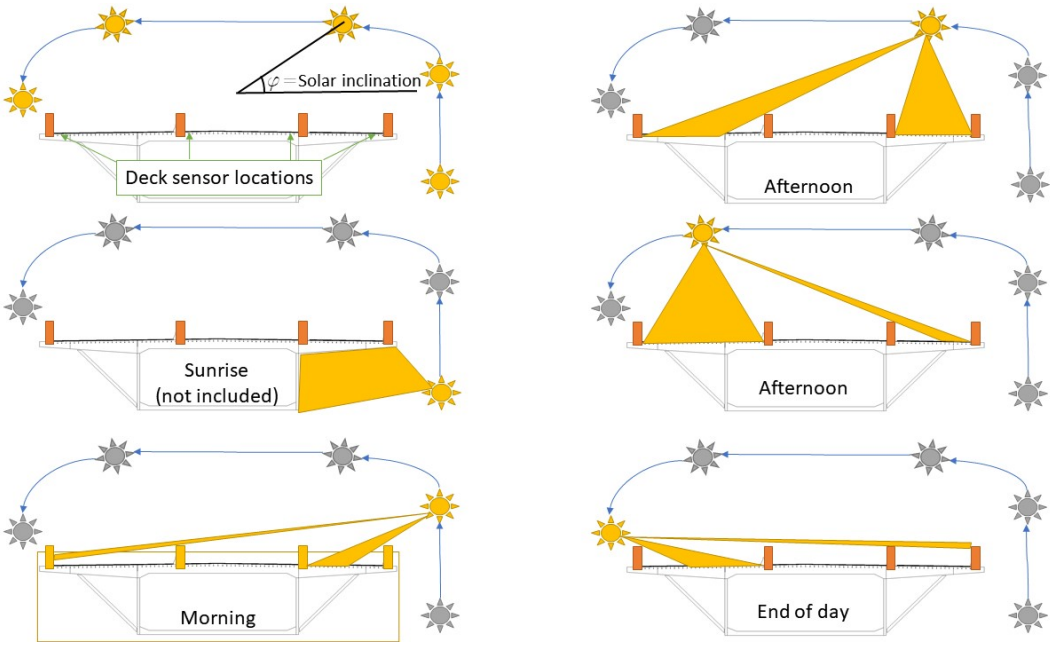

Figure B.3: Solar cycle for the bridge.

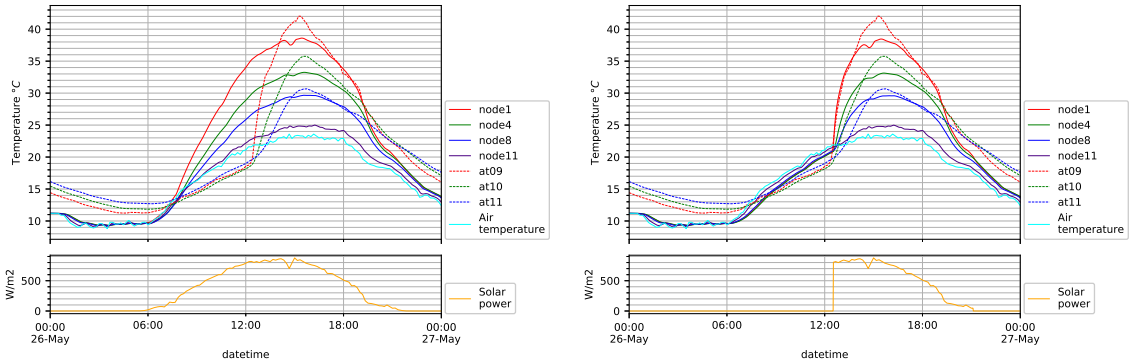

(a) Without Shade

(b) With Shade

Figure B.4: Influence of shade on East cantilever deck temperature. The dashed "at" lines are measurements, the continuous lines are the simulation.

B.3 Heat ODE Results

Temperature inversion

At night the measurements show a temperature inversion. The top of the asphalt is cooler than the bottom of the bulb. The heat ODE does not fully match this result. It is clear however that the top layer of the asphalt initially cools much faster than the steel elements. See figure B.5.
The heat model only contains linear convection. If one would fully model the airflow around the bridge with all its bulbs and crossbeams, one might find that warm air is trapped below the deck. This could act as an insulator, keeping the bottom of the deck warm, and thus explain the temperature inversion. Nu further study is made on this. Another explanation may be found in the temperature of the water below the bridge. During the day, the water is cooler than the ambient air temperature, but at night this might be the other way around. This is also not studied further.

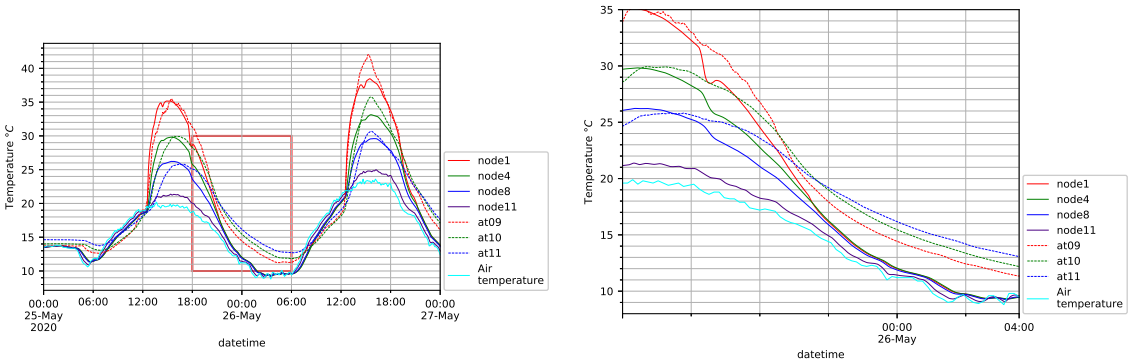

(a) 2 days plot

(b) detail

Figure B.5: Cooling of the bridge, East cantilever deck.

Asphalt temperature versus Solar radiation

For both the east and west cantilever decks. The heat ODE model shows reasonably accurate results of the temperatures near the shoulder of the deck. This implies that the temperature at the shoulder of the deck may be explained by solar radiation only.
At a later time extra Analogue sensors were placed. This time they were positioned below the area where the right wheels of the right lane contact the asphalt. The temperatures here might be described as follows:

- on hot days, the difference between the wheel-contact-area and the shoulder is negligible.
- on cool days, the wheel-contact-area is warmer than it's surroundings.

This implies that wheel-friction raises the temperature of the asphalt, but has a low influence compared to solar irradiation. This is especially true on warm sunny days.

Differences between east and west cantilever

The difference between the east- and west side of the bridge can be explained by the barrier induced shade. See figure B.6. Some small differences remain: The model matches the peak asphalt temperature on the west cantilever and slightly underestimates that temperature on the east cantilever. This difference is within 2 to 4 $^{\circ}C$, based on rudimentary solar information 27 km from the bridge. If local wind speed, wind direction, rainfall and some model updating were applied, even better results might be obtained, but that is beyond the scope of this thesis.

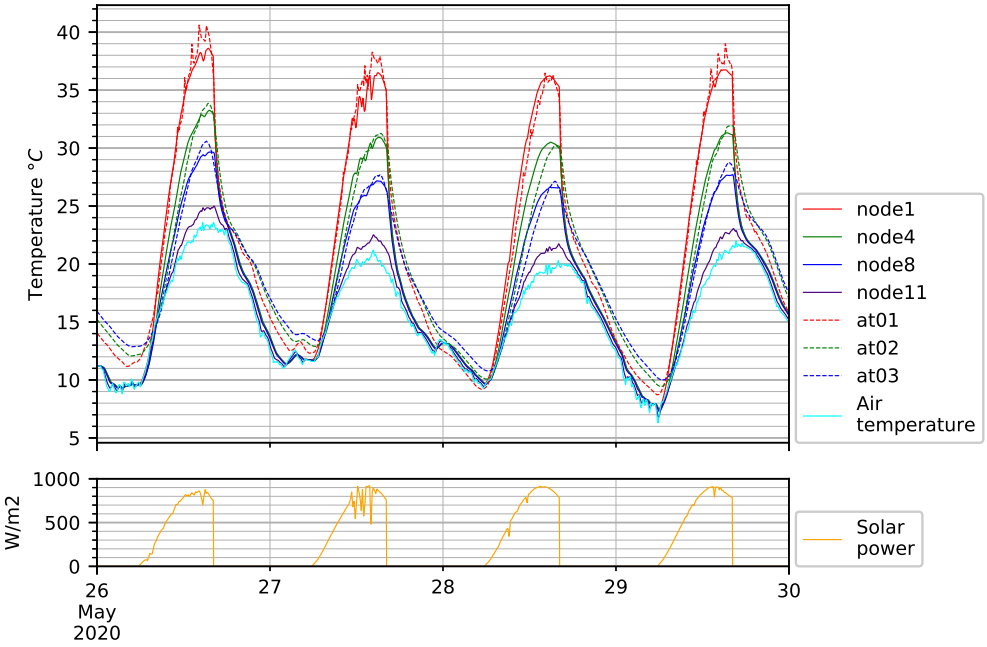

(a) West cantilever

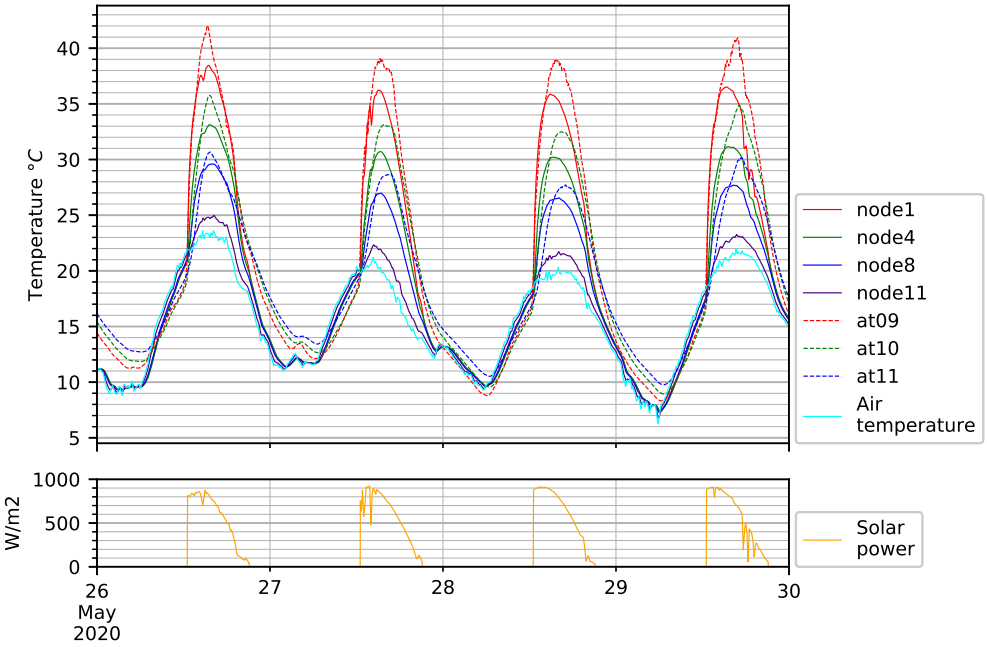

(b) East cantilever

Figure B.6: Temperatures near the edge of a lane. Lines with identical color should match: red is top asphalt, green is bottom asphalt, blue is bottom deck plate and purple is the bulb, see also figure: B.1

Differences between the box and the cantilever

For the east and west cantilever, identical parameters for radiation and convection heat loss were used. If these same parameters are also used above the box, the results deviate significantly. See figure B.7.
It seems as if 2 things happen:

1. The maximum temperature is underestimated significantly. This problem is more pronounced at the west side of the box.
2. The measurements show that the cooling rate $\frac{dT}{dt}$ above the box is smaller than the cantilever.

There is no reason to assume that convection at the top of the deck is significantly different. The geometry and material properties are also identical. This leaves convection at the bottom of the deck plate as the only remaining variable. Inside the box, the air is trapped. There is no wind, and the temperature of the air can be significantly different from the outside ambient temperature. This matches a personal observation that the air in the top of the box was significantly warmer than the outside air on a sunny summer day.

To try and account for this trapped heated air, the convection parameter has been modified. The bottom convection is reduced to 2/27 times the original value. With these values the maximum temperatures for the bottom deck plate show a better accuracy. The result is shown in figure B.8. The total match however, is still poor. For the East side the onset of warming happens too soon, and the cool down still happens too fast. The model seems to correctly account for solar radiation and traffic conditions as can be seen at the cantilevers. This implies that a significant amount of heat capacity of the bridge is unaccounted for: The air inside the box. A quick hand calculation shows that the heat capacity of the steel deck plate and bulb is approximately
$(0.01\text{m} + 0.008\text{m} * .128\text{m}/0.3) * 7850\text{kgm}^{-1} * 490\text{kJkg}^{-1}\text{C}^{-1} \approx 50\text{kJm}^{-2}$
while a $5m$ high air column inside the box has a heat capacity of approximately
$1\text{m} * 1\text{m} * 5\text{m} * 1.276\text{kgm}^{-1} * 1.005\text{kJkg}^{-1}\text{C}^{-1} \approx 6\text{kJm}^{-2}$
and thus might have a significant influence. The air might also travel in the east-west direction, transporting heat in a way that is unaccounted for with this simple 1D-ODE. Without modelling the full air temperature distribution inside the box, the results will probably remain poor. The complete heat transfer within the air inside the box is beyond the scope of this report. However, in future studies it should not be overlooked.

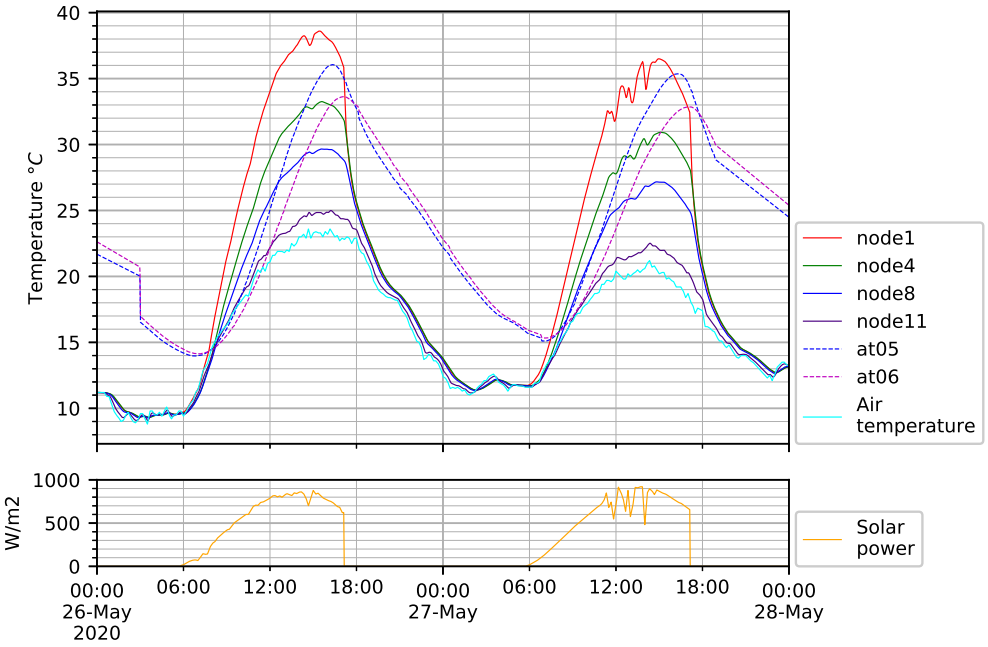

(a) West

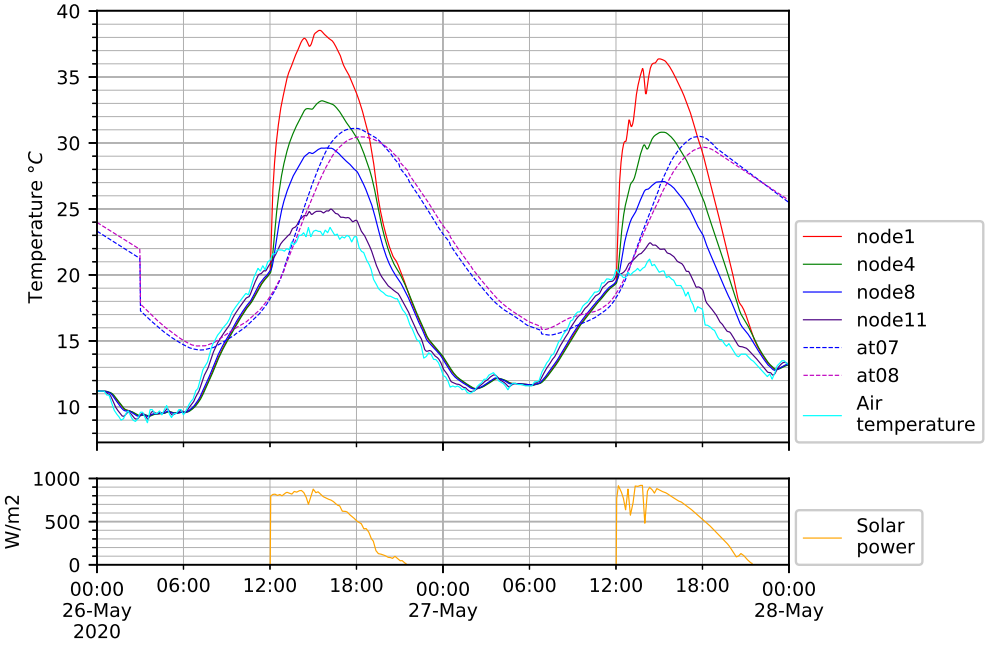

(b) East

Figure B.7: Temperatures near the edge of a lane, above the box. Lines with identical color should match: red is top asphalt, green is bottom asphalt, blue is bottom deck plate and purple is the bulb, see also figure: B.1

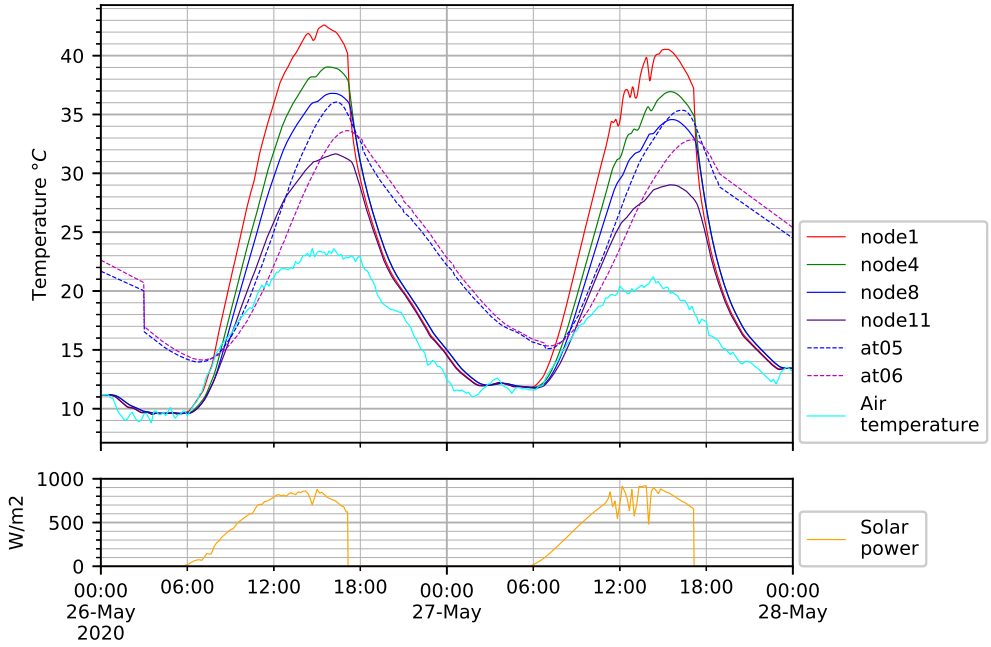

(a) West side

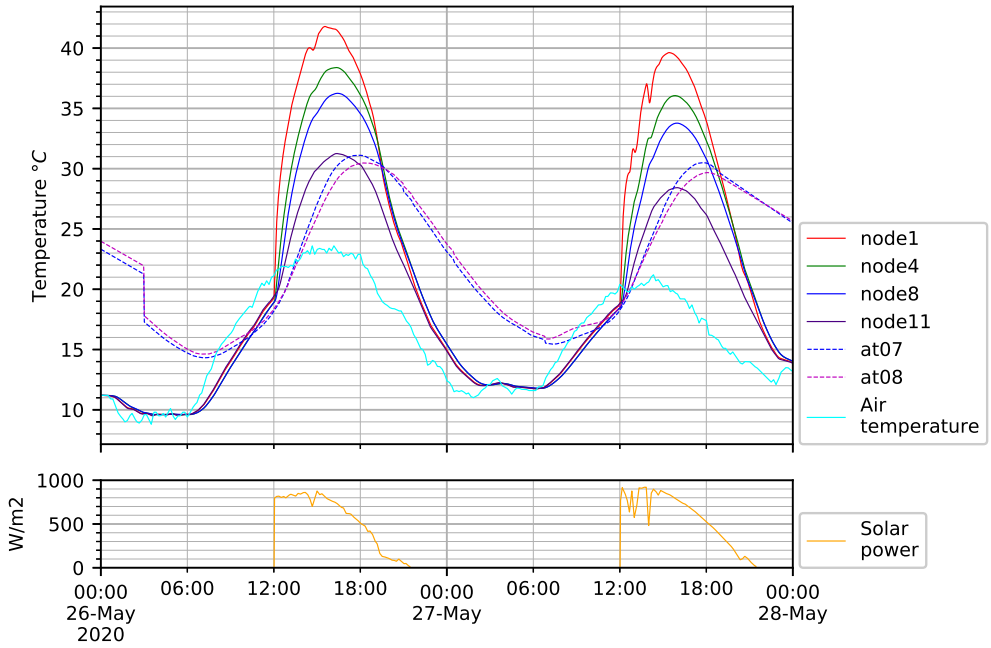

(b) East side

Figure B.8: Temperatures near the edge of a lane, above the box, with reduced bottom convection and radiation

Influence of tire friction

In September a few of the temperature sensors were moved. At02 and at04 have been disconnected and replaced with at32 and at31 respectively, measuring the deck plate and bulb of the west cantilever at a position below the wheel-contact-area. The strain sensors b37 and b04 were on these same positions.
With these sensors the influence of the tire friction and other traffic-induced-heat may be studied. A section of the measurements is shown in figure B.9. Note that this is a different timespan than all previous graphs.
The at32 sensor reaches a higher temperature than the at02 and at11 sensors. To check whether this is traffic-induced the same heat-ODE model is used.

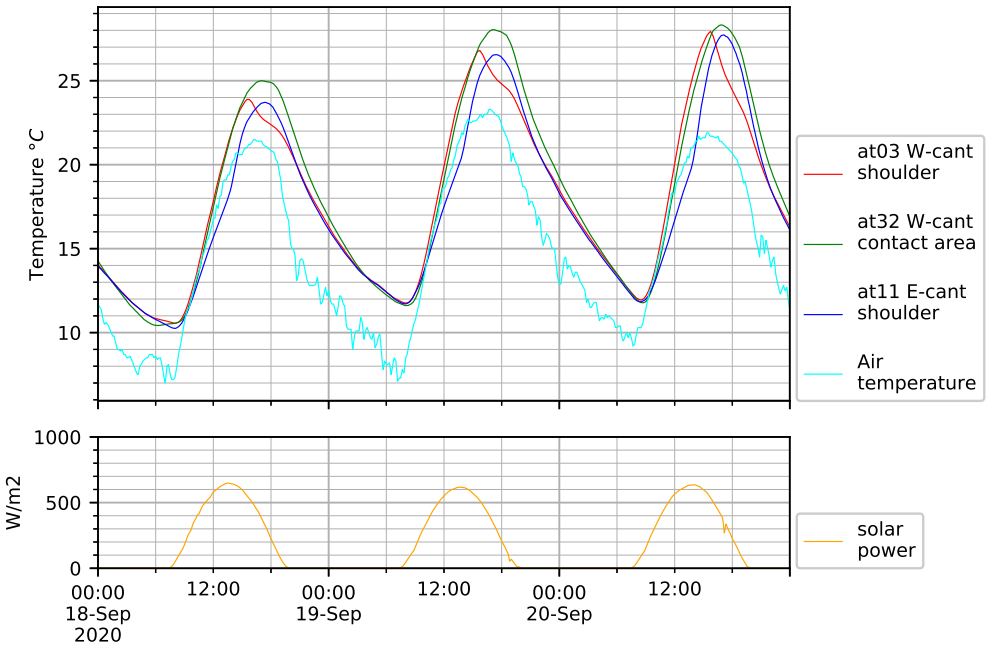

Figure B.9: Temperatures Cantilever

The parameters of the west cantilever were copied, while the position relative to the barriers was updated. The results of this new simulation is shown in figure B.10. For clarity the asphalt temperature's are omitted. One should be aware that the solar azimuth and inclination from a day in June were used, and this data is from September. This might explain the early onset of the warming. The global view however is that the ODE sometimes overestimates and sometimes underestimates the temperature of at32. This implies there is no significant rise of deck plate temperature due to tire friction and other traffic induced heat.

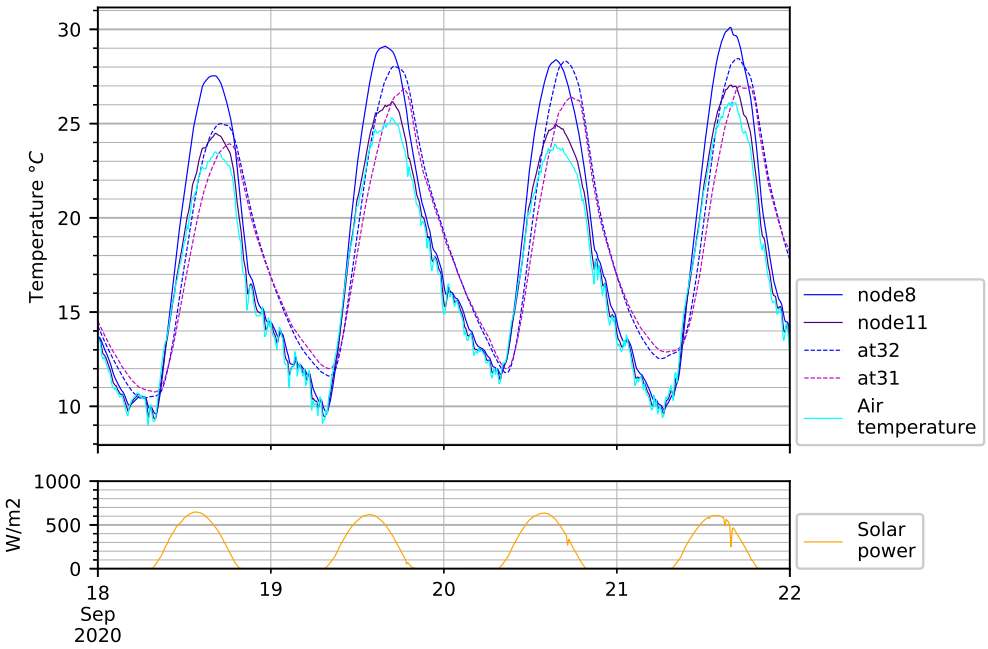

Figure B.10: West cantilever deck below wheel contact area

B.4 Heat ODE Summary

The heat ODE was studied to clarify the temperature measurements. The questions that arose due to the measurement data were answered. They are repeated here for clarity.

- During the day top asphalt is warmer than bottom deck plate, but at night this is the other way round. Is this plausible?
  –Yes, inversion might occur.
- The asphalt temperature rises significantly during the day, can this be explained by solar radiation only?
  –Yes, the heat ODE shows that solar radiation fully explains the significant temperature rise.
- There is a significant temperature difference between sensor locations. What is the cause for this difference between the following locations?
  - East-West
  - East cantilever
  - West side above the box
  - East side above the box
  - West side cantilever, directly under the wheel area. (instead of on the shoulder)

  –East-west differences are explained with barrier-induced shade.
  –The area above the box is most likely influenced by trapped air in the box. To verify this hypothesis it is advised to place a sensor that is capable of measuring the air temperature inside the box. The channel from at06 or at08 may be sacrificed for this purpose.